Iodinated polymer nanoparticles as contrast agents for spectral CT

Joëlle Balegamire

N° d'ordre NNT : 2019LYSE1047

THÈSE DE DOCTORAT DE L'UNIVERSITÉ DE LYON
opérée au sein de
l'Université Claude Bernard Lyon 1

École Doctorale ED206
Ecole Doctorale de Chimie de Lyon

Spécialité de doctorat : Sciences Pharmaceutiques
Discipline : Physico-chimie - Nanomédecine

Soutenue publiquement le 28/03/2019, par :
Joëlle BALEGAMIRE

Iodinated polymer nanoparticles as contrast agents for spectral CT

Devant le jury composé de :

Pr Laurent David, Professeur, Université de Lyon	Président
Pr Christine Vauthier, Directrice de Recherche CNRS, Université Paris Sud	Rapporteur
Dr Emmanuelle Marie-Bégué, Chargée de Recherche CNRS, ENS Paris	Rapporteur
Pr Loïc Boussel, Professeur - Praticien hospitalier, Université de Lyon	Examinateur
Pr Giuseppe Digilio, Professeur, Università degli studi di Torino	Examinateur
Dr Yves Chevalier, Directeur de Recherche CNRS, Université de Lyon	Directeur
Pr Hatem Fessi, Professeur, Université de Lyon	Invité

Acknowledgments

Un jour j'irai vivre en théorie parce qu'en théorie tout se passe bien...

Les travaux présentés dans ce mémoire ont été réalisés au sein du Laboratoire d'Automatique, de Génie des Procédés et de Génie Pharmaceutique (LAGEPP, UMR 5007 CNRS). Je tiens donc à remercier Stéphanie Briançon, directrice du LAGEPP, de m'avoir accueillie au sein du laboratoire.

Mes remerciements vont aussi à mes encadrants Yves Chevalier et Hatem Fessi qui ont su me transmettre une certaine rigueur scientifique et un esprit critique. Merci pour votre confiance, votre bienveillance et votre disponibilité. Les longues et nombreuses discussions scientifique et autres, furent plus qu'un apprentissage du monde de la recherche, des leçons de vie.

Tout livre a pour collaborateur son lecteur...

Je tiens à remercier Christine Vauthier et Emmanuelle Marie-Bégué d'avoir lu et rapporté ce travail. Merci également aux autres membres du jury, Laurent David, Giuseppe Digilio, Loïc Boussel pour leurs retours, suggestions et les discussions qui ont apporté une autre perspective à ce manuscrit.

Lorsque deux forces sont jointes, leur efficacité est double...

Ce travail n'aurait pas été possible sans diverses collaborations. Ainsi, j'exprime toute ma reconnaissance à Philippe Douek, responsable du projet Européen, qui a habilement assemblé les pièces pour former un puzzle d'innovation solidaire et efficace. Un grand merci aux membres du projet Européen (SPCCT) pour les discussions passionnantes. Cela a été extrêmement enrichissant pour moi d'évoluer dans un environnement multidisciplinaire et multiculturel.

Je souhaite également remercier toutes les personnes qui ont participé d'une façon ou d'une autre à l'obtention des différents résultats. Merci à Salim Si-Mohamed et Daniel Bar-Ness pour les tests *in vitro* ; Marc Vandamme et Emmanuel Chereul pour les études *in vivo* ; Samira Azzouz-Maache et Marion Guichard pour l'étude de biodégradation ; Rachele Stefania, Federico Capuana, Giuseppe Digilio et Laurence Heinrich-Balard pour les expériences de bioconjugaison. Cette interdisciplinarité et ce travail d'équipe constituent une base solide sur laquelle je souhaite bâtir mon avenir professionnel.

Je tiens à exprimer ma gratitude à Eyad Almouazen qui a apporté une contribution scientifique considérable à ce travail. Merci pour ton temps et ta bonne humeur. Merci aussi aux membres de l'équipe Génie Pharmaceutique (GéPharm) qui ont su répondre présents en cas de questions et qui m'ont permis de nourrir ma curiosité scientifique.

L'inspiration d'un moment vaut l'expérience d'une vie...

Il m'est important de remercier ma maître de stage, Laure Ridel. Tu as su planté la graine de la recherche pendant ce stage de M1. Cette graine a germé et a donné place à un bel arbre de connaissance. Si je suis ici aujourd'hui c'est aussi grâce à toi et pour ça merci. Je profite de ce paragraphe pour à mon tour dire un grand merci à mes stagiaires. Merci pour votre motivation. J'espère vous avoir transmis au moins autant que vous m'avez appris.

Et il y a des rencontres qui te font sourire et te feront sourire encore des années plus tard...

Je souhaite remercier chaleureusement les membres du LAGEPP avec lesquels j'ai passé trois belles années de ma vie. Géraldine, Emilie, Elodie, Sébastien, Quentin, Maroua, Maya, Greta, Claudia, Stéphane, Maité, Fabrice, Aline, Pierre, Noureddine, Claudia, Madiha, Vincent, Pascal, Daniele, Haitem, Bertrand, Louis, Marc-Aurèle, Alexis, Catherine, Claire, Nadia, Jean-Pierre, Yves simplement merci

Merci à mes spicy girls, mes 4 moskitos, Océane, Romain, Camille et Joris, qu'est-ce qu'on a ri ! Clairement grâce à vous ma thèse a été une vraie partie de franche rigolade.

Ah ces amis qui deviennent la famille...

A mes amis extra-scolaires/ordinaires : Manuela, Eléonore, Maurine, Elodie, Sébastien, la familia, vous m'avez apporté un équilibre dont j'avais besoin pour continuer dans ce projet fou qui est la thèse. Merci pour la surprise la plus surprenante de ma vie mais surtout merci d'en faire partie.

Je suis moi parce que vous êtes vous donc merci d'être là, merci d'être vous...

Une pensée spéciale à la team Belfaux (Brigitte, Pierre-Edouard et la famille Guerry toute entière) merci d'être là. Un peu comme dans une cérémonie des oscars, je ne saurais clore ces remerciements sans parler du soutien de ma famille. Maman Lolo, Senhor Papa, merci d'avoir tant sacrifié pour que Rachel, Julien, Eliane, Steve et moi-même puissions nous forger et évoluer de la meilleure façon possible. Cette thèse est celle de la starting five toute entière. Ma hantise est de vous décevoir, ma fierté est de vous rendre fière.

Résumé

Le scanner spectral à comptage photonique (SPCCT) associé à des agents de contraste spécifiques pourrait détecter certaines inflammations cardiovasculaires à un stade précoce. Les agents de contraste utilisés actuellement en imagerie à rayons X sont des petites molécules qui sont éliminées du système cardiovasculaire en quelques minutes. D'où la nécessité de développer des nanosystèmes présentant des nouvelles caractéristiques intéressantes (ciblage passif/actif, temps de circulation sanguine prolongé, etc.). Dans ce projet de recherche, des nanoparticules (NPs) de polymères iodés ont été produites à l'aide du procédé de nanoprécipitation. Dans un premier temps, les paramètres de procédé et de formulation ont été optimisés pour fournir un agent de contraste répondant à des spécifications physicochimiques précises. Des nanoparticules composées d'une matrice de polymère iodé enveloppée de PEG provenant de l'agent dispersant (PCL_{65}-*b*-PEG_{113}) ont été formulées. Ces suspensions de NPs sont extrêmement stables (jusqu'à 8 mois dans l'eau et dans le serum humain), monodisperses, avec un diamètre moyen de 150 nm. Une concentration en iode de 100 g(I).mL^{-1} obtenue après une étape de centrifugation / redispersion a fourni un agent de contraste avec une radiopacité dans la gamme appropriée pour l'imagerie du système cardiovasculaire et l'étude de la biodistribution. Les algorithmes de reconstructions implémentés dans le SPCCT (Decomposition de la matière et reconstruction K-edge), ont permis une quantification précise de l'iode, ainsi qu'une discrimination spécifique du gadolinium et de l'iode dans des phantoms contenant un mélange des deux éléments. La biodistribution a été évaluée après injection des NPs à des rats par voie intraveineuse. Les NPs permettent une visualisation détaillée du système cardio-vasculaire jusqu'à 5 heures, accompagnée d'une accumulation progressive dans le foie et la rate. Ces deux organes étaient toujours visibles 15 jours après l'injection. Une étude de biodégradation des NPs a été menée sur des cellules de macrophages. Malgré la biodégradabilité potentielle des polymères, les NP intériorisées par les macrophages par phagocytose au cours d'une incubation de 5 heures restent intactes pendant 5 semaines, tandis que certaines cellules sont dégradées. Des NPs ciblant la tropoélastine ont également été synthétisées pour l'imagerie active de la plaque d'athérosclérose au niveau moléculaire. Un test Biacore a montré une affinité des NPs conjuguées avec le peptide de ciblage vis-à-vis de la molécule réceptrice (tropoélastine).

Abstract

The Spectral Photon Counting Computed Tomography (SPCCT) technology associated with specific contrast agents could detect some cardiovascular inflammations at an early stage. Currently, contrast agents for CT are small molecules that are eliminated from the cardiovascular system within few minutes. Hence there is a need to develop nanosystems that present new interesting features (passive/active targeting, long blood circulation times, etc.). In this work, iodinated polymer nanoparticles (NPs) were produced using the nanoprecipitation process. First, the process and formulation parameters were optimized to provide a contrast agent that meets definite physicochemical specifications. Highly stable (up to 8 months in water and human serum), monodisperse suspensions of spherical NPs with an average diameter of 150 nm were obtained. The iodinated polymer matrix core is coated by a PEG shell provided by the dispersing agent (i.e. PCL_{65}-*b*-PEG_{113}). An iodine concentration of 100 g(I).mL^{-1} reached after a centrifugation/redispersion step provided radiopacity of the contrast agent in the right range for imaging cardiovascular system and studies of biodistribution. SPCCT material decomposition and K-edge reconstruction allowed accurate quantification of iodine, as well as specific discrimination of gadolinium and iodine in phantoms containing mixtures of both elements. Biodistribution was assessed after intravenous injection of iodinated polymer NPs to rats, revealing a clear visualization of the cardiovascular system up to 5h, and progressive accumulation in liver and spleen. These organs were still visible up to 15 days post-injection. A biodegradation experiment was carried out on macrophages cell culture. Despite the potential biodegradability of the polymers, NPs internalized by the macrophages after a 5h incubation via the phagocytosis mecanism, remained intact during 5 weeks, while some cells were degraded. Tropoelastin targeting NPs were also developed for active imaging of the atherosclerosis plaque at the molecular level. A Biacore test showed specific affinity of the NPs conjugated with the targeting peptide towards tropoelastin.

General Preamble

The work described in this manuscript was carried out at the Laboratoire d'Automatique, de Génie dEs Procédés et de génie Pharmaceutique (LAGEPP), which is a joint research unit (UMR 5007) of the CNRS (Centre National de la Recherche Scientifique) and of the University of Lyon 1. This work was supported by the SPCCT project. This research project has received funding from European Union through Horizon 2020 research and innovation program under grant agreement No 643694.

The manuscript is based on two publications, which form chapters 2 and 3. Chapters 4, 5 and 6 are written in scientific article style. Each publication is introduced by a preamble but the contents of the publications are unchanged except for the section, figure, table and equation numbers and the numbering of references which were adapted to follow the manuscript format.

The publication references are the following:

1. **J. Balegamire**, M. Vandamme, E. Chereul, S. Si-Mohamed, L. Ettouati, S. Azzouz Maache, H. Fessi, L. Boussel, P. Douek, Y. Chevalier, Iodinated polymer nanoparticles as contrast agent for computed tomography using a spectral photon-counting CT, Biomaterials (to be submitted, 2019)

2. **J. Balegamire**, M. Vandamme, E. Chereul, H. Fessi, S. Si-Mohamed, L. Boussel, P. Douek, Y. Chevalier, Optimization of the nanoprecipitation parameters in the fabrication of iodinated polymer nanoparticles as contrast agent for CT, Colloids and Surfaces A (to be submitted, 2019)

The following article was a fruit of multiple collaborations:

D.P. Cormode, S. Si-Mohamed, D. Bar-Ness, M. Sigovan, P.C. Naha, **J. Balegamire**, F. Lavenne, P. Coulon, E. Roessl, M. Bartels, M. Rokni, I. Blevis, L. Boussel, P. Douek, Multicolor spectral photon-counting computed tomography: *in vivo* dual contrast imaging with a high count rate scanner, Sci. Rep. vol. 7,1 4784. 6 Jul. 2017.

A patent application is under discussion following the development of iodinated polymer NPs as CT contrast agents. The main claim is long circulation time of those NPs in the bloodstream which makes them interesting blood pool agents for preclinical studies.

The work on the synthesis and characterization of the iodinated polymer nanoparticles and their application as contrast agents for CT using a SPCCT scanner (cf. chapters 2 and 3), was also presented during international conferences either through oral presentations or posters:

- NanoHybrides 14, March 2017, Corsica - France (Oral presentation).
- 8th International Colloids Conference, June 2017, Sitges/Barcelona - Spain (Poster).
- 31st Conference of the European Colloid & Interface Society (ECIS), September 2017, Madrid - Spain (Oral presentation).
- NanoTech France, June 2017, Paris - France (Oral presentation).
- French Imaging Network of Young Scientists (FINYS) 2nd annual meeting, October 2017, Varennes - France (Best oral presentation).
- Club émulsion, October 2017, Lyon - France (Oral presentation).
- Science For Biomaterials (SFB2018), April 2018, Atlanta - USA (Oral presentation).
- ANF NanoMed, June 2018, Semur-en-Auxois - France (Poster).
- Formulations Days, January 2019, Lyon - France (Oral presentation).

Contents

Remerciements i

Abstract (English and French) i

General Preamble i

Contents iii

List of Figures ix

List of Tables xiii

Introduction 1

1 State of the Art 5

1.1 X-Rays for medical diagnosis . . . 6

1.1.1 From radiations to 3D image . . . 6

1.1.1.1 X-Rays . . . 6

1.1.1.2 Interaction with matter . . . 9

1.1.1.3 When energy becomes a 3D image . . . 12

1.1.2 X-Ray Computed Tomography (CT): the story of an evolution . . . 16

1.1.2.1 Conventional CT . . . 16

1.1.2.2 Dual-Energy CT (DECT) . . . 17

1.1.2.3 Spectral Photon Counting CT (SPCCT) or Multi-Energy CT 19

1.1.3 Added value of SPCCT: focus on cardiovascular imaging . . . 22

1.1.4 Conclusion . . . 23

1.2 Contrast agents for CT . . . 24

1.2.1 Definition and properties . . . 24

1.2.1.1 Definition . . . 24

1.2.1.2 Properties of contrast agents for CT and SPCCT . . . 24

1.2.2 Iodine-based nanobiomaterials for CT imaging . . . 26

1.2.2.1 Liposomes . . . 28

1.2.2.2 Nanoemulsions . . . 29

1.2.2.3 Dendrimers . . . 30

1.2.2.4 Micelles . . . 31

1.2.2.5 Polymeric nanoparticles (PNPs) . . . 33

1.3 Processes for polymeric nanoparticles (PNPs) production . . . 35

1.3.1 Polymerization of monomers . . . 35

1.3.1.1 Emulsion polymerization . . . 36

1.3.1.2 Dispersion polymerization . . . 36

1.3.1.3 Micellar polymerization or inverse microemulsion polymerization 37
1.3.1.4 Interfacial polymerization . . . 37
1.3.2 Preformed polymer dispersion . . . 37
1.3.2.1 Emulsification solvent evaporation method . . . 38
1.3.2.2 Emulsification-solvent diffusion technique . . . 38
1.3.2.3 Salting-out . . . 39
1.3.2.4 Nanoprecipitation process . . . 40
1.3.3 Conclusion . . . 42
1.4 General conclusion and aim of the work . . . 44
1.4.1 State of the Art and conclusion . . . 44
1.4.2 Aim of the work . . . 45

2 Characterization and properties evaluation 47
2.1 Abstract . . . 49
2.2 Introduction . . . 49
2.3 Experimental section . . . 50
2.3.1 Materials . . . 50
2.3.1.1 Synthesis of the iodinated polymer (TIB-PVAL) . . . 51
2.3.1.2 Preparation of nanoparticles . . . 53
2.3.1.3 Concentration step . . . 53
2.3.2 Methods . . . 54
2.3.2.1 Characterization of the iodinated polymer . . . 54
2.3.2.2 Characterization of iodinated polymer nanoparticles . . . 55
2.3.2.3 Cytotoxicity . . . 55
2.3.2.4 CT imaging . . . 55
2.4 Results and discussion . . . 56
2.4.1 Synthesis and characterization of iodinated polymer (TIB-PVAL) . . . 56
2.4.1.1 Grafting reaction and ^{1}H NMR analysis . . . 56
2.4.1.2 Degree of substitution (DS) and iodine content (%I) . . . 56
2.4.1.3 Thermal analysis and X-ray diffraction . . . 57
2.4.2 Iodinated polymer nanoparticles: physicochemical characterization . . . 58
2.4.2.1 Nanoparticles size, morphology and stability . . . 58
2.4.2.2 Quantification of PEG on nanoparticles surface . . . 60
2.4.3 Cytotoxicity assessment . . . 65
2.4.4 Radiopacity assessment . . . 65
2.4.4.1 Iodinated polymer nanoparticles attenuation in Hounsfield Units (HU) . . . 65
2.4.4.2 Element quantification using “Material Decomposition” with SPCCT . . . 66
2.4.4.3 Discrimination of two elements in a mixture with SPCCT . . . 67
2.4.4.4 The *in vivo* study: Iodinated polymer nanoparticles . . . 68
2.5 Conclusions . . . 72

3 Formulation parameters 73
3.1 Abstract . . . 75
3.2 Introduction . . . 76
3.3 Experimental section . . . 77
3.3.1 Materials . . . 77

3.3.2 Methods . . . 77
3.3.2.1 Preparation of nanoparticles . . . 77
3.3.2.2 Characterization . . . 78
3.3.2.3 *In vivo* CT-imaging . . . 79
3.4 Results . . . 79
3.4.1 Model composition . . . 80
3.4.1.1 Polymer amount . . . 80
3.4.1.2 Choice of the dispersing agent . . . 80
3.4.2 Process conditions . . . 85
3.4.2.1 Phase addition rate . . . 85
3.4.3 Optimum formulation and process . . . 85
3.4.4 Iodinated polymer nanoparticles: radiopacity assessment . . . 86
3.4.4.1 *In-vivo* study . . . 86
3.5 Discussion . . . 90
3.6 Conclusions . . . 92

4 Degradation of iodinated polymer nanoparticles: a study on macrophages 93
4.1 Introduction . . . 95
4.1.1 Macrophages . . . 95
4.1.1.1 Definition and role . . . 95
4.1.1.2 Nanoparticles (NPs) internalization and degradation . . . 95
4.1.2 Polymeric nanoparticles (PNPs): Influence of physicochemical characteristics on uptake by macrophages . . . 98
4.1.2.1 Size . . . 98
4.1.2.2 Morphology . . . 98
4.1.2.3 Surface properties . . . 98
4.1.2.4 Rigidity . . . 99
4.1.3 Aim of the study . . . 99
4.2 Experimental section . . . 99
4.2.1 Materials . . . 99
4.2.2 Methods . . . 100
4.2.2.1 Evaluation of the nanoparticles (NPs) cytotoxicity . . . 100
4.2.2.2 Evaluation of NPs uptake and degradation by macrophages . 100
4.2.3 Characterization . . . 102
4.2.3.1 Observation of internalization and degradation (TEM) . . . 102
4.2.3.2 Iodine content assessment . . . 102
4.3 Results and discussion . . . 102
4.3.1 Definition of a viable iodine concentration . . . 102
4.3.2 TEM images of iodinated polymer NPs in macrophages . . . 103
4.4 Conclusion . . . 106

5 Atherosclerosis-targeting iodinated polymer nanoparticles 107
5.1 Introduction . . . 109
5.1.1 Atherosclerosis . . . 109
5.1.1.1 From plaque build-up to clot formation . . . 109
5.1.1.2 Plaque composition at different stages . . . 110
5.1.1.3 Plaque related diseases . . . 111
5.1.2 Imaging technology . . . 112

5.1.2.1 Invasive techniques . . . 112
5.1.2.2 Non-invasive techniques . . . 112
5.1.2.3 Spectral Photon-Counting CT (SPCCT) . . . 112
5.1.3 Molecular imaging . . . 113
5.1.3.1 Choice of the target . . . 113
5.1.3.2 Properties of the vectors for active targeting . . . 114
5.1.4 Aim of the study . . . 114
5.2 Experimental section . . . 114
5.2.1 Materials . . . 114
5.2.1.1 Synthesis of SA-PEG1000-MAL-TESMA . . . 115
5.2.1.2 Formulation of tropoelastin targeting iodinated polymer NPs 116
5.2.1.3 Concentration step . . . 116
5.2.2 Methods . . . 116
5.2.2.1 Characterization of SA-PEG1000-MAL-TESMA . . . 116
5.2.2.2 Physicochemical characterization of tropoelastin targeting NPs 118
5.2.2.3 Bioconjugation assessment . . . 118
5.3 Results and discussion . . . 119
5.3.1 Synthesis of SA-PEG1000-MAL-TESMA . . . 119
5.3.1.1 Grafting reaction and ^{1}H NMR analysis . . . 119
5.3.1.2 UPLC-MS/HPLC-MS results . . . 119
5.3.2 Tropoelastin targeting iodinated polymer NPs . . . 121
5.3.2.1 Physicochemical properties: size, morphology and ζ potential 121
5.3.2.2 Bioconjugation assessment . . . 121
5.4 Conclusion . . . 124

6 Synthesis of tantalum oxide (Ta_2O_5) nanoparticles for SPCCT K-edge imaging 125
6.1 Introduction . . . 128
6.1.1 Tantalum oxide nanoparticles in CT imaging . . . 128
6.1.2 Manufacturing process . . . 129
6.1.2.1 Microemulsion method . . . 129
6.1.2.2 Sol-gel process . . . 129
6.1.3 Aim of the study . . . 131
6.2 Experimental section . . . 132
6.2.1 Materials . . . 132
6.2.2 Protocols . . . 132
6.2.2.1 Acidic conditions . . . 132
6.2.2.2 Basic conditions . . . 132
6.2.2.3 Neutral conditions . . . 133
6.2.3 Characterization . . . 133
6.3 Results and discussion . . . 134
6.3.1 Size and morphology (TEM) . . . 134
6.3.1.1 Acidic catalysis synthesis . . . 134
6.3.1.2 Basic catalysis synthesis . . . 135
6.3.1.3 Neutral synthesis . . . 135
6.3.2 Size and particle size distribution (DLS) . . . 135
6.3.3 Dispersibility in water . . . 137
6.4 Conclusion . . . 138

Conclusion **139**

A Full TEM sample preparation for macrophages observation **143**
A.1 Materials 143
A.2 Method 143

B Synthesis of tropoelastisn targeting polypeptide **145**
B.1 Materials 145
B.2 Method 145

C Surface plasmon resonance (SPR) and Biacore technology **147**
C.1 Surface Plasmon Resonance (SPR) 147
C.1.1 Total reflection 147
C.1.2 Plasmon resonance 148
C.1.3 Response Unit (RU) 148
C.1.4 Equilibrium dissociation constant (K_D) 149
C.2 Biacore 150
C.2.1 Material 151
C.2.2 Method 151

Reference **153**

List of Figures

1.1 Operational principle of an X-ray scanner . . . 6
1.2 Electromagnetic radiations spectrum . . . 7
1.3 X-ray tube (generator) . . . 7
1.4 X-ray spectrum . . . 8
1.5 Bohr model of the structure of an atom . . . 9
1.6 X-ray photons/electrons interaction-dominant domains according to the photon energies . . . 10
1.7 Photoelectric effect . . . 11
1.8 Compton scattering . . . 11
1.9 Beer-Lamber law . . . 12
1.10 Attenuation profiles of different tissues in function of the incident X-ray energy [2] . . . 13
1.11 Beer-Lambert law when X-ray is attenuated by different profiles . . . 13
1.12 Attenuation of X-ray photons in different tissues . . . 14
1.13 Hounsfield Units (HU) scale of different tissues . . . 15
1.14 First medical X-ray picture of Anna B. Röntgen's hand bone structure and ring (1895) . . . 16
1.15 Global information provided by the energy integrating detectors . . . 16
1.16 Dual source configuration . . . 17
1.17 Dual kVp scanning configuration . . . 18
1.18 Dual fast kVp switching configuration . . . 19
1.19 Dual layer configuration . . . 20
1.20 Spectral information provided by the energy integrating detectors of DECT . 20
1.21 Spectral photon counting configuration . . . 21
1.22 Spectral information provided by the photon counting detectors of the SPCCT 21
1.23 Chemical structure of small molecules, medically approved CT contrast agents 25
1.24 Publications in the area of computed tomography and iodinated nanoparticles over the past 24 years. Data acquired from a search of "computed tomography" AND "nanoparticles" AND "Iodine" keywords in the ScienceDirect database . 26
1.25 Representation of an iodinated nanobiomaterial of CT contrast agent and the different features possible . . . 27
1.26 Structure of an iodinated liposome . . . 28
1.27 Iodinated oil-in-water nanodroplet . . . 29
1.28 Opacification of Generation 4 Poly(amidoamine) (PANAM) dendrimers . . . 30
1.29 Radiopaque micelles for CT . . . 32
1.30 Polymeric NanoParticles (PNPs) . . . 33
1.31 Polymeric nanoparticles (PNPs) formation from monomer polymerization . . . 35

1.32 Schematic representation of the emulsification-solvent evaporation process for fabrication or PNPs 38
1.33 Schematic representation of the emulsification-solvent diffusion process for fabrication or PNPs 39
1.34 Schematic representation of the salting-out process for fabrication or PNPs . . 40
1.35 Schematic representation of the nanoprecipitation process for fabrication or PNPs 41

2.1 Synthesis of iodinated polymer (TIB-PVAL): synthesis of 2,3,5-triiodobenzoyl chloride (top), covalent linkage of 2,3,5-triiodobenzoyl chloride to poly(vinyl alcohol) (bottom). 52
2.2 TIB-PVAL ^{13}C NMR position 53
2.3 The nanoprecipitation process. 53
2.4 Modified PVAL with a radiopaque tri-iodobenzoyl moiety and ^{1}H NMR spectrum of TIB-PVAL in DMSO-*d6*. 57
2.5 X-ray diffraction of TIB-PVAL 58
2.6 Variation of nanoparticles z-average diameter (from DLS) against iodinated polymer concentration in the organic solvent (THF). 59
2.7 TEM pictures of TIB-PVAL nanoparticles before (A), after (B) centrifugation/redispersion and (C) particle size distribution from CONTIN analysis of DLS. 60
2.8 Iodinated polymer nanoparticles stability in water at 4, 20 and 37°C (top) and in human serum at 4 and 37°C (bottom) 61
2.9 Reference ^{1}H NMR spectra of 1/1 PCL_{65}-*b*-PEG_{113}/TIB-PVAL mixture in DMSO-*d6*. 63
2.10 Various configurations of PEG chains according to the surface density. R_h: hydrodynamic radius of an unperturbed chain (minimum distance required between grafted molecules to achieve a mushroom configuration); *D* distance between anchoring points. 64
2.11 Cell viability after 5 h exposure to aqueous suspensions of iodinated nanoparticles of various concentrations. Viability was assessed 24 h and 48 h after the end of exposure to nanoparticles. 65
2.12 Compressed iodinated polymer (A), Phantom tube containing the suspensions of iodinated polymer nanoparticles in water (B,) graph of Iodinated polymer nanoparticles attenuation in Houndfield Units (HU) with respect to concentration (C). 66
2.13 Quantification of iodine using the SPCCT material decomposition (MD) . . . 66
2.14 Attenuation (HU) at different concentrations of a gadolinium/iodine mixture, phantoms containing increasine concentrations of iodine and decreasing concentrations of gadolinium (top). SPCCT images of the iodine and gadolinium mixure with conventional images, iodine material decomposition images, gadolinium K-edge images and overlay images (bottom). 67
2.15 CT images of rats before, 3 h, 120 h after IV injection of iodinated polymer nanoparticles (top). Biodistribution of the iodinated polymer nanoparticles over time. (1.5 mL IV injected, 536 mg[I] · kg-1). Mean ± Sem, n = 3 (bottom). . . 69
2.16 CT images of rats before, 0.5 h, 120 h after IV injection of Omnipaque (top). CT imaging of the Omnipaque biodistribution over time (0.7 mL IV injected). Mean ± Sem, n = 3 (bottom). 70

2.17 Enhancement after intravenous injection into a rats' tail vein of 1.5 mL of aqueous dispersion of iodinated polymer nanoparticles (90-100 mg(I).mL^{-1}). μCT images were acquired before and at different time points after injection. 71

3.1 Chemical structure of 2.3.5-triiodobenzoyl ester of poly(vinyl alcohol) (TIB-PVAL). x = 0.77 and y = 0.23 77
3.2 Schematic representation of the nanoprecipitation process 78
3.3 Dispersing agent structure 81
3.4 Structure of PCL_{65}-*b*-PEG_{113} with n = 65 and m = 113 81
3.5 Structure of a poloxamer 82
3.6 Structure of Brij S100 82
3.7 Structure of PVAL 83
3.8 Structure of sorbitan esters 83
3.9 Structure of Lipoid phospholipids 84
3.10 Transmission Electron Microscopy (TEM) pictures of the iodinated polymer nanoparticles stabilized by PCL_{65}-*b*-PEG_{113} (top), before (A) and after the concentration step (B). Iodinated polymer nanoparticles stabilized by Lipoid S100 before (C) and after the concentration step (D). 86
3.11 Enhancement after intravenous injection into a rat's tail vein of 1.5 mL of aqueous dispersion of iodinated polymer nanoparticles (90-100 mg(I) $\cdot$ mL-1) stabilized by lipoid S100 (top) and PCL_{65}-*b*-PEG_{113} (bottom). CT images were acquired before injection (left), 3 h (middle) and 120 h (right) after the injection. Injected does: 536 mg[I].kg^{-1}). 87
3.12 CT follow up of the biodistribution over time, after intravenous injection into a rat's tail vein of 1.5 mL of aqueous dispersion of iodinated polymer nanoparticles (90-100 mg(I).mL^{-1}) stabilized by Lipoid S100 (top) and PCL_{65}-*b*-PEG_{113} (bottom). Injected does: 536 mg[I].kg^{-1}). Mean $\pm$ Sem, n = 3 89

4.1 Pathways of entry into cells [153] 96
4.2 Endocytosis and exocytosis patterns of nanoparticles. MVBs = multivesicular bodies [160] 97
4.3 6 wells plate composed of 2 empty wells (left), 2 control wells containing 2 mL of macrophages in cell culture medium (middle) and 2 wells containing macrophages incubated 5 h with nanoparticles (right) 101
4.4 Control cell culture flask containing blank macrophages (left) and cell culture flask containing macrophages incubated 5 h with nanoparticles (right) 101
4.5 Cell viability after 5 h exposure to aqueous suspensions of iodinated nanoparticles of various concentrations. Viability was assessed 24 h and 48 h after the end of exposure to nanoparticles 103
4.6 Iodinated polymer nanoparticles internalization by J774A.1 macrophages over time 104
4.7 Representation of hypothetical opsonization and degradation of iodinated polymer NPs inspired by Feliu *et al.* [171]. The iodinated polymer nanoparticles within an *in vivo* environment comprises a matrix of iodinated polymer core (grey), a PEG shell provided by the dispersing agent (PCL_{65}-*b*-PEG_{113}) (red and blue), and at some point adsorbed proteins at the surface. Intracellular degradation may decompose the NPs into individual parts. 104

5.1 Progression of atherosclerosis 109

5.2 The development of an atherosclerotic lesion. The progression of an atherosclerotic lesion is shown in a simplified form, developing from a normal blood vessel (far left) to a vessel with an atherosclerotic plaque and superimposed thrombus (far right). Potential targets for molecular imaging at each stage are also listed. LDL, low-density lipoprotein; MMP, matrix metalloproteinase; VCAM1, vascular cell-adhesion molecule 1 [172]. 110
5.3 Acute vascular events in different sites of the body following arteries clogging [175] 111
5.4 Synthesis of SA-PEG1000-MAL-TESMA by click chemistry 115
5.5 Stack of ^{1}H NMR spectra of SA-PEG1000-MAL, TESMA peptide and SA-PEG1000-MAL-TESMA in deuterated methanol (MeOD) 119
5.6 Stack of UPLC-MS and HPLC-MS spectra of TESMA peptide (bottom), SA-PEG1000-MAL (middle) and SA-PEG1000-MAL-TESMA (top) 120
5.7 Strucure of tropoelastin targeted iodinated polymer nanoparticle 121
5.8 TEM images of non-conjugated iodinated polymer NPs (A), TESMA-conjugated NPs (B) and particle size distribution from CONTIN analysis of DLS 122
5.9 Sensogram representing RU in function of time for TESMA-conjugated NPs on tropoelastin. first jump of RU (t = 60 s) corresponds to injection of NPs, second jump of RU (t = 250 s) corresponds to the injection of the washing/running buffer 123
5.10 Sensogram representing the signal in RU in function of time for NPs-TESMA, non-conjugated-NPs on tropoelastin and NPs-TESMA on dextran after subtraction of the jumps. 123

6.1 Formation of metal oxide nanoparticles with the sol-gel process 129
6.2 Dependence of the relative rates of Si(OR_4 hydrolysis and of condensation reactions on the pH [206]. 131
6.3 Transmission electron microscopy (TEM) pictured of tantalum oxide nanoparticles prepared under acidic conditions with (top) and without (bottom) addition of a dispersing agent (PEG44-Si) 134
6.4 Transmission electron microscopy (TEM) pictured of tantalum oxide nanoparticles prepared under basic conditions with ammoniac solution (top), diethylenetriamine in water (middle) and diethylenetriamine in ethanol (bottom) 136
6.5 Transmission electron microscopy (TEM) pictured of tantalum oxide nanoparticles prepared in "neutral conditions" after substitution of ethoxide with ethylene glycol. The samples were prepared after centrifugation. 137

A.1 TEM Jeol 1400JEM 144

B.1 Tropoelastin targeting peptide (TESMA) 146

C.1 Snell–Descartes law 148
C.2 Complex formation between analyte (A) and ligand (L) 149
C.3 Representation of the Biacore technology: interactions between the analytes and the ligands fixed on the gold chip cause variations in the plasmon resonance angle. 150
C.4 Representation of sensogram 150

List of Tables

1.1 Maximum electrons per energy level 9
1.2 Iodine based nanosystems for CT imaging 34
1.3 Processes for Polymeric NanoParticles (PNPs) production 43

2.1 Optimized parameters of centrifugation and redispersion for the preparation of concentrated suspensions of iodinated polymer nanoparticles in water 59
2.2 Dry extracts of supernatant and sediment after centrifugation of suspensions of iodinated polymer nanoparticles. 62
2.3 PCL_{65}-*b*-PEG_{113}/TIB-PVAL mass ratio before and after centrifugation, in supernatant and sediment of suspensions of iodinated polymer nanoparticles in water, using using ^1H NMR spectra integrals 63

3.1 Chemical identity and HLB values of the sorbitan ester surfactants 83
3.2 Comparison of the different dispersing agents 88

5.1 UPLC analytical method for the TESMA peptide elution 117
5.2 HPLC analytical method for SA-PEG1000-MAL and SA-PEG1000-MAL-TESMA elution 117
5.3 HPLC preparative method for SA-PEG1000-MAL-TESMA elution 117

6.1 Elements with a K-edge energy in the 40-100 keV range 127
6.2 Size of particles in the supernatant after centrifugation (10 min/4500 rpm) as measured by DLS 135

Introduction

Context

This work is part of the European H2020 project: Spectral Photon Counting Computed tomography (SPCCT). The global aim of the project is to develop and validate a widely accessible, new quantitative and analytical *in vivo* imaging technology combining the SPCCT and specific contrast agents, to accurately and early detect, characterize and monitor neurovascular and cardiovascular disease. In order to do so, the project was organized into 5 work-packages (WP):

- WP1: SPCCT technology construction, image acquisition, reconstruction and post-processing
- WP2: Contrast agents for SPCCT development
- WP3: Clinical and pre-clinical applications
- WP4: Cost effectiveness analysis
- WP5: Project communication, dissemination and exploitation
- WP4: Project coordination and management

More details can be found on the project's website: http://www.spcct.eu/

The research that led to the writing of this manuscript was conducted as part of WP2. LAGEPP was in charge of developing iodine-based contrast agents in the form of polymeric nanoparticles. It is aimed at investigating the benefits of such nanosystems over conventional clinically used contrast agents, notably for their implementation to SPCCT technology. Thus, the first objective within WP2 was the synthesis and characterization of nano-sized iodinated polymer particles. The second objective was functionalization of nanoparticles with proper probes in order to target specific epitopes on the diseased cells and at the same time, to assess the role of SPCCT technology in tackling molecular imaging procedures.

Scientific issues

Nanobiomaterials development has raised considerable interest, especially in the drug delivery and diagnosis fields. They are currently coming in the field of computed tomography (CT) imaging. This can be explained by the evolution of the CT technology but also by the countless and interesting features these systems present. Among them: high local concentration of contrasting elements can be reached by using particles in place of molecules. More specifically, in the framework of the "molecular imaging" concept applied to CT, contrast agents bind to specific tissues by molecular recognition. One event of binding a nanoparticle to a specific site provides much higher contrast than binding a contrast agent made of a small molecule. The expected benefit of using nanoparticles is higher sensitivity.

However, if the spectral technology is about to be launched to the clinical market, to our knowledge, there are no clinically used CT contrast agents in the form of nanoparticles to date. The main explanation is the lack of clear information dealing with their elimination (pathway and time).

This research work focuses on exploiting all the possibilities that an iodine-based contrast agent in the form of polymeric nanoparticles can provide: high contrast element payload, possible

surface functionalization with targeting moieties or/and stealth agents and so forth. The main topics concern discussion on the several differences between solutions of soluble contrast agents and dispersions of nanoparticles, and the added value of the SPCCT technology over conventional CT. The study also addresses one of the biggest issue regarding the fate of these types of nanosystems after their injection *in vivo*.

One important parameter that also has to be taken into account when developing a nanobiomaterial is scalability. The manufacturing process must be transferable from lab to pilot or even production scale. The final product should be very simple for an industrial exploitation could be considered.

Research questions

From these considerations, some questions were raised:

1. What is the added value of the SPCCT technology over conventional CT?
2. SPCCT is at an advanced stage of development with the recent installation of a clinical prototype in Lyon. What is missing in the design of contrast products in the form of nanosystems to be on the same track?
3. How are polymeric nanoparticles cleared from the body?

Organization of the work

First, a state of the art was done and given in chapter 1. The first part presents general backgrounds on the conventional CT and spectral CT technology. The second part concerns iodinated nanobiomaterials and their manufacturing processes.

In chapter 2, full synthesis and analytical techniques used to characterize the iodinated polymer and the nanoparticles are depicted. The radiopaque properties and the *in vivo* biodistribution of iodinated polymer nanoparticles were investigated on a conventional CT. Some SPCCT features were also evaluated.

In chapter 3, different parameters that govern the nanoprecipitation process were investigated and optimized in order to meet the physicochemical specifications set for an iodinated contrast agent in the form of polymeric nanoparticles.

In chapter 4, the question regarding NPs elimination was addressed. Preliminary results on the degradation of iodinated polymer nanoparticles by macrophages are presented.

The bioconjugation of the iodinated polymer nanoparticles with a peptide targeting tropoelastin is reported in chapter 5.

Finally, in the last chapter 6, a simple method of producing tantalum based nanoparticles designed for a specific SPCCT feature (K-edge imaging) is depicted.

In appendix A, a full TEM sample preparation for macrophages observation is presented. Appendix B reports the synthesis of tropoelastin targeting polypeptide. In appendix C, the Surface Plasmon Resonance (SPR) and Biacore technologies are described.

Chapter 1

State of the Art

Contents

1.1 X-Rays for medical diagnosis 6

1.1.1 From radiations to 3D image 6

1.1.2 X-Ray Computed Tomography (CT): the story of an evolution 16

1.1.3 Added value of SPCCT: focus on cardiovascular imaging . . . 22

1.1.4 Conclusion 23

1.2 Contrast agents for CT 24

1.2.1 Definition and properties 24

1.2.2 Iodine-based nanobiomaterials for CT imaging 26

1.3 Processes for polymeric nanoparticles (PNPs) production 35

1.3.1 Polymerization of monomers 35

1.3.2 Preformed polymer dispersion 37

1.3.3 Conclusion 42

1.4 General conclusion and aim of the work 44

1.4.1 State of the Art and conclusion 44

1.4.2 Aim of the work 45

1.1 X-Rays for medical diagnosis

1.1.1 From radiations to 3D image

X-ray Computed Tomography (CT) is a medical diagnosis tool that provides contrasted images of soft and hard organs of a body. It is called tomography as cross-sectional images are acquired at different angles, in order to recover the internal structure of a tissue as a 3-dimensional (3D) image. An X-ray source generates photons in a specific energy range. The incident intensity (I_0) of these photons is attenuated by interaction with matter, depending on the thickness and the electron density of the penetrated tissue. Note that the contrast comes from the difference of attenuation of the X-rays in the different material along the propagation paths of X-rays. The intensity of attenuated X-rays is measured by the detector. The X-ray source and the detectors are placed opposite side one from the other and rotate simultaneously around the object to be imaged (Figure 1.1). Finally, the signal will be transformed into digital 3D images using mathematical reconstruction algorithms.

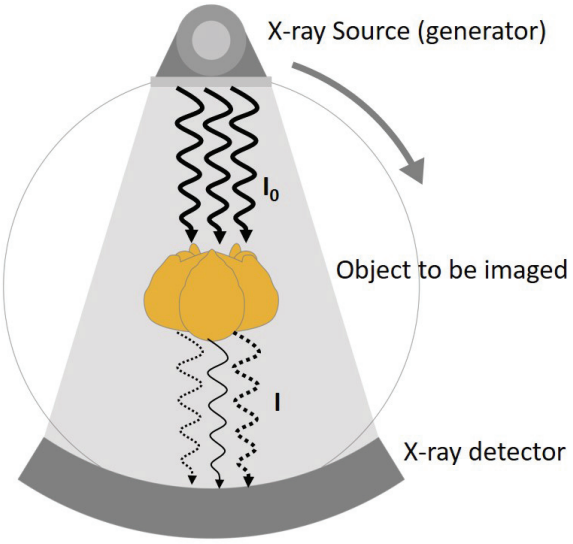

Figure 1.1: Operational principle of an X-ray scanner

1.1.1.1 X-Rays

Electromagnetic radiations are characterized by a specific range of wavelengths, frequencies and energies (Figure 1.2), which makes them suitable for given applications:

- Radio (waves): wireless communications, radio broadcasting...
- Microwaves: communication, radar, thermal energy transmission (1945 cooking revolution)...
- Infrared: thermography (thermal imaging), night vision devices, spectroscopy...
- Visible (light): part of the electromagnetic radiation spectrum visible to the human eye
- Ultraviolet: photography, protein analysis, bug zappers...

- X-rays: diagnosis, radiotherapy, crystallography...
- Gamma rays: sterilization of medical equipment, diagnosis (nuclear medicine), therapy etc.

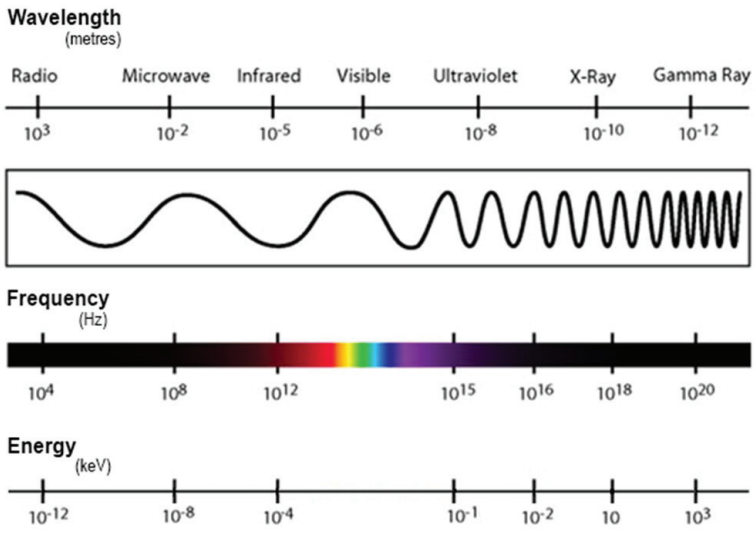

Figure 1.2: Electromagnetic radiations spectrum

X-rays X-rays are electromagnetic radiations with energies in the range of 100 eV (electron volt) to 1 MeV (million electron volts). Radiations used in CT are often produced using an X-ray tube (also known as Röntgen tube)(Figure 1.3).

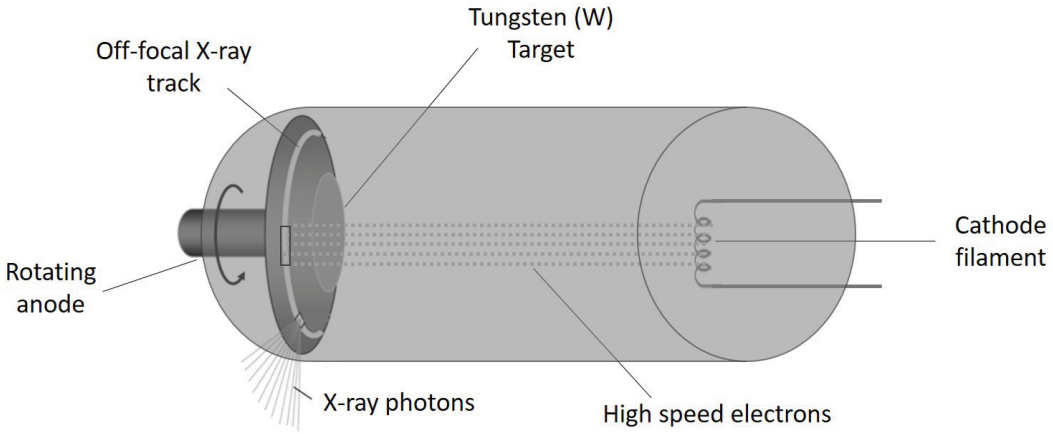

Figure 1.3: X-ray tube (generator)

X-rays are produced by collision of an electron beam with a metal target. On one side, a cathode filament is heated by Joule effect to incandescence, causing the excitation of electrons that releases them off the filament. The later are then accelerated to the tungsten anode by a strong potential difference. Tungsten atoms get excited as electrons collide them, and radiative decay to ground state emits X-rays; this is called the Bremsstrahlung effect. Only 1% of the

energy of the electrons sent will form X-rays, the other 99% will produce heat. X-ray tubes are equipped with a rotating anode which limits heating. They also have a diaphragm that allows them to tailor the X-ray beam to the size of the patient's region to explore.

The electrons flux and their energy range play a key role in obtaining a good quality of image, therefore a more accurate diagnosis. To optimize the first parameter, it is necessary to set up the intensity of the current (mA). The higher the intensity, the more electrons are generated, leading to a higher flux of X-rays and increased patient exposure. The energy of electrons, hence by extension of X-rays, is related to the voltage between each cathode/anode terminal of the tube. It often varies between 25 and 140 kV.

It is important to know that, when the electron beam from the filament is pulled under 140 kV acceleration voltage, all the emitted electrons do not have an energy of 140 keV. A polychromatic spectrum is obtained (Figure 1.4), with photons having energies ranging from 0 to 140 keV. Photons having energies corresponding to the electronic transition of the anode material are emitted, which gives sharp fluorescence peaks in the emission spectrum. Deceleration of the electron beam inside the anodic material emits a weaker spectrum of X-rays as a continuous background. Higher energies can be reached, but with no relevance to diagnosis applications. In fact, if the energy is too high (> 150 keV), there is no time for proper interaction with the matter, therefore no attenuation, which can be interesting for therapy but not for diagnosis as no contrast is made. Conversely, if the energy is too low (< 25 keV), the attenuated photons will be stuck in the body without ever reaching the detectors.

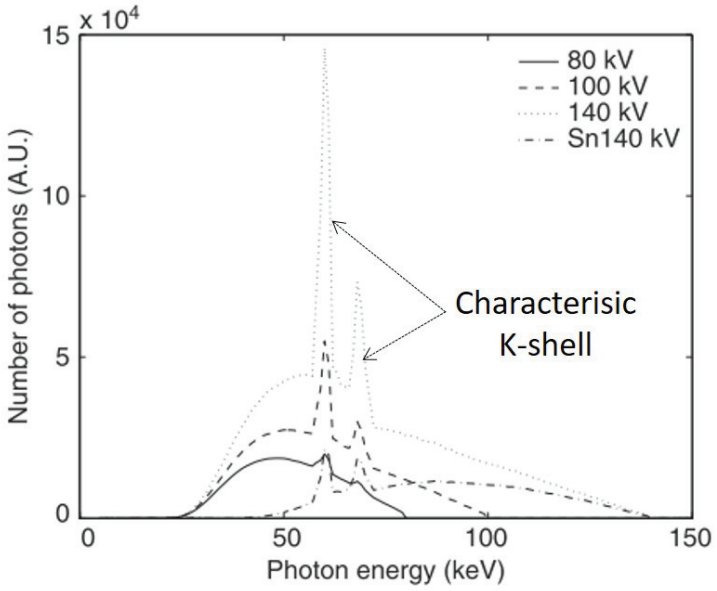

Figure 1.4: X-ray spectrum

Finally, there are three relevant categories of X-rays for imaging: soft X-rays (25-50 keV), medium X-rays (50-100 keV) and hard X-rays (100-140 keV). The radiologist selects the type of X-rays according to the region of interest and the image contrast adequate for a given pathology/application.

1.1.1.2 Interaction with matter

Generated X-rays interact with the object/patient to be imaged. The atoms of illuminated matter are made of neutrons and protons, forming the nucleus which are surrounded by a specific number of orbiting electrons necessary to ensure atom charge neutrality, like described by Niels Bohr's model (Figure 1.5). The interaction between these electrons (characterized by their energy level) and the X-ray photons is the essence of this imaging technology. These interactions cause absorption and scattering leading to attenuation of the incident X-ray photons.

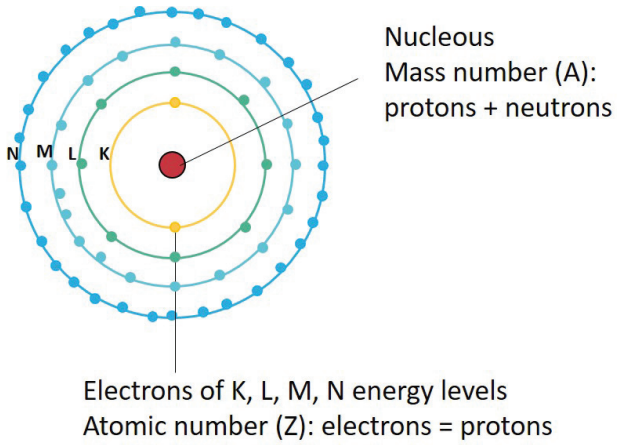

Figure 1.5: Bohr model of the structure of an atom

Table 1.1: Maximum electrons per energy level

Layer	Maximum electrons
K	2
L	8
M	18
N	32
...	...

Depending on the energy of the X-ray photon, the binding state of the electron (energy level), and the scattering angle, the type and probability of interaction varies. Several phenomena take place when an X-ray photon interacts with matter:

- The X-ray photon can transfer its full energy to an electron in a process called photoelectric absorption which is of high probability for low energy photons
- It can split into a positive and negative electron pair, in another total energy absorbing process known as the pair production (low probability)
- It can transfer part of it energy in an inelastic scattering process called Compton scattering which is of high probability for medium energy photons

- It can scatter without losing any energy in an elastic scattering processes called Rayleigh scattering by atoms or Thomson scattering by electrons (low probability).

For X-ray energies of most interest to imaging, photoelectric absorption is much more likely to happen than either kind of interaction. Secondly comes the Compton scattering (Figure 1.6) [1]. The other two interactions will not be detailed here.

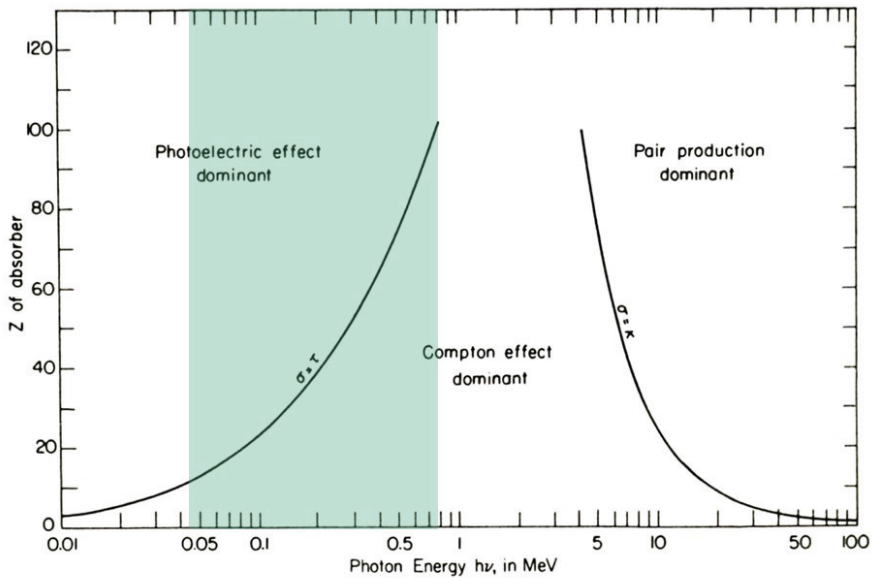

Figure 1.6: X-ray photons/electrons interaction-dominant domains according to the photon energies

Photoelectric effect During this process, the X-ray photon fully transfers its energy to an electron that is pushed out of its electron shell, resulting in total absorption. This electron is called photoelectron (photoE). In order for that to happen, the energy of the incident photon must be equal or above the binding energy of the electronic layer ($E_{binding}$). The energy balance teaches that the absorbed energy is the sum of the binding energy and the kinetic energy of the expelled electrons (KE_{photoE}) (equation 1.1):

$$E = E_{binding} + KE_{photoE} \tag{1.1}$$

This scenario is most likely to happen with soft X-rays at low energy (E < 50 keV) and when the electron is tightly bound to the shell like it is the case on the K shell of the atom. The vacancy left by the ejected photoelectron can be filled by the electrons from the other energy levels leading to the emission of fluorescence radiations of lower energy (Figure 1.7). The probability of photoelectric absorption is also proportional to the number of electrons, i.e. to the atomic number (Z) of atoms in the tissue imaged, but also to the third power of the energy of the incident photon (equation 1.2):

$$P_{Photoelectriceffect} \propto (\frac{Z}{E})^3 \tag{1.2}$$

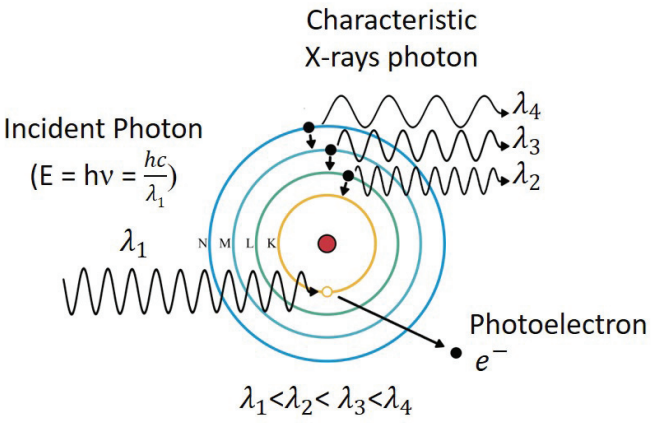

Figure 1.7: Photoelectric effect

However, when the energy of the incident photon (E) is in large excess than the energy of the electrons of the K level, the X-ray photon can only give part of it energy to an electron. This is known as Compton scattering.

Compton scattering As mentioned above, during this process, only part of the energy of the incident photon is transferred to the electron that is ejected (this is the Compton electron). The X-ray photon is scattered and goes through the tissue with an attenuated energy. The latter being useless for imaging and dangerous for the tissues because of irradiation.

$$E = E_{ScatteredX-rayphoton} + E_{Comptonelectron} \tag{1.3}$$

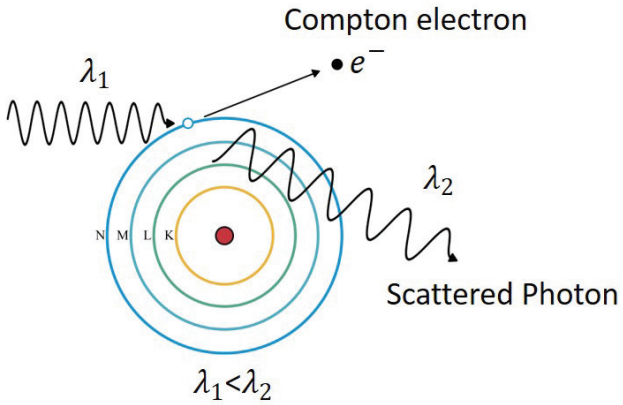

Figure 1.8: Compton scattering

The probability of this effect is maximum with hard X-rays at high energy (E > 100 keV).

It is important to note that whether it is the photoelectric absorption (fluorescence) or the Compton effect, scattered X-ray radiations of different intensity and direction than the incident electromagnetic radiation are produced. The patient becomes a source of X-rays. This not only causes a major radioprotection issue (irradiation risk for patients and operators), but also alters the quality of image. In order to cope up with it, several modifications of the device can be implemented:

- At the X-ray source level: the emission source can be confined (from a large source to a fine)
- Between the source and the patient: the diaphragm can be adjusted in order to avoid conical effects of the X-rays and therefore a too big growth. A collimator can be added, in order to also reduce the amount of Compton scattered X-rays.
- Before the detectors: an anti-scatter grid can be implemented. The grid allows only the tangential rays to pass through and reach the detectors. It also filters the oblique rays (Compton scattered X-rays) that would contaminate the image. This improves the background to noise ratio, hence the image quality

1.1.1.3 When energy becomes a 3D image

Contrast and attenuation At the energies relevant for X-ray imaging (25-140 keV), both the photoelectric effect and the Compton scattering are the most probable processes of X-ray photons/electrons interactions. Depending on the type of tissues, soft or hard X-rays are used and they are more or less attenuated. Attenuation depends on the thickness of the studied material (x) and the linear attenuation coefficient of the studied material (μ), as it is stated in the Beer-Lambert law (Figure 1.9):

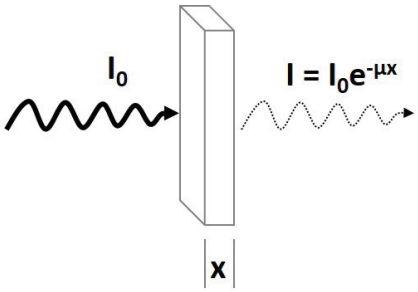

Figure 1.9: Beer-Lamber law

As mentioned previously, the CT X-ray beam is never monochromatic. As a consequence, each type of element possesses an attenuation profile that can be represented by a curve of mass attenuation coefficient in function of the photon energy. The shape of this curve is specific to each element and is connected to the atomic number (Z), the density (i.e. the concentration in electrons) and the energy of the incident photons (Figure 1.10).

The higher the atomic number is, the more electrons are involved and the more the electromagnetic radiations are likely to be attenuated, resulting in a higher attenuation coefficient curve. On the other hand, the higher the energy of the incident photons is, the faster the X-rays cross through the absorber and the less it is attenuated. The contrast results from the difference of attenuation between surrounding tissues.

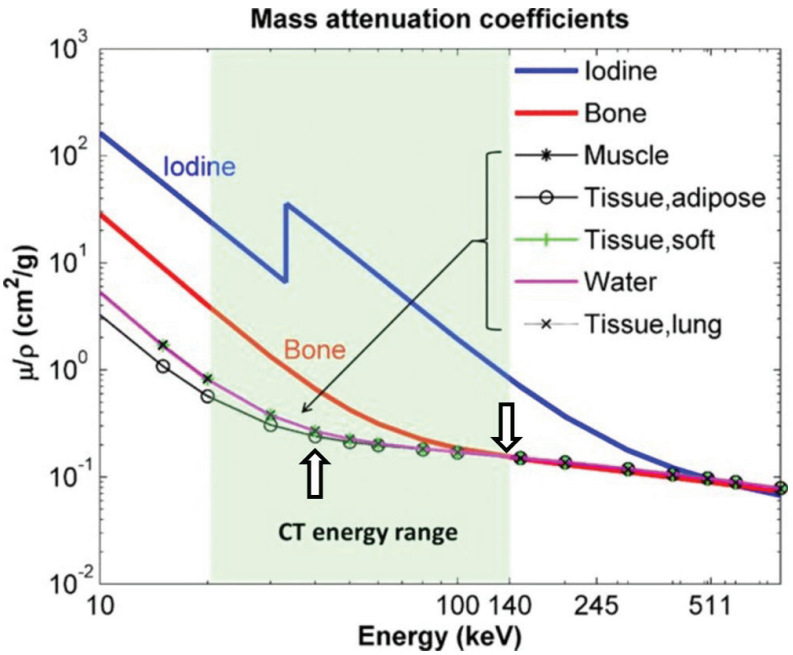

Figure 1.10: Attenuation profiles of different tissues in function of the incident X-ray energy [2]

(Figure 1.10) also shows that two elements can have the same attenuation characteristics at a given energy (for example soft tissues and bones shown as face down arrow), but be differentiated at another energy of X-rays (face up arrow).

Image formation The attenuated photons going through the imaged material reach the detectors where the energy is converted into an electrical signal. This will be transformed into a digital 3D image by reconstruction algorithms.

What is measured is the intensity (I) of the attenuated photons. From this information the attenuation coefficient (μ) can be deduced using the Beer-Lambert law. Nonetheless, the object to be imaged is a complex tissue made of different attenuation profiles. Thereby the X-ray beam can go through a single tissue (one attenuation coefficient is then retrieved) or different tissues (the attenuation coefficients are then summed up) (Figure 1.11).

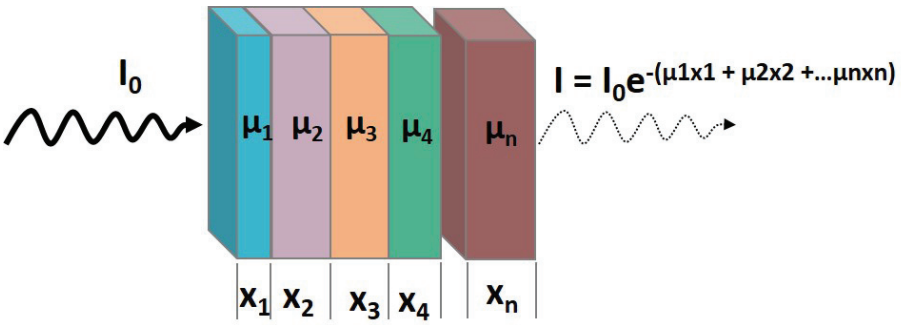

Figure 1.11: Beer-Lambert law when X-ray is attenuated by different profiles

The final linear attenuation coefficient which quantifies the capability of a tissue to attenuate an X-ray photon beam, represents all the interactions of the electron with the X-rays. The Beer-Lambert law becomes then:

$$I(\lambda, x) = I_0(\lambda) \sum_{k=0}^{n} e^{\mu_k x_k} \tag{1.4}$$

Where λ is the wavelength of the incident X-ray, k is the studied material

The CT technology divides the studied object into cross-sections, each slice represents a digital image that is also divided into a square matrix (512 × 512) of pixels. Each square is associated to a pixel and each pixel in the image represents a voxel (volume element) of tissue to be imaged [3]. Image reconstruction requires that a linear attenuation coefficient be associated to every pixel (i.e. 512 × 512 = 262 144). This is an issue as in order to do so, 262 144 equations (cf. Beer's Law) each containing 262 144 unknown values of μ must be solved simultaneously.

The mathematician Johann Radon introduced in 1917 what will since then become the bases of CT image reconstruction: the filtered back-projection method (or Radon transform) [4][5]. Thanks to this mathematical function, the original image (f) is reconstructed from its projection data. A high capacity computer is necessary to acquire and process all the data.

By putting together all these information, an image can be formed in shades of grey. By convention, when an X-ray reaches the detector a black image is formed, when it does not, meaning that it went through a radio-opaque element and was attenuated, a white shade is obtained (Figure 1.12). The need to quantify in a practical way these shades of grey arose.

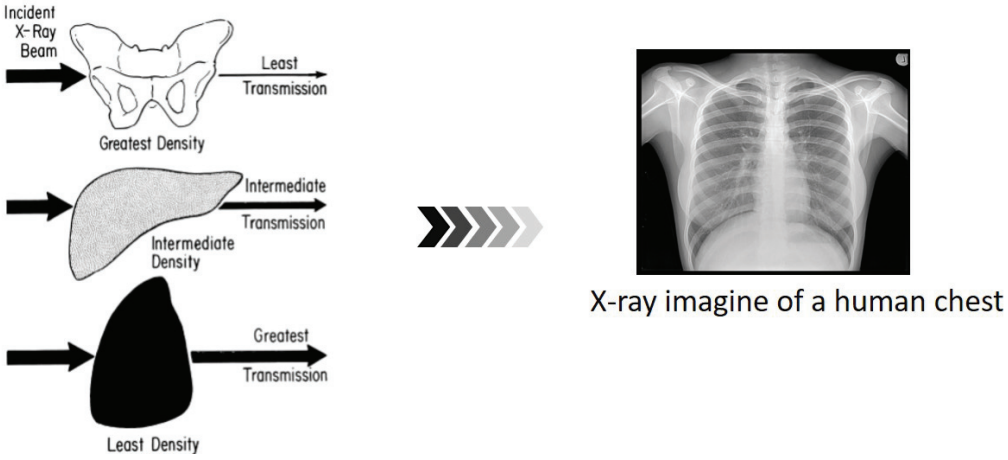

Figure 1.12: Attenuation of X-ray photons in different tissues

Hounsfield Units (HU) In the early 1970s Sir Godfrey N. Hounsfield made the first tomographic image as we know it today. To cope up with the low capacity of the detectors in processing the energy of the photons, a water bag was placed close to the patient [6]. Since then, the attenuation is expressed in function of the attenuation coefficients of water (μ_{water} = 0) and air ($\mu_{air} = -1000$) (equation 1.5). The linear attenuation coefficient measured were converted into CT numbers also known as Hounsfield Units (HU).

$$CTnumbers(HU) = (\frac{\mu - \mu_{water}}{\mu_{water} - \mu_{air}}) \times 1000 \tag{1.5}$$

The scale goes from -1000 to 3000 (i.e. 4000 levels) and the numbers are associated to shades of grey. The lower level corresponds to the least attenuating power (air = -1000 HU) and the higher level corresponds to elements with the highest attenuating power (bones up to 3000 HU). However, the computer monitor can only display 256 levels of grey and the human eye can only distinguish up to 16 different shades of grey. In order to have a clear, accurate and readable image, only a specific range of CT numbers can be displayed depending on the tissue to be imaged (Figure 1.13). This is called "windowing".

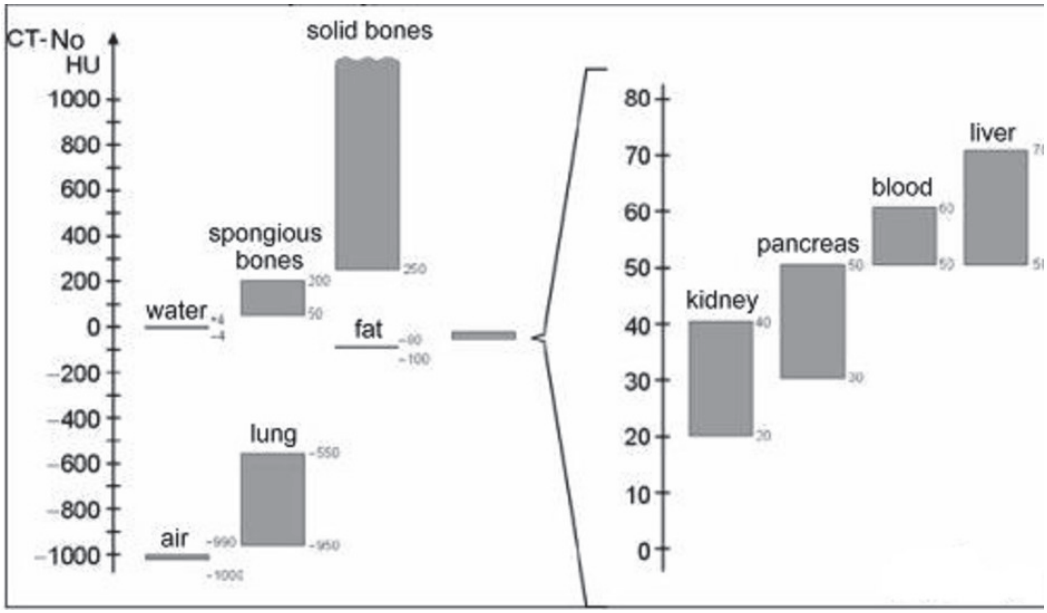

Figure 1.13: Hounsfield Units (HU) scale of different tissues

1.1.2 X-Ray Computed Tomography (CT): the story of an evolution

Over a hundred years after Sir Wilhelm C. Röntgen took a cliché of his wife's hand that will incidentally become the first medical X-ray radiography (Figure 1.14), X-ray imaging has made considerable progress and continues to evolve. The new generation of CT is finally reaching the clinical stage and the innovation mainly resides in the detectors and the reconstruction algorithms. Better accuracy, less artifact, less noise, more signal, faster, more information etc., here we are going to describe the evolution and upturn of this technology from conventional CT to Spectral CT.

Figure 1.14: First medical X-ray picture of Anna B. Röntgen's hand bone structure and ring (1895)

1.1.2.1 Conventional CT

In conventional CT, one source generates X-ray photons that are attenuated because of interaction with the matter, before reaching the energy integrating detectors. The X-ray energy spectrum of all attenuated photons is integrated as a single signal providing a global attenuation (Figure 1.15).

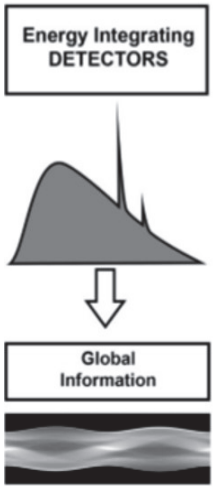

Figure 1.15: Global information provided by the energy integrating detectors

However, different tissue types can have similar attenuation values, therefore it is difficult to differentiate between very close shades of grey as the contrast between the tissues can be insufficient. Poor tissue differentiation can lead to misclassification of certain pathologies (i.e. atherosclerotic plaques, bones or iodinated blood vessels). That is why for the last decade, a variety of systems based on the analysis of the spectral information of X-rays are under investigation.

A first generation of Spectral CT is the Dual-Energy Spectral CT. The latest generation is the Multi-Energy Spectral CT. For the record, albeit the hype behind Spectral CT technology has taken another turn with the progress in computer science since the beginning of the century, back in the early 1970s Hounsfield (1973) [6] and Macovski (1976) [7] already had a glimpse of what was going to be X-ray imaging in the future.

1.1.2.2 Dual-Energy CT (DECT)

It was seen in Figure 1.10 that two materials with completely different compositions (i.e. bones and water) can have the same mass attenuation coefficient at a given energy (face down arrow), whereas the two materials could be properly differentiated at another energy level (face up arrow). It assumes that the incident photon was mono-energetic. Current X-ray tubes produce a poly-energetic spectrum. The idea behind the DECT technology is to separate the X-ray spectrum into two different data sets. One at high energies and the other one at the low energies. There are several configurations for the DECT [8]:

Dual source Dual source systems are designed with two pairs of X-ray sources/detectors [9]. Therefore, there are two independent X-ray tubes that can generate photons of different characteristics (voltage and current), each associated to a detector (Figure 1.16). The tension between electrodes of a X-ray tube is expressed as its "peak kilovoltage" (kVp) which is the maximum tension when it is an alternating (AC) or a pulsating tension. In case of a constant DC tension, the peak kilovoltage is the same as the steady-state tension.

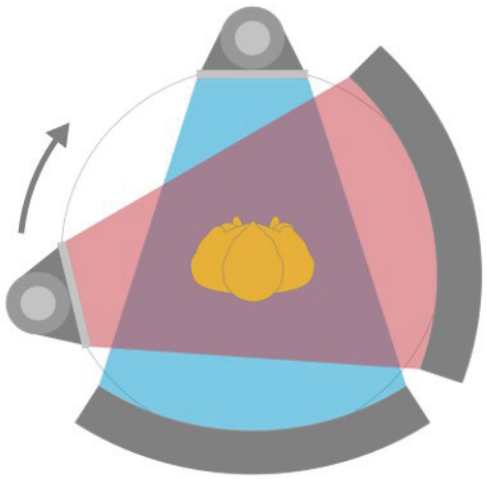

Figure 1.16: Dual source configuration

Dual kVp scanning In this configuration also known as the full volume slow kVp switching, two full body scans are made one after the other at lowest voltage setting (80 kV) and at the highest one (140 kV) (Figure 1.17 top), for better spectral separation. Data are collected and combined to form a spectral image.

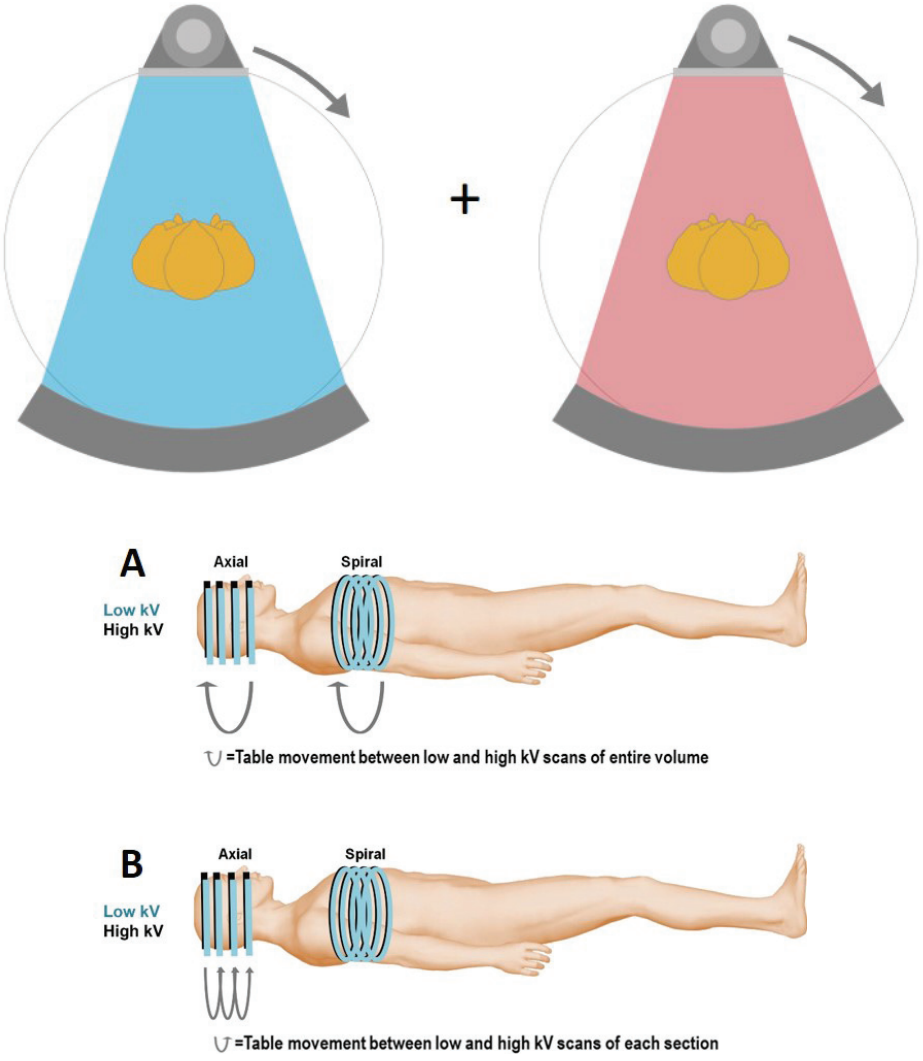

Figure 1.17: Dual kVp scanning configuration

An alternative to the full volume slow kVp switching is the 180° partial slow kVp switching. Here successive scans are acquired at different energies and angles. Contrary to the previous technique, the switch between the low energy and the high energy is done after each section and not after the entire body volume (Figure 1.17 bottom). Since the voltage switching time is shorter, the consistency between the two scans is improved but the acquisition time is longer.

Overall both techniques present three major drawbacks which are: the exposure to two energy beams leading to high radiation dose, considerable increase of the scan acquisition time and possible motion of the patient or certain tissues (i.e. cardiovascular system) in between the two scans.

Dual fast kVp switching The functioning of this system is similar to that of the slow kVp switching except that it is equipped with special X-ray tubes and detectors. In fact, the X-ray source must be capable of switching back-to-back between 80 to 140 kVp within a few milliseconds, and fast scintillation detectors are required (Figure 1.18) [10]. However, in reality the X-ray photons flow at 80 kVp is weaker than the ones at 140 kVp at the same current, due to the fact that the voltage and the current cannot vary rapidly at the same time. In order to cope up with this issue and get the same radiation dose at low and high energy, several X-ray photons are projected at low energy for one high energy projection.

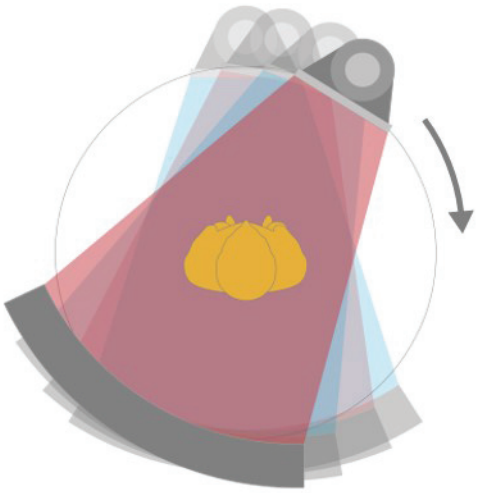

Figure 1.18: Dual fast kVp switching configuration

Dual layer This system is completely different from the ones described before, as spectral image is no longer related to the source but to the detectors placed in different layers (two in this case). The low and high energy data sets are acquired simultaneously. The low energy photons are collected by the first (most inner) layer and the high energy will go through and reach the second layer (blue detector in Figure 1.19) [11].

Whether it is the Dual Source CT or the Dual Layer CT approach, the data collected is divided into two data sets that provide two signals (Figure 1.20). One for the low energy part of the spectrum and the other one for the high energy part. From that, it is possible to discriminate two elements. Currently, most of the commercially available clinical scanners are equipped with dual energy detection.

1.1.2.3 Spectral Photon Counting CT (SPCCT) or Multi-Energy CT

This approach can be seen as the improved version of the DECT. Instead of two, several data sets (between 4 to 8 according to the literature) coming from energetically distinct X-ray spectra are processed (Figure 1.21) [12], [13]. As an example, five energy thresholds are implemented in the technology developed during this project by Philips Healthcare [14].

The segmentation of the X-ray spectrum provides extra information that can lead to multiple spectral discrimination (Figure 1.21), (Figure 1.22). On top of the information provided by the additional data set, another major innovation resides in the detector technology.

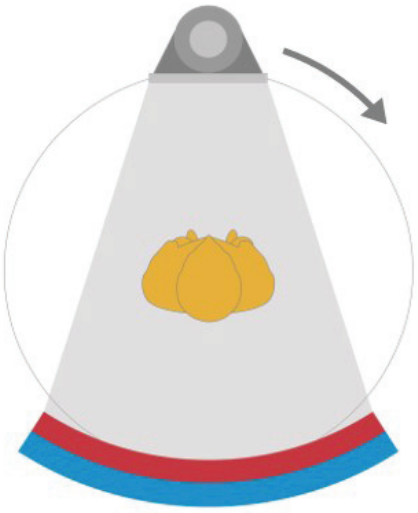

Figure 1.19: Dual layer configuration

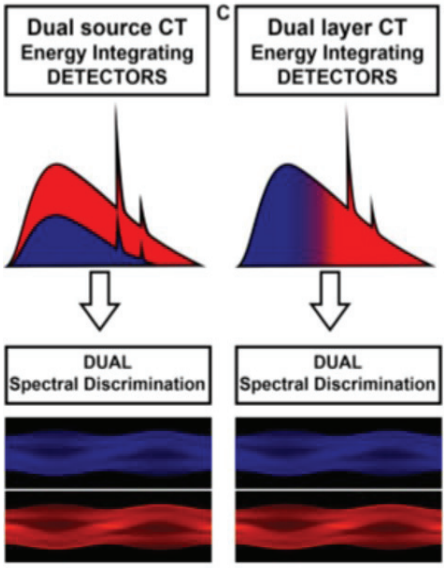

Figure 1.20: Spectral information provided by the energy integrating detectors of DECT

Photon counting detectors The energy integrating detectors of conventional CT and DECT are replaced by the energy-resolving photon counting detectors [15]. Here each photon is collected and directly transformed into individual electronic signals using special sensors that constitute the Application Specific Integrated Circuit (ASIC). The amplitude of the signal is proportional to the energy of the photon. The boom in computer and processing fields makes it possible to stock and process the quantity of data generated. As mentioned before, the signals are separated into different energy bins (Figure 1.22). As an outcome, the photon counting detectors provide better sensitivity as the noise is diminished at low radiation dose leading to the improvement of the signal-to-noise ratio and by extension the contrast-to-noise ratio [16]. The spatial resolution is also improved, resulting in better delineation of small structures [17].

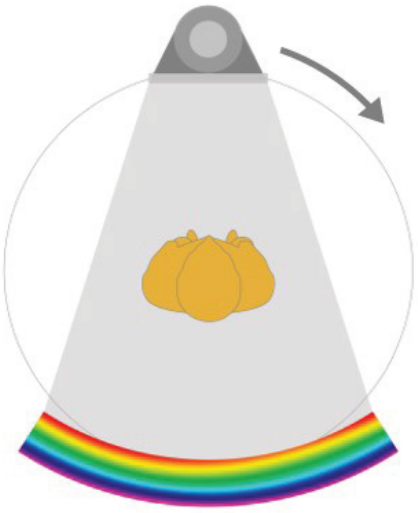

Figure 1.21: Spectral photon counting configuration

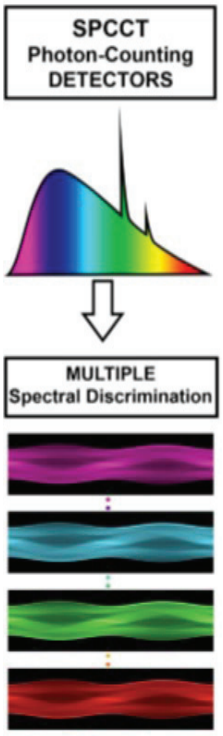

Figure 1.22: Spectral information provided by the photon counting detectors of the SPCCT

One of the major concerns of this new technology is the high flux of photons generated. The energy resolving detectors must be scrupulously designed to cope up with a certain number of limitations (i.e. electronic pileup or charge sharing). Moreover, an extremely powerful computer system is needed to store and process all the new high quality data. These are the two main challenges that CT manufacturers must address today.

Finally, two mathematical algorithms are used for image reconstruction: namely Material Decomposition (MD) and K-edge imaging.

Material Decomposition (MD) As seen previously, the SPCCT technology provides the X-ray energy spectrum split into several energy domains and the attenuation is measured at each energy bin of the spectrum. The total measured attenuation is the sum of the attenuation of each element multiplied by its concentration (Equation1.6).

$$A_{global}(HU) = \sum_{i=0}^{n} C_i \times A_i \tag{1.6}$$

Where A_i is the attenuation of one element and C_i the related concentration.

With this information, it is possible to discriminate different elements. This is called Material Decomposition (MD). It is a mathematical algorithm implemented in the software of the scanner. On one hand, specific images of a given element can be generated from MD calculation. On another hand, the concentrations of each element is obtained at each voxel, allowing the quantification of biodistribution.

K-edge imaging As can be seen in Figure 1.4, the X-ray energy spectrum comprises adsorption peaks characteristic of the binding energy of the K shell electron of an atom. As the energy needed to eject this electron is intrinsic to each element, the detection of the strong attenuation variation due to photoelectric effect can be used for a specific detection of the element. The difference between the attenuation at the top of the peak and at the bottom is specific to each element and proportional to the concentration. This is called K-edge reconstruction.

Like the DECT, the SPCCT allows reconstruction of mono-energetic images (monoE) at chosen energies in order to increase the contrast at low kVp. This is interesting for some elements (i.e. Iodine K-edge = 33 keV) that do not have a K-edge in an acceptable energy range (i.e. 40-100 keV for a 120 kVp beam as there must be enough photons before and after the K-edge energy). As for MD, K-edge reconstruction allows both the calculation of specific images of elements and their quantification.

1.1.3 Added value of SPCCT: focus on cardiovascular imaging

The reconstruction algorithms described above and the development of the photon counting detectors via the ASIC system make the potential of CT imaging higher than the DECT systems. These two features open the door to interesting applications that allow more accurate diagnosis while reducing radiation and injected contrast agent doses. First, the possibility of getting information from more than two database permits a better differentiation and classification of different tissue types and contrast agents [18] but also simultaneous discrimination of different attenuation profiles (multiple-contrast agents imaging) [19]. Last but not least, *in vivo* quantification of high atomic number elements (cf. contrast agent paragraph) in specific regions is also made possible [20]. A reference scan is no longer requisite limiting radiation dose [21].

Atherosclerosis When it comes to stating the added value of the SPCCT technology in a concrete clinical application, molecular imaging and particularity assessment of atherosclerosis at an early stage (plaque inflammation) is what immediately emerges from the literature.

Indeed, several studies on monitoring the atheroma plaque by a spectral photon counting CT in order to prevent acute vascular events (strokes or cardiac attack) can be found [22] [23], [24], [25] [26] [27].

The challenge up until now was to accurately differentiate a high atomic number contrast agent (i.e. iodine) from calcified plaques that can be found in blood vessels. Typically, here, the capability of the system to simultaneously discriminate between different attenuation profiles characterized by different biodistributions within a single scan, can be put to use. One can consider having a contrast agent that will remain in the bloodstream and provide a control image of the vascular system, while a K-edge element would target a specific biological marker, i.e. elastin, fibrin, tropoelastin etc., expressed by the plaque.

Other imaging modalities such as Magnetic Resonance Imaging (MRI) [28] [29], have been also used to detect and classify vulnerable atherosclerotic plaque. A disadvantage of the later non-invasive imaging technique over spectral CT is the spatial resolution, limiting it application for assessing atherosclerosis at the molecular level.

1.1.4 Conclusion

It was seen that in X-ray imaging, the attenuation is proportional to the probability of interaction between the incident photons and electrons. Since the number of electrons is quantified by the atomic number Z, tissues composed of elements with low atomic number such as carbon, oxygen, hydrogen, (i.e. liver, spleen, blood vessels etc...), do no naturally attenuate incident X-ray photons. There is a need to inject a substance that will enhance contrast in such organs or/and create a contrast between tissues that have similar electron density, this is the role of a contrast agent. Moreover, with all the new features brought by the SPCCT technology, a need to design novel contrast agents has never been more relevant. In the next part of this chapter, the current state of the art on contrast agents for CT is depicted.

1.2 Contrast agents for CT

1.2.1 Definition and properties

1.2.1.1 Definition

A Contrast Agent (CA) in X-ray based imaging techniques, is a chemical substance of very high atomic number (Z), used to increase the density of the organ under examination hence increasing the visibility of internal structures such as soft organs (liver, spleen, bladder...), blood vessels, molecular markers (which appear earlier than the disease's clinical symptoms), and so forth.

1.2.1.2 Properties of contrast agents for CT and SPCCT

A good contrast media for CT must have the highest attenuation coefficient and good radio-opacifying properties. This is straightly related to a high atomic number (Z). In fact, as seen previously, the higher Z is, the biggest the probability of an electron/photon interaction, the highest the attenuation and by extension the contrast. Moreover, it is important to bear in mind that the SPCCT technology is used at its full potential with elements of a specific range of K-edge energy (between 40-100 keV). The best candidates based on these criteria and considering that the optimal CT sensitivity resides withing the 20-140 keV range, are lanthanides ($60 < Z < 70$).

However, in order to make an ideal contrast agent, the radiopacity (i.e. the capability to attenuate the incident X-ray photon) of the element alone is not enough. The final injectable product must be carefully fabricated, taking into account: high contrast element concentration, ease of administration (viscosity), tolerability (best with iso-osmolar, nonionic compounds [30])), low toxicity, suitable life time depending on the applications, biocompatibility, stability, clearance, among other criteria.

For safety issues and clinical patient compliance, elements less sensitive then lanthanides are used in chemical forms with a safe pharmacokinetic profile such as iodine. Nevertheless, on its own, iodine is unsuitable as a CA as it is toxic. There is a need to attach it to a carrier (i.e. benzene ring).

Today and for the last 50 years, most clinically used CT agents are small iodinated molecules dissolved in aqueous solutions [31], [32]. Typically, gold standard X-ray CT agents comprise an aromatic platform with three iodine atoms attached either at positions 1,3, and 5 or 2,4, and 6. Hydroxyl groups are implemented to the rest of the benzene ring (either at positions 2 and 4 or 1 and 5), to increase water solubility and decrease osmolality, therefore increasing biocompatibility. These agents can be either ionic or nonionic, monomers or dimers (Figure 1.23).

CT contrast agents can be divided into four main categories:

- First pass agents: Enhance the cardiovascular system for a short imaging time (minutes) due to rapid clearance by the kidneys.
- Passive targeting agents: Reach site of disease (infarction, tumors etc.), via biological mechanisms such as the reticuloendothelial system (RES) or the enhanced permeability

and retention effect (EPR). In some studies, it was observed that particles can be extravasated through damaged fenestration of certain capillaries. In fact, the size of open fenestrae can go from 150 nm (healthy tissue) up to 700 nm (unhealthy tissue), allowing particles of given size to penetrate in the organs of interest [33], [34], [35], [36].

- Active targeting agents: Selectively accumulate in specific cells and tissues by bioconjugation of non macrophage-recognizable compounds such as antibodies, peptides, or other ligands.
- Blood pool agents: In order to reach the targeted site, agents must remain confined to the intravascular space for a prolonged time (hours), highlighting blood vessels and more generally the cardiovascular system. Usually a stealth agent (i.e. hyaluronic acid (HA), poly(ethylene glycol) (PEG) etc.) [37] is added to inhibit the action of the immune system.

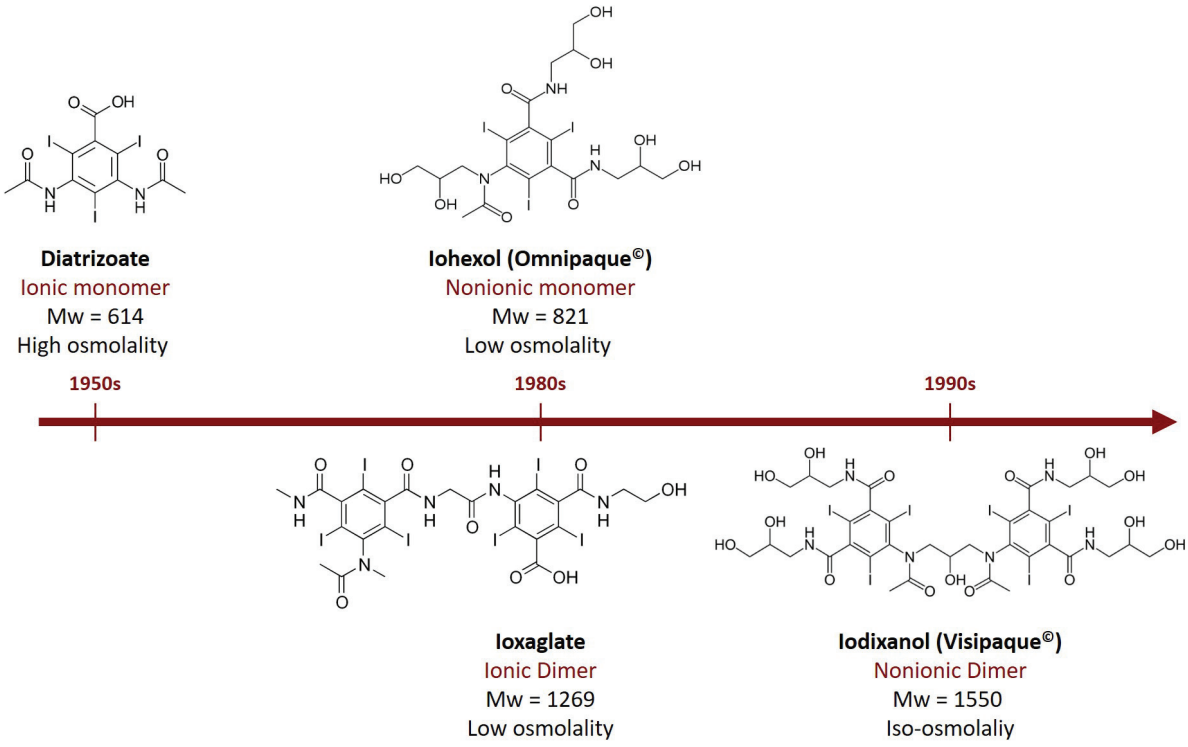

Figure 1.23: Chemical structure of small molecules, medically approved CT contrast agents

Iodinated molecules in aqueous solutions are used as first pass agents but their short retention time (i.e. seconds to couple of minutes in the bloodstream) [38], renal toxicity [39], and non-specific biodistribution makes them unsuitable for certain applications such as passive targeting, blood pool angiography or molecular imaging. In order to overcome these drawbacks different types of iodine-based agents in the form of nanobiomaterials are under investigation.

1.2.2 Iodine-based nanobiomaterials for CT imaging

According to the European commission, nanomaterials are :

"Natural, incidental or manufactured materials containing particles, in an unbound state or as an aggregate or as an agglomerate and where, for 50% or more of the particles in the number size distribution, one or more external dimensions is in the size range 1 nm-100 nm."

In the nanomedecine field, the size range of a nanomaterial is not well defined. Hence, depending on the targeted application, sizes bellow 200 nm, 500 nm or even 1 micron can be included in the nanometer scale.

The design of nanobiomaterials has generated considerable interest as highlighted by the number of publications associated to the keywords "computed tomography" AND "nanoparticles" AND "iodine" in the ScienceDirect database (Figure 1.24). This may be explained by the evolution of the CT technology but also because these systems can be customized in different interesting manners.

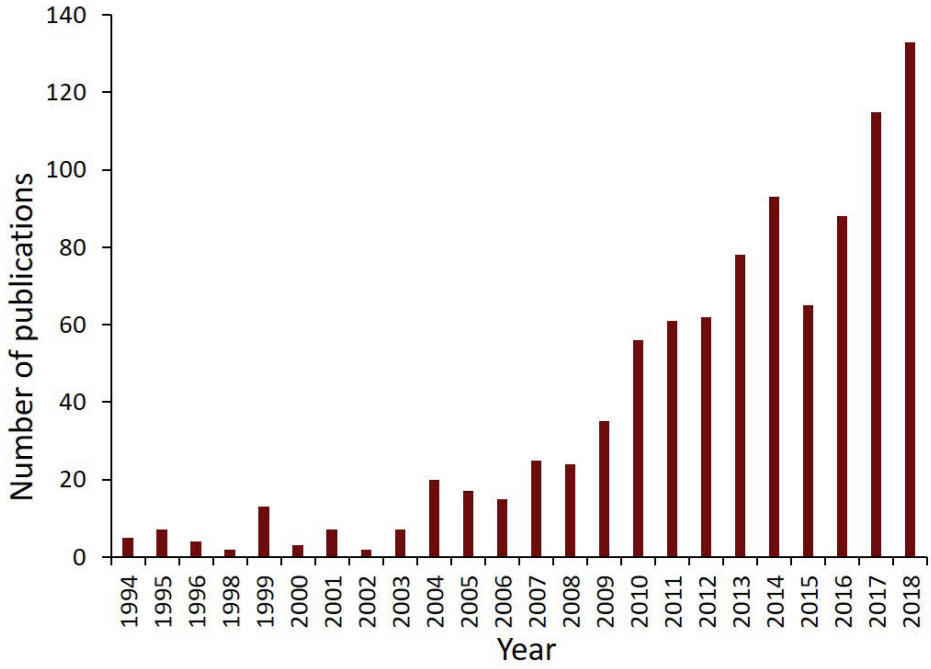

Figure 1.24: Publications in the area of computed tomography and iodinated nanoparticles over the past 24 years. Data acquired from a search of "computed tomography" AND "nanoparticles" AND "Iodine" keywords in the ScienceDirect database

Figure 1.25 shows a representation of an iodinated nanobiomaterial and the different features possible. Note that the most frequent shape for these type of materials is spherical. However, there are several other forms such as rods, cages, stars and so on.

To start, a higher payload of radiopaque elements can be loaded in a single nanomaterial core, compared to small molecules (3 to 6 iodine per unit) [40]. In this sens the injection dose can be reduced while maintaining similar contrast.

Furthermore, a stealth agent (usually a natural or synthetic polymer), can be implemented to the surface of the nanosystem in order to increase the agent's blood circulation half-life and control the clearance pathway [41]. The idea is to avoid opsonization (i.e. adsorption of protein from the immune system) and escape rapid recognition by macrophages from Kupffer cells in order to remain in the blood for a longer period. It is known that the *in vivo* biodistribution kinetics (i.e. tissue distribution and clearance behavior) of an intravenously injected particulate is influenced by the size and surface coating [42]. Small (size below 100 nm), neutral particles manage to avoid uptake by macrophages [43]. This is not the case for larger particles, hence the necessity of an efficient coating [44] [45].

Nanobiomaterials also present the possibility of using the SPCCT capability to image specific elements, by designing agents containing biomarkers capable of targeting a specific site in the body. This is a major progress in molecular imaging, that allows to improve early diagnosis by detecting biological processes at the cellular and molecular levels, eventually preventing acute events from happening. As an example, imaging of the atherosclerotic plaque at an early stage could potentially prevent stroke or myocardal infarction [23]).

Another feature involves other type of contrast generating materials in order to fabricate multimodal imaging agents [46] [47].

Finally, drugs or other active compounds can be encapsulated to make the nanosystem both therapeutically and diagnostically active. The contrast agent becomes a theranostic agent [48] [49].

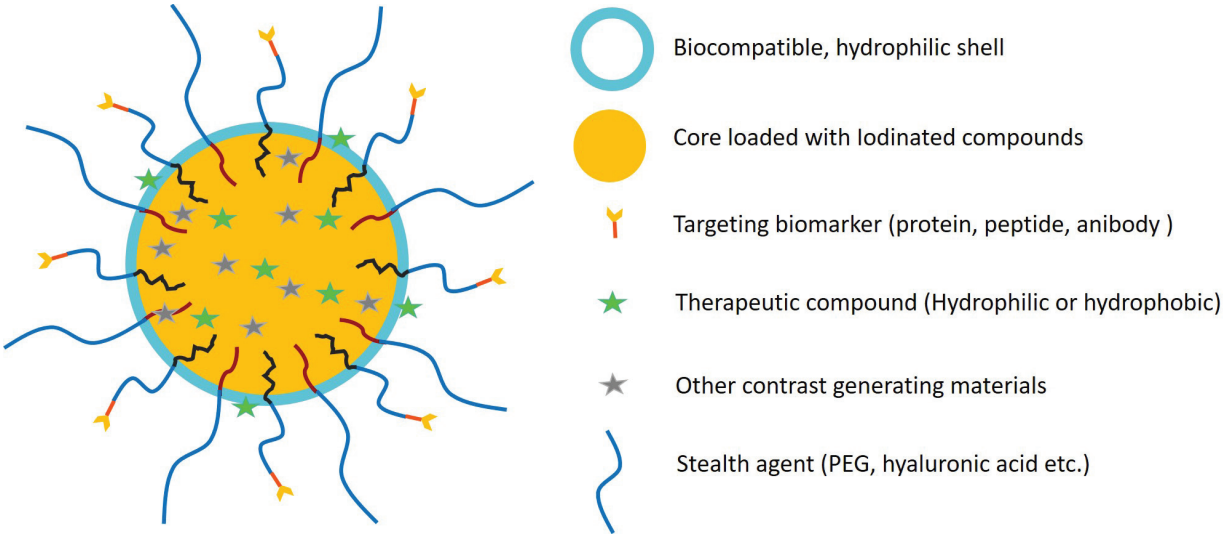

Figure 1.25: Representation of an iodinated nanobiomaterial of CT contrast agent and the different features possible

Several iodine-based nanosystems for CT, have been developed over the last years. Among them lipid-based compounds (liposomes, nanoemulsions), and polymer-based agents (dendrimers, micelles, and polymeric nanoparticles)..

1.2.2.1 Liposomes

Liposomes are amphiphilic self-assembled compounds, composed of an aqueous core surrounded by a phospholipid (two hydrocarbon chains) bilayer or multilayer. Drugs and/or radiopaque elements can be loaded either in the core or in the lipidic structure, depending on their hydrophilicity/hydrophobicity (Figure 1.26).

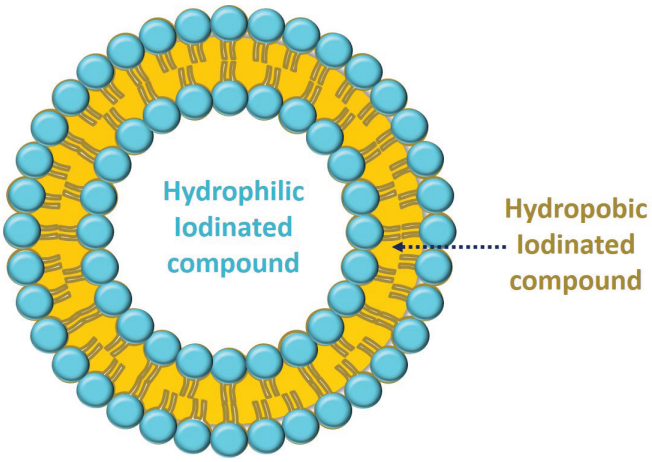

Figure 1.26: Structure of an iodinated liposome

As an example, Annapragada's team have patented a PEGylated liposomal nanoscale contrast agent for CT known as NCTX or Iodixanol pegol [50] [51]. *In vivo* biodistribution studies were carried out by intravenous injection to rats. The liposomes were characterized by an average diameter of approximately 150 nm; iodine concentration reached the 150 mg(I).mL^{-1} range. The injected dose was around 455 mg(I).kg^{-1} rat body weight. The research team claimed a blood circulation half-life of approximately 18 h. 72 h post-injection all the contrast agent was cleared from the blood vessels and was seen to accumulate in the spleen and the liver.

This compound reached phase I clinical trials in 2014 in healthy volunteers in the USA (study reference: NCT02063594). Visibly the tests have been abandoned as to date, no iodine-based nanoparticles are used clinically. One explanation can come from the lack of knowledge around the fate of these nanosystems once accumulated in the two organs mentioned above. Indeed, their mechanism of degradation and elimination is one of the biggest question marks in the field of nanoparticulate contrast agents.

Fabrication process In the literature, the most commonly used processes for liposomes fabrication are based on mechanical dispersion of the phospholipids. The starting point being the removal of the organic solvent from a lipidic solution thus obtaining a dry thin film of lipids. The later are then dispersed in an aqueous medium at a specific temperature (above the phase transition temperature) and under agitation, this is the hydration step [52]. The radiopaque elements can be incorporated either in the organic phase or in the aqueous phase. Afterwards, the formulation goes through a homogenization and sizing stage using high energy processes (i.e. ultrasonication, low or high pressure extrusion through French press cell or polycarbonate membranes, microfluidization). Finally, comes a purification step were non-encapsulated materials are removed either by dialysis, ultracentrifugation, ion-exchange resins,

or gel-permeation chromatography. The main drawback of this technique is the use of high energies that can damage the lipids.

There are other techniques for liposome production that request lower energy, based on solvent dispersion (i.e. reverse-phase evaporation, organic solvent injection), detergent removal (slow or fast dialysis, gel exclusion chromatography), preformed liposomes transformation (freeze-thawing) [53]. Nevertheless, each technique has it weak point that can go from purification of remaining detergent or/and organic solvent, to low encapsulation rates etc.

Overall, radiopaque liposome manufacturing can take several hours and simpler method to fabricate nanosystems can be found.

1.2.2.2 Nanoemulsions

An emulsion is a system where two no miscible phases are merged with the help of an amphiphilic compound called surfactant and a mechanic stirring device (rotor-stator mechanism). There are two types of emulsions: oil-in-water (the most commonly used) where the organic phase is dispersed into the aqueous phase as droplets (Figure 1.27). In this application, since the most relevant droplet size are below one micron, we consider nanoemulsions (also referred to as miniemulsions, fine dispersed emulsions or submicron emulsions). The other type of emulsion is the water-in-oil dispersion. For CT a radiopaque element is needed in order to create the contrast. Commercially available iodinated oils, such as Lipiodol, can be used.

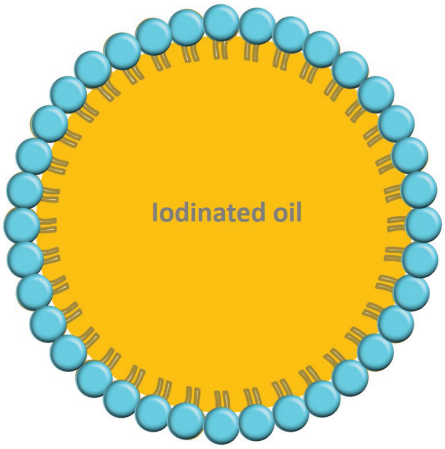

Figure 1.27: Iodinated oil-in-water nanodroplet

On top of the different experimental nanoemulsions which references are stated in Table 1.2, a nanoemulsion formulation can be found in the market, for preclinical use. In fact, in the late 1990s, Counsell *et al.* developed a nanoemulsion surrounded by a PEG coating and loaded with 1,3-bis-[7-(3-amino-2,4,6-triiodophenyl)-heptanoyl]-2-oleoyl glycerol (DHOG = iodinated oil) [54]. This product is better known by it commercial name Fenestra VC©.

The supplier (MediLumine) have made different claims such as the use of this product for vascular imaging (angiography) and hepatobiliary imaging (quantification of metastatic tumor burdens in liver), in small animals. Although the concentration in iodine (50 mg(I).mL^{-1})

is lower than the liposome based agent, similarities can be found in terms of size (diameter around 150 nm) and biodistribution at an injected dose of 0.875 g(I).kg^{-1} mouse body weight (long-circulating half life: around 8 hours before accumulation in the hepatobiliary system) [55].

Fabrication process Nanoemulsions can be made using high energy emulsification devices (high shear stirring or rotor-stator devices, high-pressure homogenizers, ultrasound generators) [56]. These methods usually involve two steps. A first step where the nanodroplets are created by disrupting a pre-emulsion and a second step where the surfactant is adsorbed at the surface to insure high stability. Because of the high energy required, these techniques generate heat. This is a major setback should any temperature sensitive compound be incorporated.

There are also low energy processes that advocate for an almost spontaneous formation of the nanodroplets. One principle is based on a rapid diffusion of an organic phase containing the iodinated oil into the aqueous phase containing the surfactant, this is the spontaneous emulsification technique. Another category relies on phase transition mechanisms, with a change of parameters such as composition of the system (Emulsion Inversion Point (EIP)) or temperature (Phase Inversion Temperature (PIT)) [57] [58].

One major limitation of the nanoemulsions as contrast agent for CT is the low iodine concentrations, forcing the administration of higher volumes of contrast media.

1.2.2.3 Dendrimers

Dendrimers for CT applications are iodine-labeled macromolecules, structured in polymeric branches chemically attached together. Typically, there is a core surrounded by different layers (also known as generations), where iodinated compounds can be entrapped. The polymers that constitute the last layer present functional groups able to react with iodinated molecules or/and other compounds capable of increasing solubility, biocompatibility and stealthiness.

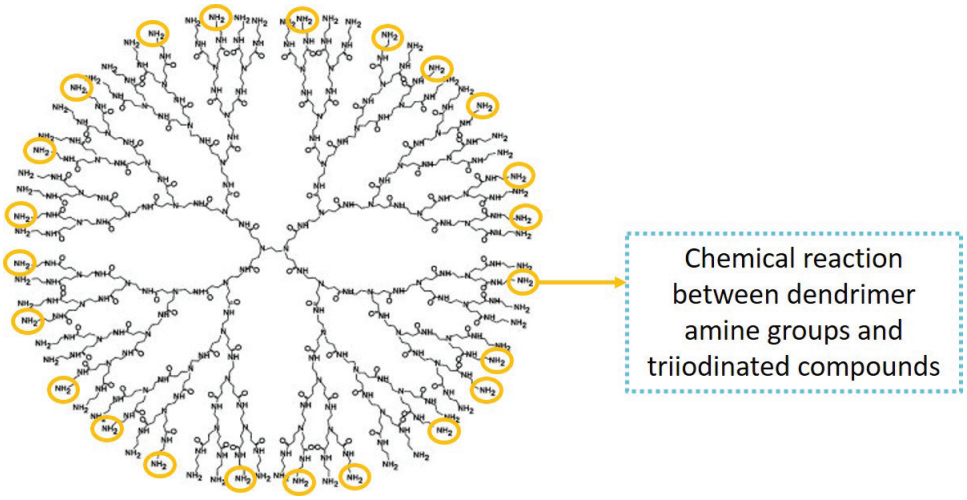

Figure 1.28: Opacification of Generation 4 Poly(amidoamine) (PANAM) dendrimers

In the early 2000s, Brechbiel's team were the first to propose a water-soluble iodinated dendritic nanoparticulate systems using Generation 4 poly(amidoamine) (PANAM) dendrimers. The clinically used iodinated solutions are made of molecules containing a maximum of three iodine atoms per aromatic ring. In this example, the PANAM dendrimers are made radiopaque by covalently linking triiodinated molecules to the amine groups (Figure 1.28). Up to 37 triiodobenzenepropanoic acid derivatives were attached (i.e. 111 iodine atoms per dendrimer units) [59]. Here it is more question of macromolecules with 33% iodine content and a hydrodynamic radius of 3.4 nm, more than nanoparticles properly speaking.

Another team tested *in vivo* a dendritic PEG-core iodinated contrast agent with 27% iodine content. The final formulation concentrated by 75 mg(I).mL^{-1} was injected in a rat's tail vein at a dose of 450 mg(I).kg^{-1} body weight. As an outcome, an intravascular enhancement was observed with a blood circulation half-life of approximately 35 minutes [60]. Albeit this result is more than a circulation time provided by a regular iodine molecule compound, it is way less than what is expected with larger particles.

Fabrication process Dendrimers can be synthesized following either the convergent or the divergent approach. The divergent approach is a layer-by-layer fabrication process starting from the core. Once the first layer is laid, the end-functions are deprotected in order to react the second layer and so on. Available reactive functions on the external shell grow exponentially with the number of generations. However, the more layers are added, the more the purification step can be difficult. Indeed, this is due to the fact that the formed dendrimer and the layer to be added can be close in molecular weight. This technique can be used to incorporate the iodinated compounds.

In the convergent approach, the dendrimer is built from the periphery to the inner core. Here the purification step is simplified in the sense that the molecular weight of the dendrimer and that of the layer that is to be implemented are different which facilitated their separation. Another problem arises concerning the accessibility therefore the reactivity of the functions of the inner layers. In fact, they may be hindered by the increasing number of the outer layers as the macromolecule grows.

In all cases, the fabrication process of iodinated dendrimers involves many steps that can prove to be long as the system start to get interesting with at least four generations (111 iodine per dendrimers), and tricky with all the purification necessary for a low final yield. As an example, even after the dendrimer is manufactered, the coupling reaction with iodinated compounds can take 3 to 5 days [60].

1.2.2.4 Micelles

Micelles are also amphiphilic self-assembled compounds. However, contrary to liposomes that aggregate from a phospholipid composed of a hydrophilic head and a hydrophobic tail with two hydrocarbon chains, micelles are formed from a surfactant made of a hydrophilic head and a tail with only one hydrocarbon chain (Figure 1.29). Polymeric micelles for CT are iodine-containing aggregates of amphiphilic block copolymers self-assembly into a core-shell structure, above the critical micellar concentration (CMC). Usually, the hydrophobic moiety constitutes the core and the shell is formed by the hydrophilic part, resulting in a colloidal system dispersed in an aqueous medium.

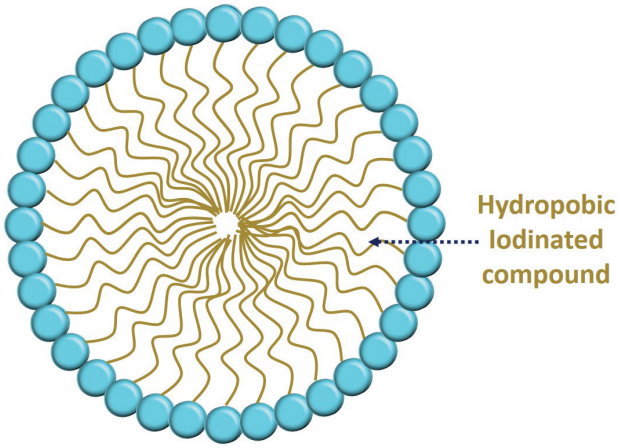

Figure 1.29: Radiopaque micelles for CT

Torchilin *et al.* proposed one of the first iodine-containing micellar nanosystems. It is in fact iodine-substituted poly(L-lysine) (MPEG-iodolysine) self-assembled into 80 nm micelles containing an iodine concentration of 33.8% (22 mg(I).mL^{-1} after concentration), in an aqueous solution [61]. 170 mg(I).kg^{-1} body weight were then intravenously injected to rats. Here again, a typical nanoparticulate blood pool behavior was observed with an enhancement of the cardiovascular system up to 3 hours with progressive accumulation in liver and spleen. Note that the injected dose is lower than the ones presented in the liposome or nanoemulsion studies. There seem to be a correlation between the injected dose and the blood circulation time in the sens that higher doses should logically result in longer blood circulation time.

Fabrication process Here a focus has been made on iodinated polymeric micelles. Their production can be divided into two steps. A first step of polymerization of hydrophilic and hydrophobic monomers in order to create an amphiphilic block copolymer. One process that is used to do so is the Reversible Addition-Fragmentation chain-Transfer (RAFT) polymerization [62]. Followed by a second step where the iodinated radiopaque compound is incorporated either by means of a covalent link or solubilized inside the micelle core which then works as a nanocarrier [63].

The biodistribution of micellar contrast agents depends on the nature of the block copolymers. In the literature, many choices in terms of chemical nature of the polymer forming micelles (i.e poly(ethylene glycol-*block*-lactic-glycolic acid), poly(ethylene glycol-*block*-(caprolactone), poly(ethylene glycol-*block*-lactic acid) etc.) can be found. The ratio between hydrophilic and hydrophobic chains also play a key role on the type of iodinated micelles formulated [64] [65] [66].

Despite all the options available, the low iodine content in the final formulations leads to the injection of a very large volumes to achieve the same performance as other nanosystems. Care must be taken regarding toxicity.

1.2.2.5 Polymeric nanoparticles (PNPs)

Polymeric nanoparticles (PNPs) are solid colloidal particles made of a macromolecular material which can be natural (gelatin, chitosan, cellulose) or synthetic (poly(vinyl alcohol), poly(alkyl cyanoacrylates), poly(lactic acid), poly(lactic-*block*-glycolic acid), poly(ethylene glycol-*block*-lactic-glycolic acid), poly(ε-caprolactone), poly (methyl metha-crylate)) (cf. Table 1.3). These macromolecules being reputed biodegradable, they make PNPs nano-systems interesting candidates for the desired application. Another advantage of PNPs over lipid based nanosystems is an increase in colloidal stability and chemical resistance.

Depending on the process used for their preparation, nanospheres or nanocapsules can be obtained (Figure 1.30). These two systems offer the possibility of encapsulating hydrophobic drugs or iodine based radiopaque elements either in the inner core of the nanocapsules or trapped in the polymeric matrix of the nanospheres. Polymeric micelles fit in the category of PNPs.

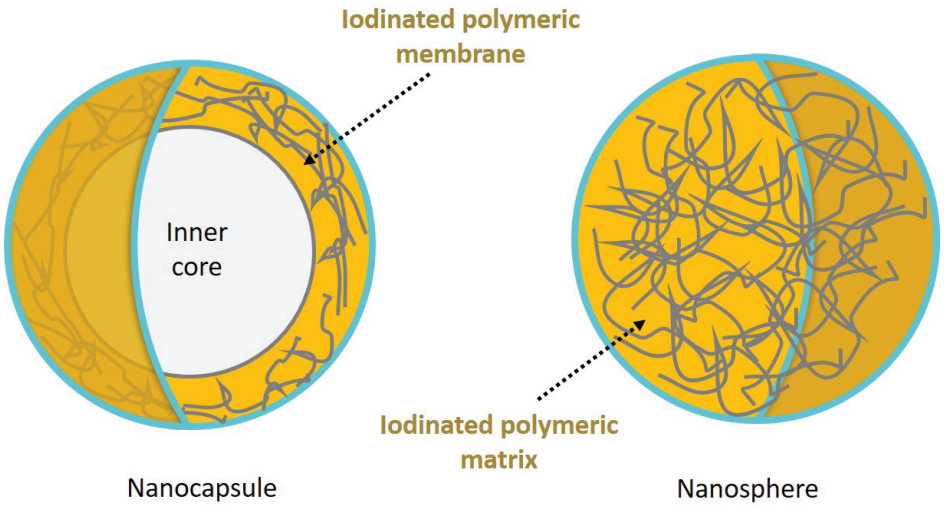

Figure 1.30: Polymeric NanoParticles (PNPs)

Several studies show that PNPs present similar characteristics and phamacokinetics as the other nanosystems mentioned above. Whether they are nanocapsules [67] or nanospheres [68], the same general trend is observed when it comes to *in vivo* biodistribution. For example, a team in Korea developed a nanocapsule with pluronic F127 shell (PEG–PPG–PEG) and a Lipiodol-loaded core, having a mean diameter of around 150 nm and a concentration of iodine ranging between 100-150 mg(I).mL^{-1} (400 mg.mL^{-1} of Lipiodol nanocapsules (LPNCs), 82% encapsulation rate). At the injected dose, 200 μL/mouse of LPNCs, the contrast agent remained in the bloodstream for 4 h. 24 h after administration, most of the LPNCs had accumulated in the spleen and liver [69].

Recently Hainfeld *et al.* developed a small (20 nm), long blood half-life (40 hours) iodinated nanoparticles by polymerization of a triiodobenzene derivative coated with PEG. In order to achieve such long circulation time, a high dose (1.75 g(I).kg^{-1} body weight) of the contrast agent with an iodine concentration of 80 mg(I).mL^{-1} was administrated with no visible toxicity. Despite their small size for PNPs, renal filtration was not possible and the clearance pathway

was similar to that of bigger particles, that is progressive accumulation in hepatic and spleenic tissues. The study was carried out for up to 9 months and only by then 81% of the iodinated compound was cleared [70].

The fate of nanoparticles when injected intravenously is a serious issue and this independently of the nanomaterial size once the renal filters can not be passed. Nevertheless, there is an interest in nanoparticles, like the long remanance in the cardiovascular system, among others. The right compromise must be found between blood pool effect and elimination should this type of nanosystem be considered for clinical stage one day. Another main advantage of PNPs is their potential biodegradability.

Fabrication process Two main strategies are commonly used to formulate polymer nanoparticles: polymerization of monomers and dispersion of preformed polymer. Both strategies are detailed in the next section.

Table 1.2: Iodine based nanosystems for CT imaging

Nanosystems	**Iodine content ($mg(I).mL^{-1}$)**	**Particle size (nm)**	**References**
Dendrimers	50-150	d = 5 - 20	[59] [71] [60] [72]
Liposomes	25-150	d = 80-500	[73] [74] [75] [76]
Micelles	20	d < 100 nm	[61] [63]
Nanoemulsions	50-70	d = 80-200	[77] [78] [79] [80]
Polymeric nanoparticles	50-100	d = 20-400	[69] [68] [81] [67] [82] [83] [70]

1.3 Processes for polymeric nanoparticles (PNPs) production

1.3.1 Polymerization of monomers

In this category, four techniques can be distinguished (Figure 1.31):

- Emulsion polymerization
- Dispersion polymerization
- Micellar polymerization (inverse microemulsion polymerization)
- Interfacial polymerization

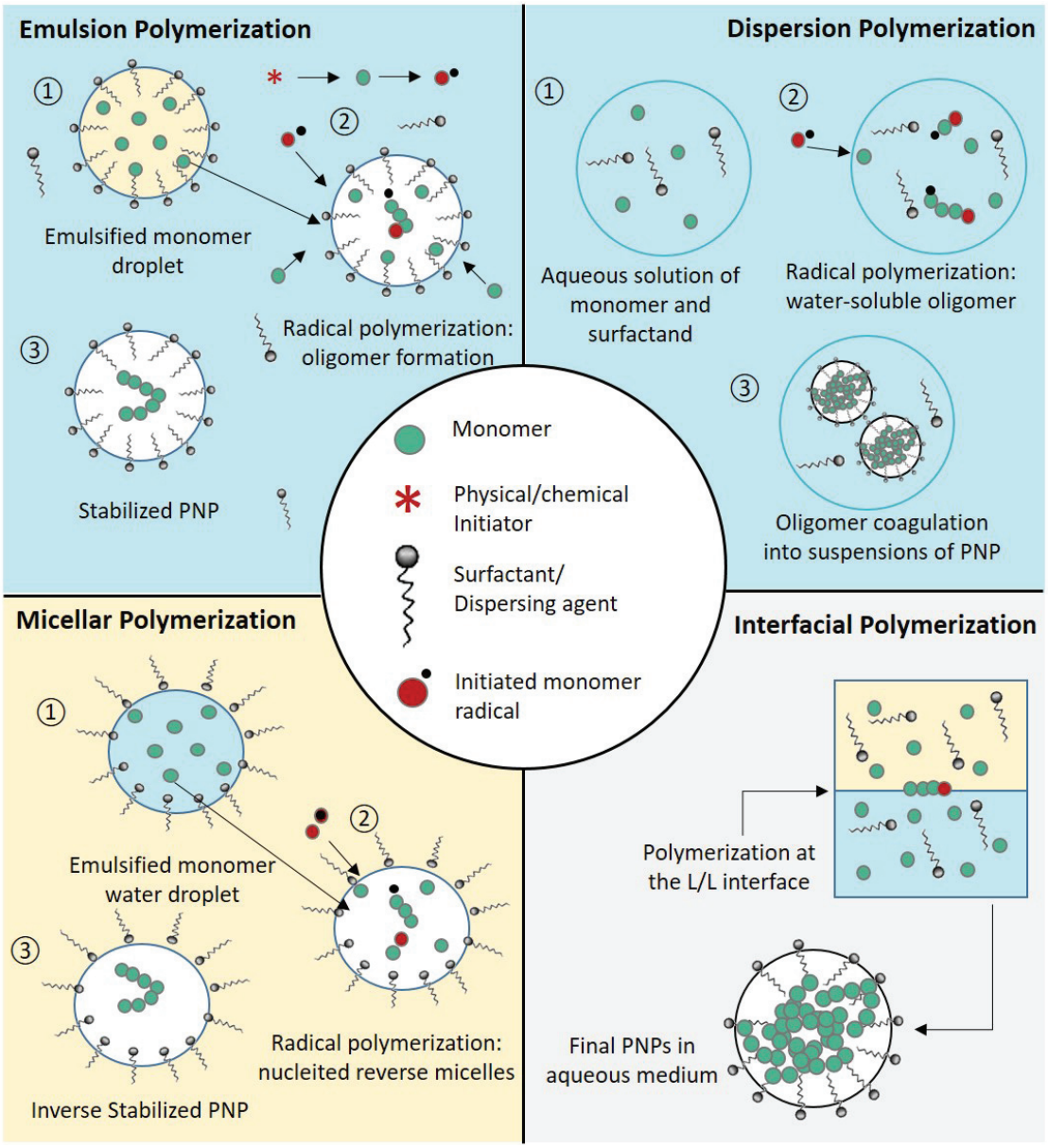

Figure 1.31: Polymeric nanoparticles (PNPs) formation from monomer polymerization

1.3.1.1 Emulsion polymerization

The starting point of this technique is an emulsion (most commonly oil-in-water) that comprise the polymerization medium (water), low water-soluble monomers and surfactant or dispersing agent. At this stage, the monomer is dispersed in water (either as droplets or micelles if the concentration of surfactant exceeds the Critical Micellar Concentration (CMC)). The radical chain polymerization that leads to the formation of suspensions PNPs is a three step process:

- Step 1: Initiation starts when a water soluble initiator is introduced in the emulsion. Since this chemical compound is not soluble in the monomer, it will initiate the dispersed monomers which will lead to the formation of oligomers.
- Step 2: Particle nucleation. During this step, either surfactants or other monomers are adsorbed onto the initiated dispersed monomer, forming stable nuclei.
- Step 3: Polymer chain growth will occur by polymerization of the stable nuclei, i.e. adsorption of new monomer/oligomer forming nanoparticles. This step ends when all the monomers in the medium have been adsorbed.

Patrick Couvreur *et al.* first described the preparation of biodegradable PNPs of poly (alkyl-cyanoacrylate) nanoparticles by emulsion polymerization, for *in vivo* drug delivery in 1979 [84].

Shlomo Margel's team has long worked on the synthesis of iodinated PNPs for CT using this method which resulted in a patent [85]. For instance, in a study carried out by Galperin *et al.*, the PNPs were developed following an emulsion polymerization of the monomer 2-methacryloyloxyethyl-(2,3,5-triiodobenzoate) (MAOTIB). The particles presented sizes ranging between 30-350 nm and a concentration in radiopaque elements of around 3 mg(I).mL^{-1} [68]. The very low concentration obtained forced a high quantity (267 mL) of contrast agent infused to the animal model (20 kg dog) tested, to reach a 40 mg(I).kg^{-1} dog body weight dose. Despite injection of such high amounts, no change in either blood tests or general health was observed 6 months after. Lymph nodes, liver, kidneys and spleen were still enhanced 24 h post-injection.

Two years later Aviv *et al.* managed to slightly improve the concentration of these nanosystem hence reducing injection dose, the contrast agent's biodistribution remained the same [86].

Note that this technique allows the size of the nanoparticles be controlled. In fact, it is possible to monitor the size during the polymer chain growth step and by optimizing the quantity of monomer introduced in the system. However, the very low iodine content yielded leads to high volume of injection, which is a major drawback.

1.3.1.2 Dispersion polymerization

In this process, the monomers are soluble in the polymerization medium (i.e. water). The starting point is an aqueous solution of monomer and surfactant or dispersing agent. The polymerization starts either by activation of an active center (from the monomer) by γ irradiation or by a chemical initiator. This leads to the formation of oligomers. At a critical molecular weight, these compounds will no longer be soluble in water, therefore will precipitate as primary unstable particles. These particles will then merge and form the final polymeric nanoparticles.

Galperin and Margel also synthesized iodinated PNPs by dispersion polymerization of an iodinated acrylate monomer. This technique, contrary to the emulsion-polymerization process, gave nano/micro-spheres of sizes ranging from 200 nm to 1.4 μm [87]. Although the later were not tested *in vivo*, one can imagine a quick uptake by macrophages considering their big size.

1.3.1.3 Micellar polymerization or inverse microemulsion polymerization

Here, as it is question of an inverse emulsion (i.e. water-in-oil), the hydrophilic monomer and surfactant will diffuse through the organic phase and will get trapped inside the water droplets/micelles. The polymerization will than take place inside these droplets or micelles formed. Here also the reaction is initiated either by irradiation or after the addition of a chemical initiator. The initiated monomers will lead to oligomers and finally small size particles, based on the fact that microemulsions create very small droplets.

The inverse microemulsion polymerization has been used to fabricate polyacrylamide nanoparticles by polymerization of acrylamide inside water swollen micelles dispersed in toluene. The experiments gave particles of around 500 nm [88].

1.3.1.4 Interfacial polymerization

In this process, two non miscible phases each containing monomers are involved. The hydrophilic monomers (in solution in the aqueous phase) will react with the hydrophobic monomers (in solution in the organic phase). The polymerization occurs at the liquid/liquid interface. Surfactants can be added in both medium, to stabilize the polymer particles [89].

Microcapsules containing octane were prepared using an interfacial polycondensation method in an emulsion system. The capsule size was around one μm [90]. The encapsulated material could be replaced by a radiopaque element like an iodinated oil.

Overall, the main drawbacks of the polymerization of monomers systems is the two steps required to form the nanoparticles and the purification steps that are necessary to remove residual subtances present after a polymerization reaction (residual monomer, or/and surfactant). Another way of producing PNPs is to create stable colloidal systems from preformed polymers.

1.3.2 Preformed polymer dispersion

Four main processes for fabrication of polymeric nanoparticles (PNPs) from preformed polymers are presented below:

- Emulsification-solvent evaporation method
- Emulsification-solvent diffusion technique
- Salting-out
- Nanoprecipitaion (or solvent displacement)

1.3.2.1 Emulsification solvent evaporation method

In this method, the polymer is dissolved in a volatile organic solvent that is not miscible with water (i.e. chloroform, dichloromethane, ethyl acetate). This organic phase is added to an aqueous solution containing a surfactant/dispersing agent. An oil-in-water emulsion is made, and the size of the droplets is reduced using a high energy process (ultrasounds, high pressure homogenization). Finally, the organic solvent is removed, by heating or/and under reduced pressure, leading to the precipitation of the polymer as nanoparticles (Figure 1.32).

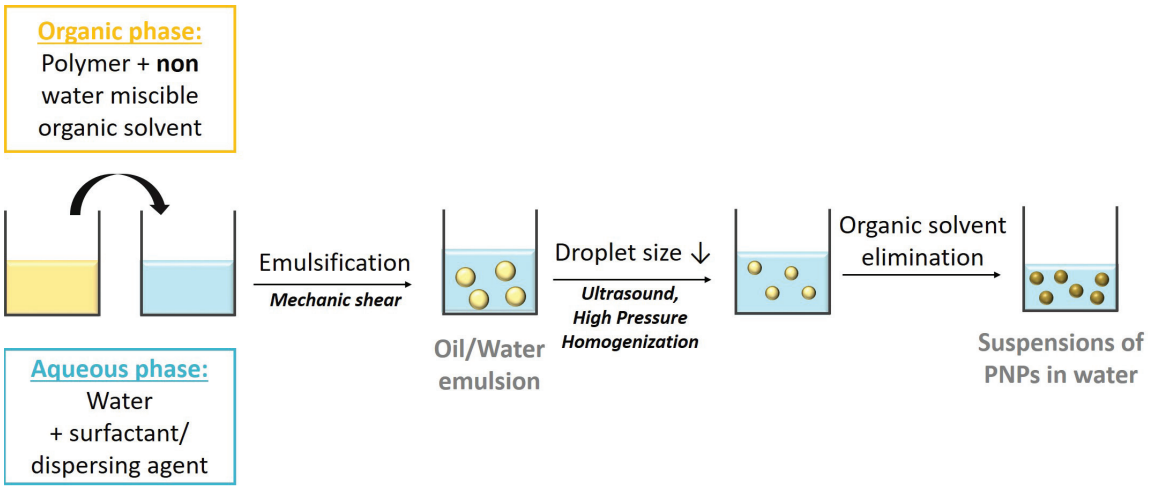

Figure 1.32: Schematic representation of the emulsification-solvent evaporation process for fabrication or PNPs

Desgouilles *et al.*, explained the transformation of nanoemulsions into nanoparticles using two different types of polymers: the first one being the ethylcellulose (EC) model, according to which the oil-in-water nanodroplets shrink and merge by coagualtion and coalescence as the organic solvent is removed, PNPs are formed afterwards. The second model is the poly (lactic acid) (PLA) theory, where there is no or limited nanodroplet coalescence, therefore one droplet generates one particle [91].

As an example, poly (lactic-co-glycolic acid) (PLA-PLGA) nanoparticles loaded with a drug (which can be replaced by a radiopaque element), were prepared using the emulsion/solvent evaporation process. The encapsulation rates varied between 10 and 30% for particle sizes between 60-200 nm.

A negative point to this technique is the use of high energy devices (here sonicator) necessary to reach the nanoscale [92].

1.3.2.2 Emulsification-solvent diffusion technique

Here, the organic solvent containing the polymer must be partially miscible in the aqueous phase containing a surfactant/dispersing agent. Before starting, the organic solvent is saturated with the aqueous phase and vice- versa, to insure initial thermodynamic equilibrium of both liquid phases prior to the emulsification step. Once the oil-in-water emulsion is made, water is added leading to the diffusion of the organic solvent into the dispersing phase, resulting in the

formation of the nanoparticles. The organic solvent is then removed under reduced pressure or by tangential flow ultrafiltration (Figure 1.33) [93].

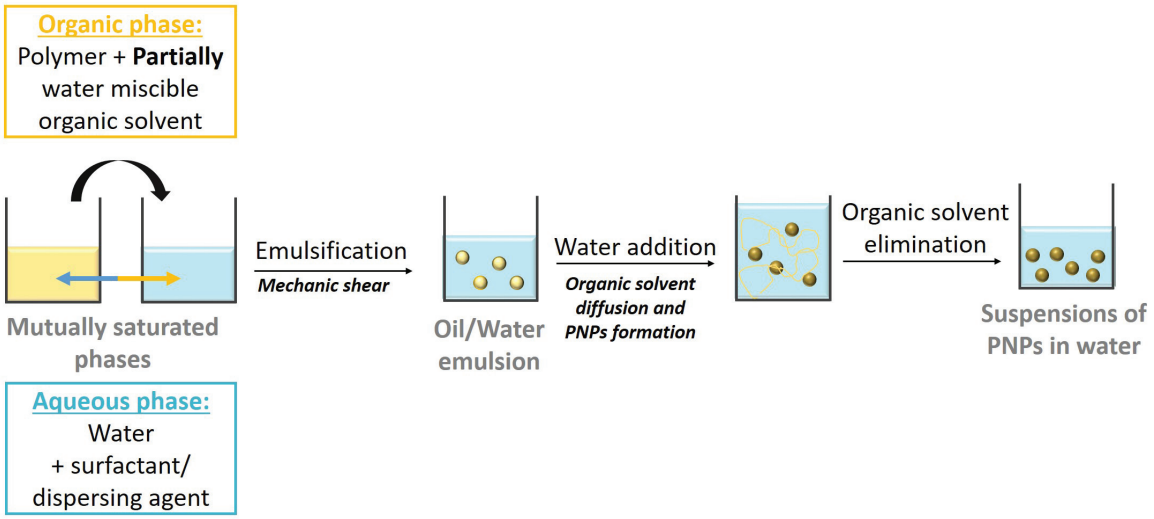

Figure 1.33: Schematic representation of the emulsification-solvent diffusion process for fabrication or PNPs

The emulsification-solvent diffusion technique was patented in the late 1990s by Quintanar *et al.* They studied a mechanism of PNPs formation using a poly(D,L-lactic acid) model. The hypothesis according to which nanoparticles are formed following a chemical instability that occurs when water is added to the o/w emulsion, was emitted. In fact, the organic solvent that is inside the nanodroplet diffuses into the dispersing phase, creating regions of local supersaturation where new nanodroplets and/or polymer aggregates are formed. Each emulsion droplet can form several nanoparticles. The PNPs are finally stabilized by the dispersing agent to avoid further coalescence or aggregation when all the organic solvent is removed [94].

Contrary to the emulsion-solvent evaporation technique, the process described above does not require high-pressure homogenizers or ultrasonication. However, a large quantity of water is needed for the solvent diffusion and PNPs creation yielding highly diluted final compounds. This is not compatible with contrast agent application as a high concentration of radiopaque element is needed.

1.3.2.3 Salting-out

The idea behind this process is to phase-separate two perfectly miscible solvents by adding an electrolyte to one of the phases. Therefore on one hand there is a solution of polymer dissolved in an organic solvent (i.e. tetrahydrofuoran, acetone), and on the other hand the aqueous phase containing surfactant in a saturated solution of electrolyte (usually $MgCl_2$ or NaCl). An oil-in-water emulsion is made and like in the emulsion solvent diffusion technique, the system is diluted by adding a large quantity of water. This allows the organic solvent to diffuse which leads to the formation of the polymer nanoparticles. Finally the organic solvent is removed under reduced pressure. A purification step is necessary to eliminate the salting-out agents (Figure 1.34) [95] [96].

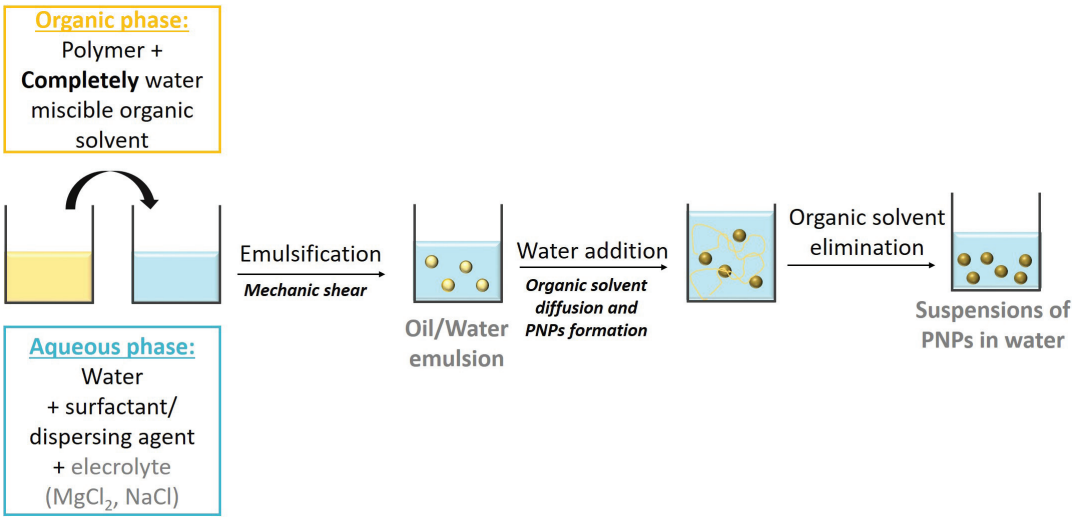

Figure 1.34: Schematic representation of the salting-out process for fabrication or PNPs

The salting-out process is quite similar to the emulsification solvent diffusion technique. The PNPs formation mechanism can also be assigned to an interfacial turbulence and polymer aggregation that happens following diffusion of the organic solvent in the aqueous medium once water is added to the preformed emulsion. Here also, the final formulation produced is highly diluted. Thereafter, a supplementary purification step is necessary to remove the salting-out agents.

1.3.2.4 Nanoprecipitation process

Nanoprecipitation also called solvent displacement or spontaneous emulsification is a technique based on the addition of a water miscible organic solvent containing the polymer to an aqueous phase where a surfactant/dispersing agent is dissolved. The addition is made drop wise under magnetic stirring. When the organic phase is poured into the aqueous phase, the organic solvent dissolves rapidly into the dispersing phase while the polymer precipitates as nanoparticles. Dilution with water creates a supersaturated solution of polymer from which precipitation of PNPs occurs. Finally, the organic solvent is removed under reduced pressure (Figure 1.35) [97] [98].

This method has also been called "Ouzo effect". It is named after the well known Greek beverage "Ouzo" which equivalent in France is "Pastis". Have you ever wondered how this dry anised-flavored drink goes from a transparent solution to a stable milky mixture when mixed with water, with only minimal agitation ? Here the organic phase is composed of an anise essential oil in solution in alcohol. The later being totally miscible with water, it quickly diffuses into the aqueous medium while the oil precipitates as nanodroplets forming a spontaneous nanoemulsion. Depending on the manufacturer, surfactants can be added to insure long term stability. Here exceptionally the organic solvent is ingested (with moderation of course).

According to Lince *et al.*, PNPs formation using the nanoprecipitation method is a three step process that involves nucleation, molecular growth and aggregation. Several physico-chemical specifications (PNPs size, size distribution etc.) depend on the rate at which these three steps

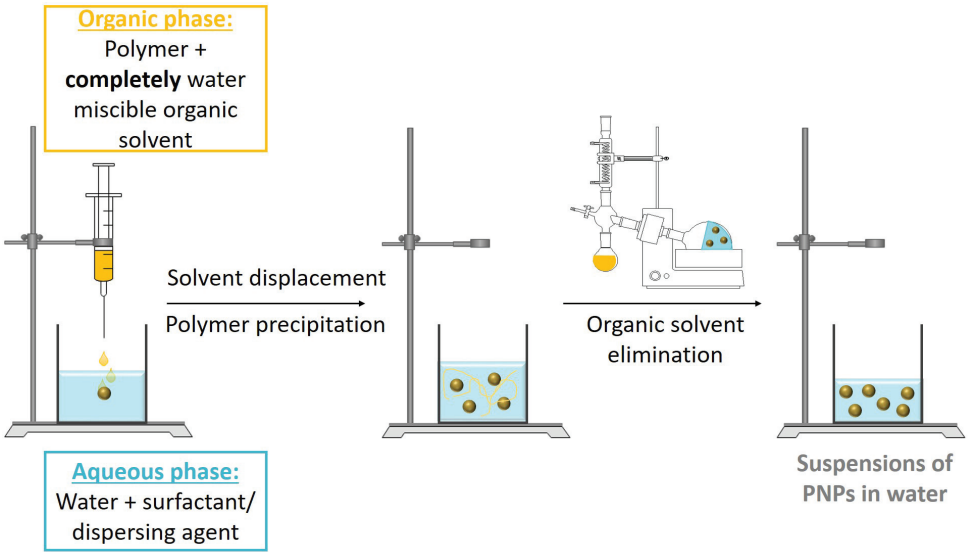

Figure 1.35: Schematic representation of the nanoprecipitation process for fabrication or PNPs

occur. The nucleation rate is essentially governed by the ratio between the polymer concentration and the polymer solubility in the organic solvent. This is known as supersaturation [99]. Practically, the polymer precipitation happens extremely fast once the organic phase droplet reaches the aqueous phase. Nucleation takes place once the polymer chains are in solution in a non-solvent environment following solvent displacement and associate together. There is a competition between aggregation of polymer particles and dispersing agent adsorption which results in formation of stable submicronic particles when stabilization is faster than aggregation.

Understanding the phenomena that lead to PNPs formation via the solvent displacement technique is important to modulate the physicochemical parameters of the nanoparticles with the desired specifications in terms of size, iodine content, size distribution and so on. It was established that the nucleation step is the most crucial step in the PNPs formation process. The later is influenced by specific chemical composition conditions (polymer concentration) or/and some operating conditions (mechanical stirring).

The main advantage of this technique is clearly the very low mechanical energy needed to generate nanoparticles. Based on that, the nanoprecipitation process was selected to formulate the nanoparticles of iodinated polymer.

1.3.3 Conclusion

As a short conclusion, globally all studied nanosystems can be used as blood pool agents once their surface has been modified by a stealth agent. They are also often used to image organs such as liver and spleen as a common trend is the accumulation in these two organs after an intravenous administration. It can be seen in Table 1.2 that choosing a nanosystem based on criteria such as iodine concentration or size is tricky as they all present similar results. However when fabrication processes are considered, some nanobiomaterials are easier to manufacture than the others. Consequentially, in this study the choice was made for a simple manufacturing technique (i.e. the nanoprecipitation process) that could provide biodegradeble and biocompatible CT agents as iodinated polymer nanoparticles.

Table 1.3: Processes for Polymeric NanoParticles (PNPs) production

Process	**Polymer**	**Organic solvent**	**Dispersing agent**	**PNPs type**	**PNPs size (nm)**	**References**
Emulsion polymerization	PCA P(MAOETIB)	- Toluene	Tween 20 SDS, PPS	Nanocapsules Nanospheres	200 30-400	[84] [68] [86]
Dispersion polymerization	P(MAOETIB)	2-methoxyethanol	PVP	Nanospheres	200-1400	[87]
Micellar polymerization	PAM	toluene	AOT	Nanospheres	< 500	[88]
Interfacial polymerization	polyurea (TDI-DETA)	cyclohexane	NP-10	Nanocapsules	1000	[90]
Emulsion solvent evaporation	PLGA	Dichloromethane/acetone	PVAL	Nanocapsules	60-200	[92]
Emulsification solvent diffusion	PLA	Ethyl acetate	PVAL	Nanocapsules Nanospheres	300-500	[100]
Salting-out	PLA	Acetone	PVAL	Nanocapsules Nanospheres	300-700	[101]
Nanoprecipitation (Solvent displacement)	PLA	Acetone	Pluronic F68	Nanocapsules	200-300	[97]

[1] Polymers: poly(cyanoacrylate)(PCA), poly(2-methacryoloyloxyethyl(2,3,5-triiodobenzoate)) (P(MAOETIB)), poly(acrylamide) (PAM), toluene-2,4-diisocyanate (TDI) and diethylenetriamine (DETA),poly(lactic-co-glycolic acid) (PLGA), poly(D,L-lactic acid) (PLA)

[2] Dispersing agents: Sodium dodecyl sulfate (SDS), poly(vinylpyrrolidone) (PVP), aerosol sodium bis(2-ethylhexyl)-sulfosuccinate (AOT), poly(ethylene glycol) nonylphenyl ether (NP-10), Poly(vinyl alcohol) (PVA)

1.4 General conclusion and aim of the work

1.4.1 State of the Art and conclusion

X-ray imaging has evolved and keeps on developing over the years. Full body scanning acquisition times have gone from hours to seconds and it only takes a few minutes to process and reconstruct a 3D image. Scientists have pushed the evolution towards providing information at the molecular scale.

It was seen that the CT technology is based on the probability of interaction between the electromagnetic radiation in a specific range of energy (25-140 keV) and electrons that constitute the matter. The atomic number Z of elements is the main parameter. The higher Z is, the higher the attenuation. The contrast in shades of grey, comes from the difference of attenuation between the tissues.

On the other hand, except for bones (calcium Z = 20), a healthy living body is mostly composed of oxygen (Z = 8), carbon (Z = 6) and hydrogen (Z = 1) that provide low radiopacity, so that it is invisible to X-rays. For soft tissues (liver, spleen, blood vessels etc.) to appear, it is necessary to use "flashlights" in order to reveal their structure. This is the role of contrast agents. These chemical substances must satisfy certain conditions, such as very high atomic number (Z) to increase the electron density of the organ under examination but also low viscosity to insure good injectability, biocompatibility (iso-osmolarity, hydrophilicity), absence of toxicity etc.

Today the gold standard clinical contrast agents for CT are small water-soluble iodinated molecules that are cleared from the organisms withing minutes. However with all the features presented by the SPCCT technology (i.e. better differentiation and classification of different tissue types, simultaneous discrimination of different attenuation profiles, in vivo quantification of high atomic number elements), there is a clear need to develop new agents with more options (active targeting, long blood circulation times etc.).

In fact, spectral CT combined to specific long lasting nanoprobes, has already proven to be an interesting tool to assess certain diseases at an anticipated level in many preclinical studies. One good example is the monitoring of the atherosclerosis plaque which depending on the stage at which it is detected could prevent acute events (i.e. stroke or myocardial infarction). At a more general level, all tissues that contain damaged vasculature are concerned since they present a risk of leackage outside the cardiovascular system. The use of both the SPCCT and iodinated polymer nanoparticles can therefore be extended to pathologies such as cancer, aneurysm, internal bleeding and so on.

There are several possible candidates (dendrimers, liposomes, nanoemulsions, micelles, PNPs etc.) that present comparable physicochemical characteristics (size, size distribution) and similar biodistribution profiles (blood pool, passive targeting of liver and spleen etc). In order to choose one among them, an easy and scalable fabrication process is a key criteria. The nanoprecipitation process was selected for formulating polymeric nanoparticles.

Finally, the SPCCT technology has reached the clinical stage, but this is not the case for contrast agents as nanoparticles. Many challenges still lay ahead, the biggest one being the elimination route. Although biodegradation of polymeric nanoparticles can be expected at some point, the residence period is a pending question that needs to be addressed.

1.4.2 Aim of the work

This work is part of a large European project which aims at developing and validating a new *in vivo* imaging technology combining a Spectral Photon Counting Computed Tomography (SPCCT) and specific contrast agents for improved diagnosis in opaque regions of the body, (i.e. bones, calcified plaque vessels and so forth). The ultimate purpose is a faster and better detection and monitoring of atherosclerosis derived neurovascular and cardiovascular diseases.

In this work, iodinated polymer nanoparticles were developed. Full physicochemical characterization of the polymer and of the polymeric nanoparticles is made in the next chapter. The radiopaque characteristics of the contrast agent is evaluated both *in vitro* and *in vivo* after biodistribution studies performed by intravenous injection (IV) in small animals. An *in vitro* study is also presented as to show the SPCCT quantification capabilities and discrimination using two radiopaque elements.

Different parameters that govern the nanoprecipitation process were investigated and optimized in order to meet the physicochemical specifications set for an iodinated contrast agent in the form of polymeric nanoparticles. The details are depicted chapter 3.

In the fourth chapter, a study was designed with the intention of breaking through one of the great concern related to the elimination of intravenously administrated nanobiomaterials. Preliminary results performed on experiments with macrophages cell cultures are presented.

In a fifth chapter, an atherosclerosis targeting agent was developed. Indeed, a tropoelastin targeting polypeptide was bound to the iodinated polymer nanoparticles. The bioconjugation was monitored via a Biacore assay with human tropoelastin as a positive control and the dextran layer of the Biacore sensor chip as the negative control.

Although iodinated polymer nanoparicles present many interesting properties as a blood pool contrast agent for CT, iodine is not a suitable element for K-edge imaging. In order to benefit from this interesting SPCCT feature, another element was studied in parallel. So in the last part, a simple method of producing tantalum-based nanomaterial designed for K-edge imaging is depicted.

Finally, a general conclusion will be made as well as potentially interesting suggestions as for studies that can be carried out to keep on improving in the field of nanoparticulate contrast agents for SPCCT.

Chapter 2

Characterization and properties evaluation

Contents

2.1 Abstract 49

2.2 Introduction 49

2.3 Experimental section 50

2.3.1 Materials 50

2.3.2 Methods 54

2.4 Results and discussion 56

2.4.1 Synthesis and characterization of iodinated polymer (TIB-PVAL) 56

2.4.2 Iodinated polymer nanoparticles: physicochemical characterization 58

2.4.3 Cytotoxicity assessment 65

2.4.4 Radiopacity assessment 65

2.5 Conclusions 72

Preamble

In this chapter, full physicochemical characterization of the polymer (thermal behavior, iodine content grafted etc.) and of the polymeric nanoparticles (size, morphology, stability etc.) is made. The iodinated polymer nanoparticles present a PEG shell on their surface. PEG chain coverage and footprint are important characteristics in predicting stability and furtivity of the nanosystem. These parameters were assessed in this study.

The radiopaque properties of the iodinated polymer and the nanoparticles were evaluated *in vitro*. Biodistribution studies were performed *in vivo* after intravenous (IV) injection in small animals and at different time points. The results were compared to the biodistribution of a clinically used solution of iodine contrast agent.

In this chapter, an *in vitro* study is also presented as to show the SPCCT quantification capabilities. The concentration provided by the scanner was compared to the quantity of iodine detected by ICP-OES. Finally, it was seen in section 1.1.3 of the state of art that the SPCCT is able to simultaneously discriminate two radiopaque elements, within a single scan. This characteristic was also covered in this part.

Iodinated polymer nanoparticles as contrast agent for Computed Tomography using a Spectral Photon Counting CT

J. Balegamire, H. Fessi, M. Vandamme, E.Chereul, S. Si-Mohamed, L.Ettouati,S. Azzouz Maache, L. Boussel, P. Douek, Y. Chevalier

Biomaterials (to be submitted, 2019)

2.1 Abstract

The synthesis and physicochemical characterization of aqueous suspensions of polymer nanoparticles of an iodine-based contrast agent for Computed Tomography (CT) and Spectral Photon Counting Computed Tomography (SPCCT) is reported. Iodine containing moieties were successfully grafted onto a low molar mass poly(vinyl alcohol) by means of a covalent ester bond. High grafting rate or degree of substitution (DS = 0.77) provided high iodine content (71 wt% from ^{1}H NMR, 65 wt% from ICP-OES). Nanoparticles stabilized by the block copolymer polycaprolactone-*b*-poly(ethylene glycol) (PCL_{65}-*b*-PEG_{113}) were prepared by the nanoprecipitation process. Highly stable (up to 8 months in water and human serum), monodisperse suspensions of iodinated polymer nanoparticles with an average diameter of 150 nm (TEM). High coverage of nanoparticles by PEG chains in a dense "brush" conformation (0.30 molecules.nm^{-2}) allowed stabilization and resistance against fast elimination by macrophages. An iodine concentration of 100 mg(I).mL^{-1} reached after a centrifugation/redispersion step provided radiopacity of the contrast agent in the right range for imaging cardiovascular system and biodistribution. SPCCT material decomposition and K-edge reconstruction allowed accurate quantification of iodine, as well as specific discrimination of gadolinium and iodine in phantoms containing mixtures of both elements. Biodistribution was assessed after intravenous injection of iodinated polymer nanoparticles to rats, revealing a clear visualization of the cardiovascular system followed by progressive accumulation in liver and spleen. These organs were still visible up to 4 days post-injection.

2.2 Introduction

Contrary to conventional CT that provides a single attenuation measurement, Dual Energy scanners (two attenuations are measured in different energy ranges), and Spectral Photon Counting CT (SPCCT), allow discriminating different elements by recording the X-ray energy spectrum of tissues attenuation at each voxel of the image. This allows material decomposition and K-edge reconstruction (for high atomic number (Z) elements with K-edge between 40-100 keV [102]), that provides relevant qualitative information and allows quantitative determination of the concentration of a specific element [13], [21], [14].

Thanks to their high atomic number (Z = 53), iodine-based materials are widely used as contrast agents for X-ray imaging. The agents currently used in clinical procedures are small iodinated molecules that have very short circulation half-lives and might show renal toxicity [103]. To overcome these drawbacks, contrast agents in the form of nanoparticles are being investigated [104], [105], [106]. Expected benefits of such contrast agents with respect to current solutions of small molecules is a high iodine concentration while retaining a low viscosity and a specific biodistribution after injection that may be suitable in some applications in radiology. In addition to providing a higher payload of radiopaque elements in a single nanomaterial [40], the later may be given a tunable surface with targeting biomarkers that can bind to specific sites where nanoparticles concentrate and provide high contrast for low injected doses. A stealth agent (i.e. PEG) can also be implemented at the surface of nanoparticles in order to increase circulation time in the blood stream. Furthermore, such organic polymer particles can be loaded with active ingredients, resulting in "theranostic" compounds [46]. Albeit iodine is not well-suited for K-edge imaging (K-edge of iodine is 33.2 keV), these features make iodine-based nano-biomaterials promising contrast agents for the SPCCT technology.

In the literature, different types of iodinated nano-systems for CT imaging have been reported (i.e. dendrimers [60], liposomes [74], micelles [61], emulsions [78], [80], organic nanoparticles [81]) together with their preparation processes [107], [108]. Special focus is presently made on polymeric nanoparticles that show much better stability and resistance to various stimuli.

Two main strategies are commonly used to formulate polymeric nanoparticles: polymerization of monomers which is a two-step process that includes techniques such as emulsion polymerization [109], [68], dispersion polymerization [110], micellar polymerization (also known as inverse microemulsion polymerization) [88] and interfacial polymerization [111]. The second fabrication route involves dispersion of a preformed polymer using various processes: emulsion-solvent evaporation, emulsification-solvent diffusion, salting-out, and nanoprecipitation (or solvent displacement) [97].

The aim of this study is to design an iodine-based contrast agent for CT and SPCCT imaging, in the form a polymeric nanoparticles of 100-200 nm size range. Preformed polymers can be made radiopaque by covalently grafting an iodine-containing moiety onto the macromolecular structure thus preventing iodine leakage [112]. The nanoprecipitation process was chosen for nanoparticle fabrication as it is a one-step process yielding nanoparticles and it does not require high energy. Physicochemical characterizations of the iodinated polymer (iodine content, crystallinity etc.) and the nanoparticles (size, morphology, stability) were performed. X-ray radiopacity of iodinated polymer nanoparticles was investigated *in vitro* on phantoms and *in vivo* by intravenous injection of the contrast agent to rats and CT imaging them. The potential of the SPCCT technology in terms of *in vitro* element quantification and discrimination of several contrasting elements within a single scan was also assessed.

2.3 Experimental section

2.3.1 Materials

Chemicals. The following analytical-grade chemicals were purchased and used without further purification: 2,3,5-triiodobenzoic acid (Changzhou Ilhang Fine Chemical Co. Ltd, China), thionyl chloride (Acros Organics, 99.5%), sodium carbonate, dichloromethane (Acros Organics, 99.9%). N-methyl-2-pyrrolidone (NMP, 99.5%), pyridine (99.5%) and 4-dimethylaminopyridine

(DMAP, 99.5%) were purchased from Acros Organics in anhydrous grade over molecular sieves in an AcroSeal® packaging. Poly(vinyl alcohol) (PVAL, Sigma-Aldrich, 98% hydrolyzed, average molar mass M_W = 13 000 - 23 000 Da) was dried at 40°C in an oven for 24 h under vacuum before use. Tetrahydrofuran (THF, Fisher Scientific), absolute anhydrous ethanol (Carlo Erba) were used in purification processes. The block copolymer polycaprolactone-*block*-poly(ethylene glycol) (PCL_{65}-*b*-PEG_{113}) was synthesized by polymerization of caprolactone initiated by poly(ethylene glycol) monomethyl ether catalyzed by tin octanoate as reported in refs [113] [114]. Deionized water of 18 Ω.cm resistivity was used for the preparation of suspensions.

Cells. The BALB/c mice peritoneal macrophage cell line J774A.1 from the European Collection of Cell Cultures (ECACC, 91051511) were used to assess cytotoxicity. These cells were maintained at 37°C with 5% CO_2 by successive passages in RPMI-1640 culture medium (PAA Laboratories, GE Healthcare, Pasching, Austria) containing 10% (v/v) fetal bovine serum (from Sigma, St-Quentin Fallavier, France), 1% MycoKill AB and 1.5% penicillin/streptomycin.

Animals. Wistar rats (male, body weight 200-300 g) from Janvier Labs (Le Genest-Saint-Isle, France) were used for the *in vivo* studies. The animals were maintained in standard cages at 20-25°C with humidity > 35%. The lighting cycle was the following: 12 hours of artificial lighting/12 hours of darkness. Water and standard laboratory food were given *ad libitum*. The rats were sedated before imaging using a mix of isoflurane (1-5%) and oxygen as a carrier gas in order to maintain general anesthesia throughout the duration of the study. A catheter was placed in the tail vein for contrast agent administration.

2.3.1.1 Synthesis of the iodinated polymer (TIB-PVAL)

TIB-PVAL was prepared by an esterification reaction of 2,3,5-triiodobenzoyl chloride (TIBCl) and the alcohol groups of PVAL according to the reaction scheme shown in Figure 2.1.

Synthesis of 2,3,5-triiodobenzoyl chloride (TIBCl). 100.53 g (0.20 mol) of 2,3,5-triiodobenzoic acid was suspended in 180 mL (1.562 mol, 7.8 eq.) of thionyl chloride in a 500 mL round bottomed flask fitted with a condenser. The suspension was refluxed under stirring until hydrochloric acid release ceased. After cooling, thionyl chloride was removed under reduced pressure with Na_2CO_3 into the receptor flash to trap acidic vapors (HCl, $SOCl_2$). Recrystallization of the brown solid from dichloromethane (80 mL, 3 days at room temperature for crystal growth) yielded TIBCl as large light brown prisms (67.28 g, yield = 65%).

^1H NMR (300 MHz, $CDCl_3$), δ in ppm from TMS): 7.89 (d, $^3J_{H-H}$ = 1.9 Hz, 1H, Arom-H_{para}), 8.37 (d, $^3J_{H-H}$ = 1.9 Hz, 1H, Arom-H_{ortho})

Synthesis of the iodinated polymer (TIB-PVAL). The radiopaque polymer was prepared by binding the TIBCl iodinated molecule to poly(vinyl alcohol) (Figure.2.1) as described in the literature [115].

Solution A was prepared in a round-bottom flask by dissolving 117.64 g (0.227 mol., 1 eq.) of TIBCl in extra dry NMP (60 mL).

Solution B was prepared in a three-neck round-bottom flask: PVAL (10 g, 1 eq.), 3.33 g of DMAP (0.027 mol, 0.12 eq.) and NMP (300 mL) were stirred for 20 min at 130°C under dry

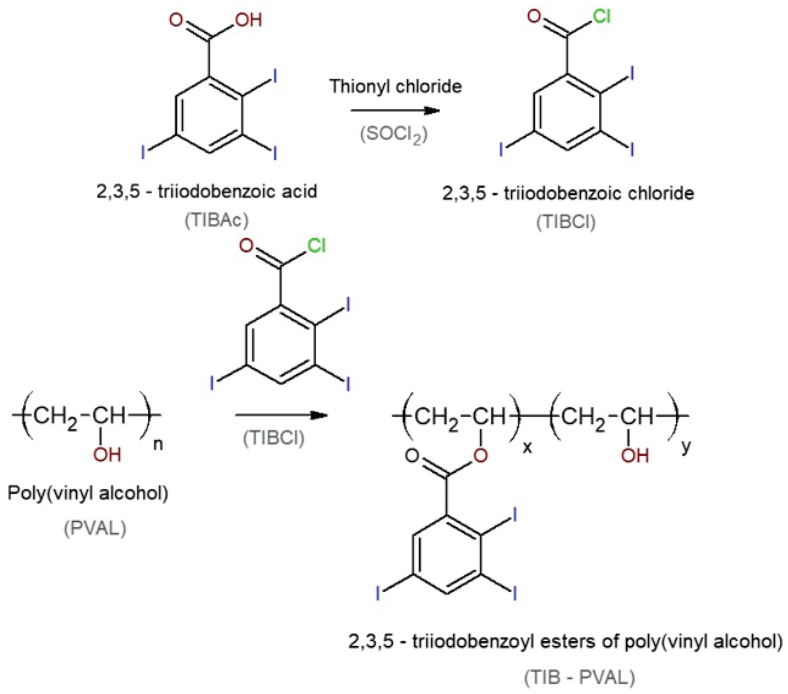

Figure 2.1: Synthesis of iodinated polymer (TIB-PVAL): synthesis of 2,3,5-triiodobenzoyl chloride (top), covalent linkage of 2,3,5-triiodobenzoyl chloride to poly(vinyl alcohol) (bottom).

nitrogen gas flow until the polymer was dissolved to completion. The solution was then cooled down to room temperature, and 21.53 g of pyridine (0.272 mol, 1.2 eq.) was added.

Solution A was poured dropwise into solution B and the mixture was heated at 60°C under magnetic stirring overnight under inert atmosphere. TIB-PVAL was recovered by precipitation from the reaction medium in 1 L of deionized water, filtration and drying in a vacuum oven at 40°C.

The dry product was purified by dissolution in a minimum amount of THF and precipitation in a large volume of ethanol under strong magnetic stirring. After filtration, TIB-PVAL was dried in an oven at 40°C under vacuum. Such precipitation process was repeated until the sharp lines of organic solvents (NMP and ethanol) and TIBCl were no longer detected in the ^1H NMR spectrum. Finally, a beige powder was recovered (78 g, yield = 61%).

^1H NMR (300 MHz, DMSO-*d6*, δ in ppm from TMS): 1.35-2.0 (m, CH_2 PVAL chain, 2(x+y)), 3.78 (s, CH_b PVAL chain, y), 3.98-4.95 (m, OH), 5.30 (s, CH_a PVAL chain, x, 7.63 (broad unresolved doublet, Arom-H_{para}, x), 8.22 (broad unresolved doublet, Arom-H_{ortho}, x)

^{13}C NMR(126 MHz, DMSO-*d6*, δ in ppm from TMS): 165.18 C_1, 148.24 C_2, 139.60 C_3, 136.22 C_4, 114.89 C_5, 107.25 C_6, 95.37 C_7, 69.85 C_8, 63.67 C_9, 41.84 C_{10}.

IR (cm^{-1}): 3360 (broad band of associated O-H), 2916.2 (C-H), 1721.6 (C=O of ester), 1519.0 (C-H aromatic), 1362.1 (C-OH), 1259.3 (aromatic ester), 1175.9 (C-H aromatic), 1097.0 (aromatic ester), 999.1 (C-H aromatic).

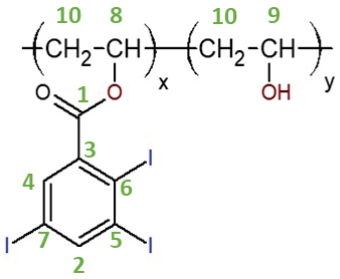

Figure 2.2: TIB-PVAL ^{13}C NMR position

2.3.1.2 Preparation of nanoparticles

Nanoparticles (NPs) of iodinated polymer were prepared using the nanoprecipitation process [97], [116]. TIB-PVAL (1 g) and the PCL_{65}-*b*-PEG_{113} dispersing agent (1 g) were dissolved together in 25 mL of THF. The weight ratio iodinated polymer/dispersing agent was set to 1/1. The organic solution was added dropwise to 50 mL of water under magnetic stirring, using a syringe fitted with a needle 21G (0.8 mm internal diameter). Note that the organic solvent/water volume ratio of (1/2) has been described in the literature as optimum to obtain suitable particle size in the nanoparticle range [100], [117]. Finally, THF was evaporated under reduced pressure, yielding an aqueous suspensions of nanoparticles. The iodine concentration of the dispersion was 17.7 mg(I)mL^{-1} (ICP-OES). A sketch of the full process is given Figure 2.3.

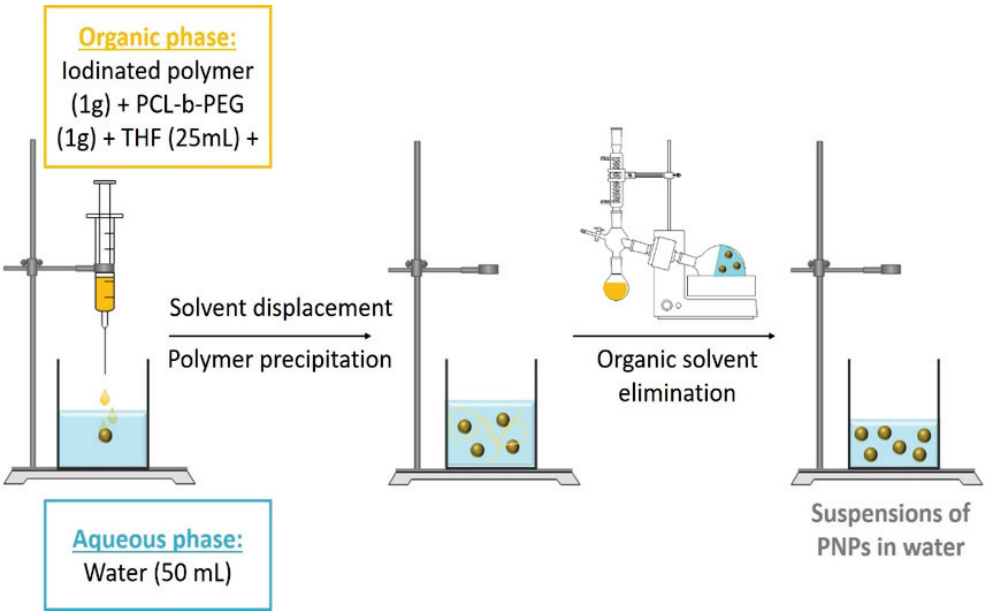

Figure 2.3: The nanoprecipitation process.

2.3.1.3 Concentration step

A concentration step has been implemented after the initial nanoprecipitation step that yielded suspensions of too low concentrations. An aliquot (10 mL) of the dispersion prepared by

nanoprecipitation was centrifuged (7930 rpm, 20 min), the supernatant was removed, and the sediment was redispersed in a minimum amount of water (1 mL), using an ultrasound bath at 40°C (2 h). The iodine concentration was 98.8 mg(I).mL^{-1} (ICP-OES) after the concentration step and the same particle size was kept.

2.3.2 Methods

2.3.2.1 Characterization of the iodinated polymer

^1H NMR Analysis. The grafting reaction of the TIBCl onto PVAL was monitored by ^1H NMR. Spectra of the TIB-PVAL solutions in deuterated dimethylsulfoxide (DMSO-*d6*) were recorded on Bruker ALS300 and DRX300 Fourier transform spectrometers (300 MHz). Data processing was done using MestrecNova (Mnova) software. The degree of substitution, DS = x/(x+1), was calculated by comparing the area under the peaks corresponding to the aromatic protons to the area under the peaks corresponding to the CH_2 of the PVAL backbone at 1.3-2.0 ppm.

IR Spectroscopy. IR spectra were recorded in ATR mode using a Thermo Scientific iS50 FTIR spectrometer equipped with an iS50 ATR module. A small amount of fine powder of compound was deposited on the diamond crystal of the ATR equipment, and the spectrum was recorded between 400 and 4000 cm^{-1} by accumulation of 32 scans at 2 cm^{-1} resolution.

UV Absorption. UV absorbance of solutions was measured in Hellma Quartz cells of 1 mm thickness using a Varian Cary 50 spectrometer. The absorbance of the solvent (THF) was subtracted as a background.

ICP-OES.The amount of iodine was determined by ICP-OES measurements on the polymer in solution using a Vista-Pro CCD simultaneous ICP-OES Varian instrument at the Institut des Sciences Analytiques (University of Lyon 1). The iodinated polymer was mineralized in HNO_3 for 24 h and the solution was subsequently diluted with water down to 0.2 ppm such that the concentration of iodine was in the working range of ICP-EOS. The mass fraction of iodine calculated from the DS determined from ^1H NMR analysis was compared to that measured by ICP-OES.

Thermogravimetric Analysis. A TGA instrument Netzsch TG 209 F1 was used for recording the mass loss of samples held in an alumina crucible under dry nitrogen flow between 20°C and 1000°C at a heating rate of 10°C.min^{-1}.

Differential Scanning Calorimetry. A DSC Q200 TA instrument was used for measurement of temperatures and heat associated with thermal transitions of the iodinated polymer. The amorphous/crystalline character of the polymer was evaluated by looking for characteristic thermal events such as glass transition (Tg), melting, and crystallization on cooling.

X-ray diffraction. X-ray crystallography was performed using a Bruker D8 Advance diffratometer at the Centre de Diffractométrie Henri Longchambon of the University Lyon 1 (http://cdalpha.univ-lyon1.fr/). The purpose was to determine whether there were crystalline parts in the polymer.

Size Exclusion Chromatography. The molar mass of the iodinated polymer was measured by size exclusion chromatography. The samples were eluted with THF..

2.3.2.2 Characterization of iodinated polymer nanoparticles

Particle size measurements. The hydrodynamic diameter and size distribution of nanoparticles dispersed in aqueous medium were determined using Dynamic Light Scattering (DLS) using a Zetasizer Nano ZS instrument from Malvern Panalytical. This technique is sensitive to particles of size in a 10-2000 nm diameter range and for diluted suspensions (ideal count rate 100-350 kHz). Two approaches can be used: the cumulant fit provides a z-average and a polydispersity index (*PdI*), and the inverse Laplace transform of the autocorrelation function by the CONTIN method provides the nanoparticle size distribution in scattered intensity, particle number or volume. Both calculation methods gave very close results. For the sake of comparison with other publications, the cumulant fit will be used to discuss on DLS results. They will be compared with size distribution in number measured by Transmission Electron Microscopy (TEM). Nanoparticle stability in water and in human serum at 4°C, 20°C and 37°C, was checked by measuring the hydrodynamic diameter over time.

Size and morphology. Transmission Electron Microscopy (TEM) pictures were obtained with a Philips CM120 electron microscope under 80 kV accelerating voltage, at the "Centre Technologique des Microstructures (CTμ)", University of Lyon 1 (http://microscopies.univ-lyon1.fr/). Samples were prepared by deposition of a drop (10 μL) of diluted formulation on a 400-mesh carbon-coated copper grid and drying in open air. The size distribution and average size of dry particles was determined from diameters of more than 100 particles determined by image analysis using the ImageJ software.

Determination of PEG density on the Nanoparticle surface. Polyethylene glycol (PEG) chain coverage was calculated using dry extract measurement (oven at 40°C under vacuum) and ^{1}H NMR analysis. The projected area per PEG chain, also known as PEG chain footprint was deduced and compared to that of pure PEG in water [118].

2.3.2.3 Cytotoxicity

J774A.1 cells were cultured in a 96 wells plate. Once cells had developed a monolayer, they were incubated with iodinated polymer nanoparticles at concentrations of iodine of 0 mg(I).mL^{-1}, 5 mg(I).mL^{-1}, 2 mg(I).mL^{-1}, 1 mg(I).mL^{-1}, 0.33 mg(I).mL^{-1}, 0.1 mg(I).mL^{-1} and 0.033 mg(I).mL^{-1} for 5 h before the culture medium was replaced by a new cell culture medium free of iodinated nanoparticles. Cell viability was determined at 24 h and 48 h using a MTS/PMS solution (CellTiter 96; Aqueous Non-radioactive cell Proliferation Assay, Promega, Madison, WI, USA). The absorbance of the formazan product was measured at 490 nm with a plate reader (Thermo Fisher Scientific 51118177 Multiskan EX Microplate Photometer, Villebon-sur-Yvette, France).

2.3.2.4 CT imaging

CT instruments. A General Electric (GE) BrightSpeed scanner equipped with an X-ray tube operating at 120 kV voltage, 100 mA tube current and the Avizo Fire reconstruction software provided multi-layer pictures of 310 μm spatial resolution.
A Bruker SkyScan 1278 micro CT equipped with an X-ray tube operating at 58 kV voltage, 753 μA tube current was used for imaging animals at higher spatial resolution of 51.7 μm.
A modified clinical base small FOV prototype Spectral Photon Counting Computed Tomography instrument (SPCCT, Philips Healthcare, Haifa, Israel) was also used to assess radiopacity. SPCCT acquisitions were performed at 100 mA tube current and 120 kVp tube voltage.

***In vitro* radiopacity of compounds**. Radiopacity of "phantoms" made of both the modified polymer in pellet and the aqueous suspensions was measured from CT scans. Pellets were prepared by pressing 20 mg of the dry iodinated polymer powder using a Pike technologies 13 mm Die Kit press at 7.4×10^8 Pa pressure. Aqueous suspensions at different concentrations were contained in 1.5 mL Eppendorf tubes.
Phantoms of two contrast elements were imaged and compared: nanoparticles of iodinated polymer and standard commercially available solution of gadolinium (ProHance/Gadoteridol, Bracco). Appropriate energy thresholds were chosen to provide optimal discrimination of gadolinium and iodine. The attenuation was measured in Hounsfield Units (HU) and elements concentrations were determined using specific reconstruction algorithms: Material Decomposition (MD) for iodine and K-edge reconstruction for gadolinium.

***In vivo* CT imaging**. Rat models (male, 250-300 g) were used to evaluate radiopacity and assess biodistribution of the contrast agent *in vivo*. A volume of 1.5 mL of aqueous suspensions of iodinated polymer nanoparticles of concentration: 90-100 mg(I).mL^{-1}) were intravenously administrated into the tail vein. This corresponded to a dose of 536 mg(I).kg^{-1}) regardless animal size. Full body CT and μCT scans were performed before injection, and from 5 min up to 15 days after injection at different time points.

2.4 Results and discussion

2.4.1 Synthesis and characterization of iodinated polymer (TIB-PVAL)

2.4.1.1 Grafting reaction and ^{1}H NMR analysis

Attachment of triiodobenzoyl graft to the PVAL backbone (Figure 2.4) was performed by reacting the corresponding acid chloride with the alcohol groups of PVAL in dry NMP medium, thus creating strong covalent ester bonds. Acid chloride was used in large excess with respect to the hydroxyl groups of PVAL. Several purification steps by dissolution in THF and recrystallization in ethanol were necessary in order to remove unreacted triiodobenzoyl chloride. These steps were repeated until all the corresponding peaks no longer appeared on the ^{1}H NMR spectra. Considering the slow molecular motions of polymers, the grafted iodinated aromatic moieties appeared as broad peaks at $\delta = 7.61$ ppm and $\delta = 8.23$ ppm ((Figure 2.4). Conversely, unreacted iodinated reagents mixed with the grafted polymer appeared as sharp peaks at $\delta =$ 7.76 ppm and $\delta = 8.34$ ppm. The absence of sharp peaks in the NMR spectrum showed that the concentration of residual small molecular impurities was lower that the detection limit of ^{1}H NMR.

2.4.1.2 Degree of substitution (DS) and iodine content (%I)

The degree of substitution (DS) or grafting rate ((Equation 2.1), was calculated from the integrals of the 2 phenyl protons specific to the grafted PVAL (CH between 7.5 and 8.5 ppm) with respect to integrals of protons of the PVAL backbone (CH_2 between 1.3 and 2.5 ppm or CHOH between 3.5 and 5.5 ppm) (Figure 2.4)..

$$DS = \frac{x}{x+y} = \frac{I(CH)_{7.5-8.5ppm}}{I(CH_2)_{1.3-2.5ppm}} \tag{2.1}$$

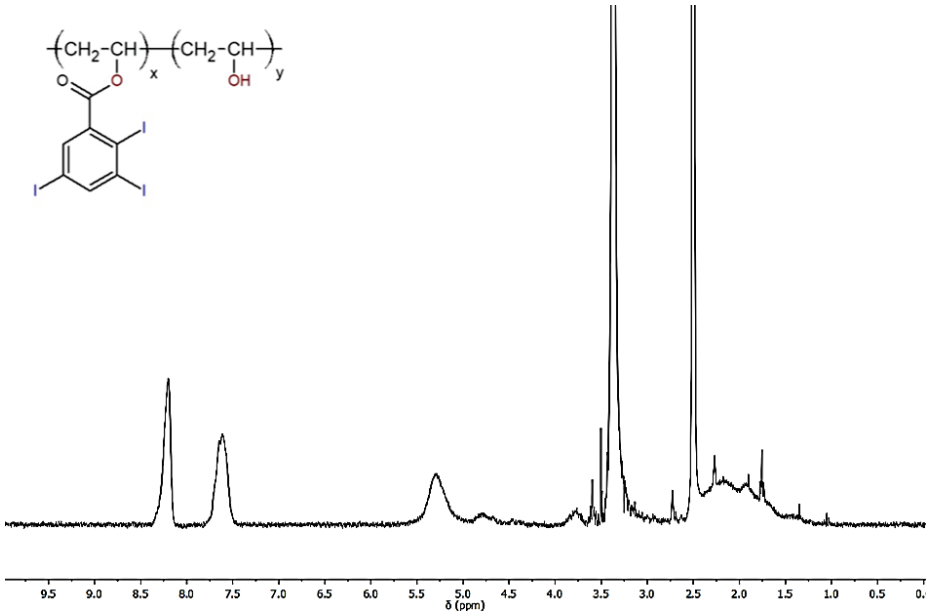

Figure 2.4: Modified PVAL with a radiopaque tri-iodobenzoyl moiety and ^{1}H NMR spectrum of TIB-PVAL in DMSO-*d6*.

DS was calculated with better accuracy from the integrals of the backbone CH_2 between 1.3 and 2.5 ppm. The substitution degree of TIB-PVAL 13 kDa was DS = 0.77. The specific iodine content (weight fraction of iodine) was calculated from the degree of substitution according to Equation 2.2,

$$wt\%I = \frac{DS \times M_{mol}(Iodine) \times n}{M_{mol}(PVAL) \times (1 - DS) + M_{mol}(TIB - PVAL) \times DS} \tag{2.2}$$

where M_{mol}(Iodine) is the molar mass of iodine atom: 127 g.mol^{-1}, n is the number of iodine atoms per benzyl group: n = 3, M_{mol}(PVAL) is the molar mass of non-grafted PVAL repeat unit: 44 g.mol^{-1}, and M_{mol}(TIB-PVAL) is the molar mass of the grafted repeat unit: 526 g.mol^{-1}. DS = 77% determined by ^{1}H NMR analysis gave 71 wt% of iodine. This experimental value was very close to the theoretical iodine concentration that would have been reached, i.e. 72 wt%, for 100% conversion of the grafting reaction (DS = 1). The very high iodine content determined by ^{1}H NMR was confirmed by ICP-OES analysis for iodine which gave an iodine content of 65 wt%.

2.4.1.3 Thermal analysis and X-ray diffraction

Thermogravimetric analysis (TGA) showed that the iodinated polymer underwent thermal degradation at around 280°C. Differential Scanning Calorimetry (DSC) gave the glass transition temperature at 160°C (note that Tg of the non-grafted PVAL is around 85°C). No other phase transition was observed in the temperature range studied (i.e. below temperature of thermal degradation). X-ray crystallography (Figure 2.5) showed that there were no crystalline peaks; a broad scattering peak was observed between 2θ = 20-30°, which was typical of an amorphous material. Therefore, the polymer was considered 100% glassy below 160°C. This is a favorable property, should any encapsulation of active molecules be considered in future studies.

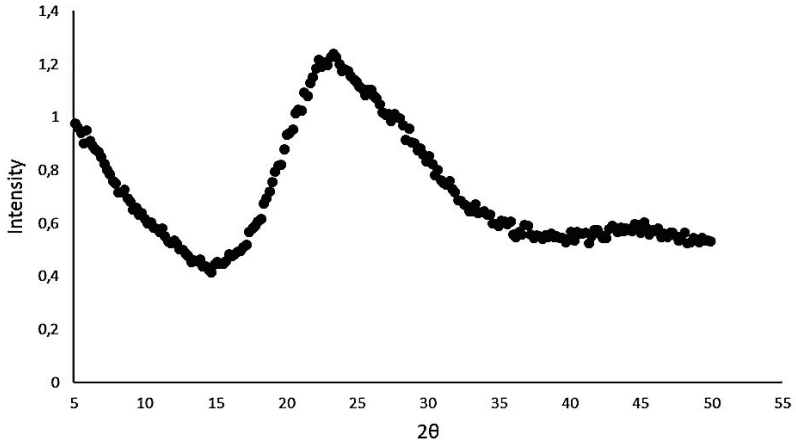

Figure 2.5: X-ray diffraction of TIB-PVAL

2.4.2 Iodinated polymer nanoparticles: physicochemical characterization

2.4.2.1 Nanoparticles size, morphology and stability

Aqueous dispersions of iodinated polymer nanoparticles were prepared using the nanoprecipitation process. A solution of TIB-PVAL iodinated polymer and PCL_{65}-*b*-PEG_{113} dispersing agent in THF was poured into water under magnetic stirring, resulting in concomitant precipitation of the polymer and dispersing agent as nanoparticles. THF was subsequently evaporated. This was followed by a concentration step by means of centrifugation/redispersion. Dynamic Light Scattering (DLS) and Transmission Electron Microscopy (TEM) allowed measurements of particle sizes and morphology assessments at each step of the preparation.

The main parameters that control the nanoprecipitation process are: the dispersing agent/iodinated polymer ratio (PCL_{65}-*b*-PEG_{113}/TIB-PVAL), the THF/water ratio and the polymer concentration in THF. As outcome of preliminary experiments, the PCL_{65}-*b*-PEG_{113}/TIB-PVAL weight ratio was set as 1/1. This ratio was considered as optimum because the size distribution of nanoparticles was broad for lower ratio. The lowest concentration of PCL_{65}-*b*-PEG_{113} allowing formation of nearly monodisperse nanoparticles corresponded to a 1/1 weight ratio. According to Foncesca *et al.* [117], doubling the aqueous phase volume resulted in a significant decrease in the size of polymeric nanoparticles. Indeed, larger amount of water in the water/THF mixture decreases the solubility of the polymer. Thus, the THF/water volume ratio was set to 1/2 based on literature reports.

Finally, the iodinated polymer concentration in the organic phase was optimized, keeping in mind that high iodine concentrations up to 100 mg(I).mL^{-1} must be reached in the final injectable product. Figure 2.6 shows that particle size increases with respect to the concentration of iodinated polymer in THF. This trend is correlated to other reports of the literature [99] [119] [120]. The highest concentration of iodinated polymer in THF yielding nanoparticles was 40 mg.mL^{-1} (i.e. 17 mg(I).mL^{-1} in water). At this concentration, the particle size was below 200 nm using DLS. Above this concentration the of PCL_{65}-*b*-PEG_{113}/TIB-PVAL mixture is not soluble in THF, so that the large particles already present in THF formed a cloudy coarse dispersion that underwent fast sedimentation.

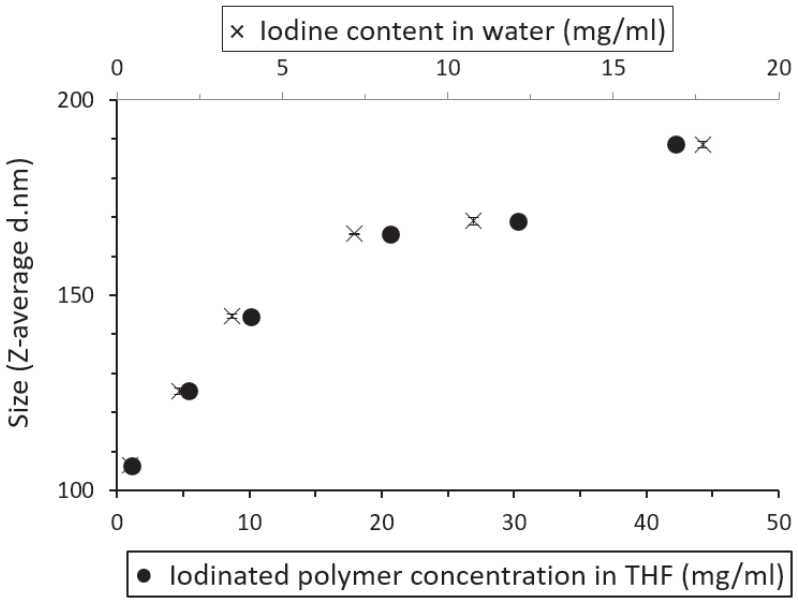

Figure 2.6: Variation of nanoparticles z-average diameter (from DLS) against iodinated polymer concentration in the organic solvent (THF).

In order to concentrate the sample and reach suitable iodine content for *in vivo* studies without increasing particle size, or broadening the particle size distribution, a centrifugation/redispersion step was implemented. Centrifugation rate of 7830 rpm for 20 min was the minimum speed allowing full sendimentation of the particles (clear supernatant). Under this condition, nanoparticles could easily be redispersed in water using simple ultrasonic bath. The optimized experimental conditions are given in Table 2.1.

	Centrifugation parameters	**Redispersion parameters**
Volume	10 mL of TIB-PVAL suspension	1 mL water
Instrument	Eppendorf Centrifuge 5430	Ultrasonic bath
Experimental conditions	20 min at 7830 rpm	120 min at 45°C
Concentration of iodine (ICP-OES)	17.7 mg(I).mL^{-1}	98.8 mg(I).mL^{-1}
Mean particle size (TEM)	118 nm	122 nm

Table 2.1: Optimized parameters of centrifugation and redispersion for the preparation of concentrated suspensions of iodinated polymer nanoparticles in water

It was possible to increase the iodine content by a factor of 5.5 and reach concentrations high enough for *in vitro* and *in vivo* tests, without altering nanoparticle size. TEM pictures in Figure 2.7A, B show monodisperse and spherical nanoparticles before and after the concentration step. The narrow particle size distribution observed by DLS supports these results (Figure 2.7C).

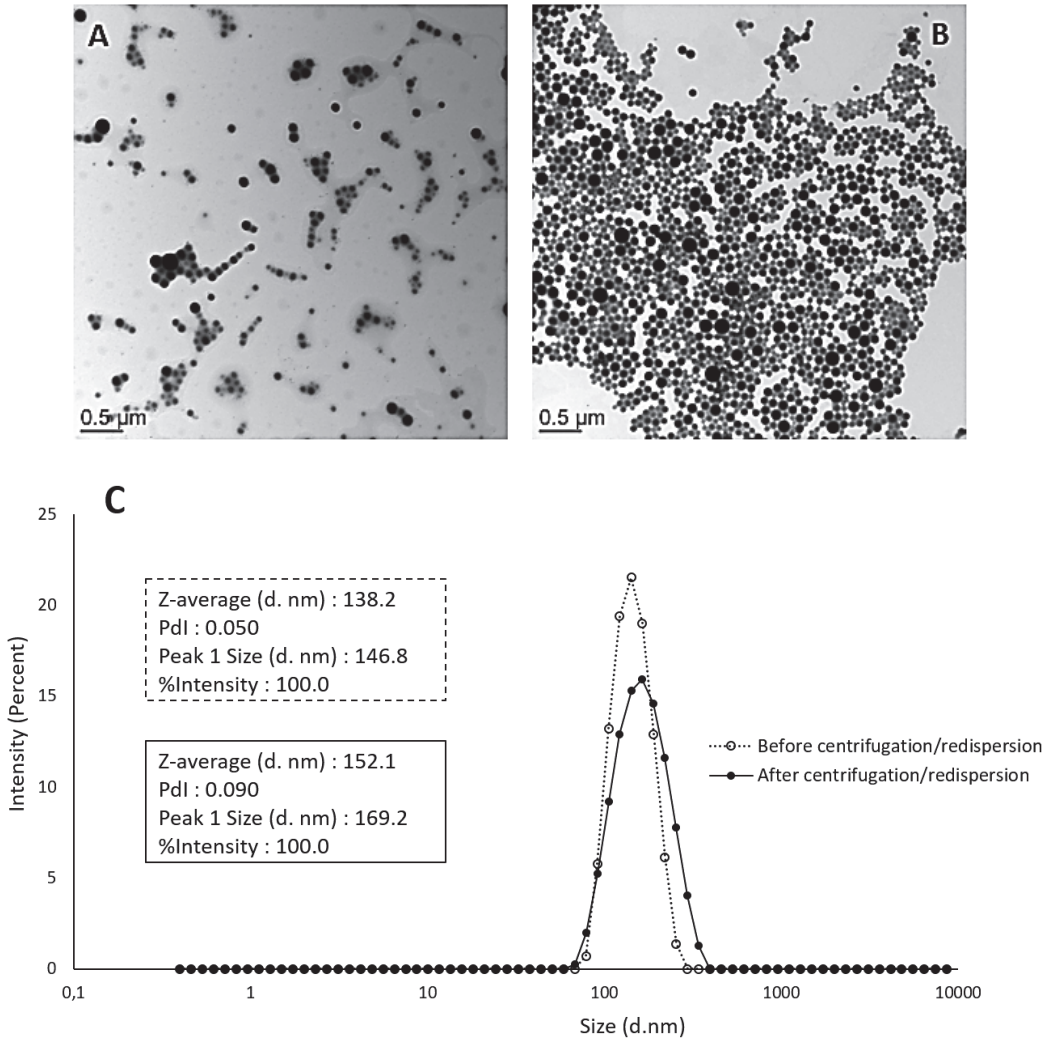

Figure 2.7: TEM pictures of TIB-PVAL nanoparticles before (A), after (B) centrifugation/redispersion and (C) particle size distribution from CONTIN analysis of DLS.

Note that the particle size reported by TEM are smaller then the ones given by DLS. One explanation is that the first technique requires an observation of the sample in the dry state whereas in the second technique there are solvent molecules (here water) associated with the particle (a hydrodynamic size is retrieved). Another explanation is that the TEM particle size measurement is number based, while the DLS is intensity based. A consequence is that since DLS is very sensitive to large particles (intensity is proportional to r^6), the z-average given is bigger than the particle size measured by TEM.

Stability of the suspensions was assessed by monitoring nanoparticles size by DLS with respect to storage time. Nanoparticles were stable and remained well-separated (Figure 2.8) for over 8 months in water at 4, 20 and 37°C and in human serum at 4 and 37°C.

2.4.2.2 Quantification of PEG on nanoparticles surface

Iodinated polymer nanoparticles were stabilized by the diblock poly(caprolactone)-*block*-poly (ethylene glycol) (PCL_{65}-*b*-PEG_{113}). A core/shell structure is expected with a core made of iodinated polymer, the hydrophobic part of the dispersing agent (i.e. poly(caprolactone))

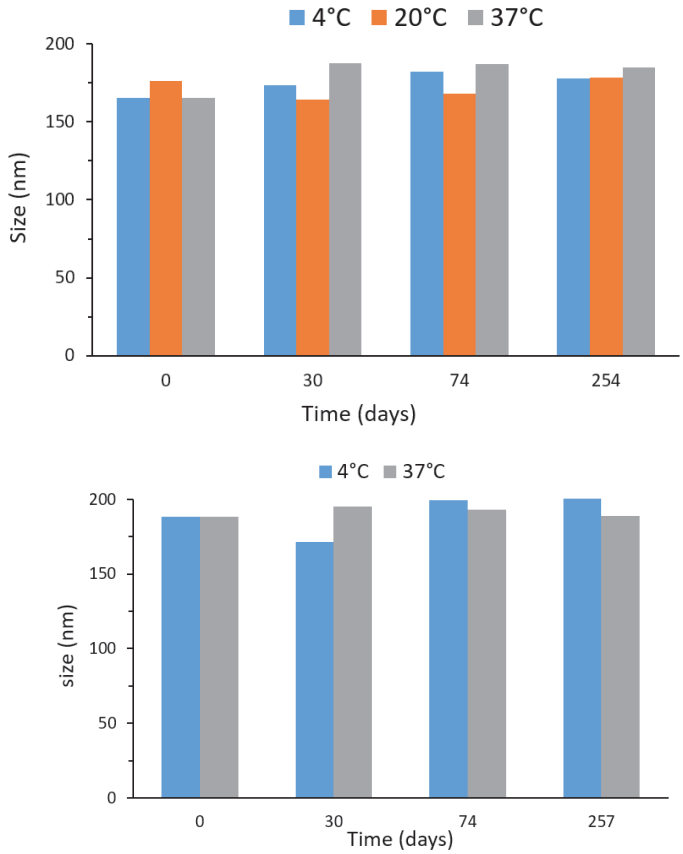

Figure 2.8: Iodinated polymer nanoparticles stability in water at 4, 20 and 37°C (top) and in human serum at 4 and 37°C (bottom)

adsorbed onto the core, and the hydrophilic PEG part forming a water-swollen PEGylated shell. It is known that the presence of a PEG layer, not only increases stability by steric repulsion, but also enables particle furtivity *in-vivo* by avoiding opsonization (absorption of recognition proteins from the immune system) or/and by preventing rapid recognition by macrophages from Kupffer cells [121], [122]. Another advantage of using polymers as stabilizing agents is enabling high surface coverage, leading to even more stable dispersions [123].

Although PEG has been widely used as stabilizing agent of nanoparticles in life sciences for over 20 years and is approved by FDA for *in vivo* applications, there is no straightforward method to detect its presence on the particles surface and determine surface coverage. PEG chain coverage, conformation of the PEG layer, type of incorporation (either grafted or adsorbed) are important parameters that have been presently evaluated.

Here, dry extract and ^{1}H NMR spectroscopy measurements were combined to quantify the density of PEG at the surface of nanoparticles.

The concentrations were determined by measuring a dry extract of a 10 mL part of the dispersion before centrifugation. As a reminder, in the initial sample 1 g of iodinated polymer and 1 g of dispersing agent were dissolved in 25 mL of THF, dispersed by mixing with 50 mL of water, and THF was subsequently removed. Therefore, the concentration of all initial compounds was 20 g.L^{-1}. 0.41 g of dry product was obtained upon drying 10 mL of dispersion, which closely corresponded to the expected sum of the dry extracts of TIB-PVAL and PCL$_{65}$-*b*-PEG$_{113}$.

After a centrifugation/redispersion step under the operating conditions given in Table 3.1, most of unbound PEG was removed with the supernatant. DLS measurements showed that non-adsorbed PCL_{65}-*b*-PEG_{113} was in the form of block copolymer micelles of size 30 nm dispersed in the aqueous phase. Therefore, after centrifugation dry extracts of the supernatant and the wet sediment were also separately performed. One step of centrifugation was enough for removing the whole non-adsorbed materials since after redispersion in 10 mL pure water and a second centrifugation, no product was recovered in the dry extract of the supernatant. Such measurement meant that water remaining in the wet sediment was hydration water of the PEG shell only. There was no free PCL_{65}-*b*-PEG_{113} trapped in between the TIB-PVAL nanoparticles in the sediment.

Reference	**Before drying**	**After drying**	**Dry extract**
Supernatant	9.15 g	0.18 g	2 %
Sediment	1.51 g	0.22 g	14.6 %

Table 2.2: Dry extracts of supernatant and sediment after centrifugation of suspensions of iodinated polymer nanoparticles.

According to Table 2.2, only 0.02 g of the dispersing agent was adsorbed to iodinated polymer nanoparticles. The rest has been removed with the supernatant in the form of block copolymer micelles. One could consider that since less than 10% of dispersing agent was adsorbed, this amount should be enough to stabilize the system both upon long term storage and during the preparation of the nanoparticles. This was actually not the case as preliminary tests made with dispersing agent/iodinated polymer weight ratios lower than 1/1, yielded unstable suspensions and/or dispersions of polydisperse particles. So, a large excess of PCL_{65}-*b*-PEG_{113} was required in order to stabilize nanoparticles in the mixed THF-water medium during the preparation process.

Samples before and after centrifugation and both supernatant and pellet, were analyzed on ^{1}H NMR spectroscopy for their PCL_{65}-*b*-PEG_{113}/TIB-PVAL ratio (Figure 2.9). Both compounds were soluble in the DMSO-*d6* solvent used.

The PCL_{65}-*b*-PEG_{113} mass ratio was calculated from the ratio I(CH_2 4 ppm)/I(CH 8 ppm) of the peak integrals of CH_2 proton at 4 ppm belonging to PCL_{65}-*b*-PEG_{113} and aromatic CH proton at 8 ppm belonging to TIB-PVAL as:

$$\frac{m(PCL-b-PEG)}{m(TIB-PVAL)} = \frac{\frac{I(CH_2)_{4ppm}}{2}}{I(CH)_{8ppm}} \times \frac{M_{mol}(CL) + \frac{dp(PEG)}{dp(PCL)} \times M_{mol}(EG)}{M_{mol}(TIB-VAL) + \frac{(1-DS)}{DS)} \times M_{mol}(VAL)} \quad (2.3)$$

where M_{mol}(CL) = 114 g.mol^{-1}, M_{mol}(EG) = 44 g.mol^{-1}, M_{mol}(TIB-VAL) = 526 g.mol^{-1} and and M_{mol}(VAL) = 44 g.mol^{-1} are the molar masses of caprolactone, ethylene oxide, triiodobenzoyl vinyl and vinyl alcohol repeat units respectively, dp(PCL) = 65 and dp(PEG) = 113 are the degrees of polymerization of the PCL and PEG blocks respectively and DS is the degree of substitution of TIB-PVAL.
Calculated PCL_{65}-*b*-PEG_{113}/TIB-PVAL mass ratios are given in Table 2.3. The mass ratio of 1 was correctly found from NMR analysis of the sample before centrifugation. No significant

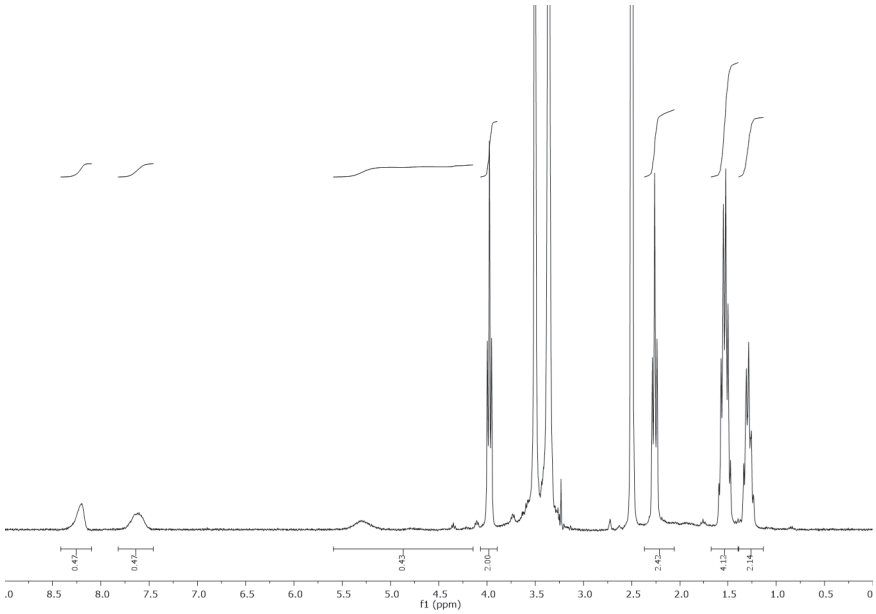

Figure 2.9: Reference ^{1}H NMR spectra of 1/1 PCL_{65}-*b*-PEG_{113}/TIB-PVAL mixture in DMSO-*d6*.

signal of the 2 aromatic protons specific of the iodinated polymer was found in spectra of supernatants, showing that the full TIB-PVAL was present inside nanoparticles. Finally the chemical composition of the iodinated particles present in the sediment was obtained.

	$\frac{\text{I(CH2)4ppm}}{\text{I(CH)8ppm}}$	$\frac{\text{m(PCL-b-PEG)}}{\text{m(IP)}}$
Before centrifugation	5.56	0.98
Supernatant	> 200	> 35
Sediment	1.06	0.19

Table 2.3: PCL_{65}-*b*-PEG_{113}/TIB-PVAL mass ratio before and after centrifugation, in supernatant and sediment of suspensions of iodinated polymer nanoparticles in water, using using ^{1}H NMR spectra integrals

In order to assess the coverage and the configuration of PEG chain at the surface, the PEG surface density expressed as the number of PEG molecules per unit area was calculated from the PCL_{65}-*b*-PEG_{113}/TIB-PVAL mass ratio. The PEG chain coverage is:

$$\sigma = \frac{m(PCL-b-PEG)}{m(TIB-PVAL)} \times N_{AV} \times \frac{\rho(TIB-PVAL)}{M_n(TIB-PVAL)} \times \frac{d}{6} \tag{2.4}$$

with N_{AV} = Avogadro constant, ρ(TIB-PVAL) = 1.31 g.cm^{-3} the density of TIB-PVAL, M_n(TIB-PVAL) = 12400 g.mol^{-1} the number-average molar mass of TIB-PVAL, and d = 150 nm the diameter of TIB-PVAL nanoparticles. Accordingly, the PEG chain surface density was found to be 0.30 PEG chains per nm^2 area.

The projected area of a single PEG chain end-grafted on a nanoparticle surface, also known as the PEG chain footprint *(FP)* was deduced:

$$FP = \frac{1}{\sigma} = 3.36 nm^2.molecule^{-1} \tag{2.5}$$

This result was compared to the area that would occupy an unperturbed PEG coil in bulk water solution as calculated from the hydrodynamic radius (R_h). Based on a series of experimental measurements, Devanand *et al.* [118] related R_h to the PEG molar mass as a power law relationship a brush configuration.

$$R_h = 0.0145(nm) \times M_w^{0.571} \tag{2.6}$$

The hydrodynamic radius of an unperturbed chain of the present PEG (M_W = 5000 g.mol^{-1}) was 1.875 nm, giving a footprint of $\pi\ R_h^2$ = 11 nm^2.

As the experimental area (FP = 3.36 nm^2.molecule^{-1}) was much lower than that of an unperturbed coil (11 nm^2), PEG chains were extended radially from the nanoparticles surface, which corresponded to a "brush" configuration [124] Figure 2.10. Such configuration is known to provide the best colloidal stability.

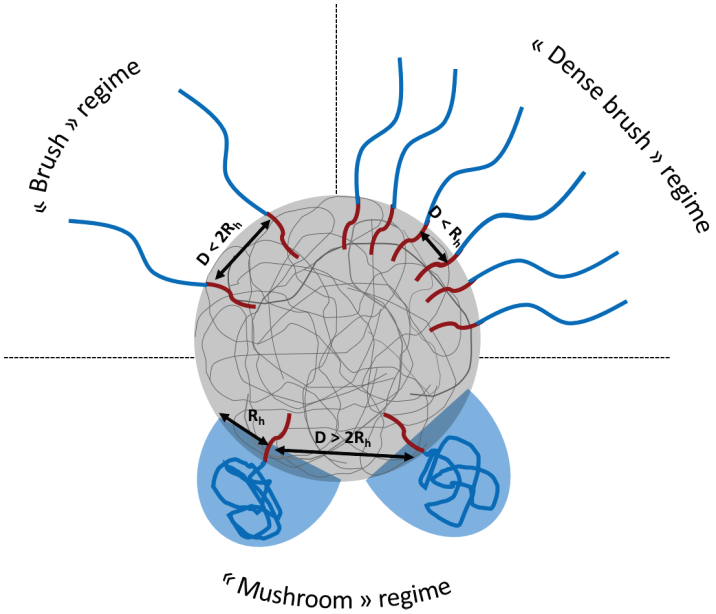

Figure 2.10: Various configurations of PEG chains according to the surface density. R_h: hydrodynamic radius of an unperturbed chain (minimum distance required between grafted molecules to achieve a mushroom configuration); D distance between anchoring points.

2.4.3 Cytotoxicity assessment

Cytotoxicity of the iodinated polymer nanoparticles was determined by MTS assays performed 24 h and 48 h after incubation of macrophages with nanoparticles of different concentrations. Cell viability was calculated from the absorbance values. A standard containing "pure" macrophages (i.e. cells that have not been incubated with iodinated nanoparticles), was taken as the control for 100% cell viability. Full cell viability was retained after 5 h exposure to all suspensions of iodinated nanoparticles (Figure 2.11). The contrast agent does not manifest cytotoxicity at the concentrations studied.

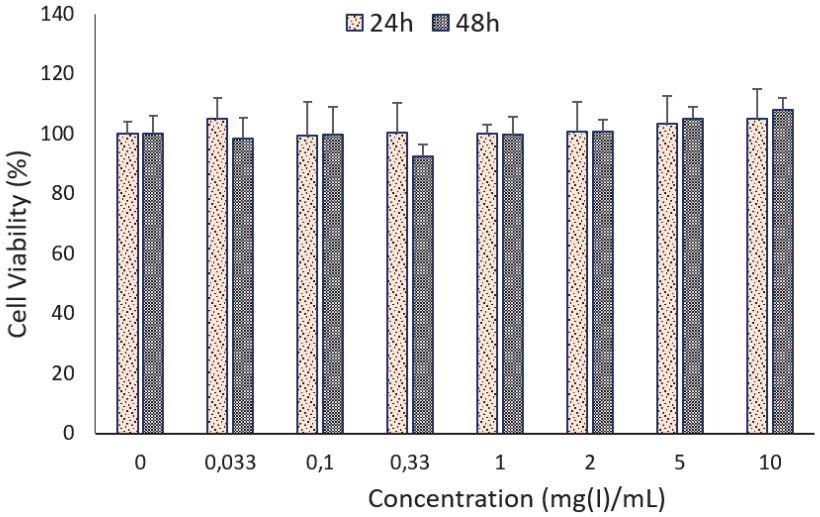

Figure 2.11: Cell viability after 5 h exposure to aqueous suspensions of iodinated nanoparticles of various concentrations. Viability was assessed 24 h and 48 h after the end of exposure to nanoparticles.

2.4.4 Radiopacity assessment

2.4.4.1 Iodinated polymer nanoparticles attenuation in Hounsfield Units (HU)

X-ray attenuation of the pure iodinated polymer was measured by taking a CT image of the polymer pressed as a pellet placed in a glass tube (Figure 2.12A). This picture highlights the excellent radiopaque nature of TIB-PVAL, compared to the surrounding material (wall of the glass container). The radiopacity of pure TIB-PVAL was 12916 HU.

Radiopacity was also assessed *in vitro* on phantoms made of aqueous suspensions of iodinated polymer nanoparticles at different concentrations (Figure 2.12B and C). Radiopacity increases linearly with respect to the concentration in iodine ($R^2 = 0.9998$) (Figure 2.12C). The concentration required to obtain a signal larger than 100 HU is 3.5 mg(I).mL^{-1}.

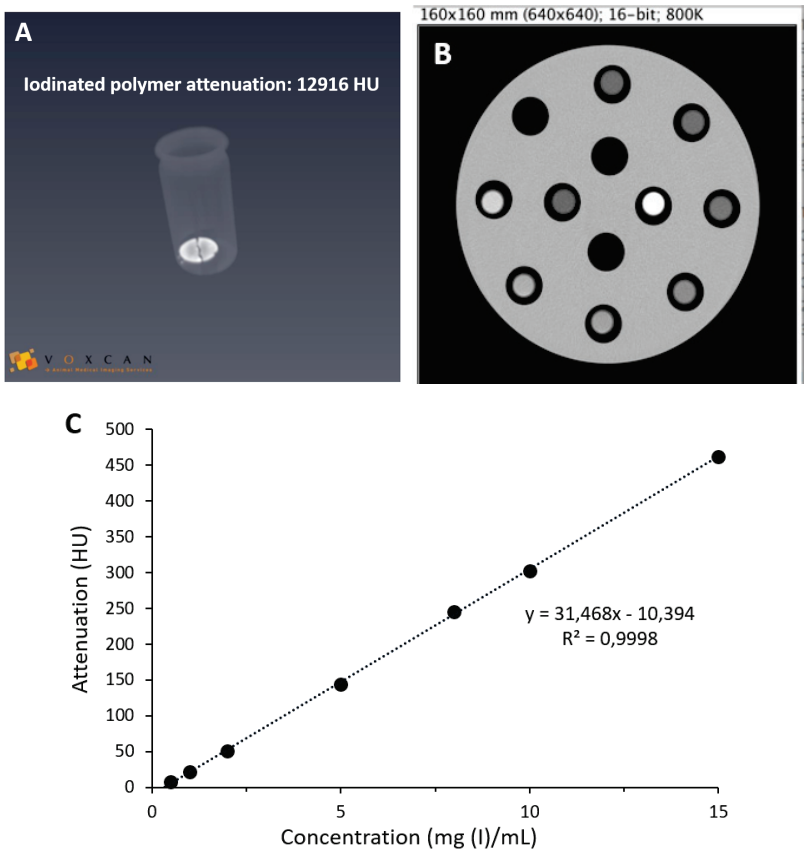

Figure 2.12: Compressed iodinated polymer (A), Phantom tube containing the suspensions of iodinated polymer nanoparticles in water (B,) graph of Iodinated polymer nanoparticles attenuation in Houndfield Units (HU) with respect to concentration (C).

2.4.4.2 Element quantification using "Material Decomposition" with SPCCT

The concentration measured with the SPCCT using the Material Decomposition (MD) algorithm was compared to the concentration determined by ICP-OES in the different samples. As shown in Figure 2.13, there is a good correlation between the two values ($R^2 = 0.9991$). This establishes a proof of concept of the capability of SPCCT for accurate quantification of a radiopaque element *in vivo*.

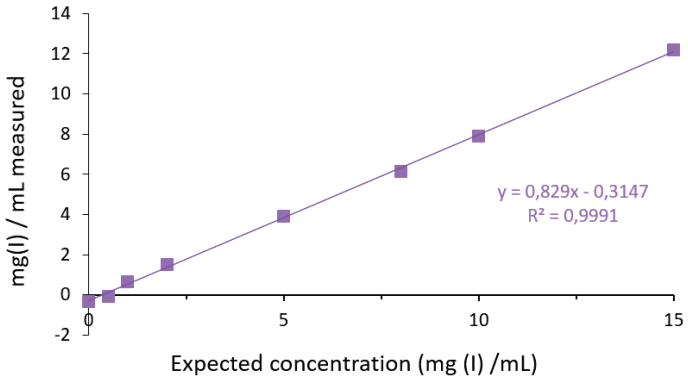

Figure 2.13: Quantification of iodine using the SPCCT material decomposition (MD)

2.4.4.3 Discrimination of two elements in a mixture with SPCCT

The ability of SPCCT technology to discriminate two different elements (iodine and gadolinium) has been assessed using phantoms images of mixtures of both elements. The solutions containing various concentrations of iodine and gadolinium were prepared in such way that all mixtures had the same overall attenuation in Hounsfield Units. Material decomposition calculation gives an iodine-specific image where the intensity of each voxel gives the concentration of iodine [125] [126]. K-edge reconstruction provides the same type of information for gadolinium [12].

Conventional, iodine-specific, gadolinium-specific and overlay images are shown in Figure 2.14. Mixed contrast agents cannot be differentiated with conventional CT. The graph shows that all samples of different solutions of mixed contrast agents had similar attenuation of 250 HU. Contrast agents were accurately differentiated in the iodine and gadolinium specific images of SPCCT, with signal intensity proportional to their absolute concentration. Moreover, the signal of the phantom container could be subtracted, which increased the signal to background ratio, providing a potentially more accurate image for improved analysis.

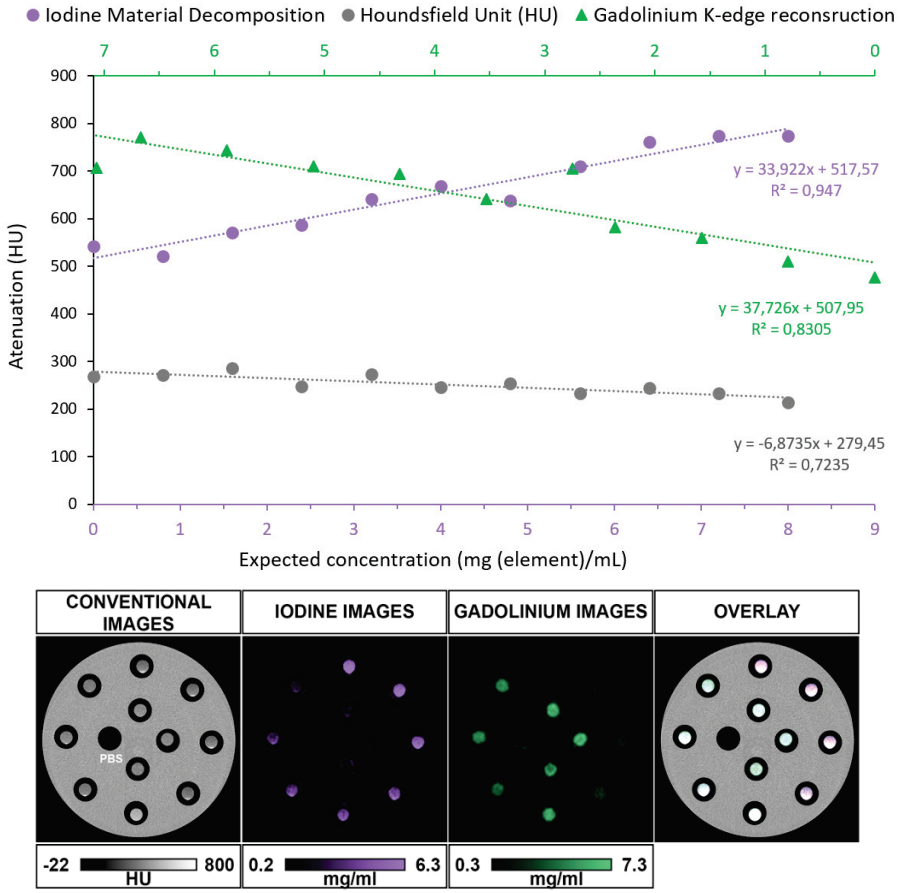

Figure 2.14: Attenuation (HU) at different concentrations of a gadolinium/iodine mixture, phantoms containing increasine concentrations of iodine and decreasing concentrations of gadolinium (top). SPCCT images of the iodine and gadolinium mixure with conventional images, iodine material decomposition images, gadolinium K-edge images and overlay images (bottom).

With its capability to quantify and discriminate simultaneously two different elements, within a single scan, the SPCCT technology is an interesting diagnostic tool for molecular imaging. For instance, it provides the possibility to image the vascular system using a blood pool agent, while targeting a specific site of disease (i.e. atherosclerosis plaque) using a bioconjugated contrast agent bearing another radiopaque element [126]. Furthermore, being able to detect and quantify the accumulation of contrast agents in the region of interest, within a single scan can also reduce toxicity related to the radiation dose. In fact, the need for two acquisitions in order to compare images before and post-injection becomes unavailing.

2.4.4.4 The *in vivo* study: Iodinated polymer nanoparticles

Biodistribution of the iodinated polymer nanoparticles of 150 nm diameter was studied *in-vivo* by experiments on small animals (intravenous injections to rats, according the experimental section) performed on conventional CT and μCT. No visible signs of toxicity were observed post-injection. The animals remained alive and healthy during the entire study.

CT. CT images show a radiopacity enhancement of the cardiovascular system as well as radioopacification of the liver and spleen 3 h and up to 5 days post injection (Figure 2.15 (top)). These observations are correlated and completed by the graph that represents the attenuation in HU as a function of time (Figure 2.15 (bottom)). The later, indicated that the abdominal aorta and the heart went back to their initial values ($<$ 50 HU) 24 h post administration and had remaining at least 5 h at three times this amount (150 HU). It also shows a slight radiopacity in the kidneys, meaning that some nanoparticles manage to pass through renal filters and be eliminated in urine. However, fifteen days later, iodinated nanoparticles are still present in the liver (200 HU) and the spleen (700-750 HU) as a result of progressive accumulation reaching respectively 4 times and 15 times the initial values. This indicates the potential clearance by phagocytic uptake and hepatic filtration [127]. The use of nanoparticles allows imaging liver and spleen for long.

The biodistribution of iodinated polymer nanoparticles was compared to that of a standard solution of soluble iodinated compound. The CT images together with the biodistribution graph showed that all the contrast agent can be found in the kidneys 30 min post injection (Figure 2.16). Moreover 4 days later, the full Omnipaque had been cleared, leaving no trace of contrast agent inside the body.

μCT. The μCT images of the *in vivo* behavior of iodinated polymer nanoparticles after IV injection confirm the observation made previously with the CT scanner. μCT allowed better visualization of smaller tissues and vessels (Figure 2.17). In all cases, these images left no doubt as to the "blood pool" character of the contrast agent developed during this study.

Due to its accumulation in both the liver and spleen for prolonged time, this product is not yet suited for clinical applications. Nevertheless, it was seen that it can be used as an excellent blood pool agent as it presents biodistribution characteristics that can compete with commercially available products for preclinical studies.

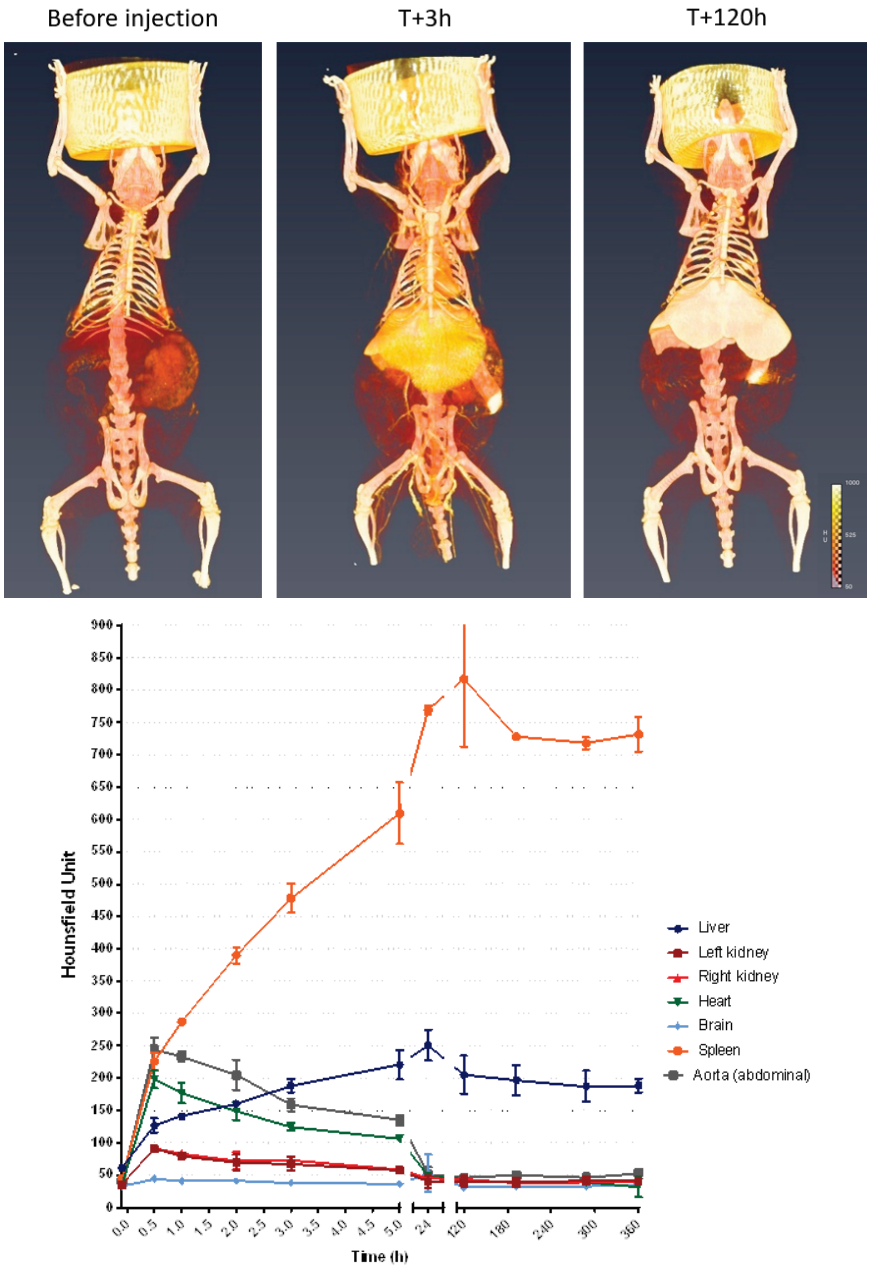

Figure 2.15: CT images of rats before, 3 h, 120 h after IV injection of iodinated polymer nanoparticles (top). Biodistribution of the iodinated polymer nanoparticles over time. (1.5 mL IV injected, 536 mg[I] · kg-1). Mean ± Sem, n = 3 (bottom).

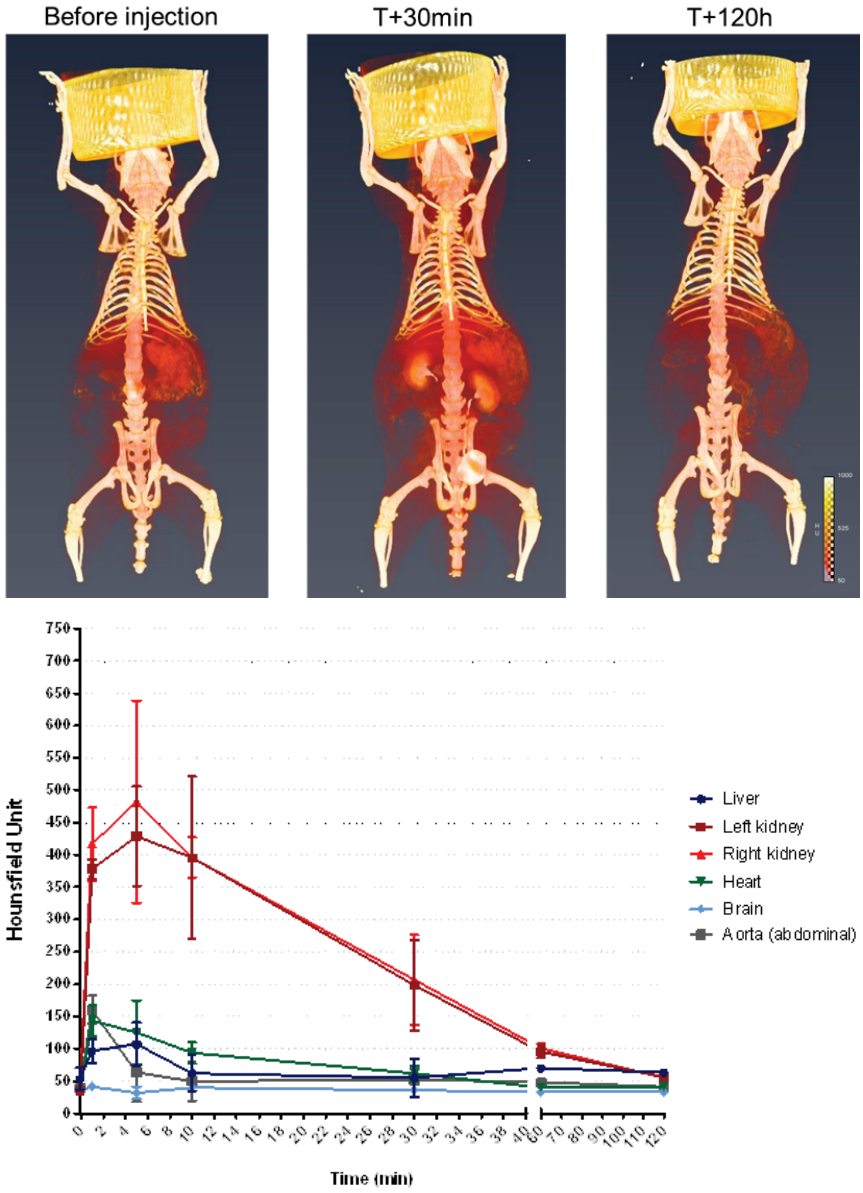

Figure 2.16: CT images of rats before, 0.5 h, 120 h after IV injection of Omnipaque (top). CT imaging of the Omnipaque biodistribution over time (0.7 mL IV injected). Mean ± Sem, n = 3 (bottom).

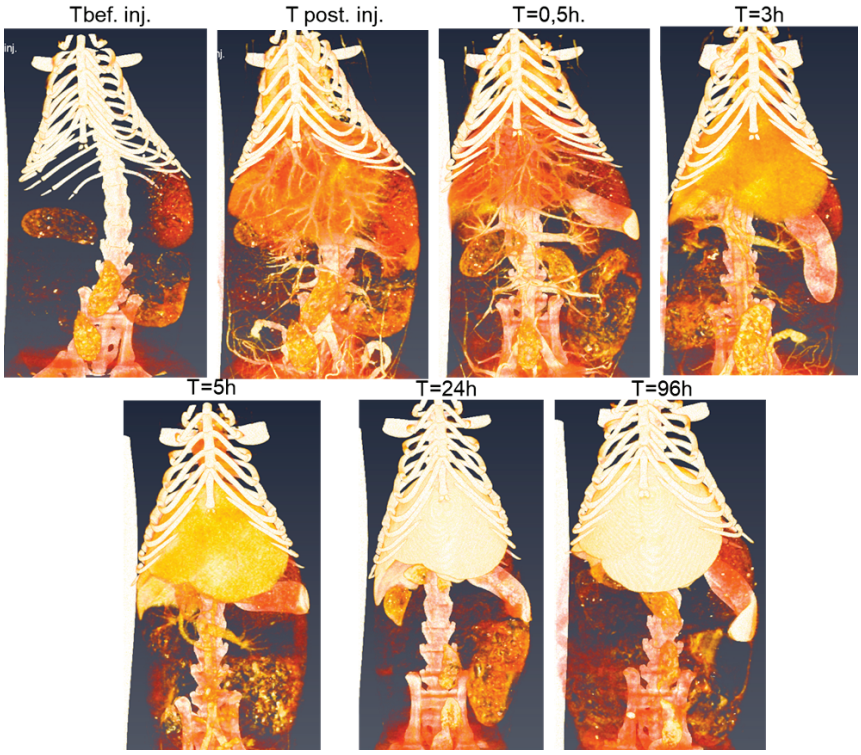

Figure 2.17: Enhancement after intravenous injection into a rats' tail vein of 1.5 mL of aqueous dispersion of iodinated polymer nanoparticles (90-100 mg(I).mL^{-1}). μCT images were acquired before and at different time points after injection.

2.5 Conclusions

Concentrated dispersions of iodinated polymer nanoparticles formed by nanoprecipitation of a triiodobenzoyl moiety covalently grafted to poly(vinyl alcohol) have been prepared. These nanoparticles are composed of a 100% amorphous core that can be used for encapsulation of hydrophobic drugs, thus creating a theranostic compound. A PEGylated shell brought by the dispersing agent, in dense brush conformation, provides steric stabilization up to 8 months in water and human serum and stealth properties against immune system when circulating in blood. This yielded a slow uptake into spleen and liver. An optimal formulation, composed of monodisperse nanoparticle core size of around 150 nm (TEM average diameter) and concentrated up to 100 mg(I).mL^{-1}, were tested *in-vitro* and *in-vivo*. The high potential of the SPCCT technology in multicolor molecular imaging, for improved diagnosis have been demonstrated in phantoms. The iodinated polymer nanoparticles provided significant enhancement of the cardiovascular system and can be used for imaging the liver and the spleen for long.

Acknowledgements

The research project has received funding from European Union through Horizon 2020 research and innovation program under grant agreement No 643694.

Chapter 3

Formulation parameters

Contents

3.1 Abstract 75
3.2 Introduction 76
3.3 Experimental section 77
3.3.1 Materials 77
3.3.2 Methods 77
3.4 Results 79
3.4.1 Model composition 80
3.4.2 Process conditions 85
3.4.3 Optimum formulation and process 85
3.4.4 Iodinated polymer nanoparticles: radiopacity assessment . . . 86
3.5 Discussion 90
3.6 Conclusions 92

Preamble

Nanobiomaterials have been widely investigated in nanomedicine for their ability to protect sensitive drugs or more generally serve as efficient vectors for active ingredients, as well as for all the possibilities they offer in the field of medical diganostics as detailed in the state of the art, section 1.2.2.

There are many different types of nanosystems (i.e. liposomes, micelles, nanoemulsions, dendrimers etc.) that have been developed to be used as contrast agents for CT. However, as presented in the state of the art in section 1.1.2, processes for production of most of the compounds cited above constitutes an issue. The fabrication route was therefore a key parameter in choosing a type of polymer nanoparticles (PNPs) as the system developed in this study. PNPs can be fabricated either par polymerization of monomer or from a preformed polymer. Nanoprecipitation which is a one step, low energy process was selected.

Formulation parameters had to be optimized in order to meet the undermentioned specifications:

- Size: the only restriction on particle size for intravenous injection is that it is smaller than the smaller capillary. According to Moghimi *et al.*., the size of long-circulating non-deformable particles should be in the range of 120-200 nm in diameter to avoid particle trapping in the space of Disse and hepatic parenchyma [41]. However when it comes to size distribution, a monodiperse formulation is preferred in order to avoid having a heterogeneous biodistribution *in vivo*.

- High radiopaque element concentration: To date the SPCCT scanner developed by Philipps Healthcare has a sensitivity towards iodine of 2 mg(I).mL^{-1}. Considering an average human body containing 5 liters of blood, a minimum amount of 10 000 mg of iodine should be injected. For example what is currently done in practice in terms of dosage is: IV administration of 100 mL Iohexol (Omnipaque 350 (350 mgI.mL^{-1})) to patients weighing below 96 kg; at 96 kg or above the dose is increased to 150 mL. Based on these information, the contrast agent developped in this work should have a minimum concentration of 100 mg(I).mL^{-1}.

- Injectability: The criteria is strongly related to the final formulation viscosity. Considering that the route of administration of the contrast medium is an intravenous injection, the ideal viscosity should be close to that of blood.

- Biocompatibility: osmalarity, hydrophilicity

The purpose of the experiments described in this chapter is to establish the optimal chemical and mechanical conditions to produce an iodinated contrast product in the form of PNPs. Formulation parameters, such as the organic solvent/water volume ratio, dispersing agent/iodinated polymer weight ratio, nature of the dispersing agent, have a direct impact on the physicochemical characteristics of the final injectable compound. These different parameters are discussed and a final, optimized formula is proposed following the given specifications.

Optimization of the nanoprecipitation parameters in the fabrication of iodinated polymer nanoparticles as contrast agent for CT

J. Balegamire, M. Vandamme, E.Chereul, H. Fessi, S. Si-Mohamed, L. Boussel, P. Douek, Y. Chevalier

Colloids and Surfaces A (to be submitted, 2019)

3.1 Abstract

Iodinated polymer nanoparticles can be produced using the nanoprecipitation process. There are several parameters that must be optimized in order make suspensions of nanoparticles that meet the specifications: i.e size below 200 nm, narrow size distribution, ease of fabrication and long term stability. The choice of the dispersing agent is one of the most important formulation parameters. The influence of stabilizers such as hydrophilic surfactants/polymers (poloxomers, alkyl ethers of poly(oxyethylene), PVAL, ethoxylated sorbitan esters (polysorbates)) and lipophilic dispersing agents (phospholipids, sorbitan esters, block copolymers) was investigated. Other operating and chemical conditions were also set in order to optimize the process. All hydrophilic dispersing agents were discarded as the formulation foamed systematically during the THF evaporation stage under reduced pressure, making the process difficult to keep under control. If most of the lipophilic stabilizers tested led to aggregates straight after organic phase addition into the aqueous phase, Lipoid S100 and PCL_{65}-*b*-PEG_{113} gave satisfactory results. Monodisperse suspensions of iodinated polymer nanoparticles with an average diameter of 150-200 nm, stable for days (Lipoid S100) and months PLC_{65}-*b*-PEG_{113} were obtained. An iodine concentration of 100 mg(I).mL^{-1} reached after a centrifugation/redispersion step provided radiopacity of the contrast agent in the right range for imaging cardiovascular system and studying biodistribution. Biodistribution was assessed after intravenous injection of iodinated polymer nanoparticles to rats, revealing a clear visualization of the cardiovascular system followed by progressive accumulation in liver and spleen. Nanoparticles stabilized by PCL_{65}-*b*-PEG_{113} remained longer in the bloodstream than those prepared wih Lipoid S100. The hepatic and spleenic tissues were still visible up to 15 days post-injection.

3.2 Introduction

Nanobiomaterials have been a cutting-edge research topic since nanomedicine started developing a couple of decades ago. Indeed several of their features bring definite improvements. For instance in therapeutic applications, they have proven being efficient vectors for delivery of sensible drugs allowing more specific drug targeting and delivery, reduction of toxicity while maintaining therapeutic effects, greater safety and biocompatibility, in addition to ensuring controlled release of drugs from a single dose and so forth [128].

In the diagnosis field, and more specifically for CT imaging, radiopaque liposomes [74], nanoemulsions [78], dendrimers [59], micelles [61] and nanoparticles [69] [68] (nanocapsules or nanosphere, inorganic or organic), have also been widely investigated. In this study the choice was made towards the development of polymer nanoparticles (PNPs). Such organic particles are made from polymers which are described in the literature as biocompatible and potentially biodegradable. Some of these polymers such as poly(lactide) (PLA), poly(D,L-lactide-co-glycolide) (PLGA), poly(caprolactone) (PCL), poly(ethylene glycol) (PEG) among others are FDA approved [129] [130].

In addition to these two interesting properties, PNPs present several other advantages from which an X-ray contrast agent can benefit. First they can be loaded with a high payload of contrasting elements (i.e. iodine). Furthermore, provided a suitable choice of the formulation parameters is made, and depending on the desired application, the surface can be tuned either by a stealth agent for a prolonged blood circulation time or by a biomarker enabling specific targeting of an organ or a a tissue through molecular imaging.

The last criteria of selection was the fabrication route. The nanoprecipitation process (also referred to as solvent displacement) is able to generate nanoparticles from a preformed polymer using a simple single step and involving a low energy process [116]. This process was selected for the development of iodinated PNPs.

The purpose of this study is to establish the optimal chemical and process conditions to produce an iodinated contrast product in the form of PNPs. Formulation parameters, such as the organic solvent/water volume ratio, dispersing agent/iodinated polymer weight ratio, nature of the dispersing agent, have a direct impact on the physicochemical characteristics of the final injectable compound. The organic solvent/water volume ratio of (1/2) has been described in the literature as optimum to obtain suitable particle size in the nanoparticle range [100], [117], therefore this parameter was fixed. The dispersing agent/iodinated polymer weight ratio was also set following preliminary results. As it is known that nonionic compounds are better tolerated by the organism [127], several neutral dispersing agents (poloxamers, sorbitans, lipoids, block copolymers etc.) were tested.

Finally, specifications were established for a final product in terms of particle size (< 200 nm), narrow particle size distribution as a monodisperse formulation leads to a homogeneous*in vivo* biodistribution, stability in order to avoid aggregation and potentially clotting of some vessels/capillaries (embolism), iodine concentration (100 mg(I).mL^{-1}). Physicochemical characterizations of the iodinated polymer nanoparticles (size, morphology, stability, iodine content) were performed. Different systems of iodinated polymer nanoparticles were tested, *in vivo* by intravenous injection of the contrast agent to rats and CT imaging them. Their X-ray radiopacity was investigated and compared.

3.3 Experimental section

3.3.1 Materials

The iodinated polymer was a 2,3,5-triiodibenzoyl ester of poly(vinyl alcohol) (TIB-PVAL) synthesized in the laboratory. The degree of substitution of triiodobenzoyl groups measured by ^{1}H NMR analysis was DS = 77%, which yielded an iodine content [I] = 71 wt%. and [I] = 65 wt% (ICP-OES)). The synthesis and full characterization are detailed in another article.

The following chemicals were purchased from Sigma-Aldrich (now Merck) and used without further purification: Pluronic F-68 (Cell culture tested), Span® 80 and Span® 85, Brij S100. Tween® 80 was supplied by VWR, poly(vinyl alcohol) (PVAL, 87.0-89.0% hydrolyzed, average molar mass M_W. 13 000 - 23 000 Da) by Acros Organics and Lipoid E80 and Lipoid S100 were supplied by the Lipoid company. The block copolymer polycaprolactone-*block*-poly(ethylene glycol) (PCL_{65}-*b*-PEG_{113}) was synthesized by polymerization of caprolactone initiated by poly(ethylene glycol) monomethyl ether catalyzed by tin octanoate as reported in the literature [113] [114]. Tetrahydrofuran (THF, Fisher Scientific) was used as the organic solvent. Deionized water of 18 MΩ.cm resistivity was used for the preparation of suspensions.

3.3.2 Methods

3.3.2.1 Preparation of nanoparticles

The iodinated polymer. Nanoparticles (NPs) were formulated from a preformed polymer (TIB-PVAL) which chemical structure can be found Figure 3.1. TIB-PVAL was prepared by esterification reaction of 2,3,5-triiodobenzoyl chloride and the hydroxyl groups of the poly(vinyl alcohol) (PVAL).

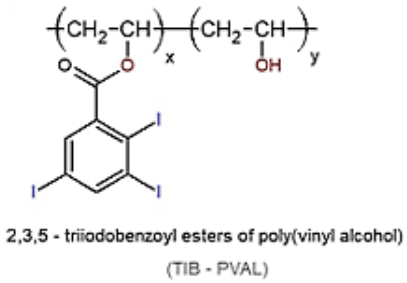

2,3,5 - triiodobenzoyl esters of poly(vinyl alcohol)
(TIB - PVAL)

Figure 3.1: Chemical structure of 2.3.5-triiodobenzoyl ester of poly(vinyl alcohol) (TIB-PVAL). x = 0.77 and y = 0.23

A small molar mass PVAL was selected as the preformed polymer. This choice was made as PVAL presents chemical functions capable of reacting with the iodinated molecules in order to form hydrolysable ester bonds. The product of this hydrolysis are small water soluble, bioeliminable molecules. PVAL has been used in many biomedical applications and is depicted in the literature as biocompatible, nontoxic, non-carcinogenic, non-immunogenic and inert in body fluids [131]. For instance PVAL hydrogels were tested and approved as soft contact lens materials [132], but also as drug delivery systems [133].

The nanoprecipitation process. The PNPs were prepared using the nanoprecipitation process [97] [116] as described bellow (Figure 3.2):

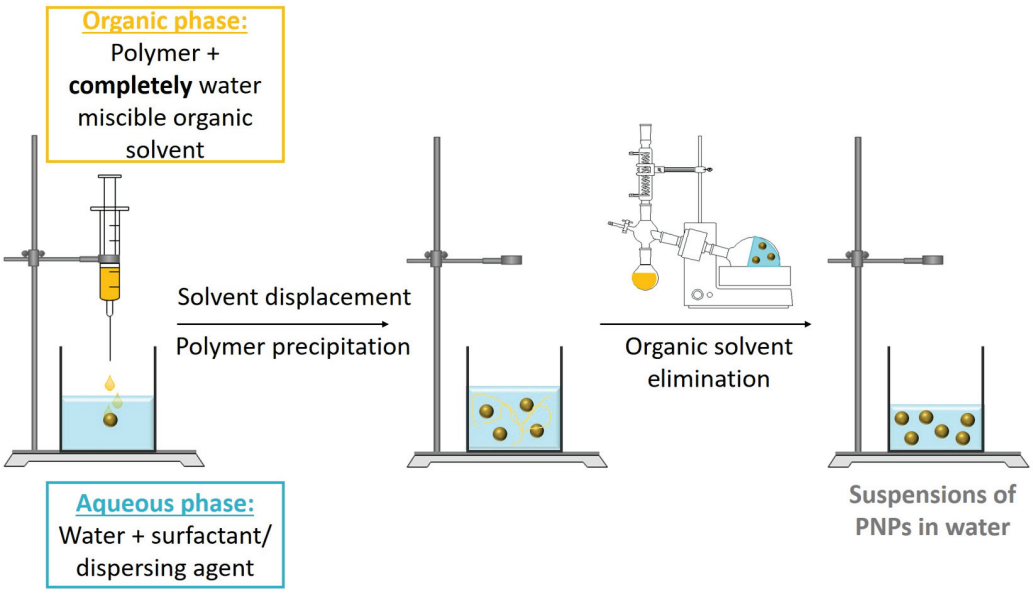

Figure 3.2: Schematic representation of the nanoprecipitation process

First the organic phase was prepared by dissolving TIB-PVAL in 25 mL of THF. 50 mL of water was used as the aqueous phase.

The organic solvent used in the nanoprecipitation process must be totally miscible with water. The most widely used solvents are acetone and ethanol. As TIB-PVAL was not soluble enough in those solvents, THF was chosen as an alternative. Finally the boiling point of THF is lower than that of water, allowing its easy removal by evaporation under reduced presure. THF was selected as the organic solvent taking into account the criteria mentioned above.

The dispersing agent was added either in the organic phase or in water depending on it nature. Several stabilizers were tested (i.e. poloxamers, sorbitan esters, polymers, phospholipids) against their ability of stabilizing suspensions of monodisperse particles with an average size below 200 nm.

25 mL of the organic solution was added dropwise to 50 mL of the aqueous phase under magnetic stirring, using a syringe fitted with a needle. The flow rate was optimized by varying the internal diameter of the needle. The stirring rate was also carefully studied in order to avoid formation of aggregates and meet the specifications.

Finally, THF was evaporated under reduced pressure, yielding an aqueous suspension of nanoparticles.

3.3.2.2 Characterization

Nanoparticle size measurements. The hydrodynamic diameter and size distribution of nanoparticles dispersed in aqueous medium were determined using Dynamic Light Scattering (DLS) with a Zetasizer Nano ZS instrument from Malvern Panalytical. This technique is sensitive to particles of size in a 10-2000 nm diameter range and for diluted suspensions (ideal count

rate 100-350 kHz). Two approaches can be used: the cumulant fit which provides a z-average and a polydispersity index (PdI), and the inverse Laplace transform of the autocorrelation function by the CONTIN method that provides the nanoparticle size distributions in scattered intensity, particle number or volume. Both calculation methods gave very close results. For the sake of comparison with other publications, the z-average diameter coming from the cumulant analysis was used to discuss on DLS results.

Before measurements, the nanoemulsions samples were diluted in ultrapure water (the dilution factor was adjusted to obtain an attenuation factor between 7 and 9). Viscosity of water was considered as the continuous phase. The measurements were performed at 25°C and the values reported were averages of three repeated measurements. They will be compared with size distribution in number measured by Transmission Electron Microscopy (TEM).

Size and morphology. Transmission Electron Microscopy (TEM) pictures were obtained with a Philips CM120 electron microscope under 80 kV accelerating voltage, at the "Centre Technologique des Microstructures (CTμ)", University of Lyon 1 (http://microscopies.univ-lyon1.fr/). Samples were prepared by deposition of a drop (10 μL) of diluted formulation on a 400-mesh carbon-coated copper grid and drying in open air. The size distribution and average size of dry particles was determined from diameters of more than 100 particles determined by image analysis using the ImageJ software.

3.3.2.3 *In vivo* CT-imaging

Wistar rat models (male, body weight 200-300 g) were used to evaluate radiopacity and assess biodistribution of the contrast agent in vivo. Animals were housed in the same conditions as in the previous chapter. A volume of 1.5 mL of aqueous suspensions of iodinated polymer nanoparticles of concentration: 90-100 mg(I).mL^{-1} were intravenously administrated into the tail vein. This corresponded to a dose of 536 mg(I).kg^{-1} regardless animal size. Full body CT scans were performed with a General Electric GE Brightspeed scanner before injection, and from 5 minutes up to 4 days after injection at different time points.

3.4 Results

The nanoprecipitation process was chosen to fabricate PNPs from a preformed iodinated polymer. Several parameters have an influence on the physicochemical characteristics (i.e. size, size distribution, iodine concentration etc.) of these nanosystems. Among them the chemical composition (the polymer concentration in the organic solvent, the nature of the dispersing agent, the polymer/dispersing agent ratio) and one operating condition (the addition rate of THF solution) were investigated.

The organic solvent/water volume ratio of (1/2) was selected as it has been described in the literature as optimum to obtain suitable particle size in the nanoparticle range [100], [117]. This ratio was kept throughout all the experimentations.

Another important process parameter is the stirring rate during mixing. The speed at which the organic phase is added to the aqueous phase as well as the way both phases are mixed have an influence. According to Asadi *et al.*, a more efficient mixing results in a more rapid diffusion of the organic solvent into the aqueous phase. Inefficient mixing causes high local concentration of polymer at the place where the drop falls that produces large particles. The

mixing time has to be shorter than the time for precipitation. Consequently, an increase of the stirring rate leads in a decrease in particle size [134]. Here the stirring rate was set at 500 rpm because it allowed regular mixing with no splash and air uptake.

3.4.1 Model composition

3.4.1.1 Polymer amount

Polymer content in the organic solvent. The starting point of the nanoprecipitation process is a solution of polymer in an organic solvent.

Galindo-Rodriguez *et al.* studied the organic solvent-polymer interaction. They observed that the increase in polymer content leads to a greater number of polymer chains per unit volume of solvent which itself results in faster polymer aggregation and the formation of bigger PNPs [135]. Care must be taken to avoid the formation of aggregates.

Another consequence of an increase of polymer concentration is a higher viscosity of the solution. The outcome is the same on the PNPs size as the diffusion of the polymer-solvent into the external aqueous phase is reduced, so that mixing of the organic and aqueous media is slow and precipitation occurs in medium of transient high local concentrations of polymer [135]. Here also, a compromise must be found between an organic phase that can be easily added and mixed into the aqueous phase and high concentrations of iodine that are seeked for application as CT contrast agent.

The solubility of TIB-PVAL in THF was very high and fluid solutions of TIB-PVAL in THF could be prepared up to 500 g.L^{-1} concentration. Fluid solutions of PCL_{65}-*b*-PEG_{113} could also be prepared up to high concentrations. However, the solubility of mixed TIB-PVAL and PCL_{65}-*b*-PEG_{113} (1/1) was 100 g.L-1, so fluid solutions containing 40 g.L^{-1} of TIB-PVAL and 40 g.L^{-1} of PCL_{65}-*b*-PEG_{113} could be used allowing controlled mixing of the organic solution with water using syringe needles. These concentrations also allowed the precipitation of nanoparticles with no formation of large aggregates

3.4.1.2 Choice of the dispersing agent

The dispersing agent's role is to ensure both short term and long term stability of the nanoparticles or in other terms, avoid rapid nanoparticle aggregation. Short term stabilization is required to avoid aggregation of nanparticles during the nanoprecipitation process. The stabilization mechanism can be seen as a kinetic competition between adsorption of the dispersing agent at the surface of nanoparticles and their aggregation. Stabilization can be done either by electrostatic or steric repulsion.

Stabilizing agents can be selected as classical surfactants (anionic, cationic, nonionic or zwitterionic) or block copolymers (Figure 3.3).

Biocompatibility is a key criterion while designing a contrast agents for intravenous administration. Therefore nonionic stabilizers are preferred and the stabilization mechanism is steric. The hydrophilic part of the dispersing agent must be bulky enough to create steric repulsion in the aqueous phase. Nonionic dispersing agents were investigated.

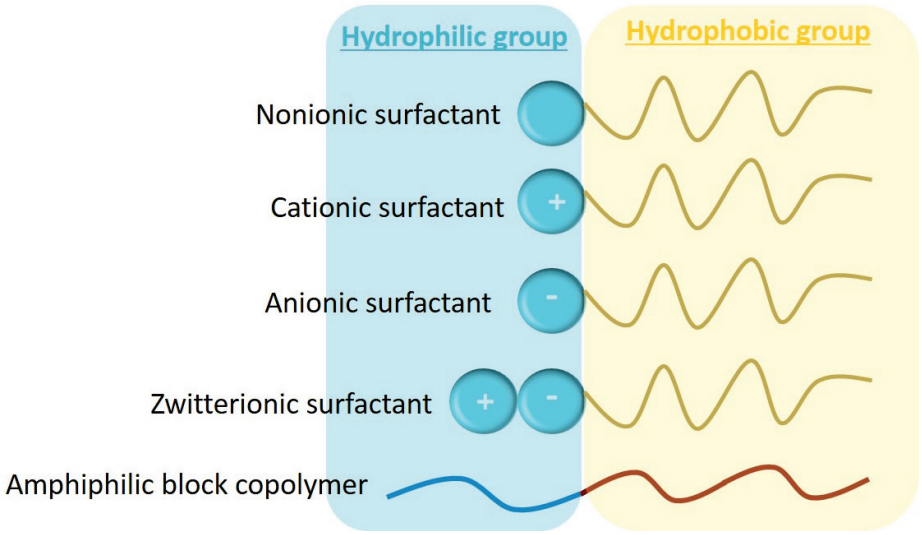

Figure 3.3: Dispersing agent structure

Poly(caprolactone)-*block*-poly(ethylene glycol) (PCL_{65}-*b*-PEG_{113}).

The diblock copolymer PCL_{65}-*b*-PEG_{113} is a polymeric dispersing agent with poly(caprolactone) (PCL) being the hydrophic part and poly(ethylene glycol) (PEG) the hydrophilic one (Figure 3.4). This block copolymer was synthesized in the laboratory, by polymerization of caprolactone initiated by poly(ethylene glycol) monomethyl ether catalyzed by tin octanoate as reported in the literature [113] [114].

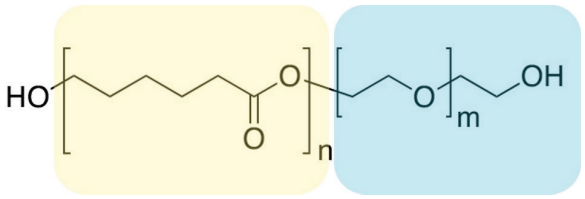

Figure 3.4: Structure of PCL_{65}-*b*-PEG_{113} with n = 65 and m = 113

This copolymer is soluble in THF, so that experiments were carried out with the dispersing agent disolved in the THF organic phase that also contained the iodinated polymer TIB-PVAL. The weight ratio 1:1 gave stable suspensions of nanoparticles with no aggregation and narrow particle size distribution which is satisfactory result. Below a PCL_{65}-*b*-PEG_{113}/TIB-PVAL weight ratio of 1:1, a polydisperse dispersion of nanoparticles was obtained; and a precipitate of large particles formed after few hours storage. Above this ratio, neither the particle size nor the particle size distribution were improved. The weight ratio PCL_{65}-*b*-PEG_{113}/TIB-PVAL was therefore fixed to 1:1 and kept for comparison with other dispersing agents.

Pluronic F-68 ©.

Pluronic F68© is a nonionic triblock copolymer from the poloxamer "family". It is made of two hydrophilic side chains of poly(ethylene glycol) (PEG) or poly(ethylene oxide) (PEO) (Figure 3.5 a)) and a central hydrophobic chain of poly(propylene oxide) (PPO) (Figure 3.5 b)).

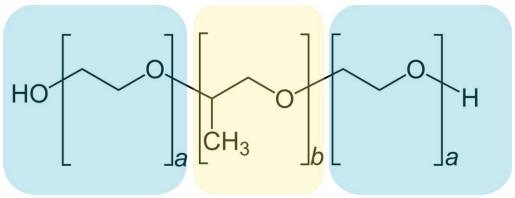

Figure 3.5: Structure of a poloxamer

Pluronic F68© is a commercial name where the letter "F" codes the physical state in which the product is solid. The two numbers quantify the balance between the hydrophobic and hydrophilic parts. In fact the first number time 300 gives the molar mass of PPO and the last number times 10 the PEG content. Therefore Pluronic F68 is made of 80% PEG and has a PPO molar mass of 1800 g.mol^{-1}.

Owing to its large PEG content (80%), this dispersing agent is soluble in water. Therefore it was incorporated in the aqueous phase at the fixed weight ratio Pluronic F-68/TIBCl-PVAL of 1:1 during the nanoprecipitation process. However aggregates of large size formed quickly upon mixing the organic phase into the aqueous phase.

In order to improve stability and avoid aggregation, the amount of dispersing agent was increased up to a weight ratio of 2.5:1 and 5:1 with respect to the iodinated polymer. Although the problem of aggregation could be fixed, evaporation of THF was difficult. The formulation foamed uncontrollably in the rotary evaporator.

Brij S100.

Brij S100 is the commercial name of the poly(oxyethylene) (100) stearyl ether. It is a nonionic surfactant with the hydrophilic part made of PEG-100 and the hydrophobic part made of a C_{18} alkyl chain (Figure 3.6).

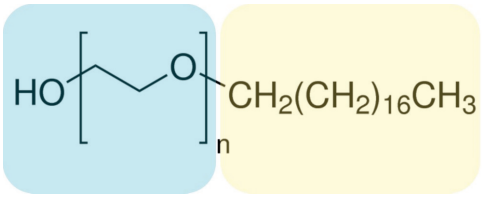

Figure 3.6: Structure of Brij S100

With an HLB of 18.0, Brij S100 is also an hydrophilic surfactant. Thus the later was incorporated in water with a Brij S100/TIB-PVAL weight ratio 1:1. No aggregates formed during the nanoprecipitation step at this ratio, but the suspension foamed during the THF elimination step under reduced pressure.

Poly(vinyl alcohol) (PVAL)

87-89% hydrolyzed PVAL was tested as a surfactant (Figure 3.7). It is a hydrophilic dispersing agent incorporated in the aqueous phase. Although polymeric surfactant like PVAL is known being a poor foaming agent, foaming occurred during evaporation of THF as in the case of Brij S100.

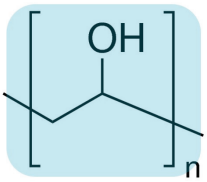

Figure 3.7: Structure of PVAL

Sorbitans.

Sorbitans are nonionic surfactants. Two types of them were tested:

- SPAN 80 and SPAN 85 (Figure 3.8) also known as sorbitan esters.
- TWEEN 80 (Figure 3.8) which is an ethoxylated Span also referred to as polysorbate 80.

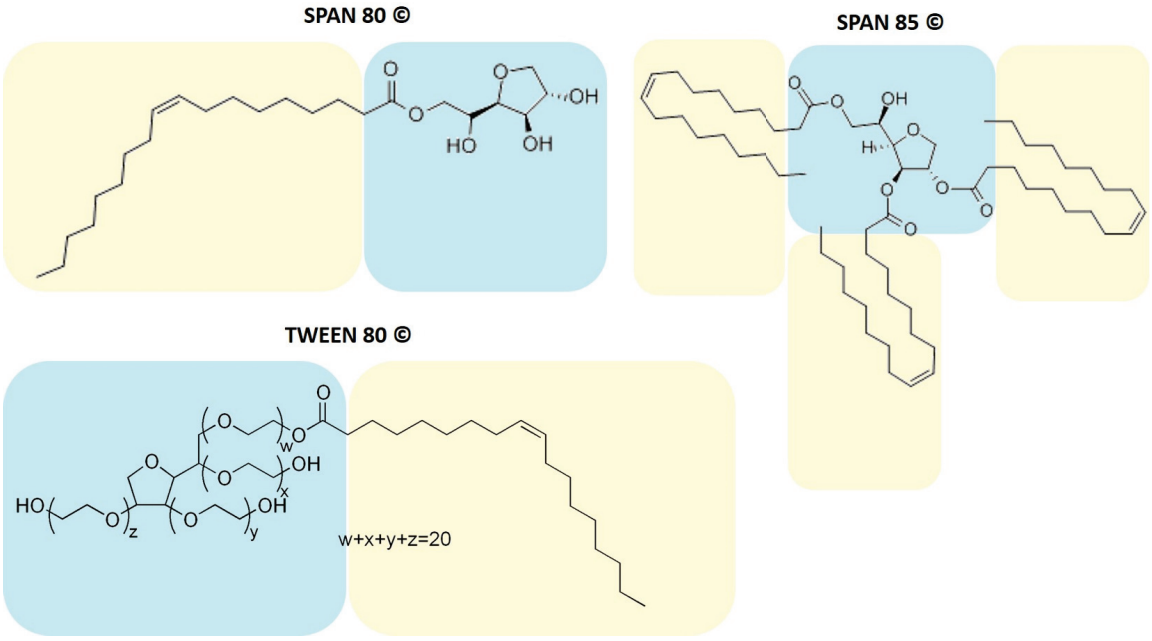

Figure 3.8: Structure of sorbitan esters

Table 3.1: Chemical identity and HLB values of the sorbitan ester surfactants

Product name	Chemical identity	HLB value
SPAN 80	Sorbitan monooleate	4.3
SPAN 85	Sorbitan trioleate	1.8
TWEEN 80	PEG-20 sorbitan monooleate	15.0

Tween 80 with an HLB of 15.0 is an hydrophilic surfactant. The same conditions as for Pluronic F68 were tested (i.e. Tween 80/TIB-PVAL weight ratio 1:1, 2.5:1, 5:1). The results with Tween 80 were the same as for Pluronic F68.

A foaming phenomenon was systematically observed for all hydrophilic dispersing agents during the THF elimination under reduced pressure. Another technique of removing the organic solvent by centrifugation was tested. However, the redispersion proved complicated because the sediment of iodinated polymer formed a film in the presence of THF.

Based on these results, especially issues coming from foaming during evaporation, lipophilic dispersing agents could be better candidates. Moreover, adsorption of the stabilizer to the surface of precipitating nanoparticles is expected faster when the stabilizer is present in the organic medium at the start, allowing a faster stabilization during the nanoprecipation process, thereby avoiding aggregation into larger particles.

Span 80 and Span 85 with an HLB of 4.3 and 1.8 respectively are hydrophobic surfactants. Thus, both surfactants were dissolved in THF together with TIB-PVAL in a weight ratio Span 80/TIB-PVAL and Span 85/TIB-PVAL of 1:1. Precipitation of large particles was observed in both cases when such mixed solutions were added dropwise to water.

Lipoids.

Lipoids are nonionic phospholipids mechanically and chemically extracted from natural sources. They are amphiphilic products with a choline head group and glycerophosphoric acid, with a variety of fatty acids. Two categories were tested here (Figure 3.9):

- Lipoid E80 where E stands for Egg as the source of the lipid and 80 is the percentage of phosphatidylcholine. It is also known as egg lecithin.
- Lipoid S100 where S stands for Soybean source of lipid and 100 is the percentage of phosphatidylcholine.

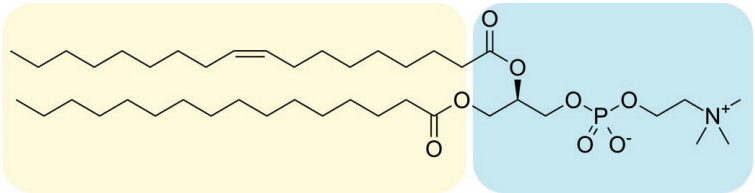

Figure 3.9: Structure of Lipoid phospholipids

These two compounds are rather lipophilic dispersing agents. Hence they were tested in the same conditions as the Spans as described above. Lipoid E80 lead to the same result as Spans, that is formation of large aggregates immediately after the mixing step. Lipoid S100 allowed a satisfactory nanoprecipitation as a homogeneous dispersion of nanoparticles.

Table 3.2 sums up the effects of the different dispersing agents on the nanoprecipitation process and on the physicochemical characteristics (i.e. size, size distribution, stability) of the TIB-PVAL particles. Lipoid S100 and PCL_{65}-*b*-PEG_{113} are the best candidates. A clear fabrication route was achieved, i.e. no foaming during THF evaporation step nor formation of aggregates

at the particle precipitation stage, particle sizes below 200 nm with a narrow size distribution. Furthermore, the suspensions remained stable for days in the case of Lipoid S100 and months for PCL_{65}-*b*-PEG_{113}.

3.4.2 Process conditions

3.4.2.1 Phase addition rate

Several flow rates for mixing the THF and aqueous solutions were tested by changing the internal diameter of the needle. A larger internal diameter (1.25 mm (18G), 1.1 mm (19G), 0.9 mm (20G)) led to a faster flow rate and resulted in the formation of large aggregates. On the contrary, a slow flow rate corresponding to a thinner internal diameter (0.6 mm (23G)) caused problems of syringe clogging for the highest concentrations of TIB-PVAL in the organic solvent. The 21G needle with 0.8 mm internal diameter provided the most satisfying results, that is efficient dropwise addition with the formation of an homogeneous milky dispersion.

3.4.3 Optimum formulation and process

The selected "optimum formulation" was as follows. The THF/water ratio was 1:2 (25 mL THF for 50 mL water in a small scale experiment); both concentrations of radiopaque polymer and dispersing agent in THF were 40 $g.L^{-1}$ (iodinated polymer/dispersing agent weight ratio = 1:1). PCL_{65}-*b*-PEG_{113} and Lipoid S100 were selected as the most promising dispersing agents. The organic solution was added dropwise to water under magnetic stirring using a syringe fitted with a needle 21G (0.8 mm internal diameter). Finally THF was evaporated under reduced pressure, so that suspensions of nanoparticles in water were obtained at the end. The iodine concentration of the dispersion should be 20 $mg(I).mL^{-1}$ according to the recipe. It was actually 17.7 $mg(I).mL^{-1}$ as measured by ICP-OES. Such concentration was lower by a factor of 5 with respect to that suitable for an iodinated contrats agent.

A concentration step was implemented after the initial nanoprecipitation step that yielded suspensions of too low concentrations. An aliquot (10 mL) of the dispersion prepared by nanoprecipitation was centrifuged (7930 rpm, 20 min), the supernatant was removed, and the sediment was redispersed in a minimum amount of water (1 mL), using an ultrasound bath at 40°C for 2 h. Redispersion has been easier with PCL_{65}-*b*-PEG_{113} than with Lipoid S100. The same particle size was kept as can be seen in TEM pictures Figure (3.10).

TEM pictures also allowed a qualitative detection of the presence of excess stabilizing agent in the aqueous phase. Such presence resulted in the formation of a thin film of dispersing agent upon drying the dispersion on the TEM grid that appeared as a grey background in the pictures. In case of dispersions stabilized by PCL_{65}-*b*-PEG_{113}, the background definitely turned to light grey to white (transparent), showing that the centrifugation/redispersion step allowed increasing the concentration of iodinated nanoparticles and washing the suspension from excess stabilizing agent. Such cleaning of the suspension was not that efficient in case of stabilization by Lipoid S100 as grey areas remained visible in TEM pictures in between the black iodinated nanoparticles. Use of PCL_{65}-*b*-PEG_{113} was better with that respect.

The iodine concentration measured by ICP-OES was 98.8 $mg(I).mL^{-1}$ after the concentration step. Such concentration increased by a factor of 5 met the expectations of the final application as contrast agent. It was less than the factor of 10 corresponding to the ratio of the initial volume to that of water added for redispersion because the sediment still contained water

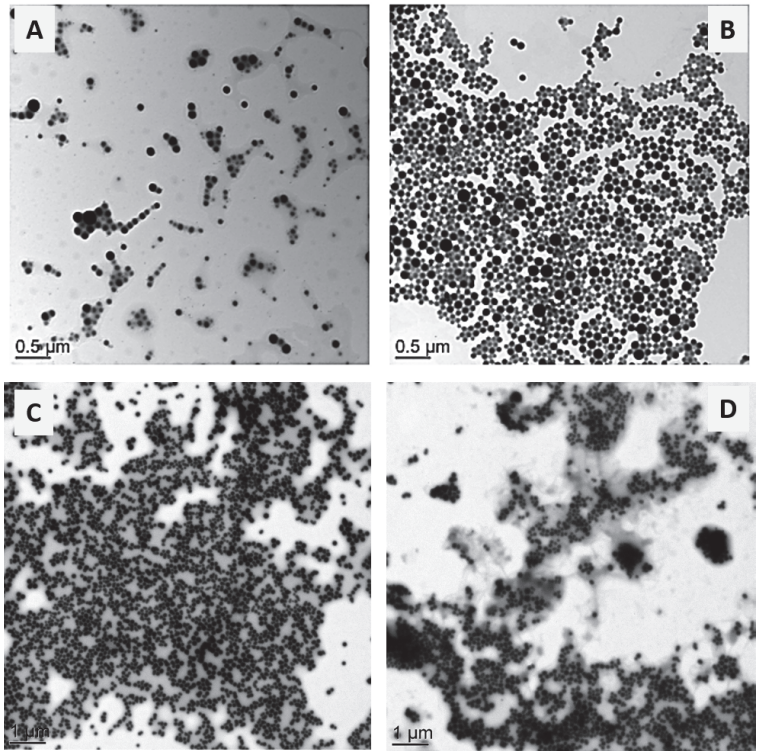

Figure 3.10: Transmission Electron Microscopy (TEM) pictures of the iodinated polymer nanoparticles stabilized by PCL_{65}-*b*-PEG_{113} (top), before (A) and after the concentration step (B). Iodinated polymer nanoparticles stabilized by Lipoid S100 before (C) and after the concentration step (D).

in between the iodinated particles (probably 50% according to the difference between final concentration and expectation).

3.4.4 Iodinated polymer nanoparticles: radiopacity assessment

3.4.4.1 *In-vivo* study

Biodistribution of the iodinated polymer nanoparticles of around 150 nm diameter was studied *in vivo* by experiments on small animals (intravenous injections to rats, according the experimental section) performed on a conventional CT. No visible signs of toxicity were observed post-injection. Animals remained alive and healthy during the entire study.

A typical CT biodistribution profile of these types of PNPs is shown in Figure 3.11). 3 h post-injection, organs from the cardiovascular system (i.e the heart and some blood vessels are still visible). The liver and the spleen are also strongly contrasted up to 120 h after administration.

According to the graphs shown in Figure (3.12 (top)) and Figure (3.12 (bottom)), the nanoparticles stabilized by Lipoid S100 accumulated in the liver and spleen faster than those stabilized by the PCL_{65}-*b*-PEG_{113} block copolymer. This accumulation was associated with a faster decrease of radiopacity in the vascular system (abdominal aorta and heart) with a decayed back to a normal CT level 2 h post injection in case of stabilization by Lipoid S100. The contrast agent stabilized with PCL_{65}-*b*-PEG_{113} remained in the bloodstream up to 5 h post injection. This longer circulation period can be attributed to the presence of PEG at the surface of the nanoparticle, which acts like a stealth agent preventing recognition by the immune system.

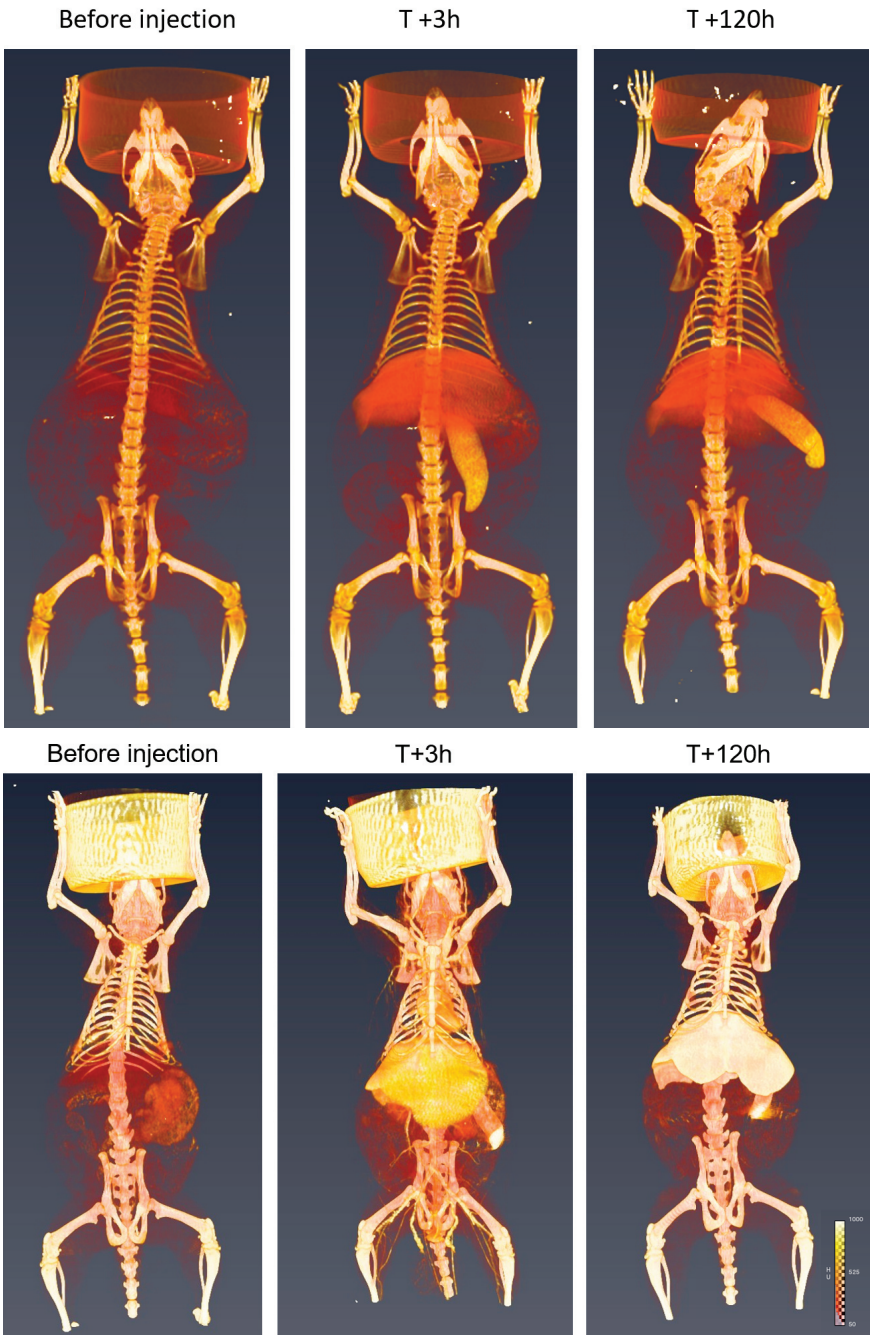

Figure 3.11: Enhancement after intravenous injection into a rat's tail vein of 1.5 mL of aqueous dispersion of iodinated polymer nanoparticles (90-100 mg(I) · mL-1) stabilized by lipoid S100 (top) and PCL_{65}-*b*-PEG_{113} (bottom). CT images were acquired before injection (left), 3 h (middle) and 120 h (right) after the injection. Injected does: 536 mg[I].kg^{-1}).

Moreover, with the same injected dose, NPs stabilized with the block copolymer provide a stronger attenuation signal in the liver (700-750 HU) than the phospholipid-stabilized NPs (550-600 HU). This trend is reversed in the spleen with an enhancement between 150-200 HU with the block copolymer NPs and 200-250 HU for NPs stabilized with phospholipids. Indeed, it has been observed that liposomes made of phospholipids mainly accumulate in the spleen and that association of phospholipid with PEG surfactants decrease such accumulation in the spleen [136].

Table 3.2: Comparison of the different dispersing agents

Dispersing agent (DA)	**Hydrophilic Lipophilic**	**DA)/(TIBCl-PVAL) weight ratio**	**Fabrication problems**	**Z-average (d.nm)**	**PDI**	**Stabilization time**
Pluronic F-68	Hydrophilic	1	Aggregates	N.A	N.A	N.A
		2.5	Foam	264.5	0.20	Hours
		5	Foam	261.3	0.15	Hours
Brij S100	Hydrophilic	1	Foam	N.A	N.A	N.A
PVAL	Hydrophilic	1	Foam	N.A	N.A	N.A
TWEEN 80	Hydrophilic	1	Aggregates	N.A	N.A	N.A
		2.5	Foam	236.1	0.03	Hours
		5	Foam	251.4	0.16	Hours
SPAN 80	Lipophilic	1	Aggregates	N.A	N.A	N.A
SPAN 85	Lipophilic	1	Aggregates	N.A	N.A	N.A
Lipoid E80	Lipophilic	1	Aggregates	N.A	N.A	N.A
Lipoid S100	Lipophilic	1	None	166.9	0.15	Days
PCL_{65}-*b*-PEG_{113}	Lipophilic	1	None	150-200	0.08	Months

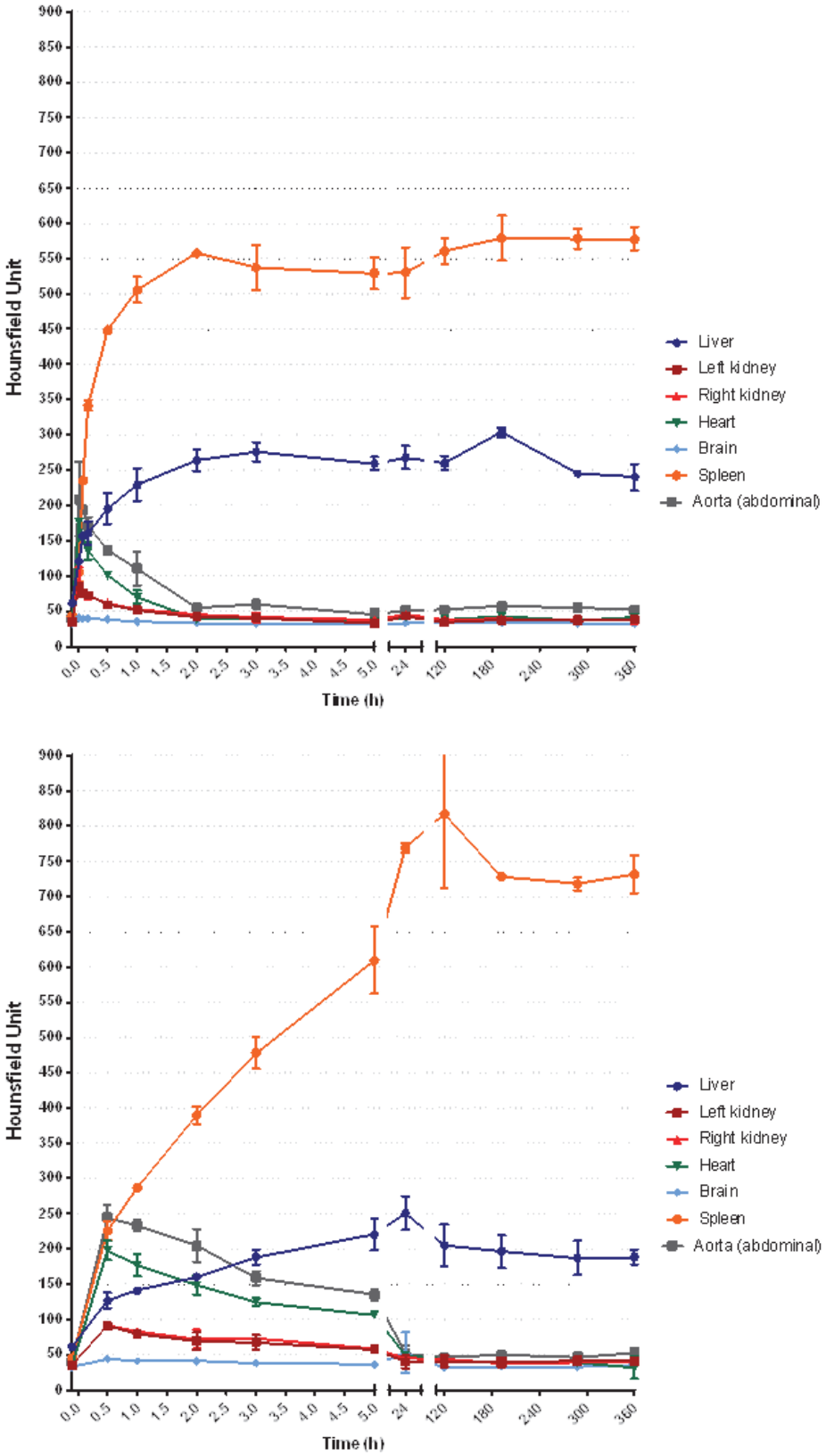

Figure 3.12: CT follow up of the biodistribution over time, after intravenous injection into a rat's tail vein of 1.5 mL of aqueous dispersion of iodinated polymer nanoparticles (90-100 mg(I).mL^{-1}) stabilized by Lipoid S100 (top) and PCL_{65}-*b*-PEG_{113} (bottom). Injected does: 536 mg[I].kg^{-1}). Mean ± Sem, n = 3

3.5 Discussion

The two types of nanoparticles stabilized by the block copolymer PCL_{65}-*b*-PEG_{113} and by the phospholipid Lipoid S100 had quite different behaviors. Both dispersing agents were able to stabilize the suspensions, stabilization by PCL_{65}-*b*-PEG_{113} being better than Lipoid S100. Conversely, PCL_{65}-*b*-PEG_{113} allowed a long circulation time in the blood stream whereas iodinated nanoparticles stabilized by Lipoid S100 accumulated quite fast in the liver and the spleen.

This could be surprising at first sight as both long term stability and resistance to uptake by macrophages rely on the presence of a hydrophilic layer at the surface of nanoparticles that prevent direct contact other materials. Colloidal stability comes from a dense coating of particles by hydrophilic materials providing steric repulsive forces acting against coagulation by mutual approach of particles. Stealthiness against macrophages is also ensured by the presence of a dense surface layer of hydrophilic materials at the surface of particles that prevents adsorption of opsonins. The difference between a PEG layer and a zwitterionic layer of Lipoid S100 phospholipids (lecithins) stands in the range of the generated repulsive forces.

The PEG layer in a brush configuration provides a long range steric repulsion as it has been shown by many experiments. The most illustrative ones are direct measurements of surface forces between solid surfaces coated by a layer of adsorbed PEG. Very long range repulsive forces of the order 20-200 nm were observed because PEGs of high molar masses (50,000 to 1,600,000 $g.mol^{-1}$) were used [137], [138], [139], [140].

The behavior was typical of a polymer brush in good solvent conditions that a theoretical description has been given by de Gennes [141], further refined by Milner *et al.* [142] and favorably validated against experimental measurements performed using the surface force apparatus [143], [144].

An estimate of the brush height can be obtained taking the picture of Alexander and de Gennes where attached PEG macromolecules in a brush configuration are made of chains of blogs which sectional area is the inverse density of PEG at the surface and where the polymer conformation is that of a free macromolecule. As the mean area per PEG determined previously was 3.36 nm2, the diameter of a blog is 2.07 nm.

Owing to the hydrodynamic radius of a free PEG chain measured by Devanand and Selser: $R_h = 0.0145 \times M_W^{0.571}$ (nm) [118], the diameter of a blog corresponds to a molar mass of a PEG fragment of 1760 $g.mol^{-1}$., so that the adsorbed PEG(5000) chains are made of 3 blogs and the full length of them is 6 nm. The range of the steric repulsion is twice the brush height, that is, 12 nm.

A surface coating by the phosphatidylcholine zwitterionic headgroup of phospholipids also generates a strong repulsive force that stabilizes dispersions, emulsions and liposomes. The origin of such "hydration" repulsion has been ascribed to the dipolar orientation of water molecules induced by the zwitterionic headgroups from the surface [145], [146]. The mechanism of hydration force has been questioned by several authors however [147].

Whatever the exact mechanism, direct measurements using the surface force apparatus have disclosed a very strong repulsive force between surfaces that effectively stabilizes dispersions. Such repulsion has a rather short range (i.e.$\sim$ 2-3 nm) that might be shorter than that of

attractive dispersion interactions [148]. As a result, particles are attracting at long separation distances and can undergo coagulation by approaching and reaching a secondary energy minimum where the strong repulsive wall of hydration repulsion prevents close contact of the particle surfaces. Thereby, the colloidal stability of nanoparticles stabilized by Lipoid S100 is good, but less than for PCL_{65}-*b*-PEG_{113}.

Coagulation slowly takes place and redispersion by gentle stirring is possible. Surface force measurement performed for phosphatidylethanolamine layers disclosed an hydration repulsion of much shorter range [149], which explains the fusogenic properties such phospholipids and provides a clue for understanding the poor stability of suspensions stabilized by Lipoid E80 that contains only 80% of phosphatidylcholine lipids and possibly 20% of phosphatidylethanolamine derivatives.

The consequences of the different ranges of repulsive force is well-illustrated by surface force measurements between adsorbed layers of mixed phospholipid-PEG showing that the characteristic force profile of phospholipids with a steep repulsive wall at short distance and a weak attractive well turns progressively into a long-range repulsive profile as PEG adsorbs onto the surface [150].

There are definitely stronger differences between PEG and phosphatidylcholine with regards to uptake by macrophages that is triggered by adsorption of opsonins. The long-range barrier built by a dense brush of PEG parts of PCL_{65}-*b*-PEG_{113} effectively inhibits adsorption of opsonins. On the contrary, the short-range repulsion coming from phosphatidylcholine did not prevent opsonin reaching a close distance from the surface; even more the organization of water coming from the hydration force might not repel small proteins like opsonins because oriented water remains liquid water. Therefore, Lipoid S100 proved to be less efficient at preventing adsorption of opsonins.

3.6 Conclusions

Dispersions of iodinated polymer (TIB-PVAL) nanoparticles were prepared using the nanoprecipitation process. Several parameters have been studied and optimized in order to get a nanoparticulate CT contrast agent that meets the specifications of the application.

The THF/water volume ratio was set to 1:2 and the dispersing agent/TIB-PVAL weight ratio to 1:1. The addition rate of the organic solution through a 21G needle (0.8 mm internal diameter) and the stirring rate of the aqueous phase (500 rpm) were chosen in such way that formation of aggregates was avoided and nanoparticles with size below 200 nm having a narrow size distribution were obtained. The recipe formulation and process operating conditions were fixed using the PCL_{65}-*b*-PEG_{113} block copolymer as dispersing agent.

However, other dispersing agents were tested. It was seen that there was a foaming phenomena with hydrophilic surfactants (i.e. poloxamers, polysorbates, PVAL, Brij S100) during the THF evaporation step. Some of the lipophilic stabilizers (i.e. sorbitan esters, Lipoid E80) failed to stabilize the PNPs since aggregates formed straight after addition of the organic solution to the aqueous phase. Only Lipoid S100 and PCL_{65}-*b*-PEG_{113} managed to achieve efficient stabilization during the nanoprecipitation process. If both systems were similar in terms of physicochemical characteristics, stabilization by PCL_{65}-*b*-PEG_{113} showed definite advantages over that by phospholipids:

- Redispersion was easier with the block copolymer during the concentration step by centrifugation/redispersion;
- Stabilization of the concentrated suspensions (100 mg(I).mL^{-1}) was better by using the block copolymer as the phospholipid-stabilized nanoparticles were stable for some days against months for the block copolymer.
- The contrast agent containing PCL_{65}-*b*-PEG_{113} remained in the blood stream for a more prolonged period of time (longer than 5 h against 2 h for the phospholipid), which was a good point for application as a blood pool contrast agent.

Acknowledgements

The research project has received funding from European Union through Horizon 2020 research and innovation program under grant agreement No 643694.

Chapter 4

Degradation of iodinated polymer nanoparticles: a study on macrophages

Contents

4.1 Introduction 95

4.1.1 Macrophages 95

4.1.2 Polymeric nanoparticles (PNPs): Influence of physicochemical characteristics on uptake by macrophages 98

4.1.3 Aim of the study 99

4.2 Experimental section 99

4.2.1 Materials 99

4.2.2 Methods 100

4.2.3 Characterization 102

4.3 Results and discussion 102

4.3.1 Definition of a viable iodine concentration 102

4.3.2 TEM images of iodinated polymer NPs in macrophages . . . 103

4.4 Conclusion 106

Preamble

Nanobiomaterials are interesting systems for the development of the future generation of CT contrast agents. However, the fate of these types of agents and notably polymeric nanoparticles (PNPs) that are intravenously administrated in the organisms is a major concern.

It was seen in previous chapters that blood pool agents tend to accumulate progressively in the spleen and liver once they are cleared from the cardiovascular system. They remain inside these organs for extremely prolonged times. This is the case for the iodinated polymer nanoparticles developed in the frame of the project, that remained in the liver and spleen for the entire period studied (i.e. 15 days). Another team has developed a different kind of PNPs that stayed in the same organs up to 9 months with only 81 % clearance [70].

One big question arises: how are intravenously administrated nanoparticles cleared?

In this chapter, a study was designed with the intention of bringing some elements to answer this great issue. First a general introduction is made, as to introduce the notions of macrophages, their roles in the organism and the different internalization routes. The different physicochemical properties of PNPs that impact clearance pathways and degradation mechanisms are also discussed.

In the experimental section, the internalization and potential degradation of the iodinated polymer nanoparticles (TIB-PVAL) by macrophages are presented. A 5-weeks study was performed after incubation of the cells by the NPs. Transmission Electron Microscopy (TEM) was used to observe NPs degradation over time. The remaining concentration of iodine was monitored by analysis using Inductively-Coupled Plasma-Optical Emission Spectrometry (ICP-OES).

4.1 Introduction

4.1.1 Macrophages

4.1.1.1 Definition and role

Macrophages from Greek "makròs" large and "phageìn" to eat, literally means "big eater". They are actually cells of the immune system that behave like sentinels whose role is to protect the body from any foreign substances. In order to do so, they engulf and degrade microbes, cancer cells, exogenous inert particles, and globally anything that does not have the type of cell-specific proteins of a healthy body on its surface and cannot pass through the renal filters.

Macrophages have different names in function of their location. They are found as resident macrophages mostly in organs directly or indirectly in contact with the "outside word" (i.e. alveolar macrophages in lungs) and tissues from the reticuloendothelial system (RES) now known as the mononuclear phagocytic system (MPS) (i.e. Kupffer cells in the liver, red pulp in the spleen, monocytes that differentiate into macrophages in the bone marrow and in the lymph nodes).

On the other hand, macrophages infiltrate other tissues in response to stimuli. In this case, their precursors (monocytes) are locally recruited at the level of the inflamed tissue and differentiated into macrophages.

It should also be emphasized that not all macrophages have the same functionalities. Indeed, they are different in their phenotype and so physiological properties, sometimes even from the same tissues. For instance, murine Kupffer cells can have variable levels of degradation activities (enzyme, phagocytic, scavenging activities) depending on their location in the liver [151].

Understanding of macrophages properties, heterogeneity and degradation mechanisms is a step towards understanding NPs *in vivo* degradation and elimination. This must be kept in mind when designing nanobiomaterials for intravenous administration.

4.1.1.2 Nanoparticles (NPs) internalization and degradation

It is well known that intravenously injected nanoparticles of given physicochemical characteristics tend to accumulate in the liver and spleen [152]. This reflects progressive uptake by macrophages from the splenic and hepatic tissues.

In the literature, two main mechanisms of internalization of nanoparticles by macrophages are described: phagocytosis and pinocytosis (Figure 4.1).

Phagocytosis. Phagocytosis is the main internalization and degradation route. It is divided into four steps:

- Step 1: Opsonization. During this step, different proteins known under the generic name "opsonins" (i.e. immunoglobulins (Ig) G (and IgM), complement components (C3, C4, C5), blood serum proteins etc.) are adsorbed at the surface of NPs. The later come into contact with the above cited proteins by random Brownian motion and interact by means of various attractive forces such as van der Walls forces, electrostatic, or hydrophobic/hydrophilic [154]. Consequently, recognition by the macrophages is triggered,

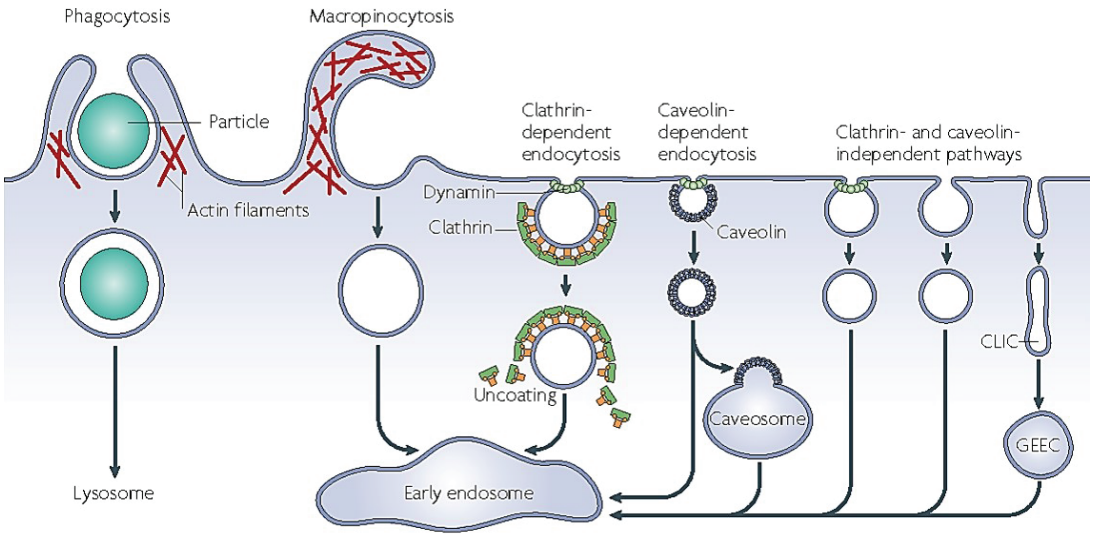

Figure 4.1: Pathways of entry into cells [153]

which leads to the next step. However, it should be mentioned that it is possible to delay this phenomenon by modifying the physicochemical properties of nanomaterials [155].

- Step 2: Adhesion of "opsonized" NPs to the surface of macrophages. This could induce the activation of specific receptors (i.e. Fc receptors or complement C3 receptors) present on the surface of macrophages. Such activation can occur either after a change in the opsonin conformation, allowing their activation and therefore their recognition by the above mentioned opsonin receptors. This occurs either by a nonspecific adhesion of the phagocytes to the serum proteins bound to hydrophobic NPs, or by activation of the complement system [155].

- Step 3: Internalization. The NPs are eventually internalized by phagocytes through endocytosis. What happens is that the macrophage membrane folds as to form a pocket in the surface in a phenomenon called invagination. This results in the NPs embedding in a vesicle called phagosome.

- Step 4: Degradation. The degradation step takes place in the macrophage cytoplasm. The phagosome containing NPs and other lysosomes full of digestive enzymes (i.e. acid hydrolases, esterases, cathepsins) merge, forming "phagolysosomes", and leading to enzymatic digestion of the contents of the phagosome. Note that phagocytes secret enzymes but also other oxidative reactive chemicals (i.e. superoxides, oxyhalide molecules, nitric oxide, hydrogen peroxide etc.) to degrade NPs.

Pinocytosis. Pinocytosis is a mechanism common to all cells. Macropinocytosis or micropinocytosis occurs depending on the size of the NPs to be internalized.

- Macropinocytosis: This mechanism concerns NPs in the 0.5-5 μm size range. Like in the phagocytosis mechanism, there is also a membrane deformation induced by rearrangements of actin, but without completely forming a vesicle (Figure 4.1) [156].

- Micropinocytosis: This mechanism is relevant to NPs under 500 nm. It can be clathrin-dependent or independent (Figure 4.1) [157].

In both cases the NPs are internalized by endocytosis. This process can be clathrin[1] dependent, caveolin[2] dependent or both clathrin and caveolin independent.

Clathrin-dependent endocytosis. Clathrin-dependent endocytosis requires the recognition of nanomaterials by mannose, "scavengers" or "toll like" receptors, present on the surface of the cells [9]. Next, the membrane invaginates and is covered with a coat of "Clathrin-1" proteins. The GTPase activity of dynamin allows the individualization of a vesicle whose clathrin-1 coat is subsequently degraded, this is known as "uncoating". Finally, the vesicle merges with endosomes, the internal environment of the latter is acidified and NPs are digested/degraded by the lysosomes (Figure 4.1).

Caveolin-dependent endocytosis Caveolin-dependent endocytosis, activated by caveolin ligands or receptors expressed in lipid rafts [158], also initiate the formation of a vesicle covered with a caveolin coat that subsequently blends with caveosomes. These are later transported to the endoplasmic reticulum in the cytosol, then into the nucleus by means of microtubules. Note that here there is no enzymatic degradation.

It should be stated that whether the NPs are released into the enzymatic environment of the lysosomes or directly in the cell cytoplasm, has an important impact on the clearance activity [159]. According to Oh and Park, nanoparticles exit the cell via three types of pathway: lysosome secretion, vesicle-related secretion, and non-vesicle-related secretion (Figure 4.2) [160].

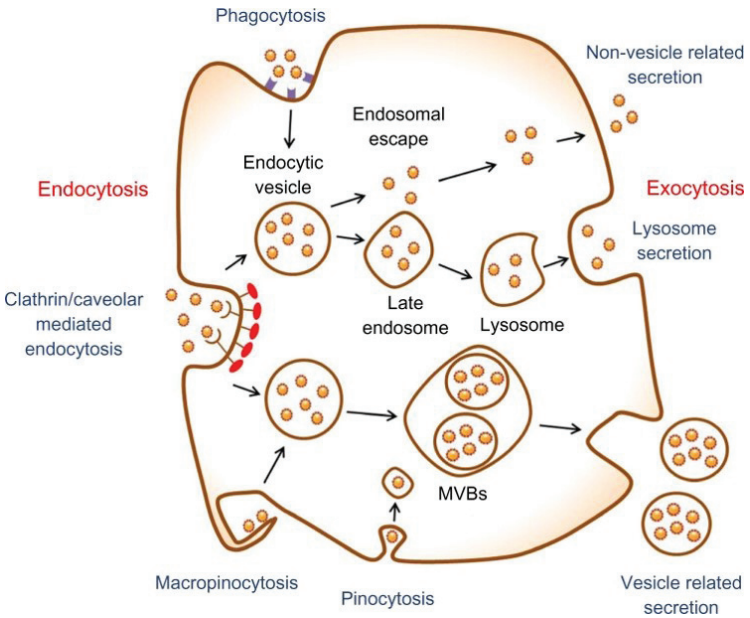

Figure 4.2: Endocytosis and exocytosis patterns of nanoparticles. MVBs = multivesicular bodies [160]

[1]Clathrin is a basket-like network of protein molecules that forms on the cell membrane in response to the attachment of ligands to receptors and becomes the inside surface of the coated vesicle during endocytosis.

[2]Caveolin is a membrane protein involved, among others, in receptor-independent endocytosis.

4.1.2 Polymeric nanoparticles (PNPs): Influence of physicochemical characteristics on uptake by macrophages

Other parameters that affect the NPs biodistribution and both the internalization pathway and the degradation mechanism are the physicochemical characteristics of the PNPs (i.e. size, morphology, size distribution etc.) and surface properties [161] [162]. In this section the impact of NPs size, morphology, surface properties and rigidity on the uptake and potential clearance of NPs by macrophages is depicted.

4.1.2.1 Size

Size is an important characteristic of nanobiomaterials, as it monitors several application properties (drug delivery, contrast element content, active and passive targeting, *in vivo* biodistribution and by extension elimination routes). However, a consensus has never yet been reached regarding size thresholds associated to different elimination pathways (renal filtration threshold, phagocytosis threshold etc.). Even if the common threshold for phagocytosis is often set at 0.5 μm, in practice macrophages cannot internalize anything with a size larger than themselves (up to 60 μm).

In the literature, some studies claim that internalization of nanoparticles smaller than 200 nm is made by clathrin-dependent endocytosis ([163] [164]) and that of nanoparticles smaller than 80 nm is made by caveolin-dependent endocytosis [156].

Moreover, according to Sharma *et al.*, the persistence of particles in macrophages is correlated with their size; the bigger the particles, the faster they are eliminated from the macrophages [165].

4.1.2.2 Morphology

Some studies have been carried out in order to determine the impact of the NPs shape on macrophage internalization. Sharma *et al.* evaluated the impact of the polymer microparticle shape (1 μm) on the phagocytic capacity of murine macrophage line RAW264.7. It was observed that particles of "oblique ellipsoid" (ellipsoidal) shape were more easily phagocytosed by macrophages than spherical particles [165].

Another team observed the internalization of polystyrene microparticles of different morphologies (spheres, discs, ellipsoids) by alveolar macrophages. As an outcome, it was demonstrated that on top of the morphology-dependence, phagocytosis of microparticles was dependent on the angle of initial contact (i.e. orientation) between the microparticles and the macrophage membrane [166]. This phenomenon depends on the actin-induced membrane deformation necessary for internalization. Thus, when ellipsoidal particles are oriented to initiate contact with the macrophage from its more curved (tip) part, a vesicle surrounded by actin is formed: there is phagocytosis. In case the contact between this same particle and macrophage is done on its flat side, attachment occurs but phagocytosis does not take place.

4.1.2.3 Surface properties

Phagocytosis is the predominant NPs internalization mechanism by macrophages. As seen previously, it involves an opsonization (protein adsorption) step which results from the ionic or hydrophobic/hydrophilic interactions between opsonins and the surface of the NPs. Therefore,

it is safe to say that the internalization is related to the surface properties of the NPs (charge, presence of hydrophobic or hydrophilic groups).

Many strategies that aim at dodging the MPS, have been described. The most commonly used is PEGylation of nanoparticles surface. A stealth agent (here PEG) is added with the intention of preventing protein adsorption by decreasing surface charge or/and hydrophobicity but also providing steric hindrance. This was demonstrated *in vitro* by Walkey *et al.* They showed that increasing the density of PEG (molar mass = 5000 Da) grafted to gold nanoparticles (from 0 to 10 PEG. nm^2) decreased serum protein adsorption by the steric hindrance caused by PEG chains, suggesting the importance of the opsonization of NPs in the phenomenon of cellular internalization [167].

Furthermore, several studies in the literature claim that positively charged nanoparticles are more internalized than neutral or negatively charged NPs. This may be explained by the electrostatic interactions with cell membranes, owing to the fact that the majority of membranes are negatively charged. He *et al.* have worked on the impact of the PNPs charge on their internalization by peritoneal murine macrophages. They observed an increase in cellular internalization with surface charge nanoparticles, whether negative or positive [168].

4.1.2.4 Rigidity

The rigidity of particles is also an important parameter influencing their internalization. Somme studies disclosed that rigid nanoparticles were easier phagocytosed by macrophages. For instance, Beningo *et al.* observed that the internalization by murine macrophages of poly(acrylamide) rigid microparticles (1 to 6 μm) was 6 times greater in comparison with the same soft particles [169]).

Similar results have been obtained for rigid PEGylated nanoparticles of about 200 nm [170]. The authors demonstrated *in vitro* on a murine macrophage line J774 cells that the rigid NPs were 4 times more internalized than their soft analogues.

One explanation can come from the fact bacteria and other pathogens have cell walls often more rigid than the surrounding tissues.

4.1.3 Aim of the study

The aim of this study is to investigate the degradation of iodinated polymer nanoparticles by macrophages *in vitro*. In order to do so, a 5 weeks' study was performed after incubation of the cells by the NPs. Transmission Electron Microscopy (TEM) was used to observe NPs degradation over time. The remaining concentration in iodine was monitored with Inductively-Coupled Plasma-Optical Emission Spectrometry (ICP-OES).

4.2 Experimental section

4.2.1 Materials

Cells. The BALB/c mice peritoneal macrophage cell line J774A.1 from the European Collection of Cell Cultures (ECACC, 91051511) were used to assess cytotoxicity. These cells were maintained at 37°C with 5% CO_2 by successive passages in RPMI-1640 culture medium (PAA

Laboratories, GE Healthcare, Pasching, Austria) containing 10%(v/v) fetal bovine serum (from Sigma, St-Quentin Fallavier, France), 1% MycoKill AB and 1.5% penicillin/streptomycin.

Nanoparticles. The iodinated polymer nanoparticles were fabricated from a preformed polymer by means of the nanoprecipitation process. Full synthesis and characterization are described in Chapter 2. The main physicochemical characteristics are: size below 200 nm, spherical shape, narrow size distribution and iodine content of 100 mg(I).mL^{-1}. Their biodistribution revealed that they stayed 5 h in the bloodstream thanks to the presence of a stealth agent (PEG) at the surface that avoids rapid protein adsorption and opsonization. There is progressive accumulation in liver and spleen.

4.2.2 Methods

4.2.2.1 Evaluation of the nanoparticles (NPs) cytotoxicity

J774A.1 cells were cultured in a 96 wells plate using RPMI-1640 culture medium containing 10% (v/v) fetal bovine serum. Once cells had reached about 80% confluence, they were incubated for 5h with iodinated polymer nanoparticles at concentrations of iodine of 10/5/2/1/0.33/0.1 and 0.033 mg(I).mL^{-1}. Then the culture medium was replaced by a new cell culture medium free of iodinated nanoparticles.

Cell viability was determined at 24 h and 48 h using a MTS/PMS solution (Cell Titer 96; Aqueous Non-radioactive cell Proliferation Assay, Promega, Madison, WI, USA). The absorbance of the formazan product was measured at 490 nm with a plate reader (Thermo Fisher Scientific 51118177 Multiskan EX Microplate Photometer, Villebon-sur-Yvette, France).

4.2.2.2 Evaluation of NPs uptake and degradation by macrophages

Suspensions of iodinated polymer nanoparticles, previously diluted in culture medium were sterilized by filtration through a 0.22 μm sterile Cellulose Esters (CE) filter, prior to incubation with the J774A.1 cells. A 5-weeks degradation study of the PNPs by macrophages was prepared as following:

- Six multi-well plates each containing 2 control wells of non-treated cells (in 2mL) and 2 wells filled of macrophages (presented in 1,5 mL) incubated with nanoparticles (by adding 0.5mL) for 5h (Figure 4.3). Subsequently, the culture medium was replaced by a new cell culture medium free of iodinated nanoparticles.

  Note that in order to maintain cell viability, 2 mL of new cell culture medium was added in the wells at half a week, and every 7 days all 4 mL of supernatant medium together with some floating cells (product of cell proliferation) were replaced with 2 mL of new cell culture medium.

  Every 7 days, starting from day 0, the samples from one plate were collected and prepared for observation by Transmission Electron Microscopy (TEM).

- Seven cell culture flasks were also prepared as follow: 1 control flask containing non-treated macrophages in 4 mL of cell culture medium and 6 flasks filled with macrophages (presented in 3 mL) and incubated with 1 mL of nanoparticle suspension (Figure 4.4). After 5 h, the culture medium was replaced by a new cell culture medium free of iodinated nanoparticles.

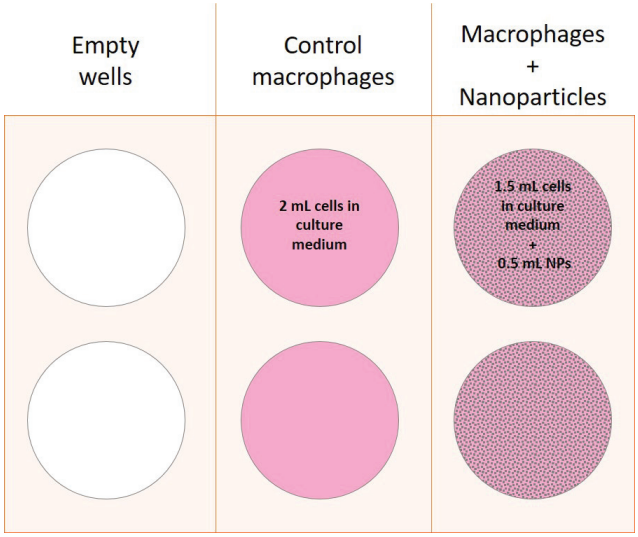

Figure 4.3: 6 wells plate composed of 2 empty wells (left), 2 control wells containing 2 mL of macrophages in cell culture medium (middle) and 2 wells containing macrophages incubated 5 h with nanoparticles (right)

Here also, to insure cell viability, 4 mL of new cell culture medium were added in the flasks at half a week, and every 7 days all 8 mL of supernatant medium were replaced with 4 mL of new cell culture medium. It is important to know that since the cells proliferate, it was necessary to centrifuge the medium to recover the floating cells in the supernatant medium.

Every 7 days starting from day 0, the samples were collected and prepared for iodine content assessment by ICP-OES.

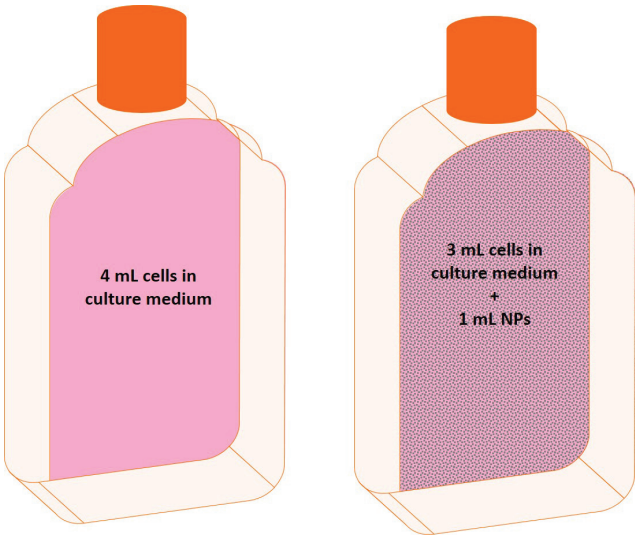

Figure 4.4: Control cell culture flask containing blank macrophages (left) and cell culture flask containing macrophages incubated 5 h with nanoparticles (right)

4.2.3 Characterization

4.2.3.1 Observation of internalization and degradation (TEM)

Sample preparation. The first step is intended to fix the cells as well as the proteins and carbohydrate groups that react with the aldehyde group.

As mentioned before, a plate is recovered and sampled after 7 days of incubation. Each plate contains 2 control wells (that were pooled together) and 2 wells containing the nanoparticles (which were also pooled). At the end 2 samples were prepared per plate.

Once the cells were detached from the wells and recovered separately, the same volume of a glutaraldehyde solution (4%) was added to each. The mixture was left to incubate for 15 min at 4°C.

The samples were then recovered and centrifuged (5 min, 1200 rpm). The supernatant was removed and the sediment was redispersed with 1 mL of a mixture containing: 1 volume of glutaraldehyde (2%) and 1 volume of cacodylate (0.2 M pH 7.4). The solutions were kept 30 min at 4°C before transmission to the microscopy center for the rest of the sample preparation.

Note that overall there are 6 other steps before the observation by TEM. A full description is given in the appendix A.

TEM observation. Transmission Electron Microscopy (TEM) pictures were obtained with a JEOL JEM1400 electron microscope under 120 kV accelerating voltage, at the "Centre d'Imagerie Quantitative Lyon Est (CIQLE)", University of Lyon 1 (http://ciqle.univ- lyon1.fr/).

4.2.3.2 Iodine content assessment

Sample preparation. First the cells were detached from the flasks using cell scraper. Afterwards, the cell culture medium was centrifuged (5 min, 1200 rpm), the supernatant was removed and kept for measuring potential iodine concentration coming from the products of degradation of the iodinated polymer nanoparticles. The sediment was redispersed in 1 mL of PBS, frozen and stored for measurement of remaining iodine content.

ICP-OES. The amount of iodine was determined by Inductively-Coupled Plasma-Optical Emission Spectrometry (ICP-OES) measurements on the polymer in solution using a Vista-Pro CCD simultaneous ICP-OES Varian instrument at the Institut des Sciences Analytiques (University of Lyon 1).

4.3 Results and discussion

4.3.1 Definition of a viable iodine concentration

Cytotoxicity of the iodinated polymer nanoparticles was determined by MTS assays performed 24 h and 48 h after incubation of macrophages with nanoparticles of different concentrations. Cell viability was calculated from the absorbance values. A standard containing non-exposed macrophages (negative control), was taken as the control for 100% cell viability. Full cell viability was retained after 5 h exposure to all suspensions of iodinated nanoparticles (Figure 4.5). The contrast agent did not manifest any cytotoxic activity at the studied concentrations.

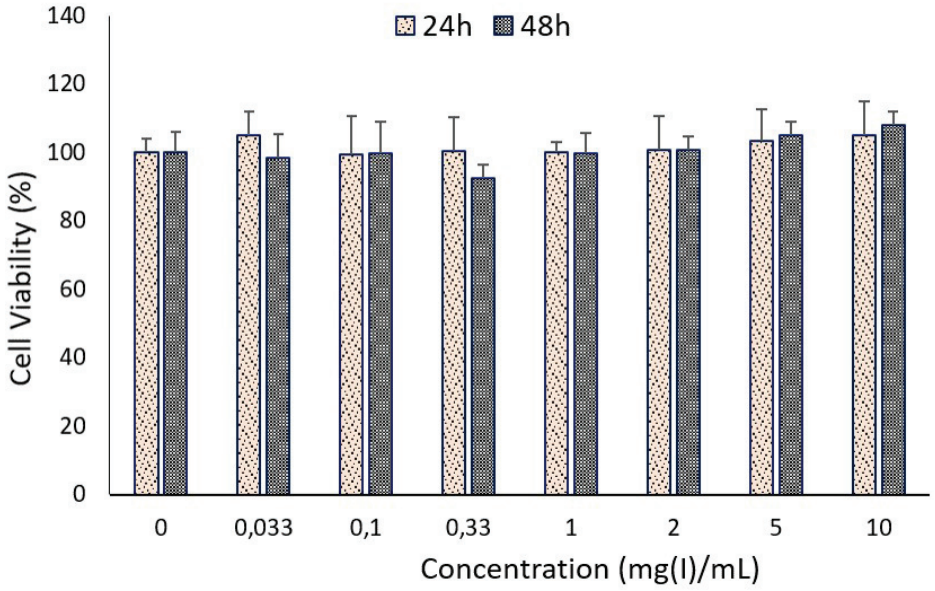

Figure 4.5: Cell viability after 5 h exposure to aqueous suspensions of iodinated nanoparticles of various concentrations. Viability was assessed 24 h and 48 h after the end of exposure to nanoparticles

The iodinated polymer nanoparticles have been tested *in vivo* on rat models with an injected dose of 536 mg(I).kg^{-1} regardless of animal size. The NPs presented a typical biodistribution of a blood pool agent for CT (i.e. they remained in the bloodstream for 5 h before eventually accumulating in the liver and spleen). The animals remained healthy for the entire experimentation (i.e. 15 days), showing the NPs did not show any toxicity. Since samples did not present any toxicity towards the macrophages at all concentrations studied *in vitro* either, a choice was made to incubate the NPs with the macrophages for 5 h at a concentration of 6 mg(I).mL^{-1}.

4.3.2 TEM images of iodinated polymer NPs in macrophages

TEM images of internalization of the iodinated polymer NPs can be seen Figure 4.6. If the exact pathway of NPs internalization is not represented, one can image uptake from the bloodstream by phagocytosis. In fact, pictures taken from day 0 samples show particles in the endolysosomal vesicles. Day 7 and until the end of the experience (day 35), some cells already presented signs of autophagy indication a potential exocytosis of nanoparticle and their cellular clearance. *In vitro* cell culture the endocytosis of released nanoparticles could be done by other cells. Nevertheless, the nanoparticles seem to have the same aspects throughout the entire experience.

Since the iodinated polymer NPs are made from a preformed polymer that is a triiodobenzoyl ester of polyvinyl alcohol (TIB-PVAL), the latter is presumed hydrolysable at its ester bond and the products of hydrolysis are water-soluble PVAL and TIBAc. The dispersing agent which is a block-copolymer of PCL_{65}-*b*-PEG_{113} is also known as a biodegradable polymer. Therefore, the iodinated polymer NPs should undergo hydrolysis by intracellular esterases. Cleavage of triiodobenzoyl pendant groups should increase the hydrophilicity of the polymer backbone until it become water-soluble as depicted on (4.7).

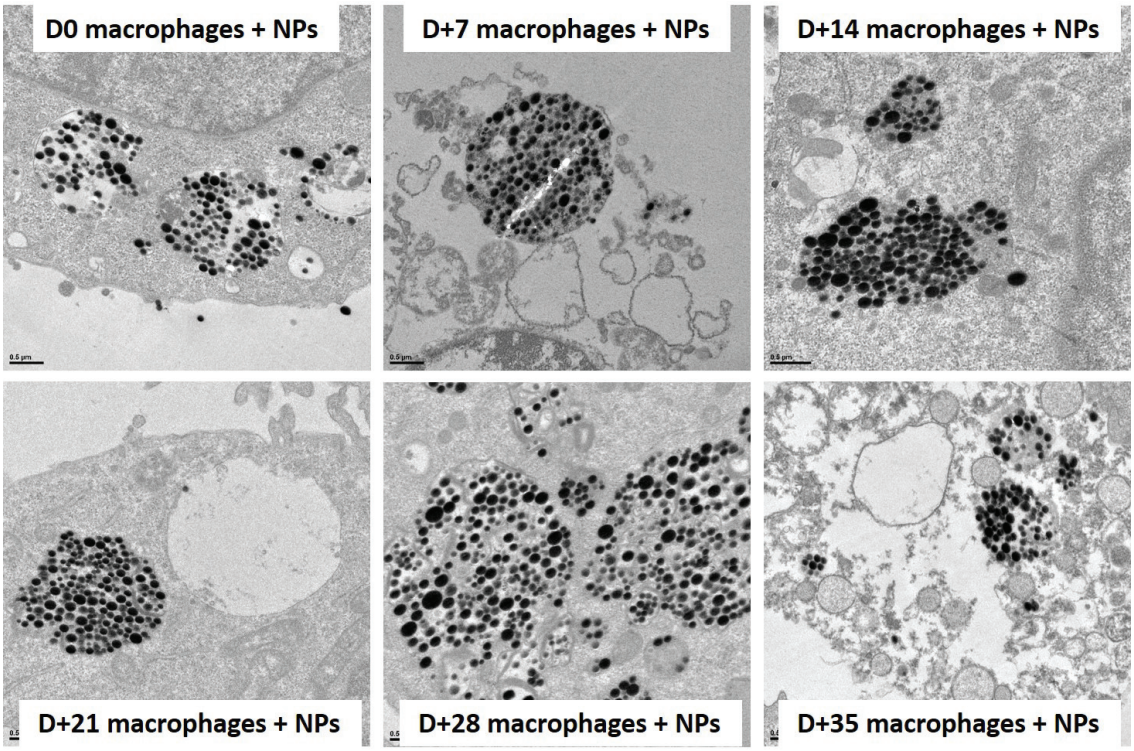

Figure 4.6: Iodinated polymer nanoparticles internalization by J774A.1 macrophages over time

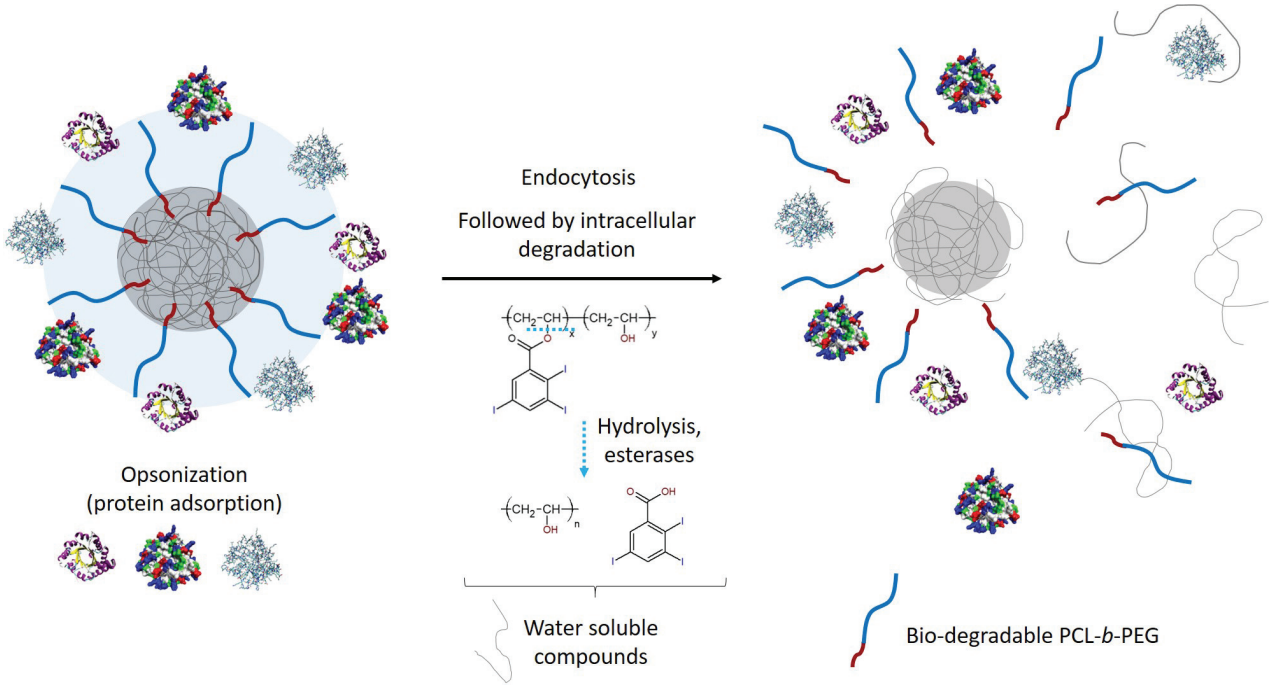

Figure 4.7: Representation of hypothetical opsonization and degradation of iodinated polymer NPs inspired by Feliu *et al.* [171]. The iodinated polymer nanoparticles within an *in vivo* environment comprises a matrix of iodinated polymer core (grey), a PEG shell provided by the dispersing agent (PCL_{65}-*b*-PEG_{113}) (red and blue), and at some point adsorbed proteins at the surface. Intracellular degradation may decompose the NPs into individual parts.

However, NPs seem to resist enzymatic degradation based on the TEM images. It may be hypothesized that the presence of PCL_{65}-*b*-PEG_{113} layer at the surface of NPs impedes hydrolysis of the iodinated polymer core; therefore the NPs remains intact and cannot be degraded by macrophages. The polymers may be biodegradable as they are taken separately, whereas they are quite stable when formulated as NPs. Since they are not eliminated by renal filtration nor degraded by enzymes, they are stored in the organs of the MPS. But for how long ?

According to Owens *et al.*, non-biodegradable PNPs cannot be degraded in the phagocytes. Depending on their size and mass, they will be removed either by the renal system (threshold 5000-100,000 Da) or sequestered and stored in organs from the MPS (here liver and spleen) [154].

Another hypothesis can be a lack of degradation of the TIB-PVAL. It can be interesting to create a hydrosoluble iodinated polymer with the same ester bound to see if the latter is hydrolyzed.

To study the degradation in more details, the qualitative results should be supplemented with quantitative data. In order to do so the iodine content should be evaluated by ICP-OES in both the supernatant and the sediment as described in the characterization section above. Unfortunately, these results cannot be presented here as there are still under investigation.

4.4 Conclusion

Depending on the nanoparticles physicochemical characteristics (i.e. size, morphology, rigidity, surface properties etc.), different elimination routes can be considered: renal filtration, uptake by macrophages (essentially from the MPS) via different mechanisms (i.e. phagocytosis, pinocytosis, calvolin- or cathrin-dependent and caveolin- and cathrin-independent).

The compounds studied here are spherical NPs, in the 150-200 nm range that present a core/shell structure. The core is made of an iodinated polymer matrix and there is PEGylated shell. A typical biodistribution of these types of agents when intravenously injected, is circulation in the bloodstream for prolonged time (hours), before accumulation in the hepatic and splenic tissues. This reflects the typical behavior of uptake by macrophages from the liver (Kupffer cells) and spleen (red pulp cells).

It was seen with the TEM images that, once the NPs are in the phagosomes/endosomes, there are not clearly degraded as it could be expected. However, these results should be supplemented with quantitative data (ICP-OES), but also extra qualitative information. In fact, it would be interesting to make Scanning Electron Microscopy (SEM) observations to track possible surface degradation over time. In such case, the intracellular degradation kinetics could be considered extremely long but not absent. In order to trigger and/or accelerate the degradation process, this study can be performed on activated macrophages cell culture.

On the other hand, since lysosomes are an acidic environment, it can also be interesting to assess stability of the NPs *in viro* at pH 4. The iodinated polymer nanoparticles might be degraded through a hydrolytic mechanism facilitated by low pH.

Another *in vitro* study that can be done is NPs enzymatic degradation. In fact, since physicochemical properties of the NPs can vary once in highly complex biological environment, it can be interesting to monitor NPs stability (size and morphology evolution over time by DLS and TEM) in a biological medium.

Finally, the ideal and ultimate degradation evaluation would be to follow the processing of NPs within an *in vivo* system until complete elimination.

Chapter 5

Atherosclerosis-targeting iodinated polymer nanoparticles

Contents

5.1 Introduction 109

5.1.1 Atherosclerosis 109

5.1.2 Imaging technology 112

5.1.3 Molecular imaging 113

5.1.4 Aim of the study 114

5.2 Experimental section 114

5.2.1 Materials 114

5.2.2 Methods 116

5.3 Results and discussion 119

5.3.1 Synthesis of SA-PEG1000-MAL-TESMA 119

5.3.2 Tropoelastin targeting iodinated polymer NPs 121

5.4 Conclusion 124

Preamble

As mentioned on the SPCCT project website (http://www.spcct.eu):

"Atherosclerosis and its consequences remain the main cause of mortality in industrialized and developing nations. Despite major advances in treatment, a large number of victims die or are disabled either because the first manifestation is sudden death or an acute cardiovascular event, or because of lack of treatment efficacy, that can be partly caused by the inadequacy of the treatment and diagnosis.

In order to reduce the risk of an acute event, unstable atherosclerosis has to be detected at an early stage of its development. However, the imaging tools that are currently available to detect the spread of atherosclerosis and to predict the associated risk are mainly based on morphological plaque and arterial wall criteria such as calcium scoring or Intima-Media Thickness (IMT). However morphological features only represent the changes in the arterial wall, while it is inflammation that causes plaque evolution. So, obtaining direct, whole body information on plaque inflammation, including coronary arteries, using target-specific contrast agents would strongly improve the prediction of acute cardiovascular events and thus lead to a better stratification of patients' risk as well as a better fine-tuning of (preventive) treatment."

Developments in imaging technologies have made it possible to deliver a diagnosis at the cellular and molecular level. Most techniques need to be combined with contrast agents able to target certain molecules/cells, in order to provide the most accurate diagnoses possible. In this study, tropoelastin which is an elastin precursor (two molecules highly expressed during inflammation), was chosen as the molecular target. Thus tropoelastin-targeting iodinated polymer nanoparticles were produced.

This chapter starts with a general introduction where the building of atherosclerotic plaque is described as well as the process leading to the plaque rupture and its consequences. The different imaging techniques used to assess atherosclerosis so far are also presented and the choice of the targeted molecule is discussed. Optimal characteristics when designing active targeting NPs are stated.

In the experimental section, the development of the tropoelastin targeting iodinated polymer nanoparticles is presented. The physicochemical characteristics (size, zeta potential (DLS)) of these NPs are given. The (SPR) based technique that allowed monitoring of the NPs/tropoelastin binding described.

5.1 Introduction

5.1.1 Atherosclerosis

Atherosclerosis is a vascular disease triggered by the build-up of an atherosclerotic plaque inside of an artery. In order to determine the interest of a precise and anticipated diagnosis of this disease, it seems important to go back to the various stages of its formation and the consequences engendered.

5.1.1.1 From plaque build-up to clot formation

Arteries are a system of tubes that transport clean, oxygen-filled blood around the body. They are made of three layers: from the innermost to the outermost layer there is the intima (that contains the endothelium which is in direct contact with blood and insures toned and smooth flow), the media and the adventitia. Atheroma plaque formation begins with endothelium damage that can be caused by several factors (i.e. obesity, diabetes, hypertension, smocking, low-density lipoprotein (LDL also referred to as "bad cholesterol" among others...). As the plaque develops, the arteries walls narrow and straight consequences are: calcium deposit (calcified arteries) and lesser and lesser oxygen-filled blood supply to different tissues forcing the heart to work harder. At some point, a blood clot may form, blocking completely the artery and the blood flow (Figure 5.1).

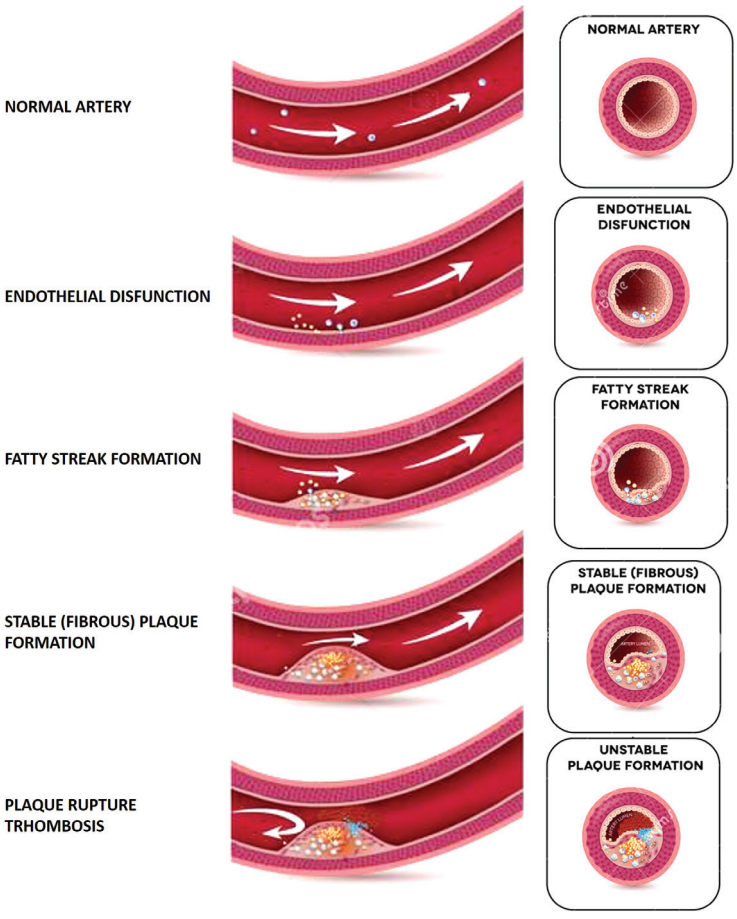

Figure 5.1: Progression of atherosclerosis

5.1.1.2 Plaque composition at different stages

The evolution of atheroma plaque happens in three main stages after the endothelial cells start malfunctioning (Figure 5.2)). First there is formation of a fatty streak, followed by formation of a stable fibrous plaque and finally formation of unstable plaque that can evolve into thrombosis.

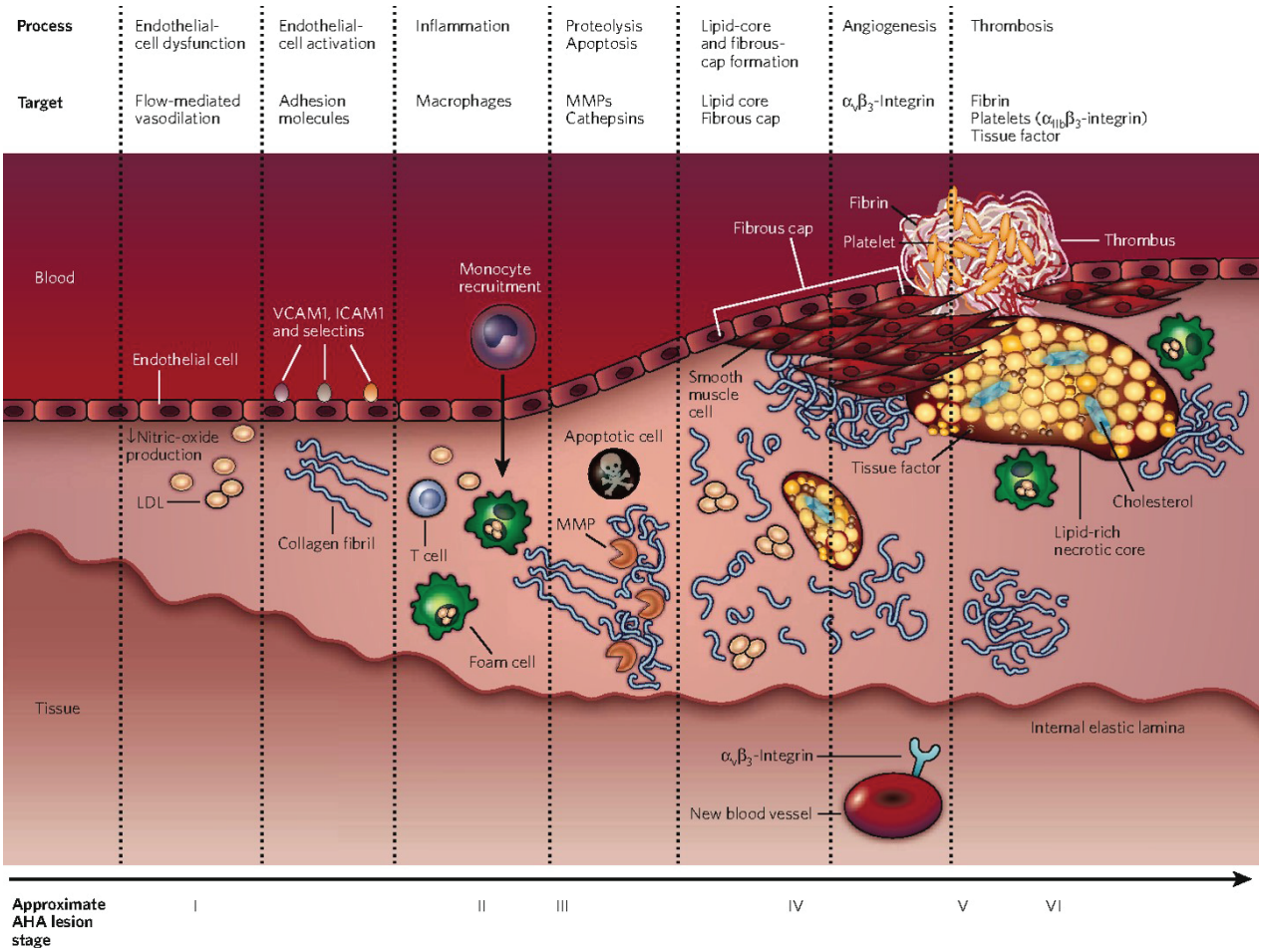

Figure 5.2: The development of an atherosclerotic lesion. The progression of an atherosclerotic lesion is shown in a simplified form, developing from a normal blood vessel (far left) to a vessel with an atherosclerotic plaque and superimposed thrombus (far right). Potential targets for molecular imaging at each stage are also listed. LDL, low-density lipoprotein; MMP, matrix metalloproteinase; VCAM1, vascular cell-adhesion molecule 1 [172].

Fatty streak formation. As the endothelium gets damaged, it enables migration of toxins such as LDL particles from blood to the intima followed by progressive accumulation of the later. Modification of those lipid particles by enzymes and oxidation triggers the innate inflammatory system. When the endothelial cells are activated, a cascade of reactions is initiated: intracellularly monocytes and other compounds are secreted, they transform into macrophages, then into foam cells after LDL internalization. Outside the arterial wall, other matrices are secreted (i.e. collagen, elastin etc.) by intimal smooth muscle cells. Note that the degree of lipid accumulation is critical for early-stage diagnosis of atherosclerosis [173].

Stable (fibrous) plaque formation. Inflammation continues to proceed as follow: on one hand the foam cells and other activated inflammatory cells keep on accumulating inside the artery walls. On the other hand, the extracellular matrices secreted (i.e. proteoglycans, collagen, and elastic fibers) start binding other lipids. As those lipids assemble into pools causing cell necrosis (apoptotic cells), the intima ends up disrupting, releasing the lipid-rich necrotic pools in the central part of the intima, ultimately occupying 30% to 50% of arterial wall volume. Subsequently, a fibrous cap forms over this necrotic lipid-rich core [173].

Unstable plaque formation: plaque rupture (thrombosis). At this stage the fibrous cap wrapping the necrotic lipid-rich core also known as thin-cap fibroatheroma is highly unstable/vulnerable. Kolodgie *et al.* defined "vulnerable plaque" as a lesion with a fibrous cap $<$ 65 μm thick and infiltrated by macrophages ($>$ 25 cells per 0.3 mm diameter field) [174]. Due to some enzyme activities, the fibrous cap can become thinner and weaker, ending up breaking and producing a thrombus which will eventually clog the arterial lumen.

5.1.1.3 Plaque related diseases

The main consequence of atherosclerosis is plaque formation that reduces blood flow, resulting in less blood and oxygen in the organs/tissues powered by the arteries. In function of the plaque location and its progression, several symptoms may be experienced before formation and rupture of a blood clot leading to acute vascular events (Figure 5.3):

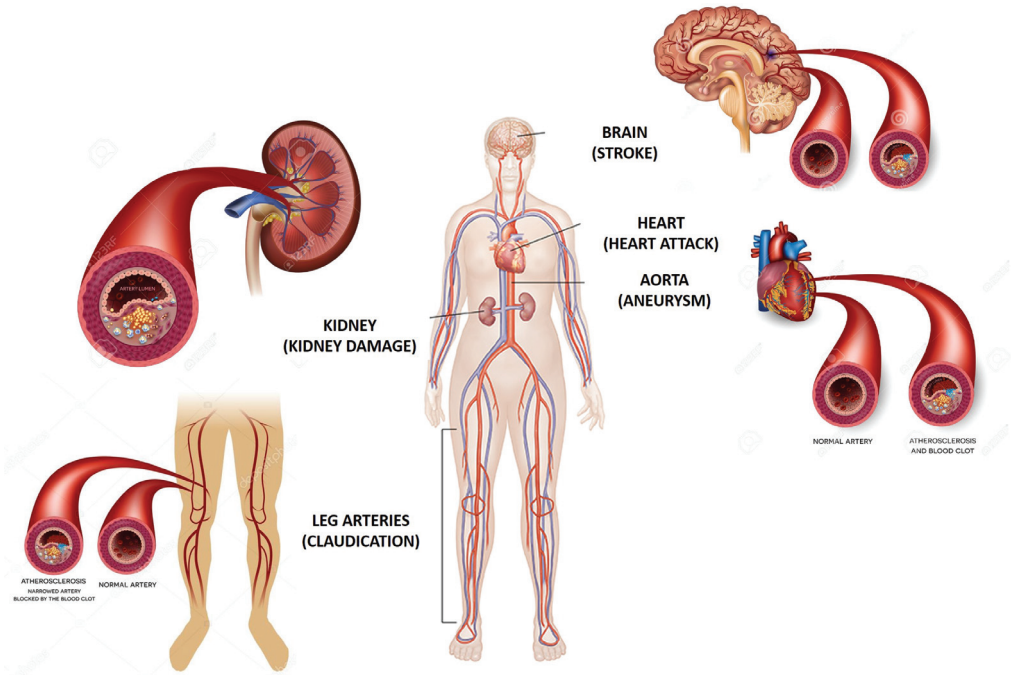

Figure 5.3: Acute vascular events in different sites of the body following arteries clogging [175]

- Arteries leading to the brain: sudden numbness or weakness in the arms or legs, difficulty speaking or slurred speech, temporary loss of vision in one eye, or drooping muscles in the face. These signal a transient ischemic attack (TIA), which, if left untreated, may progress to a stroke.

- Heart arteries: chest pain or/and pressure (angina pectoris) that can lead to myocardial infarction (MI) commonly referred to as heart attack.
- Kidneys arteries: high blood pressure or kidney failure.
- Arms and legs arteries: leg pain when walking (claudication) that may lead to peripheral artery disease.

5.1.2 Imaging technology

Fortunately, albeit atherosclerosis is a progressive disease, it can be treated to significantly alter arterial lesions and reduce their clinical consequences, provided the treatment occurs at an appropriate stage [173]. In order to do so, there is a need to develop accurate diagnosis tools to observe the evolution of this plaque (i.e. fibrous cap thickness, the size of the lipid core etc.), to avoid the above mentioned vascular diseases that can have a dramatic issue.

5.1.2.1 Invasive techniques

Several invasive (catheter-based) techniques have been used to evaluate the morphology of the plaque and other features of the vessel wall but generally at an advanced stage (high risk vulnerable plaque). These techniques include intravascular ultrasound, intravascular MRI and optical coherence tomography that are able to provide information on the fibrous cap covering the lipid pool. Angioscopy (direct visualization of the inner surface of the vessel wall by using optical-fiber technology, i.e. color change), intracoronary thermography (based on temperature heterogeneity in plaque inflammation), near-infrared spectroscopy ("Raman shift" of cholesterol core). These techniques allow physicians to learn more about the lipid-rich core [176].

5.1.2.2 Non-invasive techniques

Ultrasound, single-photon-emission CT (SPECT), positron-emission tomography (PET) and, more recently, magnetic resonance imaging (MRI) have been used to assess cardiac function, perfusion and contractility. In many studies, MRI stands-out as the best technique to assess non-invasively in a single session, multiple cardiac parameters (i.e. ischemic regions, stenosis, superimposed thrombus, intra-plaque hemorrhage etc.) [177], and provide insight into the composition (i.e. lipids, fibro-cellular tissue, calcium), of different types of atherosclerotic lesion [178] [179]. However, it also presents few drawbacks notably in the temporal and spatial resolutions. Therefore, MRI is mainly used to study extra-cardiac vessels.

5.1.2.3 Spectral Photon-Counting CT (SPCCT)

CT which is a non-invasive imaging technique that is often used to study vascular regions, calcium deposits etc. It rivals with invasive techniques such as catheterization on detecting artery narrowing. As seen in Chapter 1, one added value of the SPCCT technology is that it allows differentiation and classification of different tissue types (i.e. bones, calcified plaques) and contrast agents.

Moreover, the small size of normal vessel walls ($<$ 1 mm for most arteries) presents a huge challenge for imaging. With an improvement in spatial and temporal resolutions, SPCCT has found to be an interesting candidate to overcome this issue, as well as to compensate the fast motion of the cardiovascular system.

Furthermore, many of the targets of interest are located in deep organs and are present at very low (nanomolar) concentrations; imaging modalities therefore need to be highly sensitive. One drawback of the CT technology in assessing atherosclerosis is sensitivity related, the photon counting detector technology is foreseen as a solution to this problem.

5.1.3 Molecular imaging

It is important to mention that diagnosis of atherosclerosis has been possible for many years now, but only at advanced stages of the disease, either by directly revealing the narrowing of the arterial lumen (stenosis) or by evaluating the effect of arterial stenosis on organ perfusion [172]. With the improvement of imaging technologies, on top of assessing the morphology of blood vessels, it was made possible to monitor atherosclerosis at the cellular and molecular levels, this is known as molecular imaging. Thus, it is necessary to develop appropriate probes/vectors that present certain characteristics and select relevant molecules for active targeting molecular imaging.

5.1.3.1 Choice of the target

There are several targets possible as the atheroma plaque builds-up, evolves and ruptures:

Macrophages. Macrophages are currently one of the most appealing targets [180] [181]. This can be explained by the fact that inflammation has a crucial role at all stages of atherosclerosis (i.e. early plaque development, lipid modification, smooth muscle cell proliferation, extracellular-matrix formation, angiogenesis, plaque rupture and thrombosis (Figure 5.2))[172].

Thrombi. According to Sanz *et al.*, thrombi are another attractive target for imaging, because acute clinical events often occur as a result of thrombosis triggered by plaque rupture [172]. However, it appears at a late stage in plaque development.

Cell-adhesion molecules.VCAM1, ICAM1, endothelial selectin (E-selectin) participate in the early development of lesions by mediating the adhesion of inflammatory cells to the endothelium and facilitating the recruitment of leukocytes into the vessel wall [172]. In an animal model, increased amounts of vascular cell-adhesion molecule 1 (VCAM1) were found in aortic plaques by using a dual contrast agent detectable by both MRI and optical imaging [182]. A similar approach, which used ultrasound detection of microbubbles, found increased expression of endothelial selectins in the heart of rats that had been subjected to transient myocardial ischemia followed by reperfusion [183].

Connective remodeling molecules. Protti *et al.*assessed myocardial remodeling using elastin/tropoelastin. According to the authors, elastin deposition begins with the synthesis and secretion of the soluble precursor tropoelastin (small protein 50-70 kDa) that becomes cross-linked into insoluble elastin by enzymatic reaction immediately after their synthesis by the cell and during their export into the extracellular matrix. It should be emphasized that tropoelastin is a disease marker whereas elastin can be present in a non-diseased tissue. In fact, under normal conditions, cross-linked elastin is the only form of the molecule present in the myocardium, whereas tropoelastin is absent. Conversely, under pathological conditions elastin/tropoelastin proteins are believed to increase in the infarcted myocardium from early to late stages of the infarction [184]

Botnar's team in London (King's college (KCL)) that is part of the European consortium, studied tropoelastin as a novel marker for plaque progression and instability [185]. Considering the sensitivity of CT, the fact that tropoelastin is abundant during inflammation makes it an ideal target. Based on their work, tropoelastin was selected as the atherosclerosis target for this study.

5.1.3.2 Properties of the vectors for active targeting

There is plethora of nanovectors (i.e. nanoemulsions, liposomes, dendrimers etc.) that have been studied for active targeting using CT as the imaging technology. In this study a focus has been made on polymeric NPs. As seen above, several different types of molecules can be attached to nanoparticles to make them active targeting agents, however some physicochemical properties can impact the delivery of NPs to the site of interest.

Overall, general prerequisites concerning vascular active targeting nanoparticles seem to be a prolonged time in the bloodstream in order for the NPs to have a chance of reaching the desired site *in vivo*.

Size seems to be an important criterion too. According to Cormode *et al.*, the size of NPs has a considerable impact on the biodistribution of the particles and thus plays a prominent role in the ability to target different cells. Inflamed pathological tissues that possess highly permeable vasculature, such as tumors or atherosclerotic plaques, can be infiltrated by nanoparticles. This infiltration is more likely if the NPs are small [186]. In fact, one can imagine that too large particles may not attach to the receptor. However, there is no consensus on a specific threshold regarding this criterion.

5.1.4 Aim of the study

The objective of this study is to detect atherosclerosis at an early stage and for that it is necessary to combine effective imaging technology and agents capable of targeting the plaque at the molecular level. Many targets were considered such as: inflammation reporter (VCAM and ICAM-1), thrombi detection (Fibrin), connective remodeling (Elastin). Finally, tropoelastin which is an elastin precursor was selected in the project.

A tropoelastin-targeting polypeptide was incorporated to the iodinated polymer nanoparticles developed in Chapter 3. The physicochemical characteristics (size, zeta potential) of the targeted NPs were compared to those of the non-targeted ones using dynamic light scattering (DLS). The bioconjugation was monitored via a Biacore assay with human tropoelastin as a positive control and the dextran layer of the Biacore sensor chip as the negative control.

5.2 Experimental section

5.2.1 Materials

Chemicals. The following analytical-grade chemicals were purchased and used without further purification: Stearic acid-poly(ethylene glycol)-maleimide (SA-PEG1000-MAL, average molar mass $M_W = 1462.9$ g.mol^{-1} (1000 Da for PEG)) (Nanosoft Polymers, USA). Methanol, HPLC grade for gradient analysis and tetrahydrofuran (THF, Fisher Scientific), N-ethyldiisopropylamine (DPA, 99%), (Alfa Aesar™).

The iodinated polymer (TIB-PVAL) was synthesized at the LAGEPP in the frame of this project. Full synthesis and characterization are described Chapter 3. The block copolymer polycaprolactone-*block*-poly(ethylene glycol)(PCL_{65}-*b*-PEG_{113}) was synthesized by polymerization of caprolactone initiated by poly(ethylene glycol) monomethyl ether catalyzed by tin octanoate as reported in refs [113] [114]. Deionized water of 18 MΩ.cm resistivity was used for the preparation of suspensions.

Peptide. The sequence of tropoelastin targeting peptide (here called "TESMA") is: Resin-SLPSAEDQASPSGVVC. This peptide was synthesized by the Department of Molecular Biotechnologies and Health Sciences (UNITO, Italy) in collaboration with the Biomedical Engineering Department (King's College London, UK). The full synthesis is described in the Appendix B. Human tropoelastin was purchased from Advanced Biomatrix as a recombinant, lyophilized, powder.

5.2.1.1 Synthesis of SA-PEG1000-MAL-TESMA

SA-PEG-MAL-TESMA was synthesized using he thiol-maleimide click chemistry (Figure 5.4).

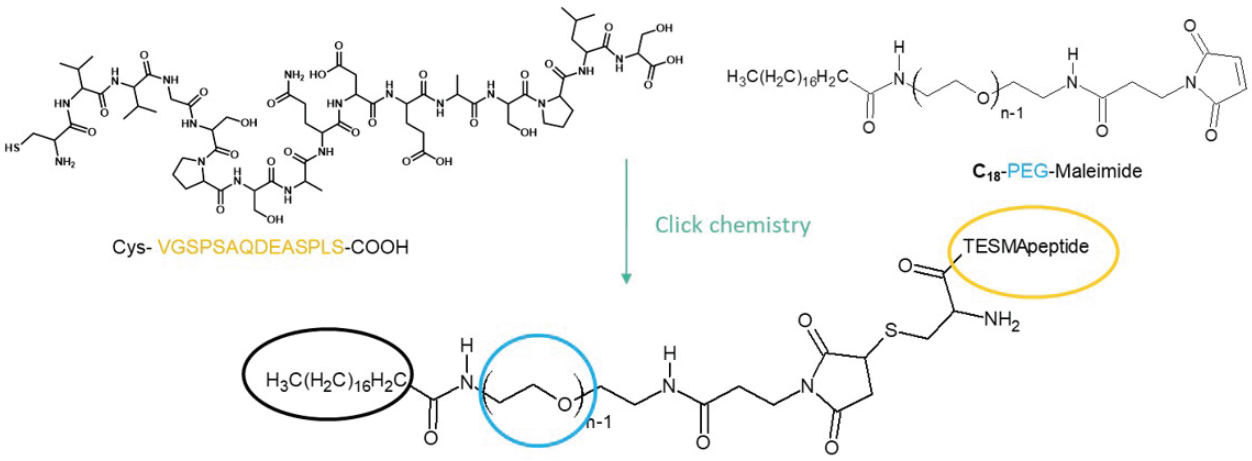

Figure 5.4: Synthesis of SA-PEG1000-MAL-TESMA by click chemistry

The thiol side chain brought by the cysteine at the N-terminus of the peptide reacted with the maleimide group of the SA-PEG1000-MAL as follows:

A solution of 20.7 mg (0.014 mmol, 1 eq.) of SA-PEG1000-MAL and 11.4 mg (0.088 mmol, 6.28 eq.) of DPA in 1 mL of methanol was added dropwise to a 2 mL solution of TESMA (22 mg, 0.014 mmol, 1 eq.) also in methanol. Note that DPA is added to avoid unwanted peptide reactions such as TESMA dimerization.

The mixture was left to stir for 20 min, at room temperature and under nitrogen atmosphere. The final solution was purified by high-performance liquid chromatography (HPLC) coupled with mass spectrometry (MS). The later was collected in an acetonitrile (ACN)/water mixture, ACN was subsequently removed under reduced pressure and the product was lyophilized. A yellow film was recovered.

In order to facilitate the subsequent handling of the product, the compound was collected in a minimum amount of methanol than dispersed in water after the organic solvent was

eliminated under reduced pressure. Finally, the reaction medium was before lyophilized and a white "cotton candy" like product was obtained (9 mg, yield = 45%).

5.2.1.2 Formulation of tropoelastin targeting iodinated polymer NPs

TESMA-conjugated NPs of iodinated polymer were prepared using the nanoprecipitation process as described in Chapter 3:

TIB-PVAL (1 g) and the PCL_{65}-*b*-PEG_{113} dispersing agent (1 g) were dissolved together in 25 mL of THF. The weight ratio iodinated polymer/dispersing agent was set to 1/1. Here SA-PEG1000-MAL-TESMA (1 mg)[1] was also included in the organic phase. The later was then added dropwise to 50 mL of water under magnetic stirring, using a syringe fitted with a needle 21G (0.8 mm internal diameter). Finally, THF was evaporated under reduced pressure, yielding aqueous suspensions of TESMA-conjugated NPs.

5.2.1.3 Concentration step

Like for the non-conjugated NPs, a concentration step has been implemented after the initial nanoprecipitation step that yielded suspensions of too low concentrations. An aliquot (10 mL) of the dispersion prepared by nanoprecipitation was centrifuged (7930 rpm, 20 min), the supernatant was removed, and the sediment was redispersed in a minimum amount of water (1 mL), using an ultrasound bath at 40°C (2 h).

5.2.2 Methods

5.2.2.1 Characterization of SA-PEG1000-MAL-TESMA

^1H NMR Analysis. Reaction of TESMA with SA-PEG1000-MAL to form SA-PEG1000-MAL-TESMA, was monitored by ^1H NMR. Spectra of the initial compounds and the product in deuterated methanol (MeOD) were recorded on Bruker ALS300 and DRX300 Fourier transform spectrometers (300 MHz). Data processing was done using MestrecNova (Mnova) software.

UPLC-MS. 1 mg of the starting materials (i.e. SA-PEG1000-MAL (M_w = 1462.9) and the TESMA peptide (M_w = 1546)) were dissolved in 1 mL of methanol (HPLC grade). The solution was then filtered through a 0.2 μm syringe filter (PVDF) and analyzed by UPLC-MS (ACQUITY UPLC H-Class PLUS (Waters), coupled with the QDa and TUV Detectors).

An Acquity UPLC BEH C_{18} peptide column (300 Å, 1.7 μm, 2.1 mm × 100 mm, 1/pKg) was used as a stationary phase.

The mobile phase was composed of %A: H_2O/TFA (trifluoroacetic acid) 0.1% and %B: ACN (Acetonitrile)/TFA 0.1%.

[1]Surface tension measurements of SA-PEG1000-MAL-TESMA compound were made in order to determine its critical micellar concentration (CMC). It was found in the 0.1-0.4 mg.mL^{-1} range. In order to ensure maximum TESMA presence at the surface of the NPs, the SA-PEG1000-MAL-TESMA amount should be between CMC and CMC/10 where adsorption is the highest.

10 μL aliquot of the TESMA peptide was eluted under the conditions stated below (Table 5.1):

Time (min)	**Flow (mL.min^{-1})**	**%A**	**%B**
0	0.4	95	5
4	0.4	70	30
6	0.4	20	80

Table 5.1: UPLC analytical method for the TESMA peptide elution

HPLC-MS. Same sample preparation as in UPLC-MS was done to analyze the product (i.e. SA-PEG1000-MAL-TESMA, M_w 3008). However due to it higher molecular weight, UPLC was no longer adapter. Therefore, a HPLC-MS (Waters AutoPurification system, 3100 Mass Detector, 600 Quaternary Pump Gradient Module, 2767 Sample Manager and 2487 UV/Visible Detector), was used.

A XTERRA®RP8 column (5 μm, 4.6 $\times$ 150 mm) was used as stationary phase for analysis.

A XTERRA®prep RP8 OBD™ column (5 μm, 19 X 100 mm) was used for purification of a larger amount of product.

SA-PEG1000-MAL and SA-PEG1000-MAL-TESMA were eluted under the following analytical method (Table 5.2):

Time (min)	**Flow (mL.min^{-1})**	**%A**	**%B**
0	1	70	30
10	1	50	50
22	1	20	80
23	1	0	100

Table 5.2: HPLC analytical method for SA-PEG1000-MAL and SA-PEG1000-MAL-TESMA elution

SA-PEG1000-MAL-TESMA was eluted using the undermentioned purification conditions (Table 5.3):

Time (min)	**Flow (mL.min^{-1})**	**%A**	**%B**
0	20	70	30
6	20	50	50
14	20	20	80
15	20	0	100

Table 5.3: HPLC preparative method for SA-PEG1000-MAL-TESMA elution

5.2.2.2 Physicochemical characterization of tropoelastin targeting NPs

Particle size and zeta potential measurements. The hydrodynamic diameter, size distribution and zeta potential of targeted and non-targeted nanoparticles dispersed in aqueous medium were determined using Dynamic Light Scattering (DLS) using a Zetasizer Nano ZS instrument from Malvern Panalytical. This technique is sensitive to particles of size in a 10-2000 nm diameter range and for diluted suspensions (ideal count rate 100-350 kHz). The results were recorded as the average of three measurements.

Two approaches can be used for size measurement: the cumulant fit provides a z-average diameter and a polydispersity index (PdI), and the inverse Laplace transform of the autocorrelation function by the CONTIN method provides the nanoparticle size distribution in scattered intensity, particle number or volume. Both calculation methods gave very close results. For the sake of comparison with other publications, the cumulant fit will be used to discuss on DLS results.

5.2.2.3 Bioconjugation assessment

Surface Plasmon Resonance (SPR) and Biacore assay. A Bioacore assay was made in order to verify tropoelastin targeting peptide presence on the NPs. A full description of the Biacore and SPR technologies is given in the Appendix C. The SPR assays were performed using a Biacore2000 biosensor. The instrument was equipped with a CM5 (GE Healthcare Life Sciences, France) sensor chip. All SPR experiments were performed at 25°C.

The first step of the Biacore assay is the surface preparation/immobilization on a Biacore sensor chip. The covalent immobilization of tropoelastin was carried out by amine coupling via EDC/NHS reaction between the carboxylic acids derived from the carboxymethyl dextran and the available primary amines derived from the peptides. However, this reaction takes place in continuous flow of solvent. It is therefore necessary to choose the pH of the immobilization buffer in order to produce an electrostatic interaction between the negatively charged dextran and the protein to be deposited.

After the chip activation by EDC/NHS during 7 min, tropoeleastin was injected on flow cell 2 (fc2): 200 μg.mL^{-1} in acetate buffer pH 4 at a flow rate of 5 μL.min^{-1} during 12 min for tropoelastin. The immobilization level was 6700 Response Units (R.U.). The flow cell (fc) 1 from this chip was activated by EDC/NHS during 7 min and then deactivated by ethanolamine during 7 min and used as reference surface. Subsequently, fc2 was washed with ethanolamine after immobilization in order to deactivate the unreacted carboxylic acid functions.

After the immobilization step, the non-conjugated and the TESMA-conjugated NPs were tested. The experiments gathered data from different cycles of sample injection and regeneration, for each studied analytes. One cycle consisted in the injection of the compound to be tested, at a concentration of 500 μg.mL^{-1} in running buffer (HBS-P), for 3 min. A washing step under running buffer followed sample injection.

Finally, the surface was regenerated by injecting solutions from the regeneration scouting kit to remove the analyte from the chip. This step is crucial as it allows to get back to the baseline in order to perform other analysis on the same sensor chip.

5.3 Results and discussion

5.3.1 Synthesis of SA-PEG1000-MAL-TESMA

5.3.1.1 Grafting reaction and ^{1}H NMR analysis

SA-PEG1000-MAL-TESMA was synthesized via click chemistry by the reaction of the thiol group of the tropoelastin targeting peptide (TESMA) and the maleimide group of the PEG compound as described in the experimental section. Figure 5.5 shows a stack of ^{1}H NMR spectra of SA-PEG1000-MAL, TESMA peptide and SA-PEG1000-MAL-TESMA in deuterated methanol (MeOD). The first observation is that the SA-PEG1000-MAL-TESMA spectrum is the sum of the spectra of SA-PEG1000-MAL and TESMA, but the lines corresponding to the maleimide. The signal at around 6.7 ppm corresponding to the maleimide on the SA-PEG1000-MAL initial compound can no longer be seen in the final product.

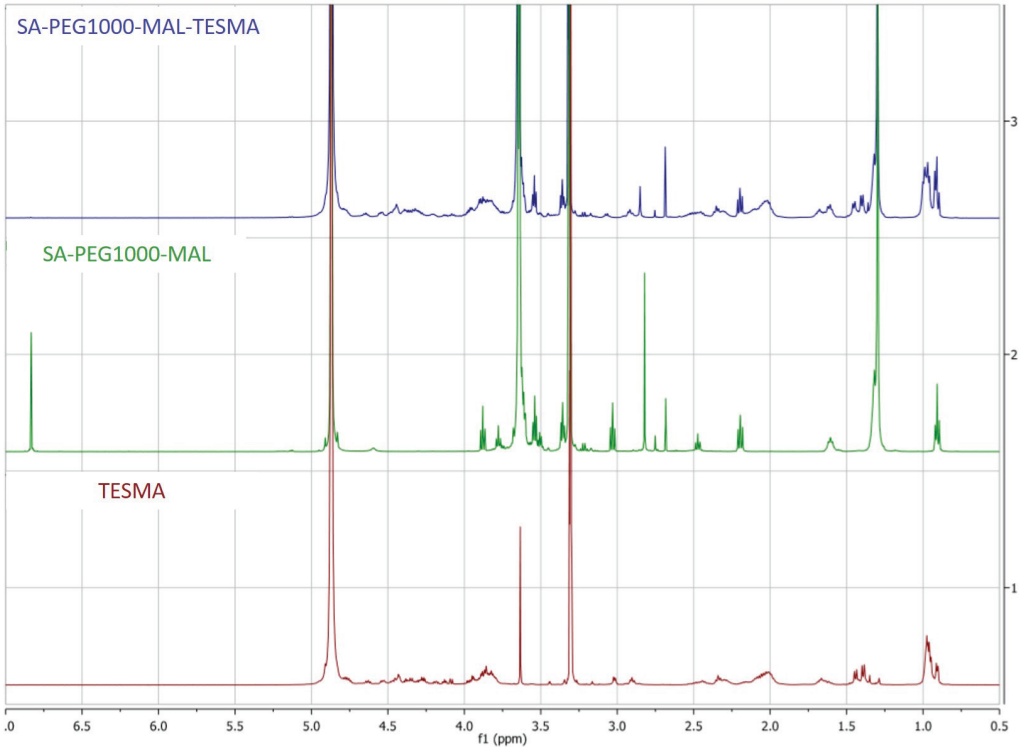

Figure 5.5: Stack of ^{1}H NMR spectra of SA-PEG1000-MAL, TESMA peptide and SA-PEG1000-MAL-TESMA in deuterated methanol (MeOD)

More accurate NMR analysis can be done to assign the spectra and confirm the structure of the ligands: Either three-dimensional (3D) NMR experiments (TOCSY, NOESY/ROESY). If the ^{1}H NMR spectrum show that the maleimide group has reacted, with the NOESY analysis for instance, it would be possible to see if the maleimide-thiol link was created.

5.3.1.2 UPLC-MS/HPLC-MS results

UPLC-MS and HPLC-MS results (Figure 5.6) show that the bioconjugated compound (i.e. SA-PEG1000-MAL-TESMA) with a retention time $t_R = 12.10$ min has better affinity towards

the mobile phase compared to the initial SA-PEG1000-MAL (t_R = 14.35 min). This is another confirmation that a more hydrophilic compound was associated. Moreover, the mass spectroscopy of the SA-PEG1000-MAL-TESMA turns out to fit the sum of the average molar masses of the TESMA (M_w 1546) peptide and SA-PEG1000-MAL (M_w 1462.9).

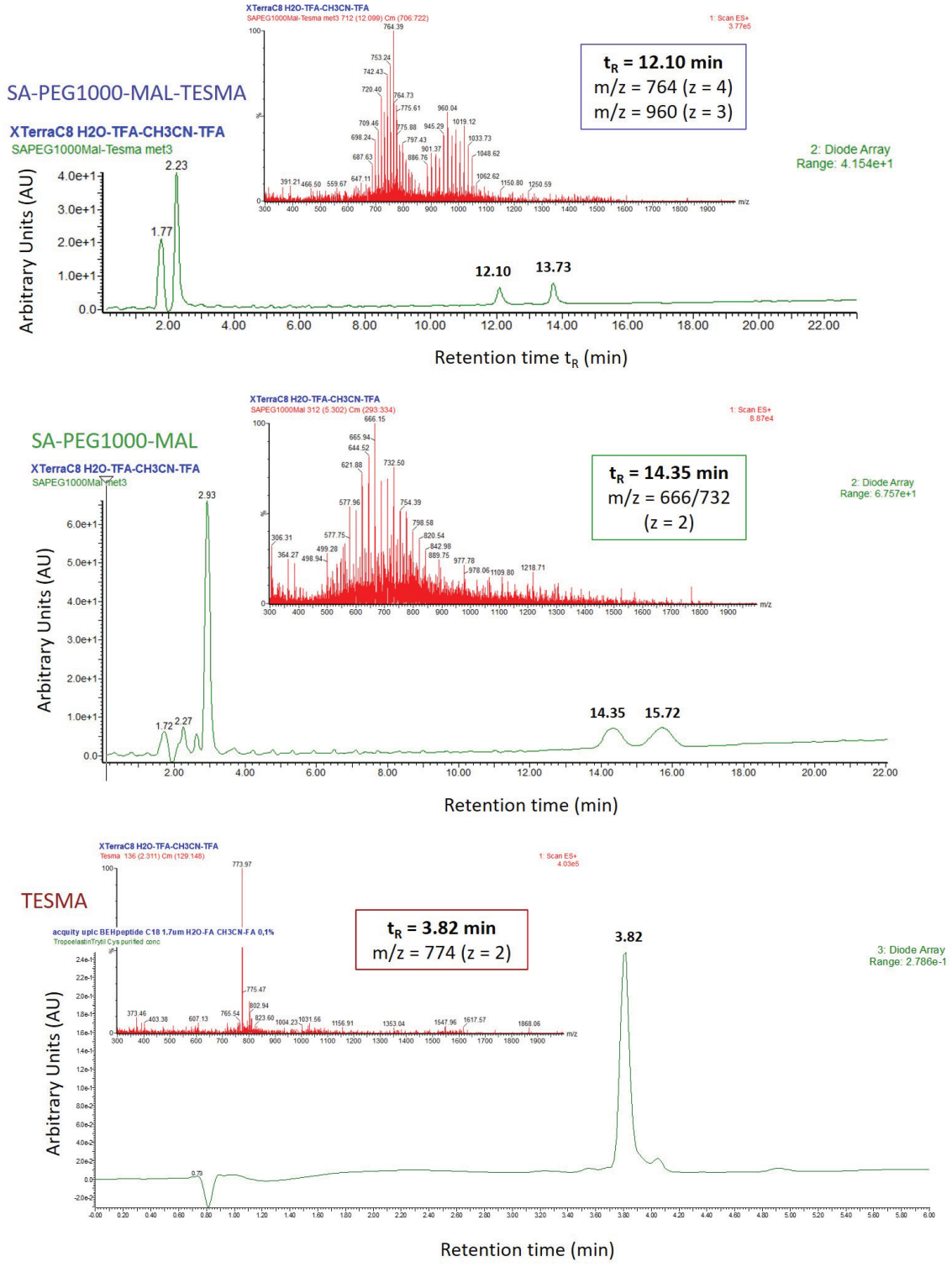

Figure 5.6: Stack of UPLC-MS and HPLC-MS spectra of TESMA peptide (bottom), SA-PEG1000-MAL (middle) and SA-PEG1000-MAL-TESMA (top)

Note that an improved analysis that can be considered is Matrix Assisted Laser Desorption Ionization - Time of Flight (MALDI-TOF).

5.3.2 Tropoelastin targeting iodinated polymer NPs

After the successful synthesis of the SA-PEG1000-MAL-TESMA compound, the tropoelastin-targeting iodinated polymer NPs could be formulated. The idea was to use the PEG-TESMA compound as a co-dispersing agent together with the block copolymer PCL_{65}-*b*-PEG_{113} and get a system that looks like the representation in Figure 5.7.

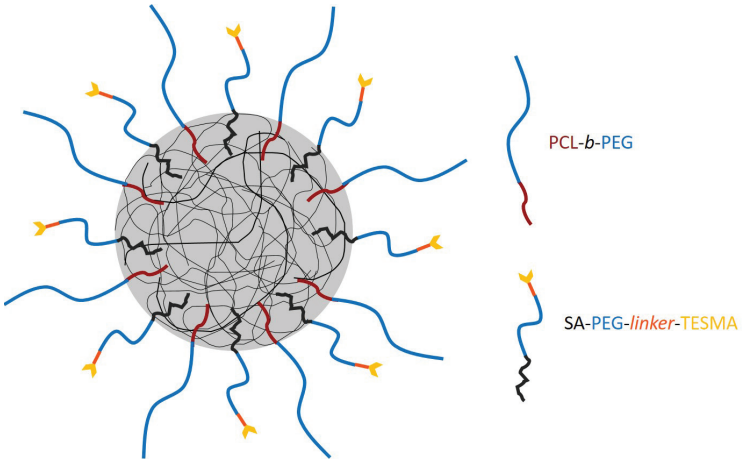

Figure 5.7: Strucure of tropoelastin targeted iodinated polymer nanoparticle

5.3.2.1 Physicochemical properties: size, morphology and ζ potential

The TEM and DLS results (Figure 5.8) show that both the TESMA-conjugated and the non-conjugated nanoparticles have the same diameter below 200 nm (DLS bottom) and a narrow size distribution (PdI < 0.1). They also have the same value of ζ-potential. The TEM images are also similar, which confirms that addition of the TESMA-conjugated compound did not change the physicochemical properties of the nanoparticles.

5.3.2.2 Bioconjugation assessment

The immobilization signal obtained confirm that the tropoelastin (6700 RU) has been successfully grafted onto the Biacore chip. Nanoparticles (NPs) conjugated with the TESMA peptide and non-conjugated NPs were tested at a concentration of 500 μg.mL^{-1} on the flow cell containg tropoelastin (fc2) and on the blank flow cell (fc1). The baseline measured before injection was subtracted to that of the flow cell. The results of three measurements were the same, showing satisfactory repeatability of the experiments.

Figure 5.9 shows the sensogram obtained for the binding of the TESMA-conjugated NPs on tropoelastin. The jumps observed at t = 60s and t = 250s come from changes of the circulating liquids of different refractive indices, respectively injection of the analyte and washing with the running buffer. In the signal reduction, the first and second jumps were subtracted such that signal varies continuously, indicating the adsorption.

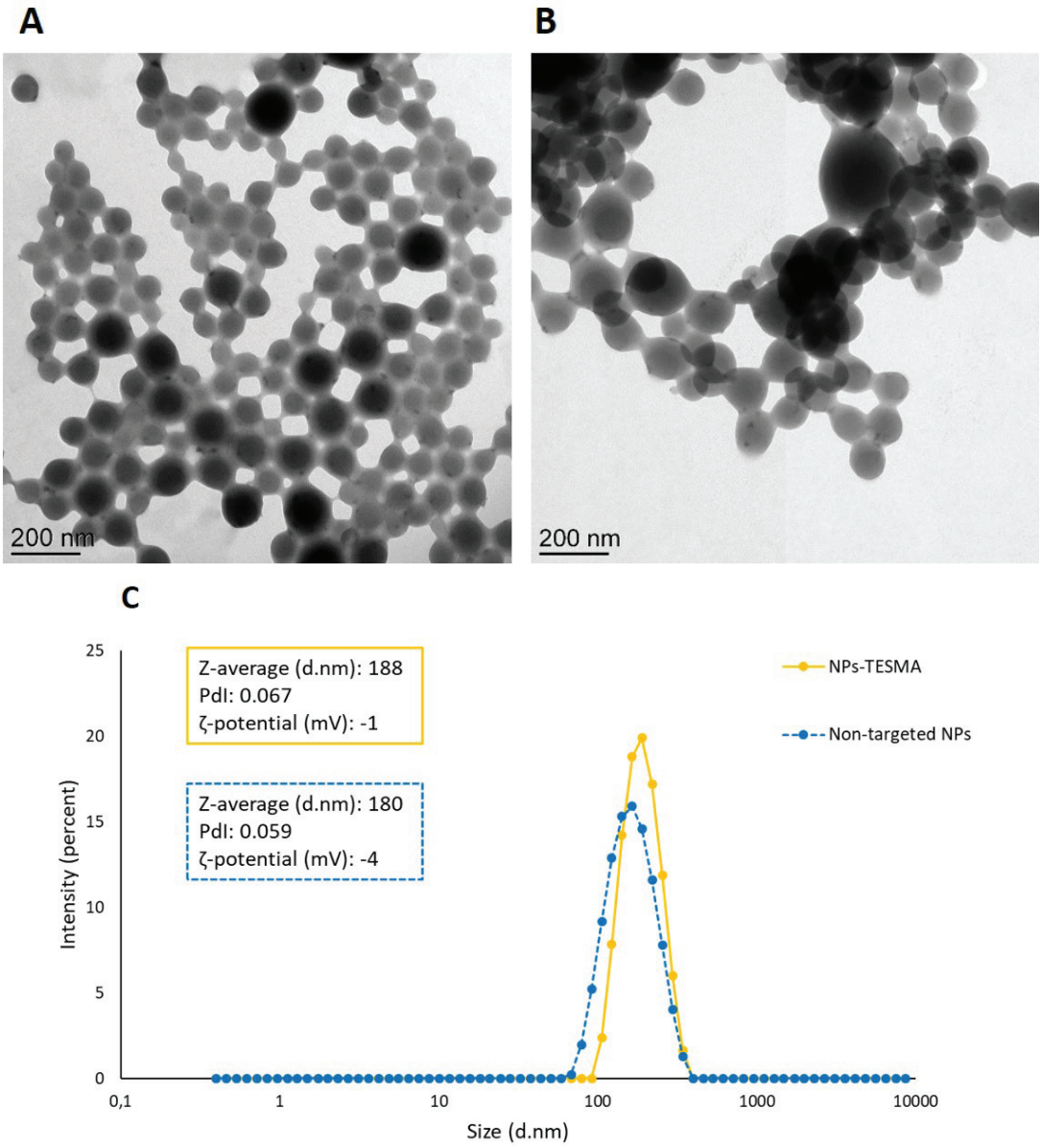

Figure 5.8: TEM images of non-conjugated iodinated polymer NPs (A), TESMA-conjugated NPs (B) and particle size distribution from CONTIN analysis of DLS

As can be seen in the sensogram after data processing (Figure 5.10), there is a continuous increase of the signal corresponding to adsorption of the NPs-TESMA on tropoelatin. Conversely, non-conjugated NPs on tropoelastin and NPs-TESMA on dextran have very low signal meaning a very weak adsorption.

Moreover, there is a very weak signal decrease upon washing which shows that irreversible binding of the TESMA-NPs occurred. This attests for specific adsorption on tropoelastin coming from the conjugation of NPs by the TESMA peptide.

The shape of the plot indicates slow adsorption kinetics that prevents reaching adsorption equilibrium within a short time. The determination of an affinity/dissociation constant would require measurements at equilibrium for different concentrations of NPs. Such measurements would be difficult because long experiments are biased by experimental drifts of the instrument.

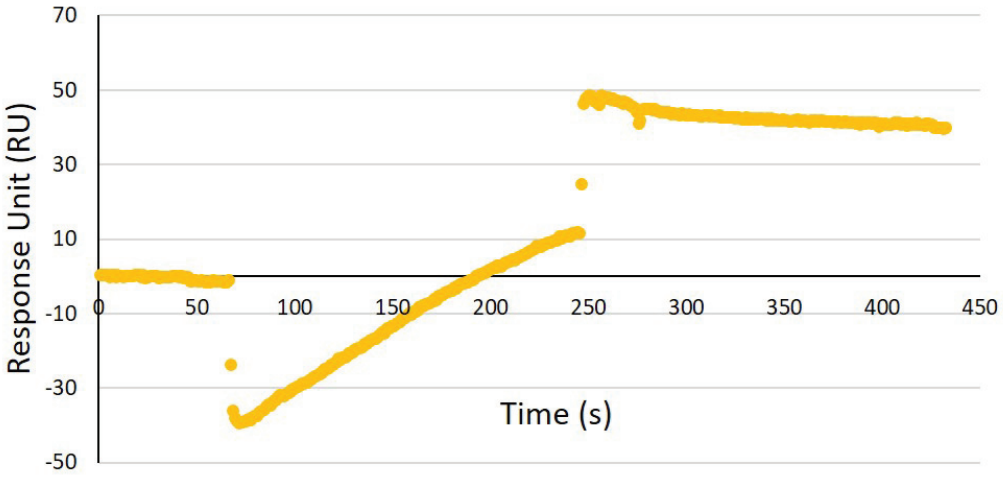

Figure 5.9: Sensogram representing RU in function of time for TESMA-conjugated NPs on tropoelastin. first jump of RU (t = 60 s) corresponds to injection of NPs, second jump of RU (t = 250 s) corresponds to the injection of the washing/running buffer

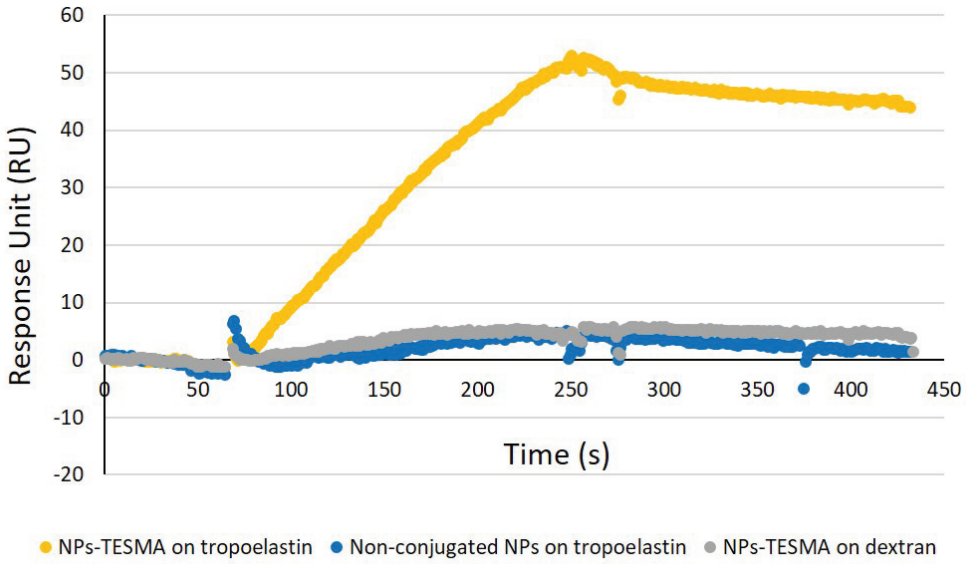

Figure 5.10: Sensogram representing the signal in RU in function of time for NPs-TESMA, non-conjugated-NPs on tropoelastin and NPs-TESMA on dextran after subtraction of the jumps.

Furthermore, regeneration of the tropoelastin surface is a matter of long and repetitive washing with regeneration buffer. However, such experiments would be interesting to compare adsorption of TESMA-conjugated NPs and TESMA alone.

5.4 Conclusion

Atherosclerosis is a progressive vascular disease that can evolve into deadly acute events (i.e. heart attack, stroke). In order to prevent those events from happening, the plaque evolution can be monitored at an early stage using molecular imaging. This diagnosis modality requires a combination of a performant imaging technique and specific active targeting agents capable of unveiling the disease at the molecular/cellular level. The spectral photon counting CT developed in the course of the project presented the ideal characteristics (specificity, sensitivity, improved spatial and temporal resolution).

Iodinated polymer NPs were conjugated with a peptide able of targeting Tropoelastin (a disease marker peptide) using the nanoprecipitation process. These nanoparticles present same physicochemical characteristics than the non-targeted NPs in terms of size (below 200 nm), zeta potential (neutral), morphology (spheres) and narrow size distribution (PdI < 0.1). Nonetheless, the peptide-conjugated NPs showed specificity towards tropoelastin ex vivo on a Biacore test, compared to the non-conjugated NPs and NPs-TESMA on dextran that showed very weak adsorption. .

Future experiments involve testing the bioconjugated and non-bioconjugated NPs *in vivo* on animal models for atherosclerosis on the SPCCT.

Chapter 6

Synthesis of tantalum oxide (Ta_2O_5) nanoparticles for SPCCT K-edge imaging

Contents

6.1 Introduction 128

6.1.1 Tantalum oxide nanoparticles in CT imaging 128

6.1.2 Manufacturing process 129

6.1.3 Aim of the study 131

6.2 Experimental section 132

6.2.1 Materials 132

6.2.2 Protocols 132

6.2.3 Characterization 133

6.3 Results and discussion 134

6.3.1 Size and morphology (TEM) 134

6.3.2 Size and particle size distribution (DLS) 135

6.3.3 Dispersibility in water 137

6.4 Conclusion 138

Preamble

The capability of SPCCT to discriminate specific attenuation profiles of several elements, better differentiate between different tissue types and contrast agents as well as its ability to quantify contrast elements *in vivo*, within a single scan open the door to interesting applications, thus allowing more accurate diagnosis while reducing radiation and contrast agent injection doses. All this is possible thanks to the photon counting detectors and also the reconstruction algorithms: i.e. material decomposition and K-edge reconstruction.

As seen in the state of the art section (Chapter 1), elements eligible for K-edge imaging must have a K-edge energy in the range 40-100 keV for a 120 kVp beam. This constraint comes from the high attenuation of X-ray photons of low energy by tissues. Good sensitivity requires that enough photons are measured at energies just lower and just higher than the K-edge energy. With a K-edge of 33.2 keV, iodine is not a suitable element for this detection tool, so that other compounds should be considered.

There are several possible candidates suitable for K-edge CT (Table 6.1). Among them are the rare earth metals (lanthanides), transition metals, "poor" metals, but also nonmetals.

However, having a K-edge in the right range is not sufficient. The elements must fulfill other important criteria, such as low toxicity, biocompatibility, availability and low cost. Based on these properties, gadolinium [187], ytterbium [188] [189] [190], bismuth [191] [192] [193], tungsten [194] [195] [196], and tantalum have been reported in the literature as candidates for consideration as CT contrast materials. Moreover, despite a high cost, gold [197] [198] has also been widely investigated in pre-clinical studies, as the manufacturing process is well known and the physicochemical properties of the nanoparticles produced (size, morphology) can be controlled.

Recently, Kim *et al.* . have assessed gadolinium, ytterbium, tungsten, bismuth, gold and tantalum based compounds as potential contrast agents for SPCCT. As an outcome, at scanning condition tested in the study (i.e. 120 kVp tube voltage), gadolinium, ytterbium and tantalum provided higher attenuation signal and better element-specific image contrast-to-noise ratio. The authors also claimed that at a higher tube voltage (i.e. 140 kVp), elements with higher atomic number and K-edge energy (i.e. gold, bismuth) should provide better results [102]. Note that these results establish a proof of concept valid for a prototype scanner and that evolution of imaging technology may change the requirements in terms of contrast agents' characteristics; however, the overall trend should remain the same.

The growing concern regarding toxicity of gadolinium compounds due to their potential instability and brain retention, makes the use of this element and more generally lanthanides questionable [199]. Bismuth is also known to be intrinsically toxic and gold is extremely expensive.

A reasonable alternative is tantalum. In fact, its oxide form has been depicted as being chemically inert [200] and biocompatible. As a matter of fact, it has been widely used in medical applications in interaction with biological tissues without manifesting any toxicity. For instance, it has been administrated orally for tracheobronchial and gastrointestinal imaging. It has also been reported as a constituent of medical devices (i.e. prosthesis). And there is a growing interest in the investigation of tantalum oxide nanoparticles coated with an organic shell, for intravenous administration and particularly CT/SPCCT imaging.

Element	Symbol	Atomic number (Z)	K-edge (keV)
Lanthanides/Rare earth metals			
Cerium	Ce	58	40.41
Praseodymium	Pr	59	41.96
Neodymium	Nd	60	43.54
Promethium	Pm	61	45.152
Samarium	Sm	62	46.80
Europium	Eu	63	48.49
Gadolinium	**Gd**	**64**	**50.21**
Terbium	Tb	65	51.96
Dysprosium	Dy	66	53.76
Holmium	Ho	67	55.59
Erbium	Er	68	57.46
Thulium	Tm	69	59.37
Ytterbium	**Yb**	**70**	**61.32**
Lutelium	Lu	71	63.31

Element	Symbol	Atomic number (Z)	K-edge (keV)
Transition metals			
Hafnium	Hf	72	65.35
Tantalum	**Ta**	**73**	**67.41**
Tungsten	**W**	**74**	**69.52**
Rhenium	Re	75	71.67
Osmium	Os	76	73.87
Iridium	Ir	77	76.11
Platinum	Pt	78	78.40
Gold	**Au**	**79**	**80.73**
Mercury	Hg	80	83.11
Poor metals			
Thalium	Tl	81	83.53
Lead	Pb	82	88.01
Bismuth	**Bi**	**83**	**90.54**
Polonium	Po	84	93.11
Non-metals/Halogens			
Astatine	At	85	95.73
Iodine	**I**	**53**	**33.17**
Noble gases			
Radon	Rn	86	98.40

High cost	Low availability
Toxicicity	Radioactivity
Suitable K-edge candidates	
Gas: no stable solid compound at RT	

Table 6.1: Elements with a K-edge energy in the 40-100 keV range

In this chapter, different synthesis methods and applications of tantalum oxide nanoparticles are reported in the introduction, the sol-gel process is also introduced. Different synthetic approaches aiming at generating intravenously administrable tantalum agent are also discussed.

In the result and discussion section, the physicochemical characteristics of the developed tantalum oxide nanoparticles are given as well as several ways for improving the current formulation in order to obtain an optimal system in terms of stability, concentration of contrasting element suitable for *in vivo* studies.

6.1 Introduction

6.1.1 Tantalum oxide nanoparticles in CT imaging

Tantalum oxide nanoparticles can be used in many applications (i.e. photovoltaic, medical devices, imaging applications etc.). There are more and more studies focusing on the development of tantalum oxide nanoparticles for CT imaging.

Bonitatibus *et al.* [201] synthesized nanoparticles of tantalum oxide smaller than 10 nm functionalized by silane groups. The method used consists in controlling the hydrolysis of tantalum ethoxide in a mixture of propanol and isobutyric acid under dry nitrogen atmosphere. The nanoparticles thus synthesized were then functionalized with (2-diethylphosphatoethyl)triethoxysilane (PHS-TaO) to make them more hydrophilic and to allow their dispersion in an aqueous medium. These nanoparticles were formulated in the form of freeze-dried powders that were redispersed in water and filtered through a 20 nm membrane. The authors were able to reach a final tantalum concentration of about 1M (180-190 mg(Ta).mL^{-1}) and a viscosity of 25 mPa $\cdot$ s. After intravenous injection of 1 mL of the contrast agent to rats, the nanoparticles were eliminated from the bloodstream within seconds and accumulated in the kidneys and in the liver [201]. The presence of the nanoparticles induced pathological response in the kidneys. Although the in vitro phantom studies carried out in this paper showed that tantalum gave greater image contrast than a solution of iodine at the same element concentration, the short circulation period does not allow the use of these nanoparticles as blood pool agents.

Two years later, Bonitatibus *et al.* developed another tantalum based agent coated with a more hydrophilic zwitterionic siloxane polymer (ZMS-TaO). Two different organosilanes were used in equal amounts to ultimately generate a mixed charged siloxane polymer shell. At same concentration in tantalum, the authors claim that they were able to reduce the viscosity by a factor of 5 compared to the PHS-Ta. According to the authors, they were able to reach a concentration of 275 mg(Ta).mL^{-1} with a viscosity of 20 mPa.s. The NPs were injected in two doses (400 and 1500 mg(Ta).kg^{-1}). As an outcome, the compound was also rapidly excreted through renal filtration but did not manifest any pathological behavior neither in the kidneys nor in the liver [202].

A Korean team proposed another method of preparing tantalum oxide nanoparticles functionalized with silane derivatives using microemulsion as a reaction medium. The derivatives chosen were PEG silanes for increased hydrophilicity and furtivity *in vivo* and RITC-APTES (3-aminopropyltriethoxysilane and isocyanate rhodamine B) as a dye for fluorescence imaging. The nanoparticles were tested *in vivo* by intravenous injection to rats at an injected dose of 840 mg.kg^{-1}). They behaved like blood pool agents as the enhancement of the vascular system lasted for 3 h before accumulation in the liver and spleen. Fluorescence analysis *ex vivo* confirmed that most of the nanoparticles were stored in these two organs. The authors performed a time-course histological studies and liver toxicity test that revealed no adverse effect of the nanoparticles [203].

6.1.2 Manufacturing process

Tantalum oxide nanoparticles and in general inorganic metal nanoparticles can be obtained in different manners. Two main synthesis routes for preparing dispersed nanoparticles for CT imaging emerge from the literature, the microemulsion method and the sol-gel process.

6.1.2.1 Microemulsion method

The microemulsion method used to synthesize the PEG-RITC-APTES coated tantalum oxide nanoparticles tested above by Oh *et al.* was inspired by a synthesis of silica nanoparticles [204] [205]. The system is composed for the aqueous phase of a solution of NaOH, for the oily phase of Igepal, cyclohexane and ethanol. Tantalum ethoxide was then added. Subsequently, the functionalization agents could be added (i.e. APTES, RITC, PEG-Si). The ammonia catalyst was replaced by a weaker nucleophile (NaOH) because the reaction rate of tantalum ethoxide is much higher than that of silica and the use of a too powerful catalyst would result in uncontrolled aggregates formation . The authors showed that the size of the nanoparticles could vary from 5 to 15 nm with the amount of ethanol. The nanoparticles were functionalized by a simple sol-gel reaction between the hydroxyl groups of the tantalum complexes and the silane derivatives to be grafted [203].

One drawback of this method is the high quantity of surfactant added to stabilize the system resulting in heavy purification steps.

6.1.2.2 Sol-gel process

The other synthetic route is the sol-gel process. Albeit the latter method is usually used to make porous materials and thin films, some parameters can be adapted to obtain a compound with desired characteristics. One good point is that the process can be carried out under mild conditions. This method is also known to provide more possibilities of controlling the properties of the final materials. Bonitatibus *et al.* used this method to fabricate the nanoparticles presented above and implemented a functionalization step for facilitating the dispersion and stability of the nanoparticles.

This method was also chosen to generate the nanoparticles of tantalum oxide in this study. The process is described below.

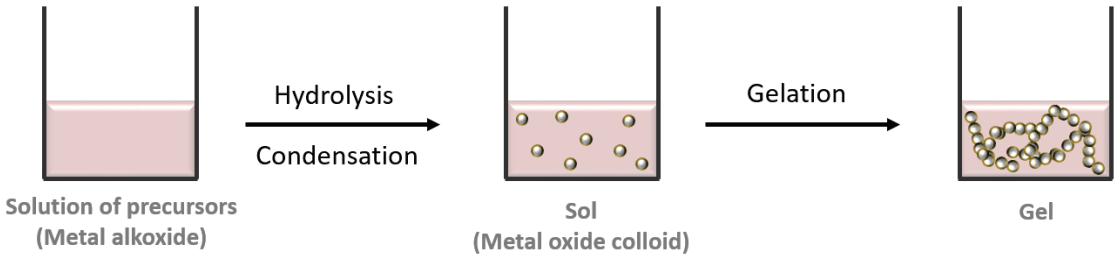

Figure 6.1: Formation of metal oxide nanoparticles with the sol-gel process

The sol-gel process is an inorganic polymerization process that involves a precursor (usually metal alkoxides) in successive reactions of hydrolysis and condensation. As a result, a solution (sol) in which the nanoparticles are dispersed in a given medium is formed. Beyond a point

called "gel point", the growing chains agglomerate by condensation and form clusters, it is the sol-gel or gelation transition. The sol evolves into a three-dimensional structure swollen with solvent (gel) which can also transform into other materials once dried under specific conditions.

Note that in the development of tantalum oxide nanoparticles for CT imaging application, the challenge is to reach a stable "sol" stage (Figure 6.1).

Hydrolysis

The hydrolysis reaction is a nucleophilic substitution reaction triggered by the addition of water. It consists in replacing the –OR groups of the precursor with –OH groups. The hydrolysis reaction is as follows:

- $M(OR)_n$ + n $H_2O \longrightarrow M(OH)_n$ + n ROH

In this study, the metal M is Ta (tantalum) and the alkoxide group -OR is OEt (ethoxide). The hydrolysis reaction becomes:

- $Ta(OEt)_5$ + 5 $H_2O \longrightarrow Ta(OH)_5$ + 5 EtOH

Condensation

The hydrolysis reaction is followed by the condensation reaction. There are two possible mechanisms that lead to the formation of a M-O-M bond also known as an "oxo" bridge between two metallic centers.

Alkoxolation is a condensation between the -OR groups and the -OH groups with the release of the alcohol:

- $M(OR)_n + M(OH)_n \longrightarrow$ M-O_n-M + n ROH
- $Ta(OEt)_5 + Ta(OH)_5 \longrightarrow Ta_2O_5$ + 5 EtOH

Oxolation is a condensation between two -OH groups followed by dehydration (i.e. elimination of water molecules):

- $M(OH)_n + M(OH)_n \longrightarrow$ M-O_n-M + n H_2O
- $Ta(OH)_5 + Ta(OH)_5 \longrightarrow Ta_2O_5$ + 5 H_2O

It should be stated that when metal coordination is not sufficient and steric hindrance is important, a third reaction called "olation" can occur. This reaction happens between two -OR groups and lead to the formation of a "hydroxo" bridge (M-OX-M).

Important parameters

In this work, the idea is to form stable colloidal suspensions of tantalum oxide nanoparticles. In order to do so hydrolysis and condensation reactions must be controlled. It is important to emphasize that these two reactions are in constant competition. There are several parameters that have to be taken into account in order to favor one or the other. Moreover, the rate of hydrolysis or condensation has an impact on the structure and the morphology of the

nanoparticles formed. This rate is governed by criteria such as catalyst pH (basic OH^- or acidic H^+), nature of the solvent and the precursor (alkoxide), the speed of addition of the alkoxide and the temperature of the reaction.

Metal alkoxide precursors

Metals are more electrophilic than silicon and thus more reactive to a nucleophilic attack. The alkoxide chain length also has an influence. The hydrolysis rate is influenced by the chain length of the alkoxide precursor. Increasing the chain length results in decreasing the hydrolysis rate.

pH influence

One of the most important parameters of this sol-gel system is pH. Indeed, the latter acts directly on the hydrolysis/condensation reactions rates as shown Figure 6.2. An acidic catalyst contains H_3O^+ cations that bind to oxygen, facilitating the substitution of the -OR groups and the hydrolysis. A basic catalyst with OH^- anions binds to the electropositive metal (M), favoring the formation of the M-O-M bonds by polycondensation.

In addition, the type of catalysis also influences the structures of the final material. Acid catalysis leads to the formation of longitudinal fibers, whereas basic catalysis generates rather spherical polymeric clusters.

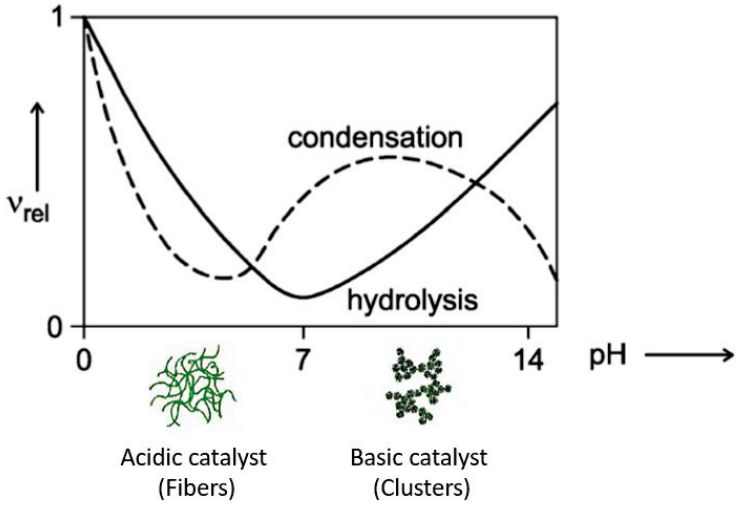

Figure 6.2: Dependence of the relative rates of $Si(OR_4$ hydrolysis and of condensation reactions on the pH [206].

6.1.3 Aim of the study

The aim of this study is to propose a simple protocol for the synthesis of tantalum oxide nanoparticles that can be administered intravenously. The ultimate interest is to have a contrast agent able to take advantage of the K-edge technology provided by the SPCCT. This contrast agent can be obtained in colloidal form or as a redispersible powder in function of the manufacturing route. Nevertheless, it must meet certain specifications in terms of stability, narrow size distribution and radiopaque element concentration in order to be tested *in vivo*.

6.2 Experimental section

Three synthetic routes that gave tantalum oxide nanoparticles of different physicochemical properties have been exploited. In some cases, a stabilizing agent was implemented to increase nanoparticles stability.

6.2.1 Materials

Chemicals. The following analytical-grade chemicals were purchased and used without further purification: Tantalum(V) ethoxide ($Ta(OEt)_5$. Sigma-Aldrich now Merck, 99.98%), absolute anhydrous ethanol (Carlo Erba). Butyric acid (Alfa Aesar, 99+%) was used as acidic catalyst, ammonia solution 25% (NH_3, VWR-BDH Prolabo) and diethylenetriamine (DETA, Fluka/Sigma-Aldrich Chemie GmbH, >97%) were used as basic catalysts. Poly(ethylene oxide) mono(trimethoxysilylpropyl)-terminated, mono-(methyl)-terminated (PEO 44) (ABCR GmbH, PEG44-Si) and poly(ethylene oxide) biphosphonate (PEG-biphosphonate of different length of PEG were synthesized in the LAGEPP laboratory: PEG21P2, PEG51P2) were used as dispersing agents to stabilize the nanoparticles. Ethylene glycol (ROTH, > 99%) was used in the neutral conditions synthesis. Deionized water of 18 MΩ.cm resistivity was used in all experiments.

6.2.2 Protocols

6.2.2.1 Acidic conditions

The following protocol is a simplified version of a protocol described in the literature [201] [207]

1 g of tantalum(V) ethoxide ($Ta(OEt)_5$, 0.64 mL 1 eq.) was added dropwise to a solution of ethanol (128 eq., 18 mL), butyric acid (1.27 eq., 290 μL) and deionized water (6.09 eq, 270 μL) while stirring under nitrogen, at room temperature (RT). Two reactions were prepared. To one mixture, a solution of 1 g of PEG44-Si in 12.5 mL of water was added to functionalize the NPs with a PEG coating. This solution was refluxed under stirring at 75°C. After cooling two phases were obtained: a white sediment and a cloudy supernatant. The supernatant was transferred to another round bottomed flask where 30 mL of water where added. Subsequently, ethanol was removed under reduce pressure, yielding Ta_2O_5 NPs in suspension in water.

A test was made without addition of PEG44-Si. Here again, a white sediment and a cloudy supernatant were obtained. Same protocol was followed afterwards.

Finally, the samples were centrifuged 10 min at 4500 rpm and characterized in terms of size (DLS, TEM when possible) and aspect (TEM).

6.2.2.2 Basic conditions

The following experiments were adapted from the Stöber reaction [208]. Here two basic catalysts were tested: a solution of ammonia 25% and diethylenetriamine.

Ammonia 25% protocol. 1 g (0.64 mL, 1 eq.) of $Ta(OEt)_5$ was added dropwise to a solution of 18 mL of ethanol (128 eq.), 340 μL of NH_3 (7.4 eq.) and 686 μL of deionized water (23 eq.) while stirring under nitrogen, at room temperature (RT). Although no precipitate was

observed, a gel formed on the walls of the flask. The solution was transferred to another round bottomed flask where 18 mL of water where added. Subsequently, ethanol was removed under reduce pressure, yielding Ta_2O_5 NPs in suspension in water. The sample was centrifuged 10 min at 4500 rpm and characterized in terms of size (DLS, TEM when possible) and aspect (TEM).

Diethylenetriamine (DETA) protocol. 1 mL (1 eq.) of $Ta(OEt)_5$ was added drop-wise to a solution of 15 mL of deionized water containing 11 μL of diethylenetriamine (0.1 mmol, 0.026 eq.) and 0.1 g of PEG21P2. This solution was refluxed under stirring at 60°C. The opaque white mixture obtained was then centrifuged under the same conditions as the previous synthesis.

To limit the very rapid hydrolysis of tantalum ethoxide and further control the size and morphology of particles obtained, water was replaced by ethanol as a solvent. The addition of a small amount of water is however necessary not only to trigger the hydrolysis reaction but also to dissolve the PEG phosphonate that is poorly soluble in organic solvents.

1 mL (1 eq.) of $Ta(OEt)_5$ was added dropwise to a solution of 15 mL of ethanol containing 11 μL of diethylenetriamine (0.1 mmol 0.026 eq.), 0.1 g PEG21P2 and 2 mL of water. This solution was refluxed under stirring at 60°C. The opaque white mixture obtained was then centrifuged under the same conditions as the previous synthesis.

6.2.2.3 Neutral conditions

In the following reaction the tantalum oxide nanoparticles were fabricated by an ethylene glycol mediated route. This experiment was inspired by a synthesis described in the literature [209]. The protocol is the following:

1 mL of tantalum ethoxide was added to 40 mL of ethylene glycol in a flask filled with nitrogen. The mixture was left to stir overnight, at room temperature (RT), under nitrogen atmosphere. A solution of 100 mL of acetone/ 0.5% water containing 0.1 g of PEG21P2 was subsequently added. The mixture was left to stir at RT until the solution became cloudy, sign of sol formation. The reaction medium was finally centrifuged and the nanoparticles were washed with acetone and dried in an oven. 53 mg of a white powder were recovered.

6.2.3 Characterization

Particle size measurements. The hydrodynamic diameter and size distribution of nanoparticles dispersed in aqueous medium were determined using Dynamic Light Scattering (DLS) using a Zetasizer Nano ZS instrument from Malvern Panalytical. This technique is sensitive to spherical particles of size in a 10-2000 nm diameter range and for diluted suspensions (ideal count rate 100-350 kHz).

Two approaches can be used: the cumulant fit provides a z-average diameter and a polydispersity index (PdI), and the inverse Laplace transform of the autocorrelation function by the CONTIN method provides the nanoparticle size distribution in scattered intensity, particle number or volume. Both calculation methods gave very close results. For the sake of comparison with other publications, the cumulant fit will be used to discuss on DLS results.

Size and morphology. Transmission Electron Microscopy (TEM) pictures were obtained with a Philips CM120 electron microscope under 80 kV accelerating voltage, at the "Centre Technologique des Microstructures (CTμ)", University of Lyon 1 Samples were prepared by deposition of a drop (10 μL) of diluted formulation on a 400-mesh carbon-coated copper grid and drying in open air.

6.3 Results and discussion

6.3.1 Size and morphology (TEM)

6.3.1.1 Acidic catalysis synthesis

As it can be seen Figure 6.3, tantalum oxide nanoparticles of size below 50 nm were fabricated. If the synthesis containing the dispersing agent gave well dispersed nanoparticles, the formulation without PEG44-Si led to more aggregated nanoparticles. This is an expected result as PEG44-Si prevents aggregation by creating a steric barrier between the particles. In both cases, the nanoparticles did not present perfectly round shape.

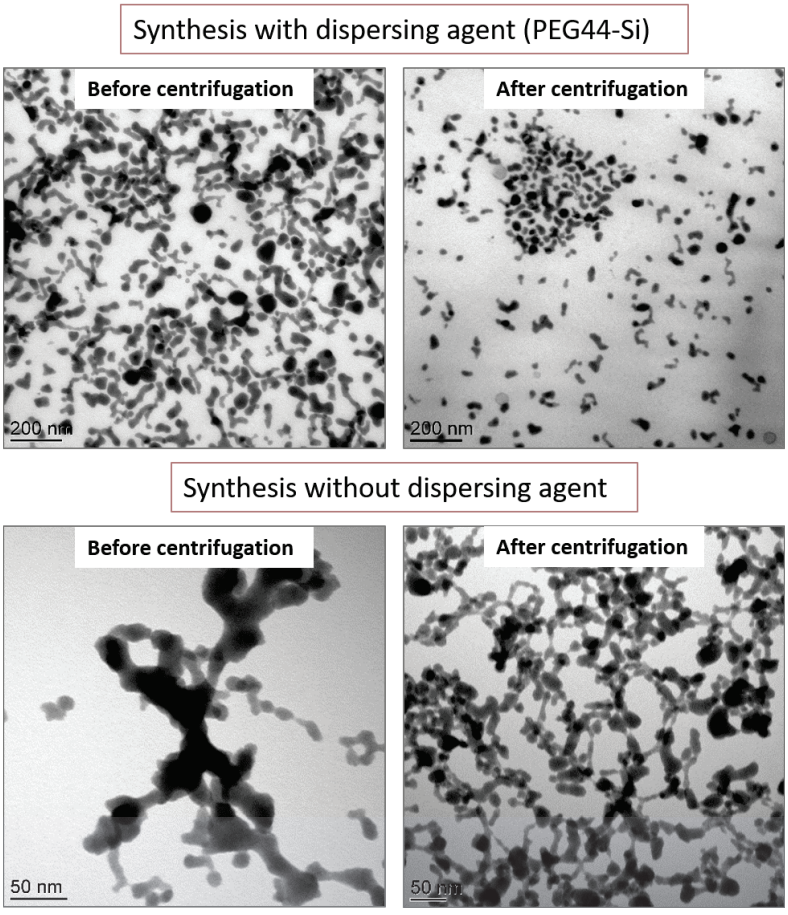

Figure 6.3: Transmission electron microscopy (TEM) pictured of tantalum oxide nanoparticles prepared under acidic conditions with (top) and without (bottom) addition of a dispersing agent (PEG44-Si)

6.3.1.2 Basic catalysis synthesis

Here also sub-50 nm tantalum oxide nanoparticles were obtained. However, their aspect and morphology are different from the ones observed under acidic conditions and vary according to the basic catalyst used. The synthesis made with ammonia solution in water yielded clusters of porous nanoparticles. The diethylenetriamine catalyzed reaction gave same results when the synthesis was carried out in water and resulted in formation of dispersed nanoparticles in the form of nanorods when the synthesis happened in ethanol. The centrifugation step was efficient to remove bigger particles that seem to be aggregates of smaller ones (Figure 6.4). Although this operation reduces significantly the synthesis yield as a large part of the tantalum oxide is removed in the sediment, it yields stable colloidal dispersions in the supernatant.

6.3.1.3 Neutral synthesis

Tantalum ethoxide is an extremely reactive precursor. In order to better control the hydrolysis step, Baruwati and Varma [209] proposed a synthesis that consists in replacing the ethoxy ligand of tantalum ethoxide with ethylene glycol ligands. This substitution makes the tantalum complex less reactive with respect to hydrolysis and slows down the reaction. With the same purpose, neither acidic nor basic catalyst was added. Furthermore, the reaction was carried out at room temperature. It is also important to highlight that the reaction was entirely performed in an anhydrous environment.

The images presented Figure 6.5 show nanoparticles of regular shape but with a broad distribution of sizes ranging from 100 to 500 nm. Such large polydispersity can be attributed to a long waiting time during the centrifugations. Indeed, as long as the nanoparticles remain in the solvent, the hydrolysis continues and the size of the nanoparticles increases. This hypothesis is supported by Baruwati and Varma studies that correlated the hydrolysis time to the size of the particles [209]. Thus it was possible to better control the nanoparticles size, by adjusting the hydrolysis time.

6.3.2 Size and particle size distribution (DLS)

Samples were centrifuged in order to collect sediments that could be redispersed. The sediment could not be redispersed using ultrasounds. The supernatant contained particles in suspension and their size was measured by DLS as described in the characterization section. The cumulant fit was chosen to report size measurements (z-average diameter nm) and size distribution (*PdI*) as presented Table 6.2.

Solvent	**Catalyst**	**Z-average (d.nm)**	***PdI***
Ethanol	butyric acid	192	0.145
Water	ammonia 25%	103	0.218
Water	DETA	175	0.153
Ethanol	DETA	385	0.198
Ethylene glycol Acetone	-	388	0.292

Table 6.2: Size of particles in the supernatant after centrifugation (10 min/4500 rpm) as measured by DLS

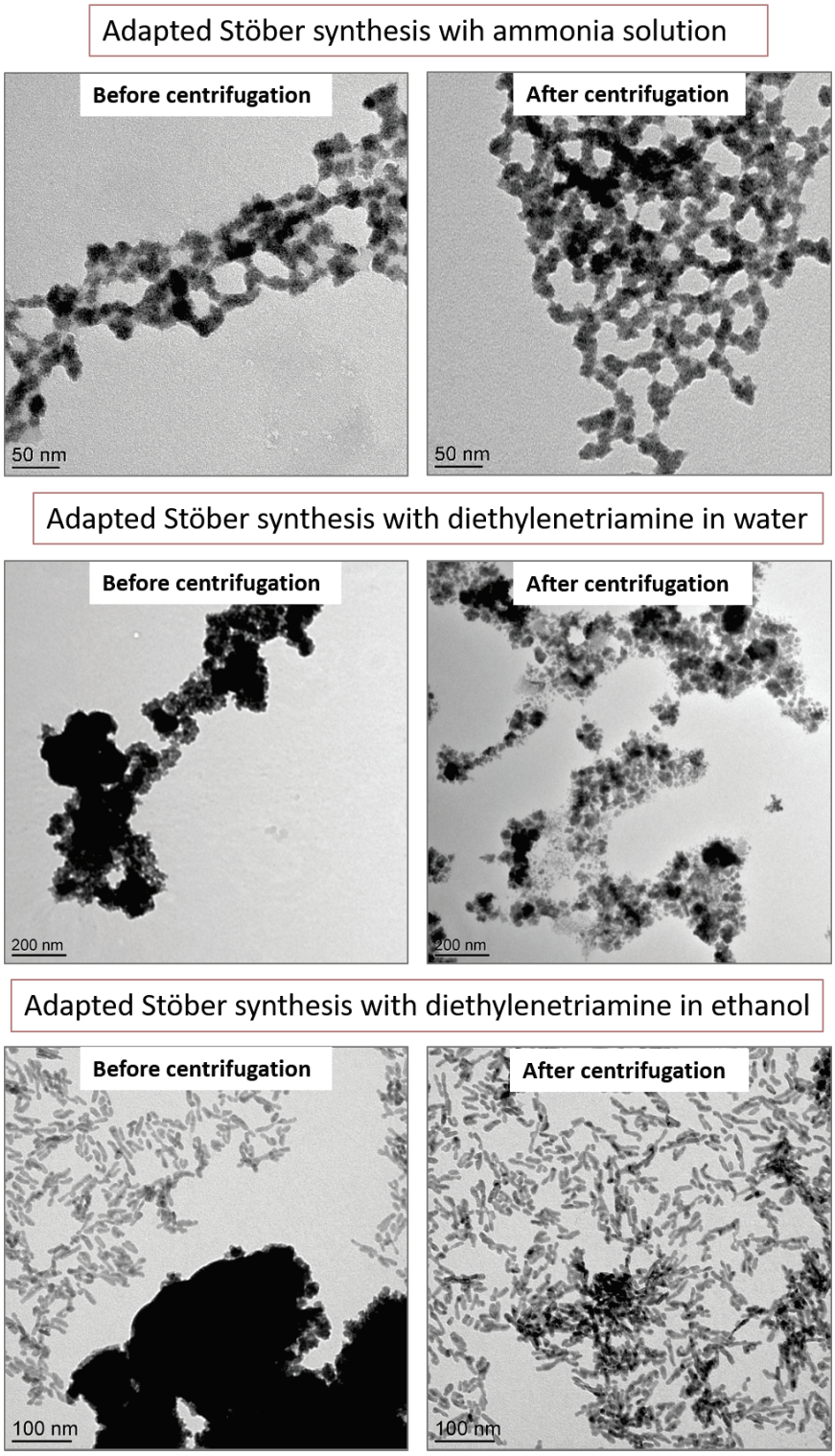

Figure 6.4: Transmission electron microscopy (TEM) pictured of tantalum oxide nanoparticles prepared under basic conditions with ammoniac solution (top), diethylenetriamine in water (middle) and diethylenetriamine in ethanol (bottom)

The sizes are larger than that of elementary particles (TEM), showing that particles are still aggregated. The smallest size of aggregates was obtained with the synthesis in basic conditions using ammonia.

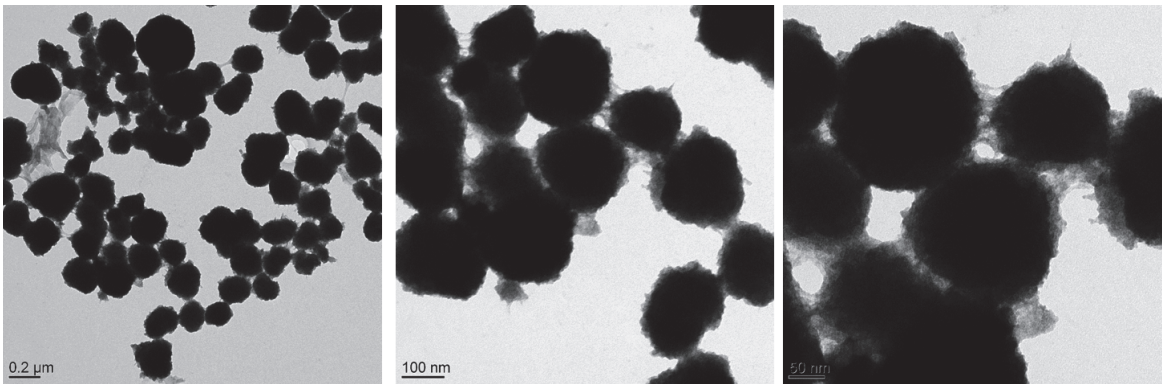

Figure 6.5: Transmission electron microscopy (TEM) pictured of tantalum oxide nanoparticles prepared in "neutral conditions" after substitution of ethoxide with ethylene glycol. The samples were prepared after centrifugation.

6.3.3 Dispersibility in water

It should be reminded that all syntheses led to the formation of a precipitate that suggested a fast formation of tantalum oxide aggregated as an irreversible network.

In the case of synthesis with no dispersing agents, it was observed that 1 h after the end of magnetic agitation, the tantalum oxide particles aggregated and formed a white powder that settled very rapidly, leaving a relatively clear supernatant poor in particles. After drying, the powder was redispersed in water at a very low concentration (i.e. 1 $mg.L^{-1}$) with an ultrasound bath for few minutes. The dispersion obtained was not stable over time as the sample had completely sedimented after 12 h.

The addition of PEG compounds (PEG44-Si or PEG21P2) at the concentration used did not prevent sedimentation. However, this phenomenon was strongly slowed as the supernatant remained relatively opaque for several hours, meaning that it was rich in particles. Redispersion after sedimentation by manual agitation also seemed easier. It can therefore be assumed that the dispersing agents were efficient at particles stabilization.

Some samples containing dispersing agents were dried and redispersed in water at specific dry compound concentrations. For instance, a concentration of 8.9 $mg.mL^{-1}$ was obtained with the synthesis in water with diethylenetriamine. This product remained stable for several days.

For the synthesis made after ethoxide substitution with ethylene glycol, the dried tantalum oxide powder was redispersed in water at 0.5/10/20$mg.mL^{-1}$. For the samples at 10 and 20 $mg.mL^{-1}$, the redispersion required the use of an ultrasound bath for a prolonged time. Sedimentation was visible after 12 h.

6.4 Conclusion

Several sol-gel conditions were tested in order to obtain stable, monodisperse, small size nanoparticles. It was seen that the pH of the medium has an influence on the morphology, homogeneity and structure of the nanoparticles. It was also observed that dispersing agents play a key role in stabilizing the nanoparticles. In fact, synthesis made without neither PEG44-Si nor PEG21P2 showed poor dispersibility in water and/or very low colloidal stability and that regardless of the experimental conditions.

All syntheses led to the formation of a precipitate that suggested a fast formation of tantalum oxide aggregated in an irreversible network. Depending on the experimental conditions, the supernatant was clear, slightly blurred or radiopaque in function of the quantity and size of nanoparticles dispersed in the sol. A centrifugation of the reaction medium was made to keep only the smallest particles. The inconvenience was that the synthesis yield was greatly reduced.

According to homogenous nucleation theory, high hydrolysis rate produces high amounts of oligomers, leading to high supersaturation and fast nucleation rates. Each nucleus grows into nanoparticles. Since the number of particles is large, their sizes are small. In acidic catalyst conditions, the hydrolysis rate is the fastest, resulting to very small elementary nanoparticles; but such nanoparticles aggregate extensively and the fragmentation of aggregation into elementary particles was not possible. Although hydrolysis under basic catalyst conditions is slower, aggregates of nanoparticles were also obtained.

Since tantalum ethoxide is extremely reactive toward moisture, controlling hydrolysis and /or condensation is a real challenge. Although both of these reactions can be slowed down by changing the pH of the synthesis medium, the temperature or by substituting the alkoxide group of the precursor by a less reactive group, the formation of a precipitate is almost inevitable at the tantalum concentrations one seeks to achieve. The dispersibility of tantalum oxide nanoparticles needs to be improved so as to achieve appropriate tantalum concentrations for *in vivo* biodistribution studies.

In order to do so, coating of the nanoparticles by an organic additive providing steric repulsion is necessary. Many parameters still need to be investigated regarding the dispersing agent coating: i.e. the length of the PEG chain, the amount of dispersing agent necessary to stabilize the NPs, the redispersion parameters, the ideal addition time (during or after the reaction).

Based on these preliminary results, the synthesis made under basic conditions (i.e. ammonia catalyst in water) gave most satisfying results. Future studies should focus on the later conditions. Nevertheless, synthesis under acidic conditions with PEG phosphonate should be checked.

General conclusion

General conclusions of the work

The general aim of the work was to develop specific contrast agents that, when combined to the SPCCT, would be able to accurately and early detect, characterize and monitor neurovascular and cardiovascular diseases. For doing so, iodinated polymer nanoparticles were produced and customized such to manage with the requirements of the application to SPCCT imaging.

First, the formulation conditions and nanoprecipitation process parameters were optimized. The THF/water volume ratio (1:2), the dispersing agent/iodinated polymer weight ratio (1:1), the phase addition rate (needle 21G, 0.8 mm internal diameter) and the stirring rate (500 rpm) were set. Many dispersing agents were tested (i.e. poloxamers, polysorbates, polymers, sorbitans, phospholipids etc.). The block copolymer PCL_{65}-*b*-PEG_{113} gave nanoparticles with the best physicochemical and biodistribution properties.

Spherical nanoparticles with an average diameter bellow 200 nm and a narrow size distribution were obtained. These nanoparticles are composed of an amorphous core that can be used for encapsulation of hydrophobic drugs. A PEGylated shell coming from the dispersing agent adsorbed in dense brush conformation provides steric stabilization up to 8 months in water and human serum and stealth properties against immune system when circulating in blood. A centrifugation/redispersion step allowed reaching concentrations of iodine (i.e. 100 $mg.mL^{-1}$) high enough for the *in vivo* investigations. Since the nanoparticles did not manifest any cytotoxicity, radiopacity and biodistribution were assessed after intravenous injection to rats. As an outcome, the cardiovascular system could be visualized for at least 5 h with progressive accumulation of iodinated nanoparticles in liver and spleen. These organs were still visible in CT images up to 15 days post-injection.

In parallel, the spectral photon counting computed tomography (SPCCT) specific properties were also tested. SPCCT material decomposition and K-edge reconstruction allowed accurate quantification of iodine, as well as specific discrimination of gadolinium and iodine in phantoms containing mixtures of both elements.

Afterward, the degradation and elimination routes of the iodinated polymer nanoparticles were investigated. Albeit the nanoparticles manage to avoid opsonization for a period of time, they are subsequently cleared from the vascular system by macrophages from the mononuclear phagocyte system (MPS). Thus they end up internalized in cells of the hepatic and splenic tissues by phagocytosis, where they remain for a long time. Transmission electron microscopy (TEM) images of macrophages incubated with nanoparticles (for 5 h), did not show any particle degradation 5 weeks after. However, some cells were degraded.

In a following part, the iodinated polymer nanoparticles were functionalized with a tropoelastin-targeting peptide. A Biacore test showed the good affinity of the conjugated nanoparticles towards tropoelastin in comparison to the non-conjugated ones and against a negative control (i.e. the dextran layer of the sensor chip).

Finally, in the last chapter, tantalum oxide nanoparticles were developed in order to provide a contrast agent suitable for the K-edge imaging. Three synthesis routes derived from the sol-gel process were explored: acidic, basic and neutral. The basic condition route gave the most promising results. Two definite issues are the aggregation of elementary particles and the redispersion after centrifugation aiming at increasing the concentration of tantalum. PEG-phosphonate dispersing agents were added in order to fix these issues.

Final discussion

Here stable iodinated polymer nanoparticles have been fabricated using a simple one step process. These nanoparticles met specifications in terms of physicochemical characteristics and concentration in radiopaque element high enough for intravenous administration. They also showed good blood pool contrast agent properties, which make them excellent candidates for angiography, interventional radiology but also permits imaging liver and spleen for long time. Their use can be extended to tissues with damaged vasculature and pathologies like cancer, aneurysm, internal bleeding and so on. In this case, iodinated polymer nanoparticles work also as passive targeting agents. It was seen that the surface of the nanoparticles could be functionalized with an atherosclerosis marker that appears at an early stage of the disease, thus iodinated polymer nanoparticles can also be used for active targeting in molecular imaging, preventing acute events from happening.

It is indisputable that nanoparticles hold a bright future as the next generation of CT contrast agents. However, there are still many pending questions that need to be addressed before reaching the clinical stage. The main one being the elimination route. For now, the belief is that size matters. Nanoparticles smaller than 5-10 nm should be able to pass the renal filters, often giving up the long persistence in the bloodstream. Above this threshold, they accumulate in the liver and spleen where the degradation kinetics can be extremely slow. Assuredly, the surface coating is also an important criterion for both organic and inorganic nanoparticles. In fact, the surface coating is responsible for the system stability, *in vivo* biodistribution and elimination. A good compromise would be a small inorganic biocompatible core (i.e. tantalum oxide nanoparticles d $<$ 5-10 nm) and a biodegradable organic shell (i.e. a PEGylated "iodinated" polymer).

Up to now, the most noticeable progress is the long circulation time in the bloodstream and the near future is targeting atherosclerotic plaque by binding tropoelastin.

Prospects

Prospects of future studies and applications are the following:

- Complete quantitative evaluation of the iodinated polymer NPs bioditribution, comparison between the SPCCT *in vivo* and *ex vivo* data and ICP-OES *ex vivo* measurements in different organs
- *In vivo* evaluation of the biodistributaion of the bioconjugated and non-bioconjugated nanoparticles in a atherosclerosis animal model
- Complete the degradation and elimination study with quantitative data
- Design a more biodegradable iodinated polymer as a block copolymer containing both an iodinated polymer moiety and a PEG moiety. The aim is to obtain smaller nanoparticles in the form of polymeric micelles.
- Optimize tantalum oxide nanoparticles redispersion in order to reach suitable concentrations for *in vivo* K-edge imaging.

Appendix A

Full TEM sample preparation for macrophages observation

This protocol was provided by Elisabeth Errazuriz-Cerda from the "Centre d'Imagerie Quantitative Lyon Est" (CIQLE) (http://ciqle.univ-lyon1.fr/).

A.1 Materials

Glutaraldehyde 2%
Glutaraldehyde 4%
Sodium Cacodylate Buffer 0.2 M pH 7.4 (Prepared from sodium cacodylate trihydrate and hydrochloric acid)
Sodium Cacodylate Buffer 0.3 M pH 7.4 (Prepared from sodium cacodylate trihydrate and hydrochloric acid)
Saccharose 0.4 M
Osmium tetroxide (OsO_4) 2%
Ethanol 30°, 50°, 70°, 95°, 100°
Epon™ A and B
DMP30 1.7%
Uranyl acetate

A.2 Method

- Step 1: Cells were fixed in glutaraldehyde 2%. The same volume of a glutaraldehyde solution (4%) was added to the samples. The mixture was left to incubate for 15 min at 4°C. The later were then recovered and centrifuged (5 min, 1200 rpm). The supernatant was removed and the sediment was redispersed with 1 mL of a mixture containing 1 volume of glutaraldehyde (2%) and 1 volume of sodium cacodylate buffer (0.2 M pH 7.4). The solutions were kept 30 min at 4°C before transmission to the microscopy center for the rest of the sample preparation.

- Step 2: The samples were washed three times in one volume of saccharose 0.4 M and sodium cacodylate buffer 0.2 M pH 7.4 for 1 h at 4°C.

- Step 3: The sample was post-fixed with 2% OsO_4 and sodium cacodylate buffer 0.3 M pH 7.4 during 30 minutes at room temperature (RT).

- Step 4: The cells were dehydrated with an increasing ethanol gradient (5 min in 30°, 50°, 70°, 95°, and 3 times for 10 min in absolute ethanol 100°).
- Step 5: Impregnation was performed with a mixture of Epon™ A(50%) plus Epon™ B (50%) plus DMP30 (1.7%).
- Step 6: Inclusion was obtained by polymerization at 60°C for 72 hrs.
- Step 7: Ultra-thin sections (approximately 70 nm thick) were cut on a ultracut UC7 (Leica) ultramicrotome, mounted on 200 mesh copper grids coated with 1: 1,000 polylysine, stabilized for 1 day at RT and, contrasted with uranyl acetate.
- Step 8: Sections were examined with a Jeol 1400JEM (Tokyo, Japan) transmission electron microscope (TEM) equipped with an Orius 600 camera and Digital Micrograph.

Figure A.1: TEM Jeol 1400JEM

Appendix B

Synthesis of tropoelastisn targeting polypeptide

This protocol was provided by Federico Capuana from the Department of Molecular Biotechnologies and Health Sciences (UNITO, Italy).

B.1 Materials

Solvents: Dichloromethane (DCM), methanol (MeOH), diethyl ether (Et_2O)

Resin: 2-chlorotrityl chloride resin (100-200 mesh), 1% DVB Novabiochem®

Coupling solution: 2 eq. of amino acid (a.a.), 2 eq. of benzotriazol-1-yl-oxytripyrrolidinophosphonium hexafluorophosphate (PyBOP), 4 eq. of N,N-diisopropylethylamine (DI-PEA), 10 mL of dimethylformamide (DMF).

End-capping solution: 0.5 mL of MeOH + 0.5 mL DIPEA + 4.0 mL DCM

Deprotection solution: 10 mL piperidine/DMF (20% of piperidine)

Cleavage solution: 4.4 mL of DCM, 4.4 mL of trifluoroacetic acid (TFA), 500 μL of phenol, 500 μL of water, 200 μL of triethylsilane (TIS)

B.2 Method

The TESMA peptide was synthesized in manual phase as follows:

- Resin (loading 1.63 mmol.g−1): 0.5 g (0.816 mmol, 1 eq.) of resin were put to swell in the reactor with 10 mL of DCM for 25 min. The organic solvent was subsequently washed out.
- Coupling of the first a.a.: 313 mg (1 eq., M_w: 383.4 mg.mmol^{-1}) of Fmoc-Ser(OtBu)-OH, were dissolved in 10 mL of DCM. The solution was introduced in the reactor with 353 μL (2.5 eq., M_w: 129.25 mg.mmol^{-1}, d: 0.747 mg.μL^{-1}) of DIPEA. The mixture was left to stirring at room temperature (RT) for 1h, then washed out before repeating the coupling reaction with the same conditions

- End-capping reaction: The end-capping solution was introduced in the reactor. The reaction mixture was left under agitation at RT for 20 min before washing out the solution the resin three times with DMF.
- Deprotection: After the three wash-outs with DMF, the loop starts again. Swelling with 10 mL of DMF (20 min), deprotection 1 (10 min), deprotection 2 (10 min), 3 wash-outs with DMF, coupling 1 (1 h), coupling 2 (2 h) and so on one a.a. after the other until the sequence is completed.
- Cleavage method: After the resin was dried (5 wash-outs with DMF, 5 with MeOH and 2 with Et_2O), the cleavage solution was added and he mixture was left under stirring at RT for 3h. The solution was collected in a flask and the volume was reduced under vacuum. Fresh TFA was added and again the mixture was left under agitation, at RT overnight. Finally the peptide was precipitated with Et_2O, yielding a white powder.

NB: at the end of the day, it is better to dry the resin (5 wash-outs with DMF, 5 with MeOH and 2 with Et_2O) and to store the reactor at 4°C.

The finale peptide sequence is Resin-SLPSAEDQASPSGVVC with the following compounds:

A Fmoc-Ala-OH
D Fmoc-Asp(OtBu)-OH
C Fmoc-Cys(Trt)-OH
Q Fmoc-Gln(Trt)-OH
E Fmoc-Glu(OtBu)-OH
G Fmoc-Gly-OH
L Fmoc-Leu-OH
P Fmoc-Pro-OH
S Fmoc-Ser(OtBu)-OH
V Fmoc-Val-OH

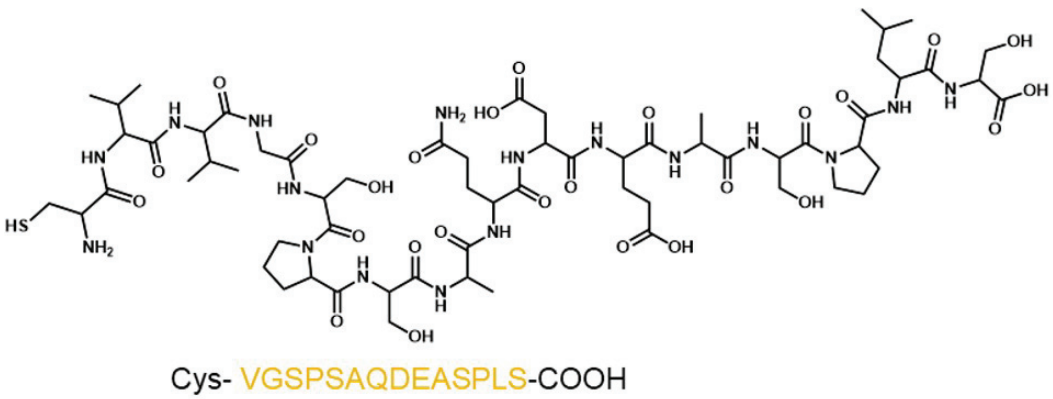

Figure B.1: Tropoelastin targeting peptide (TESMA)

Appendix C

Surface plasmon resonance (SPR) and Biacore technology

The Biacore assay is based on the SPR phenomenon and allows monitoring of biomolecular interactions (protein/receptor, antibody/virus, protein/protein etc.) without using additional markers (i.e. fluorophores, chromophores etc.). These techniques are known for their excellent sensitivity.

This study was done in collaboration with Laurence Heinrich-Balard (I2B, MATEIS) and Eyad Al Mouazen (LAGEPP).

Some images were taken from a Biacore training presentation:
(http://web.bf.uni-lj.si/bi/sprcenter/BiacoreT100/Session1%20BasicIntroduction.pdf)

C.1 Surface Plasmon Resonance (SPR)

SPR is a physical phenomenon in which the electrons of a metal surface (for example gold) oscillate collectively under the stimulation of a light radiation under conditions of total reflection.

C.1.1 Total reflection

When a polarized light radiation reaches an interface between media of two different refractive indexes n_1 and n_2, a part of the light is reflected, while the other part is refracted at an angle (θ) described by the Snell-Descartes law (Figure C.1):

In the case where the refractive index n_1 of the medium crossed by the incident ray is greater than that of the other medium, a total internal reflection phenomenon can occur. The angle at which incident radiation reaches the surface is also important. Indeed, above an angle called "critical angle for total internal reflected light", the light will be totally reflected. When this phenomenon occurs, the electric field of the photons penetrates the interface in the form of an evanescent wave over a distance approximately equal to the wavelength of the incident ray.

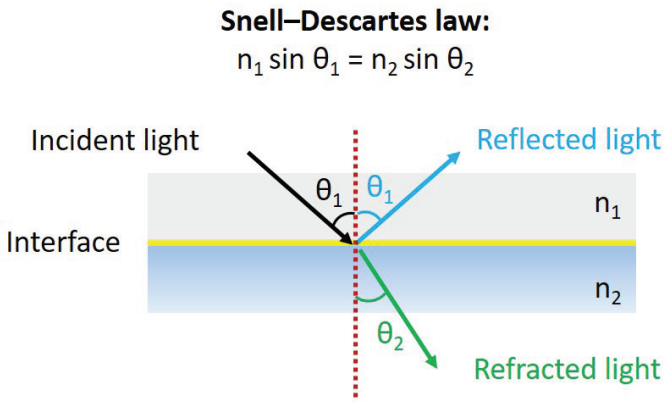

Figure C.1: Snell–Descartes law

C.1.2 Plasmon resonance

If the interface between the two media is covered with a thin metal layer (generally gold), there is a specific angle (θ_{SPR}), where the surface electrons of the latter resonate with the electric field of the photons coming from the incident ray; this is surface plasmon resonance (SPR). This phenomenon results in a drastic drop of the intensity of reflected light and is function of the refractive indexes of the two medium but also of the metallic layer.

Thus, the general principle of this technique is based on the fact that a change in the refractive index n_2 in the direct vicinity of the gold layer, coming for example from adsorption of a molecule, causes a variation of the angle at which the reflected beam intensity is minimal.

C.1.3 Response Unit (RU)

Feijter *et al.* [210] established a relationship between the amount adsorbed on the surface of the sensor chip, the refractive index increment of the adsorbed molecule (dn/dc)[1], the thickness of a layer of the adsorbed molecules (h_A) and the difference between the refractive indexes of this layer (n_A) and the background medium/ running buffer (n_B). The Feijter equation is the following:

$$\Delta n = n_A - n_B = \frac{(dn/dc) \times C_{A,S} \times M_A}{h_A} \tag{C.1}$$

where $C_{A,S}$ is the concentration of the molecule adsorbed to the surface, M_A is the molar mass of the same molecule

SPR measures the variation of the difference of refractive index (Δn) caused by the addition of a running buffer containing the analyte. Based on the Feijter equation, several manufacturers defined the Response Unit (RU) given by the software of the instruments as follows:

$$RU = \Delta n \times 10^6 \tag{C.2}$$

It is important to know that RU is proportional to the change in the reflected light angle caused by a change in the refractive index. An increase in RU attests for binding of the sample

[1]There are many assumptions claiming that $dn/dc = 0.182$ g.cm^{-3} for most proteins

to the surface of the sensor chip. This value is proportional to the concentration of adsorbed molecule in the surface layer.

C.1.4 Equilibrium dissociation constant (K_D)

The equilibrium dissociation constant is the ligand concentration required to occupy 50% of the receptors in case of a 1:1 stoichiometry of the association. This constant allows quantification of the affinity between the ligand (here the NPs) and the receptor (here tropoelastin). The lower the K_D value, the stronger the interaction. Thus, K_D in the 10^{-3} range is considered as weak interaction whereas K_D lower 10^{-3} M is seen as particularly strong interaction.

The equilibrium dissociation constant could be calculated using a 1:1 Langmuir model which is the simplest model describing the interaction between an analyte (A) and a ligand (L) forming a complex AL (A + L = AL). Note that association and dissociation occur at the same. At equilibrium association and dissociation rates are equal which results in the following equilibrium dissociation constant:

$$K_D = \frac{[A][B]}{[AL]} = \frac{k_d}{k_a} \tag{C.3}$$

with [A], [L], [AL] the concentrations of the analyte (A), the ligand (L) and the complex (AL) formed after binding and:

- k_a the association rate constant (i.e. number of complexes formed per second): d[AL]/dt = ka[A][L]
- k_d the dissociation rate constant (i.e. portion of the complex that dissociates per second): - d[AL]/dt = kd[AL]

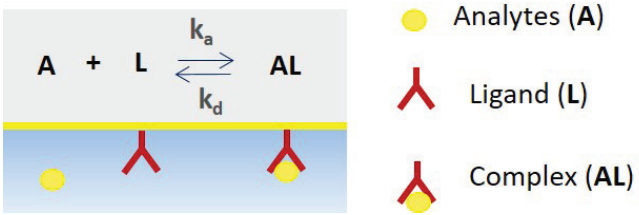

Figure C.2: Complex formation between analyte (A) and ligand (L)

These constants can be deduced by fitting the analytical expressions of the response R(t) to the R(t) curves in RU obtained by the Biacore system.

$$\frac{d[R]}{dt} = k_a C[R_{max} - R] - k_d[R] \tag{C.4}$$

where C is the concentration of analyte in the solution, R the number of RU, R_{max} the maximum number of RU that can be immobilized on the chip. At the equilibrium adsorption R_{max} = 2 × R_{eq}

C.2 Biacore

Biacore technology is designed to study the interactions between different biological targets by monitoring changes in plasmon resonance angle in real time. This device is composed of a sensor covered with a thin layer of gold.

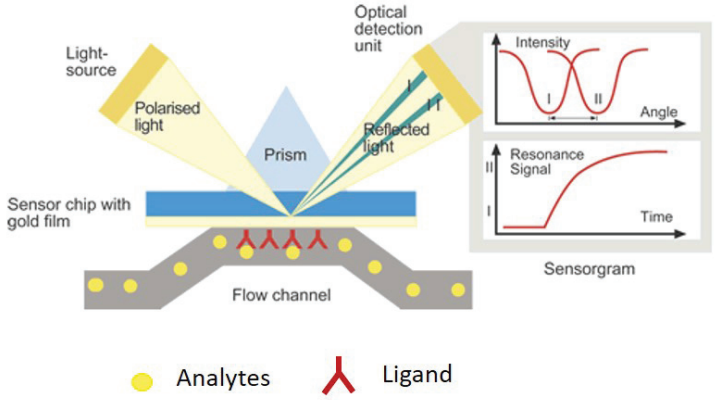

Figure C.3: Representation of the Biacore technology: interactions between the analytes and the ligands fixed on the gold chip cause variations in the plasmon resonance angle.

When the receptor and the ligand interact, the refractive index n_2 in the direct vicinity of the gold surface is modified, causing a shift in the plasmonic resonance angle. These variations are proportional to the amount of analyte adsorbed on the chip. Subsequently, the resonance signal is converted into a resonance unit (RU), providing real-time monitoring of the interactions between the analyte and the target in the form of a sensorgram (Figure C.4). Note that this technique is extremely sensitive since a variation of 1000 R.U. corresponds to a shift of the resonance angle of only 0.1°.

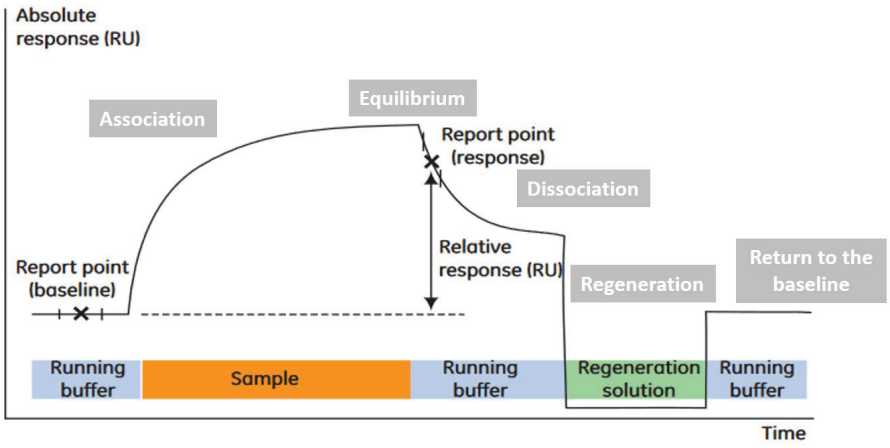

Figure C.4: Representation of sensogram

The sensorgram obtained after injection of the analyte can be divided into different stages. First, only the running buffer is introduced on the chip and the number of RUs measured corresponds to the baseline. After injection of the sample, the analyte binds gradually on

the chip leading to an increase in the signal until a plateau is obtained corresponding to the equilibrium of adsorbed molecules and molecules in solution. The surface is then rinsed by the running buffer. This step makes it possible to wash out analytes adsorbed on the chip by very weak and/or non-specific interactions; but it retains molecules having a stronger affinity for the target.

To unbind the molecules having a very strong affinity for the target, it is necessary to rinse the chip with a regeneration solution. The idea is to break the strong interactions (ex: ionic, hydrophobic ...) without damaging the immobilized receptors on the surface. Finally, the chip is rinsed by the race buffer solution and the observed signal returns back to the baseline.

In this study, Biacore assay was used to measure binding affinities between tropoelatin and TESMA-conjugated iodinated polymer NPs, but also specificity towards this molecule with a negative control (i.e. blank channel).

C.2.1 Material

All solutions were part of the GE Healthcare Life Sciences Biacore kit.

Amine coupling kit: The amine coupling reagents kit contains 0.2 M 1-ethyl3-(3-dimethylaminopropyl) carbodiimide hydrochloride (EDC) in water, 0.05 M N-hydroxy-succinimide (NHS) in water and 1.0 M ethanolamine-HCl pH 8.5.

Buffers: 10 mM sodium acetate pH 4.0 (immobilization buffer) and HBS-P buffer (0.01 M 4-(2-hydroxyethyl) piperazine-1-ethanesulfonic acid (HEPES) pH 7.4, 0.15 M NaCl, 0.005% v/v surfactant P20) was used as running buffer.

Regeneration scouting kit: Ethylene glycol (p.a.), 10 mM glycine-HCl pH 1.5, 10 mM glycine-HCl pH 2.0, 10 mM glycine-HCl pH 2.5, 10 mM glycine-HCl pH 3.0, 4.0 M magnesium chloride, 0.2 M sodium hydroxide, 0.5% sodium dodecyl sulphate (SDS), 5.0 M sodium chloride, 10% Surfactant P20.

Sensor ship: Biacore sensor chip CM5 gold chip functionalized with carboxymethylated dextran to allow the covalent grafting of the receptor of interest. The sample containing the analyte circulates directly on this surface which is an integral part of the microfluidic system.

C.2.2 Method

A Bioacore assay was made in order to verify tropoelastin targeting peptide presence on the NPs. The SPR assays were performed using a Biacore®2000 biosensor. The instrument was equipped with a CM5 (GE Healthcare Life Sciences, France) sensor chip. All SPR experiments were performed at 25°C.

The first step of the Biacore assay is the surface preparation/immobilization on a Biacore sensor chip. The covalent immobilization of tropoelastin was carried out by amine coupling via EDC/NHS reaction between the carboxylic acids derived from the carboxymethyl dextran and the available primary amines derived from the peptides. However, this reaction takes place in continuous flow of solvent. It is therefore necessary to choose the pH of the immobilization buffer in order to produce an electrostatic interaction between the negatively charged dextran and the protein to be deposited.

After the chip activation by EDC/NHS during 7 min, tropoeleastin was injected on flow cell 2 (fc2): 200 μg.mL^{-1} in acetate buffer pH 4 at a flow rate of 5 μg.min^{-1} during 12 min. The immobilization levels were 6700 Response Units (R.U.). The flow cell (fc) 1 from this chip was activated by EDC/NHS during 7 min and then deactivated by ethanolamine during 7 min and used as reference surface. Finally, fc2 was washed with ethanolamine after immobilization in order to deactivate the unreacted carboxylic acid functions.

After the immobilization step, the non-conjugated and the TESMA-conjugated NPs were tested. The experiments gathered data from different cycles of sample injection and regeneration, for each studied analytes. One cycle consisted in the injection of the compound to be tested, at a concentration of 500 μg.mL^{-1} in running buffer (HBS-P), for 3 min. A washing step under running buffer followed sample injection.

Finally, the surface was regenerated by injecting solutions from the regeneration scouting kit to remove the analyte from the chip. This step is crucial as it allows to get back to the baseline in order to perform other analysis on the same sensor chip. Here the regeneration of the tropoelastin fc2 was tricky as the conjugated NPs were strongly bound to the receptor. It took a great number of regeneration solutions and cycles to get back to the baseline. This step must be optimized before considering further experiments.

Bibliography

[1] P. Sprawls, Physical principles of medical imaging, Aspen Publishers, Rockville, Md, 1987.

[2] T. Xia, A. M. Alessio, P. E. Kinahan, Dual energy CT for attenuation correction with PET/CT, Med Phys 41 (1) (2014) 012501. doi:10.1118/1.4828838.

[3] G. Michael, X-ray Computed Tomography, Physics Education 36 (6) (2001) 442–51.
URL https://www.learntechlib.org/p/93130/

[4] J. Radon, {Ü}ber die {B}estimmung von {F}unktionen durch ihre {I}ntegralwerte längs gewisser {M}annigfaltigkeiten, Akad. Wiss. 69 (1917) 262–277.

[5] J. Radon, On the determination of functions from their integral values along certain manifolds, IEEE Transactions on Medical Imaging 5 (4) (1986) 170–176. doi:10.1109/TMI.1986.4307775.
URL http://ieeexplore.ieee.org/document/4307775/

[6] G. N. Hounsfield, Computerized transverse axial scanning (tomography). 1. Description of system, Br J Radiol 46 (552) (1973) 1016–1022. doi:10.1259/0007-1285-46-552-1016.

[7] A. Macovski, R. E. Alvarez, J. L. H. Chan, J. P. Stonestrom, L. M. Zatz, Energy dependent reconstruction in X-ray computerized tomography, Computers in Biology and Medicine 6 (4) (1976) 325–336. doi:10.1016/0010-4825(76)90069-X.
URL http://www.sciencedirect.com/science/article/pii/001048257690069X

[8] C. H. McCollough, S. Leng, L. Yu, J. G. Fletcher, Dual- and Multi-Energy CT: Principles, Technical Approaches, and Clinical Applications, Radiology 276 (3) (2015) 637–653. doi:10.1148/radiol.2015142631.
URL https://pubs.rsna.org/doi/full/10.1148/radiol.2015142631

[9] T. G. Flohr, C. H. McCollough, H. Bruder, M. Petersilka, K. Gruber, C. Sub, M. Grasruck, K. Stierstorfer, B. Krauss, R. Raupach, A. N. Primak, A. Küttner, S. Achenbach, C. Becker, A. Kopp, B. M. Ohnesorge, First performance evaluation of a dual-source CT (DSCT) system, Eur Radiol 16 (2) (2006) 256–268. doi:10.1007/s00330-005-2919-2.
URL https://doi.org/10.1007/s00330-005-2919-2

[10] W. A. Kalender, W. H. Perman, J. R. Vetter, E. Klotz, Evaluation of a prototype dual-energy computed tomographic apparatus. I. Phantom studies, Medical Physics 13 (3) (1986) 334–339. doi:10.1118/1.595958.
URL https://aapm.onlinelibrary.wiley.com/doi/abs/10.1118/1.595958

[11] D. L. Ergun, C. A. Mistretta, D. E. Brown, R. T. Bystrianyk, W. K. Sze, F. Kelcz, D. P. Naidich, Single-exposure dual-energy computed radiography: improved detection and processing., Radiology 174 (1) (1990) 243–249. doi:10.1148/radiology.174.1.2294555.
URL https://pubs.rsna.org/doi/abs/10.1148/radiology.174.1.2294555

[12] E. Roessl, R. Proksa, K-edge imaging in x-ray computed tomography using multi-bin photon counting detectors, Phys Med Biol 52 (15) (2007) 4679–4696. doi:10.1088/0031-9155/52/15/020.

[13] J. P. Schlomka, E. Roessl, R. Dorscheid, S. Dill, G. Martens, T. Istel, C. Baumer, C. Herrmann, R. Steadman, G. Zeitler, A. Livne, R. Proksa, Experimental feasibility of multi-energy photon-counting K-edge imaging in pre-clinical computed tomography, Phys Med Biol 53 (15) (2008) 4031–4047. doi:10.1088/0031-9155/53/15/002.

[14] S. Si-Mohamed, D. Bar-Ness, M. Sigovan, D. P. Cormode, P. Coulon, E. Coche, A. Vlassenbroek, G. Normand, L. Boussel, P. Douek, Review of an initial experience with an experimental spectral photon-counting computed tomography system, Nuclear Instruments and Methods in Physics Research Section A: Accelerators, Spectrometers, Detectors and Associated Equipment 873 (2017) 27–35. doi:10.1016/j.nima.2017.04.014.
URL http://www.sciencedirect.com/science/article/pii/S016890021730462X

[15] P. M. Shikhaliev, Energy-resolved computed tomography: first experimental results, Phys Med Biol 53 (20) (2008) 5595–5613. doi:10.1088/0031-9155/53/20/002.

[16] R. Gutjahr, A. F. Halaweish, Z. Yu, S. Leng, L. Yu, Z. Li, S. M. Jorgensen, E. L. Ritman, S. Kappler, C. H. McCollough, Human Imaging With Photon Counting-Based Computed Tomography at Clinical Dose Levels: Contrast-to-Noise Ratio and Cadaver Studies, Invest Radiol 51 (7) (2016) 421–429. doi:10.1097/RLI.0000000000000251.

[17] W. Zhou, J. I. Lane, M. L. Carlson, M. R. Bruesewitz, R. J. Witte, K. K. Koeller, L. J. Eckel, R. E. Carter, C. H. McCollough, S. Leng, Comparison of a Photon-Counting-Detector CT with an Energy-Integrating-Detector CT for Temporal Bone Imaging: A Cadaveric Study, American Journal of Neuroradiology 39 (9) (2018) 1733–1738. doi:10.3174/ajnr.A5768.
URL http://www.ajnr.org/content/39/9/1733

[18] D. P. Cormode, E. Roessl, A. Thran, T. Skajaa, R. E. Gordon, J.-P. Schlomka, V. Fuster, E. A. Fisher, W. J. M. Mulder, R. Proksa, Z. A. Fayad, Atherosclerotic plaque composition: analysis with multicolor CT and targeted gold nanoparticles, Radiology 256 (3) (2010) 774–782. doi:10.1148/radiol.10092473.

[19] D. Muenzel, D. Bar-Ness, E. Roessl, I. Blevis, M. Bartels, A. A. Fingerle, S. Ruschke, P. Coulon, H. Daerr, F. K. Kopp, B. Brendel, A. Thran, M. Rokni, J. Herzen, L. Boussel, F. Pfeiffer, R. Proksa, E. J. Rummeny, P. Douek, P. B. Noël, Spectral Photon-counting CT: Initial Experience with Dual-Contrast Agent K-Edge Colonography, Radiology 283 (3) (2017) 723–728. doi:10.1148/radiol.2016160890.

[20] K. Taguchi, J. S. Iwanczyk, Vision 20/20: Single photon counting x-ray detectors in medical imaging, Medical Physics 40 (10) (2013) 100901. doi:10.1118/1.4820371.
URL https://aapm.onlinelibrary.wiley.com/doi/abs/10.1118/1.4820371

[21] A. de Vries, E. Roessl, E. Kneepkens, A. Thran, B. Brendel, G. Martens, R. Proska, K. Nicolay, H. Grüll, Quantitative Spectral K-Edge Imaging in Preclinical Photon-Counting X-Ray Computed Tomography, Investigative Radiology 50 (4) (2015) 297. doi:10.1097/RLI.0000000000000126.
URL https://journals.lww.com/investigativeradiology/Abstract/2015/04000/Quantitative_Spectral_K_Edge_Imaging_in.16.aspx

[22] S. Feuerlein, E. Roessl, R. Proksa, G. Martens, O. Klass, M. Jeltsch, V. Rasche, H.-J. Brambs, M. H. K. Hoffmann, J.-P. Schlomka, Multienergy photon-counting K-edge imaging: potential for improved luminal depiction in vascular imaging, Radiology 249 (3) (2008) 1010–1016. doi:10.1148/radiol.2492080560.

[23] D. P. Cormode, E. Roessl, A. Thran, T. Skajaa, R. E. Gordon, J.-P. Schlomka, V. Fuster, E. A. Fisher, W. J. M. Mulder, R. Proksa, Z. A. Fayad, Atherosclerotic plaque composition: analysis with multicolor CT and targeted gold nanoparticles, Radiology 256 (3) (2010) 774–782. doi:10.1148/radiol.10092473.

[24] R. Zainon, J. P. Ronaldson, T. Janmale, N. J. Scott, T. M. Buckenham, A. P. H. Butler, P. H. Butler, R. M. Doesburg, S. P. Gieseg, J. A. Roake, N. G. Anderson, Spectral CT of carotid atherosclerotic plaque: comparison with histology, Eur Radiol 22 (12) (2012) 2581–2588. doi:10.1007/s00330-012-2538-7.
URL https://doi.org/10.1007/s00330-012-2538-7

[25] P. Baturin, Y. Alivov, S. Molloi, Spectral CT imaging of vulnerable plaque with two independent biomarkers, Phys. Med. Biol. 57 (13) (2012) 4117. doi:10.1088/0031-9155/57/13/4117.
URL http://stacks.iop.org/0031-9155/57/i=13/a=4117

[26] L. Boussel, P. Coulon, A. Thran, E. Roessl, G. Martens, M. Sigovan, P. Douek, Photon counting spectral CT component analysis of coronary artery atherosclerotic plaque samples, The British Journal of Radiology 87 (1040) (2014) 20130798. doi:10.1259/bjr.20130798.
URL http://www.birpublications.org/doi/10.1259/bjr.20130798

[27] P. Rajiah, S. Abbara, S. S. Halliburton, Spectral detector CT for cardiovascular applications, Diagn Interv Radiol 23 (3) (2017) 187–193. doi:10.5152/dir.2016.16255.
URL https://www.ncbi.nlm.nih.gov/pmc/articles/PMC5410998/

[28] T. Saam, T. S. Hatsukami, N. Takaya, B. Chu, H. Underhill, W. S. Kerwin, J. Cai, M. S. Ferguson, C. Yuan, The Vulnerable, or High-Risk, Atherosclerotic Plaque: Noninvasive MR Imaging for Characterization and Assessment, Radiology 244 (1) (2007) 64–77. doi:10.1148/radiol.2441051769.
URL https://pubs.rsna.org/doi/abs/10.1148/radiol.2441051769

[29] T. S. Hatsukami, C. Yuan, MRI in the early identification and classification of high-risk atherosclerotic carotid plaques, Imaging Med 2 (1) (2010) 63–75. doi:10.2217/iim.09.33.
URL https://www.ncbi.nlm.nih.gov/pmc/articles/PMC2953811/

[30] A. Asif, M. Epstein, Prevention of radiocontrast-induced nephropathy, Am. J. Kidney Dis. 44 (1) (2004) 12–24.

[31] R. W. Katzberg, Urography into the 21st century: new contrast media, renal handling, imaging characteristics, and nephrotoxicity., Radiology 204 (2) (1997) 297–312. doi:10.1148/radiology.204.2.9240511.
URL https://pubs.rsna.org/doi/10.1148/radiology.204.2.9240511

[32] S.-B. Yu, A. D. Watson, Metal-Based X-ray Contrast Media, Chem. Rev. 99 (9) (1999) 2353–2378. doi:10.1021/cr980441p.
URL https://doi.org/10.1021/cr980441p

[33] E. T. M. Dams, W. J. G. Oyen, O. C. Boerman, G. Storm, P. Laverman, P. J. M. Kok, W. C. A. M. Buijs, H. Bakker, J. W. M. v. d. Meer, F. H. M. Corstens, 99mtc-PEG Liposomes for the Scintigraphic Detection of Infection and Inflammation: Clinical Evaluation, J Nucl Med 41 (4) (2000) 622–630.

[34] F. Braet, R. De Zanger, M. Baekeland, E. Crabbé, P. Van Der Smissen, E. Wisse, Structure and dynamics of the fenestrae-associated cytoskeleton of rat liver sinusoidal endothelial cells, Hepatology 21 (1) (1995) 180–189.

[35] O. C. Boerman, G. Storm, W. J. G. Oyen, L. v. Bloois, J. W. M. v. d. Meer, R. A. M. J. Claessens, D. J. A. Crommelin, F. H. M. Corstens, Sterically Stabilized Liposomes Labeled with Indium-111 to Image Focal Infection, J Nucl Med 36 (9) (1995) 1639–1644.
URL http://jnm.snmjournals.org/content/36/9/1639

[36] F. Roerdink, J. Regts, B. Van Leeuwen, G. Scherphof, Intrahepatic uptake and processing of intravenously injected small unilamellar phospholipid vesicles in rats, Biochim. Biophys. Acta 770 (2) (1984) 195–202.

[37] S. Salmaso, P. Caliceti, Stealth Properties to Improve Therapeutic Efficacy of Drug Nanocarriers (2013). doi:10.1155/2013/374252.
URL https://www.hindawi.com/journals/jdd/2013/374252/

[38] M. Bourin, P. Jolliet, F. Ballereau, An overview of the clinical pharmacokinetics of x-ray contrast media, Clin Pharmacokinet 32 (3) (1997) 180–193. doi:10.2165/00003088-199732030-00002.

[39] F. Stacul, A. J. van der Molen, P. Reimer, J. A. W. Webb, H. S. Thomsen, S. K. Morcos, T. Almén, P. Aspelin, M.-F. Bellin, O. Clement, G. Heinz-Peer, Contrast Media Safety Committee of European Society of Urogenital Radiology (ESUR), Contrast induced nephropathy: updated ESUR Contrast Media Safety Committee guidelines, Eur Radiol 21 (12) (2011) 2527–2541. doi:10.1007/s00330-011-2225-0.

[40] D. P. Cormode, T. Skajaa, Z. A. Fayad, W. J. M. Mulder, Nanotechnology in medical imaging: probe design and applications, Arterioscler Thromb Vasc Biol 29 (7) (2009) 992–1000. doi:10.1161/ATVBAHA.108.165506.
URL https://www.ncbi.nlm.nih.gov/pmc/articles/PMC2844987/

[41] S. M. Moghimi, A. C. Hunter, J. C. Murray, Long-Circulating and Target-Specific Nanoparticles: Theory to Practice, Pharmacol Rev 53 (2) (2001) 283–318.
URL http://pharmrev.aspetjournals.org/content/53/2/283

[42] M. J. Poznansky, R. L. Juliano, Biological approaches to the controlled delivery of drugs: a critical review., Pharmacol Rev 36 (4) (1984) 277–336.
URL http://pharmrev.aspetjournals.org.docelec.univ-lyon1.fr/content/36/4/277

[43] J. Senior, G. Gregoriadis, Is half-life of circulating liposomes determined by changes in their permeability?, FEBS Letters 145 (1) (1982) 109–114. doi:10.1016/0014-5793(82)81216-7.
URL http://febs.onlinelibrary.wiley.com/doi/abs/10.1016/0014-5793%2882%2981216-7

[44] J. Senior, J. C. Crawley, G. Gregoriadis, Tissue distribution of liposomes exhibiting long half-lives in the circulation after intravenous injection, Biochim. Biophys. Acta 839 (1) (1985) 1–8.

[45] D. V. Devine, K. Wong, K. Serrano, A. Chonn, P. R. Cullis, Liposome-complement interactions in rat serum: implications for liposome survival studies, Biochim. Biophys. Acta 1191 (1) (1994) 43–51.

[46] J. Zheng, G. Perkins, A. Kirilova, C. Allen, D. A. Jaffray, Multimodal Contrast Agent for Combined Computed Tomography and Magnetic Resonance Imaging Applications, Investigative Radiology 41 (3) (2006) 339. doi:10.1097/01.rli.0000186568.50265.64.
URL https://journals.lww.com/investigativeradiology/Abstract/2006/03000/Multimodal_Contrast_Agent_for_Combined_Computed.18.aspx

[47] J. Ding, Y. Wang, M. Ma, Y. Zhang, S. Lu, Y. Jiang, C. Qi, S. Luo, G. Dong, S. Wen, Y. An, N. Gu, CT/fluorescence dual-modal nanoemulsion platform for investigating atherosclerotic plaques, Biomaterials 34 (1) (2013) 209–216. doi:10.1016/j.biomaterials.2012.09.025.
URL http://www.sciencedirect.com/science/article/pii/S0142961212010290

[48] J.-H. Park, G. von Maltzahn, E. Ruoslahti, S. Bhatia, M. Sailor, Micellar Hybrid Nanoparticles for Simultaneous Magnetofluorescent Imaging and Drug Delivery, Angewandte Chemie International Edition 47 (38) (2008) 7284–7288. doi:10.1002/anie.200801810.
URL https://onlinelibrary.wiley.com/doi/full/10.1002/anie.200801810

[49] J. Xie, S. Lee, X. Chen, Nanoparticle-based theranostic agents, Advanced Drug Delivery Reviews 62 (11) (2010) 1064–1079. doi:10.1016/j.addr.2010.07.009.
URL http://www.sciencedirect.com/science/article/pii/S0169409X1000164X

[50] E. Karathanasis, R. M. Lebovitz, A. Annapragada, R. V. Bellamkonda, Nano-scale contrast agents and methods of use (Oct. 2009).
URL https://patents.google.com/patent/US20090263326A1/en?q=composition&q=liposomes&q=method&q=phospholipid&q=images&before=priority:20071205&scholar

[51] A. Annapragada, R. V. Bellamkonda, E. Hoffman, C. Vijayalakshmi, Compositions and methods for enhancing contrast in imaging (Aug. 2010).
URL https://patents.google.com/patent/US7785568/en

[52] A. D. Bangham, M. M. Standish, J. C. Watkins, Diffusion of univalent ions across the lamellae of swollen phospholipids, Journal of Molecular Biology 13 (1) (1965) 238–IN27. doi:10.1016/S0022-2836(65)80093-6.
URL http://www.sciencedirect.com/science/article/pii/S0022283665800936

[53] A. Akbarzadeh, R. Rezaei-Sadabady, S. Davaran, S. W. Joo, N. Zarghami, Y. Hanifehpour, M. Samiei, M. Kouhi, K. Nejati-Koshki, Liposome: classification, preparation, and applications, Nanoscale Research Letters 8 (1) (2013) 102. doi:10.1186/1556-276X-8-102.
URL https://doi.org/10.1186/1556-276X-8-102

[54] R. E. Counsell, M. A. Longino, J. P. Weichert, Blood-pool carrier for lipophilic imaging agents (Oct. 1998).
URL https://patents.google.com/patent/WO1998046275A2/en

[55] A. Choukèr, M. Lizak, D. Schimel, T. Helmberger, J. M. Ward, D. Despres, I. Kaufmann, C. Bruns, F. Löhe, A. Ohta, M. V. Sitkovsky, B. Klaunberg, M. Thiel, Comparison of Fenestra VC Contrast-enhanced computed tomography imaging with gadopentetate dimeglumine and ferucarbotran magnetic resonance imaging for the in vivo evaluation of murine liver damage after ischemia and reperfusion, Invest Radiol 43 (2) (2008) 77–91. doi:10.1097/RLI.0b013e318155aa2e.

[56] J. P. Weichert, M. A. Longino, D. A. Bakan, M. G. Spigarelli, T. S. Chou, S. W. Schwendner, R. E. Counsell, Polyiodinated triglyceride analogs as potential computed tomography imaging agents for the liver, J. Med. Chem. 38 (4) (1995) 636–646.

[57] K. Shinoda, H. Saito, The effect of temperature on the phase equilibria and the types of dispersions of the ternary system composed of water, cyclohexane, and nonionic surfactant, Journal of Colloid and Interface Science 26 (1968) 70–74. doi:10.1016/0021-9797(68)90273-7.
URL http://adsabs.harvard.edu/abs/1968JCIS...26...70S

[58] P. Izquierdo, J. Esquena, T. F. Tadros, C. Dederen, M. J. Garcia, N. Azemar, C. Solans, Formation and Stability of Nano-Emulsions Prepared Using the Phase Inversion Temperature Method, Langmuir 18 (1) (2002) 26–30. doi:10.1021/la010808c.
URL https://doi.org/10.1021/la010808c

[59] A. T. Yordanov, A. L. Lodder, E. K. Woller, M. J. Cloninger, N. Patronas, D. Milenic, M. W. Brechbiel, Novel Iodinated Dendritic Nanoparticles for Computed Tomography (CT) Imaging, Nano Letters 2 (6) (2002) 595–599. doi:10.1021/nl020246x.
URL http://pubs.acs.org/doi/abs/10.1021/nl020246x

[60] Y. Fu, D. E. Nitecki, D. Maltby, G. H. Simon, K. Berejnoi, H.-J. Raatschen, B. M. Yeh, D. M. Shames, R. C. Brasch, Dendritic Iodinated Contrast Agents with PEG-Cores for CT Imaging: Synthesis and Preliminary Characterization, Bioconjugate Chem. 17 (4) (2006) 1043–1056. doi:10.1021/bc060019c.
URL https://doi.org/10.1021/bc060019c

[61] V. P. Torchilin, M. D. Frank-Kamenetsky, G. L. Wolf, CT visualization of blood pool in rats by using long-circulating, iodine-containing micelles, Academic Radiology 6 (1) (1999) 61–65. doi:10.1016/S1076-6332(99)80063-4.
URL http://www.sciencedirect.com/science/article/pii/S1076633299800634

[62] Z. Wang, T. Chang, L. Hunter, A. M. Gregory, M. Tanudji, S. Jones, M. H. Stenzel, Radio-opaque Micelles for X-ray Imaging, Aust. J. Chem. 67 (1) (2014) 78–84. doi:10.1071/CH13391.
URL http://www.publish.csiro.au/ch/CH13391

[63] V. S. Trubetskoy, Polymeric micelles as carriers of diagnostic agents, Advanced Drug Delivery Reviews 37 (1) (1999) 81–88. doi:10.1016/S0169-409X(98)00100-8.
URL http://www.sciencedirect.com/science/article/pii/S0169409X98001008

[64] K. Novakova, M. Laznicek, F. Rypacek, L. Machova, Pharmacokinetics and Distribution of 125i-PLA-b-PEO Block Copolymers in Rats, Pharmaceutical Development and Technology 8 (2) (2003) 153–161. doi:10.1081/PDT-120018484.
URL https://doi.org/10.1081/PDT-120018484

[65] J. Liu, F. Zeng, C. Allen, In vivo fate of unimers and micelles of a poly(ethylene glycol)-block-poly(caprolactone) copolymer in mice following intravenous administration, Eur J Pharm Biopharm 65 (3) (2007) 309–319. doi:10.1016/j.ejpb.2006.11.010.

[66] R. Tong, N. P. Gabrielson, T. M. Fan, J. Cheng, Polymeric Nanomedicines Based on Poly(lactide) and Poly(lactide-co-glycolide), Curr Opin Solid State Mater Sci 16 (6) (2012) 323–332. doi:10.1016/j.cossms.2013.01.001.
URL https://www.ncbi.nlm.nih.gov/pmc/articles/PMC3728009/

[67] F. Hallouard, S. Briançon, N. Anton, X. Li, T. Vandamme, H. Fessi, Poly(ethylene glycol)-poly(caprolactone) iodinated nanocapsules as contrast agents for X-ray imaging, Pharm. Res. 30 (8) (2013) 2023–2035. doi:10.1007/s11095-013-1047-y.

[68] A. Galperin, D. Margel, J. Baniel, G. Dank, H. Biton, S. Margel, Radiopaque iodinated polymeric nanoparticles for X-ray imaging applications, Biomaterials 28 (30) (2007) 4461–4468. doi:10.1016/j.biomaterials.2007.06.032.

[69] W. Ho Kong, W. Jae Lee, Z. Yun Cui, K. Hyun Bae, T. Gwan Park, J. Hoon Kim, K. Park, S. Won Seo, Nanoparticulate carrier containing water-insoluble iodinated oil as a multifunctional contrast agent for computed tomography imaging, Biomaterials 28 (36) (2007) 5555–5561. doi:10.1016/j.biomaterials.2007.08.044.
URL http://www.sciencedirect.com/science/article/pii/S0142961207006990

[70] J. F. Hainfeld, S. M. Ridwan, Y. Stanishevskiy, N. R. Smilowitz, J. Davis, H. M. Smilowitz, Small, Long Blood Half-Life Iodine Nanoparticle for Vascular and Tumor Imaging, Scientific Reports 8 (1) (2018) 13803. doi:10.1038/s41598-018-31940-2.
URL https://www.nature.com/articles/s41598-018-31940-2

[71] A. T. Yordanov, N. Mollov, A. L. Lodder, E. Woller, M. Cloninger, S. Walbridge, D. Milenic, M. W. Brechbiel, A water-soluble triiodo amino acid and its dendrimer conjugate for computerized tomography (CT) imaging, Journal of the Serbian Chemical Society 70 (2) (2005) 163–170.
URL http://www.doiserbia.nb.rs/Article.aspx?ID=0352-51390502163Y

[72] S. You, H.-y. Jung, C. Lee, Y. H. Choe, J. Y. Heo, G.-T. Gang, S.-K. Byun, W. K. Kim, C.-H. Lee, D.-E. Kim, Y. I. Kim, Y. Kim, High-performance dendritic contrast agents for X-ray computed tomography imaging using potent tetraiodobenzene derivatives, Journal of Controlled Release 226 (2016) 258–267. doi:10.1016/j.jconrel.2016.01.036.
URL http://www.sciencedirect.com/science/article/pii/S0168365916300335

[73] P. J. Ryan, M. A. Davis, L. R. DeGaeta, B. Woda, D. L. Melchior, Liposomes loaded with contrast material for image enhancement in computed tomography. Work in progress., Radiology 152 (3) (1984) 759–762. doi:10.1148/radiology.152.3.6611564.
URL https://pubs.rsna.org/doi/10.1148/radiology.152.3.6611564

[74] S. Mukundan, K. B. Ghaghada, C. T. Badea, C.-Y. Kao, L. W. Hedlund, J. M. Provenzale, G. A. Johnson, E. Chen, R. V. Bellamkonda, A. Annapragada, A liposomal nanoscale contrast agent for preclinical CT in mice, AJR Am J Roentgenol 186 (2) (2006) 300–307. doi:10.2214/AJR.05.0523.

[75] J. Zheng, J. Liu, M. Dunne, D. A. Jaffray, C. Allen, In Vivo Performance of a Liposomal Vascular Contrast Agent for CT and MR-Based Image Guidance Applications, Pharm Res 24 (6) (2007) 1193–1201. doi:10.1007/s11095-006-9220-1.
URL https://doi.org/10.1007/s11095-006-9220-1

[76] N. Anton, T. F. Vandamme, Nanotechnology for computed tomography: a real potential recently disclosed, Pharm. Res. 31 (1) (2014) 20–34. doi:10.1007/s11095-013-1131-3.

[77] T. D. Henning, A. W. Weber, J. S. Bauer, R. Meier, J. Carlsen, E. J. Sutton, S. Prevrhal, S. I. Ziegler, H. Feußner, H. E. Daldrup-Link, E. J. Rummeny, Imaging characteristics of DHOG, a hepatobiliary contrast agent for preclinical microCT in mice., Academic radiology 15 (3) (2008) 342–349. doi:10.1016/j.acra.2007.10.007.

[78] A. de Vries, E. Custers, J. Lub, S. van den Bosch, K. Nicolay, H. Grüll, Block-copolymer-stabilized iodinated emulsions for use as CT contrast agents, Biomaterials 31 (25) (2010) 6537–6544. doi:10.1016/j.biomaterials.2010.04.056.
URL http://www.sciencedirect.com/science/article/pii/S0142961210005727

[79] S.-J. Lim, J. S. Lim, J. Choi, J.-Y. Choi, W. J. Hyung, H. S. Kim, J. Suh, K. W. Kim, Nanoscaled iodized oil emulsion as a CT contrast agent for the detection of experimental liver tumors in a rat model, Acad Radiol 17 (8) (2010) 985–991. doi:10.1016/j.acra.2010.03.021.

[80] M. F. Attia, N. Anton, M. Chiper, R. Akasov, H. Anton, N. Messaddeq, S. Fournel, A. S. Klymchenko, Y. Mély, T. F. Vandamme, Biodistribution of X-Ray Iodinated Contrast Agent in Nano-Emulsions Is Controlled by the Chemical Nature of the Oily Core, ACS Nano 8 (10) (2014) 10537–10550. doi:10.1021/nn503973z.
URL https://doi.org/10.1021/nn503973z

[81] F. Hyafil, J.-C. Cornily, J. E. Feig, R. Gordon, E. Vucic, V. Amirbekian, E. A. Fisher, V. Fuster, L. J. Feldman, Z. A. Fayad, Noninvasive detection of macrophages using a nanoparticulate contrast agent for computed tomography, Nature Medicine 13 (5) (2007) 636–641. doi:10.1038/nm1571.
URL https://www.nature.com/articles/nm1571

[82] Q. Yin, F. Y. Yap, L. Yin, L. Ma, Q. Zhou, L. W. Dobrucki, T. M. Fan, R. C. Gaba, J. Cheng, Poly(iohexol) Nanoparticles As Contrast Agents for in Vivo X-ray Computed Tomography Imaging, J. Am. Chem. Soc. 135 (37) (2013) 13620–13623. doi:10.1021/ja405196f.
URL https://doi.org/10.1021/ja405196f

[83] J. Wallyn, N. Anton, C. A. Serra, M. Bouquey, M. Collot, H. Anton, J.-L. Weickert, N. Messaddeq, T. F. Vandamme, A new formulation of poly(MAOTIB) nanoparticles as an efficient contrast agent for in vivo X-ray imaging, Acta Biomaterialia 66 (2018) 200–212. doi:10.1016/j.actbio.2017.11.011.

[84] P. Couvreur, B. Kante, M. Roland, P. Guiot, P. BAuduin, P. Speiser, Polycyanoacrylate nanocapsules as potential lysosomotropic carriers: preparation, morphological and sorptive properties, Journal of Pharmacy and Pharmacology 31 (1) (1979) 331–332. doi:10.1111/j.2042-7158.1979.tb13510.x.
URL https://onlinelibrary.wiley.com/doi/abs/10.1111/j.2042-7158.1979.tb13510.x

[85] S. Margel, A. Galperin, Core and core-shell nanoparticles containing iodine for X-ray imaging (Aug. 2011).
URL https://patents.google.com/patent/US8003079B2/fr?assignee=Shlomo+Margel

[86] H. Aviv, S. Bartling, F. Kiesslling, S. Margel, Radiopaque iodinated copolymeric nanoparticles for X-ray imaging applications, Biomaterials 30 (29) (2009) 5610–5616. doi:10.1016/j.biomaterials.2009.06.038.

[87] A. Galperin, S. Margel, Synthesis and characterization of new radiopaque microspheres by the dispersion polymerization of an iodinated acrylate monomer for X-ray imaging applications, Journal of Polymer Science Part A: Polymer Chemistry 44 (12) (2006) 3859–3868. doi:10.1002/pola.21487.
URL https://onlinelibrary.wiley.com/doi/abs/10.1002/pola.21487

[88] Y. S. Leong, F. Candau, Inverse microemulsion polymerization, J. Phys. Chem. 86 (13) (1982) 2269–2271. doi:10.1021/j100210a001.
URL https://doi.org/10.1021/j100210a001

[89] E. L. Wittbecker, P. W. Morgan, Interfacial polycondensation. I., Journal of Polymer Science 40 (137) (1959) 289–297. doi:10.1002/pol.1959.1204013701.
URL https://onlinelibrary.wiley.com/doi/abs/10.1002/pol.1959.1204013701

[90] J.-S. Cho, A. Kwon, C.-G. Cho, Microencapsulation of octadecane as a phase-change material by interfacial polymerization in an emulsion system, Colloid Polym Sci 280 (3) (2002) 260–266. doi:10.1007/s00396-001-0603-x.
URL https://doi.org/10.1007/s00396-001-0603-x

[91] S. Desgouilles, C. Vauthier, D. Bazile, J. Vacus, J.-L. Grossiord, M. Veillard, P. Couvreur, The Design of Nanoparticles Obtained by Solvent Evaporation: A Comprehensive Study, Langmuir 19 (22) (2003) 9504–9510. doi:10.1021/la034999q.
URL https://doi.org/10.1021/la034999q

[92] C. X. Song, V. Labhasetwar, H. Murphy, X. Qu, W. R. Humphrey, R. J. Shebuski, R. J. Levy, Formulation and characterization of biodegradable nanoparticles for intravascular local drug delivery, Journal of Controlled Release 43 (2) (1997) 197–212. doi:10.1016/S0168-3659(96)01484-8.
URL http://www.sciencedirect.com/science/article/pii/S0168365996014848

[93] D. Quintanar, H. Fessi, E. Doelker, E. Allemann, Method for preparing vesicular nanocapsules (Apr. 2005).
URL https://patents.google.com/patent/US6884438/en

[94] D. Quintanar-Guerrero, E. Allémann, E. Doelker, H. Fessi, A mechanistic study of the formation of polymer nanoparticles by the emulsification-diffusion technique, Colloid Polym Sci 275 (7) (1997) 640–647. doi:10.1007/s003960050130.

[95] C. E. Matkovich, G. D. Christian, Salting-out of acetone from water. Basis of a new solvent extraction system, Anal. Chem. 45 (11) (1973) 1915–1921. doi:10.1021/ac60333a023.
URL https://doi.org/10.1021/ac60333a023

[96] E. Allémann, R. Gurny, E. Doelker, Preparation of aqueous polymeric nanodispersions by a reversible salting-out process: influence of process parameters on particle size, International Journal of Pharmaceutics 87 (1) (1992) 247–253. doi:10.1016/0378-5173(92)90249-2.
URL http://www.sciencedirect.com/science/article/pii/0378517392902492

[97] H. Fessi, F. Puisieux, J. P. Devissaguet, N. Ammoury, S. Benita, Nanocapsule formation by interfacial polymer deposition following solvent displacement, International Journal of Pharmaceutics 55 (1) (1989) R1–R4. doi:10.1016/0378-5173(89)90281-0.
URL http://www.sciencedirect.com/science/article/pii/0378517389902810

[98] J.-P. Devissaguet, H. Fessi, F. Puisieux, Process for the preparaton of dispersible colloidal systems of a substance in the form of nanocapsules (Sep. 1991).
URL https://patents.google.com/patent/US5049322A/fr?inventor=fessi&oq=fessi

[99] F. Lince, D. L. Marchisio, A. A. Barresi, Strategies to control the particle size distribution of poly-caprolactone nanoparticles for pharmaceutical applications, Journal of Colloid and Interface Science 322 (2) (2008) 505–515. doi:10.1016/j.jcis.2008.03.033.
URL http://www.sciencedirect.com/science/article/pii/S0021979708003159

[100] D. Quintanar-Guerrero, E. Allémann, H. Fessi, E. Doelker, Preparation techniques and mechanisms of formation of biodegradable nanoparticles from preformed polymers, Drug Dev Ind Pharm 24 (12) (1998) 1113–1128. doi:10.3109/03639049809108571.

[101] J.-C. Leroux, E. Allémann, F. De Jaeghere, E. Doelker, R. Gurny, Biodegradable nanoparticles — From sustained release formulations to improved site specific

drug delivery, Journal of Controlled Release 39 (2) (1996) 339–350. doi:10.1016/0168-3659(95)00164-6.

[102] J. Kim, D. Bar-Ness, S. Si-Mohamed, P. Coulon, I. M. Blevis, P. Douek, D. P. Cormode, Assessment of candidate elements for development of spectral photon-counting CT specific contrast agents (2018).
URL /paper/Assessment-of-candidate-elements-for-development-of-Kim-Bar-Ness/7ca705b3603c5af7f57e0bd57305ee1125f2a930

[103] E. Seeliger, M. Sendeski, C. S. Rihal, P. B. Persson, Contrast-induced kidney injury: mechanisms, risk factors, and prevention, Eur Heart J 33 (16) (2012) 2007–2015. doi:10.1093/eurheartj/ehr494.
URL https://academic.oup.com/eurheartj/article/33/16/2007/447091

[104] M. Shilo, T. Reuveni, M. Motiei, R. Popovtzer, Nanoparticles as computed tomography contrast agents: current status and future perspectives, Nanomedicine 7 (2) (2012) 257–269. doi:10.2217/nnm.11.190.
URL https://www.futuremedicine.com/doi/abs/10.2217/nnm.11.190

[105] D. P. Cormode, Z. A. Fayad, Nanoparticle contrast agents for CT: their potential and the challenges that lie ahead, Imaging in Medicine 3 (3) (2011) 263–266. doi:10.2217/iim.11.17.
URL http://www.futuremedicine.com/doi/abs/10.2217/iim.11.17

[106] C. O. Schirra, B. Brendel, M. A. Anastasio, E. Roessl, Spectral CT: a technology primer for contrast agent development, Contrast Media Mol Imaging 9 (1) (2014) 62–70. doi:10.1002/cmmi.1573.

[107] F. Hallouard, N. Anton, P. Choquet, A. Constantinesco, T. Vandamme, Iodinated blood pool contrast media for preclinical X-ray imaging applications – A review, Biomaterials 31 (24) (2010) 6249–6268. doi:10.1016/j.biomaterials.2010.04.066.
URL http://www.sciencedirect.com/science/article/pii/S014296121000582X

[108] H. Lusic, M. W. Grinstaff, X-Ray Computed Tomography Contrast Agents, Chem Rev 113 (3). doi:10.1021/cr200358s.
URL https://www.ncbi.nlm.nih.gov/pmc/articles/PMC3878741/

[109] C. Chauvierre, D. Labarre, P. Couvreur, C. Vauthier, Radical Emulsion Polymerization of Alkylcyanoacrylates Initiated by the Redox System Dextran−Cerium(IV) under Acidic Aqueous Conditions, Macromolecules 36 (16) (2003) 6018–6027. doi:10.1021/ma034097w.
URL https://cdn-pubs.acs.org/doi/10.1021/ma034097w

[110] A. J. Paine, W. Luymes, J. McNulty, Dispersion polymerization of styrene in polar solvents. 6. Influence of reaction parameters on particle size and molecular weight in poly(N-vinylpyrrolidone)-stabilized reactions, Macromolecules 23 (12) (1990) 3104–3109. doi:10.1021/ma00214a012.
URL https://doi.org/10.1021/ma00214a012

[111] S. K. Karode, S. S. Kulkarni, A. K. Suresh, R. A. Mashelkar, New insights into kinetics and thermodynamics of interfacial polymerization, Chemical Engineering Science 53 (15) (1998) 2649–2663. doi:10.1016/S0009-2509(98)00083-9.
URL http://www.sciencedirect.com/science/article/pii/S0009250998000839

[112] F. Mottu, D. A. Rüfenacht, A. Laurent, E. Doelker, Iodine-containing cellulose mixed esters as radiopaque polymers for direct embolization of cerebral aneurysms and

arteriovenous malformations, Biomaterials 23 (1) (2002) 121–131. doi:10.1016/S0142-9612(01)00087-4.
URL http://www.sciencedirect.com/science/article/pii/S0142961201000874

[113] F. Laredj-Bourezg, Y. Chevalier, O. Boyron, M.-A. Bolzinger, Emulsions stabilized with organic solid particles, Colloids and Surfaces A: Physicochemical and Engineering Aspects 413 (2012) 252–259. doi:10.1016/j.colsurfa.2011.12.064.
URL http://www.sciencedirect.com/science/article/pii/S092777571100817X

[114] F. Laredj-Bourezg, M. A. Bolzinger, J. Pelletier, J. P. Valour, M. R. Rovère, B. Smatti, Y. Chevalier, Skin delivery by block copolymer nanoparticles (block copolymer micelles)., Int J Pharm 496 (2) (2015) 1034–1046. doi:10.1016/j.ijpharm.2015.11.031.
URL http://europepmc.org/abstract/med/26602293

[115] G. Agusti, O. Jordan, G. Andersen, r. Doelker, Y. Chevalier, Radiopaque iodinated ethers of poly(vinyl iodobenzyl ether)s: Synthesis and evaluation for endovascular embolization, J. Appl. Polym. Sci. 132 (14) (2015) n/a–n/a. doi:10.1002/app.41791.
URL http://onlinelibrary.wiley.com/doi/10.1002/app.41791/abstract

[116] S. Stainmesse, H. Fessi, J.-P. Devissaguet, F. Puisieux, C. Theis, Process for the preparation of dispersible colloidal systems of a substance in the form of nanoparticles (Jul. 1992).
URL https://patents.google.com/patent/US5133908A/en?q=nanoprecipitation&inventor=fessi

[117] C. Fonseca, S. Simões, R. Gaspar, Paclitaxel-loaded PLGA nanoparticles: preparation, physicochemical characterization and in vitro anti-tumoral activity, J Control Release 83 (2) (2002) 273–286.

[118] K. Devanand, J. C. Selser, Asymptotic behavior and long-range interactions in aqueous solutions of poly(ethylene oxide), Macromolecules 24 (22) (1991) 5943–5947. doi:10.1021/ma00022a008.

[119] B. J. Nehilla, M. Bergkvist, K. C. Popat, T. A. Desai, Purified and surfactant-free coenzyme Q10-loaded biodegradable nanoparticles, International Journal of Pharmaceutics 348 (1) (2008) 107–114. doi:10.1016/j.ijpharm.2007.07.001.
URL http://www.sciencedirect.com/science/article/pii/S0378517307005674

[120] E. Plasari, P. H. Grisoni, J. Villermaux, Influence of Process Parameters on the Precipitation of Organic Nanoparticles by Drowning-Out, Chemical Engineering Research and Design 75 (2) (1997) 237–244. doi:10.1205/026387697523507.
URL http://www.sciencedirect.com/science/article/pii/S0263876297715223

[121] S. Sant, S. Poulin, P. Hildgen, Effect of polymer architecture on surface properties, plasma protein adsorption, and cellular interactions of pegylated nanoparticles, Journal of Biomedical Materials Research Part A 87A (4) 885–895. doi:10.1002/jbm.a.31800.
URL https://onlinelibrary.wiley.com/doi/abs/10.1002/jbm.a.31800

[122] D. Bazile, C. Prud'homme, M. T. Bassoullet, M. Marlard, G. Spenlehauer, M. Veillard, Stealth Me.PEG-PLA nanoparticles avoid uptake by the mononuclear phagocytes system, J Pharm Sci 84 (4) (1995) 493–498.

[123] J.-M. Rabanel, P. Hildgen, X. Banquy, Assessment of PEG on polymeric particles surface, a key step in drug carrier translation, J Control Release 185 (2014) 71–87. doi:10.1016/j.jconrel.2014.04.017.

[124] P. G. de Gennes, Conformations of Polymers Attached to an Interface, Macromolecules 13 (5) (1980) 1069–1075. doi:10.1021/ma60077a009.
URL https://doi.org/10.1021/ma60077a009

[125] B. Brendel, E. Roessl, J.-P. Schlomka, R. Proksa, Empirical projection-based basis-component decomposition method, in: Medical Imaging 2009: Physics of Medical Imaging, Vol. 7258, International Society for Optics and Photonics, 2009, p. 72583Y. doi:10.1117/12.811006.
URL https://www.spiedigitallibrary.org/conference-proceedings-of-spie/7258/72583Y/Empirical-projection-based-basis-component-decomposition-method/10.1117/12.811006.short

[126] D. P. Cormode, S. Si-Mohamed, D. Bar-Ness, M. Sigovan, P. C. Naha, J. Balegamire, F. Lavenne, P. Coulon, E. Roessl, M. Bartels, M. Rokni, I. Blevis, L. Boussel, P. Douek, Multicolor spectral photon-counting computed tomography: in vivo dual contrast imaging with a high count rate scanner, Sci Rep 7. doi:10.1038/s41598-017-04659-9.
URL https://www.ncbi.nlm.nih.gov/pmc/articles/PMC5500581/

[127] F. Alexis, E. Pridgen, L. K. Molnar, O. C. Farokhzad, Factors affecting the clearance and biodistribution of polymeric nanoparticles, Mol. Pharm. 5 (4) (2008) 505–515. doi:10.1021/mp800051m.

[128] W. H. De Jong, P. J. Borm, Drug delivery and nanoparticles: Applications and hazards, Int J Nanomedicine 3 (2) (2008) 133–149.
URL https://www.ncbi.nlm.nih.gov/pmc/articles/PMC2527668/

[129] A. Mahapatro, D. K. Singh, Biodegradable nanoparticles are excellent vehicle for site directed in-vivo delivery of drugs and vaccines, Journal of Nanobiotechnology 9 (1) (2011) 55. doi:10.1186/1477-3155-9-55.

[130] P. Couvreur, L. Grislain, V. Lenaerts, F. Brasseur, P. Guiot, A. Biernacki, L. Grislain, V. Lenaerts, F. Brasseur, P. Guiot, A. Biernacki, Biodegradable Polymeric Nanoparticles as Drug Carrier for Antitumor Agents (Jan. 2018). doi:10.1201/9781351075893-2.
URL https://www.taylorfrancis.com/

[131] G. Paradossi, F. Cavalieri, E. Chiessi, C. Spagnoli, M. K. Cowman, Poly(vinyl alcohol) as versatile biomaterial for potential biomedical applications, J Mater Sci Mater Med 14 (8) (2003) 687–691.

[132] S. H. Hyon, W. I. Cha, Y. Ikada, M. Kita, Y. Ogura, Y. Honda, Poly(vinyl alcohol) hydrogels as soft contact lens material, J Biomater Sci Polym Ed 5 (5) (1994) 397–406.

[133] T. Yamaoka, Y. Tabata, Y. Ikada, Comparison of body distribution of poly(vinyl alcohol) with other water-soluble polymers after intravenous administration, J. Pharm. Pharmacol. 47 (6) (1995) 479–486.

[134] H. Asadi, K. Rostamizadeh, D. Salari, M. Hamidi, Preparation of biodegradable nanoparticles of tri-block PLA-PEG-PLA copolymer and determination of factors controlling the particle size using artificial neural network, J Microencapsul 28 (5) (2011) 406–416. doi:10.3109/02652048.2011.576784.

[135] S. Galindo-Rodriguez, E. Allémann, H. Fessi, E. Doelker, Physicochemical Parameters Associated with Nanoparticle Formation in the Salting-Out, Emulsification-Diffusion, and Nanoprecipitation Methods, Pharm Res 21 (8) (2004) 1428–1439. doi:10.1023/B:PHAM.0000036917.75634.be.
URL https://doi.org/10.1023/B:PHAM.0000036917.75634.be

[136] S. S. Nunes, R. S. Fernandes, C. H. Cavalcante, I. da Costa César, E. A. Leite, S. C. A. Lopes, A. Ferretti, D. Rubello, D. M. Townsend, M. C. de Oliveira, V. N. Cardoso, A. L. B. de Barros, Influence of PEG coating on the biodistribution and tumor accumulation of pH-sensitive liposomes, Drug Deliv Transl Res 9 (1) (2019) 123–130. doi:10.1007/s13346-018-0583-8.

[137] J. Klein, P. F. Luckham, Long-range attractive forces between two mica surfaces in an aqueous polymer solution, Nature 308 (5962) (1984) 836. doi:10.1038/308836a0.
URL https://www.nature.com/articles/308836a0

[138] G. J. C. Braithwaite, A. Howe, P. F. Luckham, Interactions between Poly(ethylene oxide) Layers Adsorbed to Glass Surfaces Probed by Using a Modified Atomic Force Microscope, Langmuir 12 (17) (1996) 4224–4237. doi:10.1021/la9601541.
URL https://doi.org/10.1021/la9601541

[139] R. J. Owen, J. C. Crocker, R. Verma, A. G. Yodh, Measurement of long-range steric repulsions between microspheres due to an adsorbed polymer, Phys Rev E Stat Nonlin Soft Matter Phys 64 (1 Pt 1) (2001) 011401. doi:10.1103/PhysRevE.64.011401.

[140] D. Kleshchanok, P. R. Lang, Steric Repulsion by Adsorbed Polymer Layers Studied with Total Internal Reflection Microscopy, Langmuir 23 (8) (2007) 4332–4339. doi:10.1021/la062607k.
URL https://doi.org/10.1021/la062607k

[141] P. G. de Gennes, Polymers at an interface; a simplified view, Advances in Colloid and Interface Science 27 (3) (1987) 189–209. doi:10.1016/0001-8686(87)85003-0.
URL http://www.sciencedirect.com/science/article/pii/0001868687850030

[142] S. T. Milner, T. A. Witten, M. E. Cates, Theory of the grafted polymer brush, Macromolecules 21 (8) (1988) 2610–2619. doi:10.1021/ma00186a051.
URL https://doi.org/10.1021/ma00186a051

[143] S. T. Milner, Compressing Polymer "Brushes": a Quantitative Comparison of Theory and Experiment, EPL 7 (8) (1988) 695–699. doi:10.1209/0295-5075/7/8/005.
URL https://doi.org/10.1209%2F0295-5075%2F7%2F8%2F005

[144] H. J. Taunton, C. Toprakcioglu, L. J. Fetters, J. Klein, Forces between surfaces bearing terminally anchored polymer chains in good solvents, Nature 332 (6166) (1988) 712. doi:10.1038/332712a0.
URL https://www.nature.com/articles/332712a0

[145] D. M. Leneveu, R. P. Rand, V. A. Parsegian, Measurement of forces between lecithin bilayers, Nature 259 (5544) (1976) 601. doi:10.1038/259601a0.
URL https://www.nature.com/articles/259601a0

[146] V. A. Parsegian, N. Fuller, R. P. Rand, Measured work of deformation and repulsion of lecithin bilayers., Proc Natl Acad Sci U S A 76 (6) (1979) 2750–2754.
URL https://www.ncbi.nlm.nih.gov/pmc/articles/PMC383686/

[147] J. N. Israelachvili, H. Wennerstroem, Hydration or steric forces between amphiphilic surfaces?, Langmuir 6 (4) (1990) 873–876. doi:10.1021/la00094a028.
URL https://doi.org/10.1021/la00094a028

[148] R. G. Horn, Direct measurement of the force between two lipid bilayers and observation of their fusion, Biochimica et Biophysica Acta (BBA) - Biomembranes 778 (1) (1984) 224–228. doi:10.1016/0005-2736(84)90466-8.
URL http://www.sciencedirect.com/science/article/pii/0005273684904668

[149] J. Marra, J. Israelachvili, Direct measurements of forces between phosphatidylcholine and phosphatidylethanolamine bilayers in aqueous electrolyte solutions, Biochemistry 24 (17) (1985) 4608–4618. doi:10.1021/bi00338a020.
URL https://doi.org/10.1021/bi00338a020

[150] T. L. Kuhl, A. D. Berman, S. W. Hui, J. N. Israelachvili, Part 2. Crossover from Depletion Attraction to Adsorption: Polyethylene Glycol Induced Electrostatic Repulsion between Lipid Bilayers, Macromolecules 31 (23) (1998) 8258–8263. doi:10.1021/ma9714326.
URL https://doi.org/10.1021/ma9714326

[151] R. M. Hoedemakers, H. W. Morselt, G. L. Scherphof, T. Daemen, Secretion pattern of the rat liver macrophage population following activation with liposomal muramyl dipeptide in vivo and in vitro, J Immunother Emphasis Tumor Immunol 15 (4) (1994) 265–272.

[152] S. M. Moghimi, A. C. Hunter, T. L. Andresen, Factors controlling nanoparticle pharmacokinetics: an integrated analysis and perspective, Annu. Rev. Pharmacol. Toxicol. 52 (2012) 481–503. doi:10.1146/annurev-pharmtox-010611-134623.

[153] S. Mayor, R. E. Pagano, Pathways of clathrin-independent endocytosis, Nature Reviews Molecular Cell Biology 8 (8) (2007) 603–612. doi:10.1038/nrm2216.
URL https://www.nature.com/articles/nrm2216

[154] D. E. Owens, N. A. Peppas, Opsonization, biodistribution, and pharmacokinetics of polymeric nanoparticles, International Journal of Pharmaceutics 307 (1) (2006) 93–102. doi:10.1016/j.ijpharm.2005.10.010.
URL http://www.sciencedirect.com/science/article/pii/S037851730500668X

[155] H. H. Gustafson, D. Holt-Casper, D. W. Grainger, H. Ghandehari, Nanoparticle Uptake: The Phagocyte Problem, Nano Today 10 (4) (2015) 487–510. doi:10.1016/j.nantod.2015.06.006.
URL https://www.ncbi.nlm.nih.gov/pmc/articles/PMC4666556/

[156] L. Kou, J. Sun, Y. Zhai, Z. He, The endocytosis and intracellular fate of nanomedicines: Implication for rational design, Asian Journal of Pharmaceutical Sciences 8 (1) (2013) 1–10. doi:10.1016/j.ajps.2013.07.001.
URL http://www.sciencedirect.com/science/article/pii/S1818087613000020

[157] G. J. Doherty, H. T. McMahon, Mechanisms of endocytosis, Annu. Rev. Biochem. 78 (2009) 857–902. doi:10.1146/annurev.biochem.78.081307.110540.

[158] A. L. Kiss, E. Botos, Endocytosis via caveolae: alternative pathway with distinct cellular compartments to avoid lysosomal degradation?, J Cell Mol Med 13 (7) (2009) 1228–1237. doi:10.1111/j.1582-4934.2009.00754.x.
URL https://www.ncbi.nlm.nih.gov/pmc/articles/PMC4496137/

[159] H. Hillaireau, P. Couvreur, Nanocarriers' entry into the cell: relevance to drug delivery, Cell. Mol. Life Sci. 66 (17) (2009) 2873–2896. doi:10.1007/s00018-009-0053-z.

[160] N. Oh, J.-H. Park, Endocytosis and exocytosis of nanoparticles in mammalian cells, Int J Nanomedicine 9 Suppl 1 (2014) 51–63. doi:10.2147/IJN.S26592.

[161] M. J. Poznansky, R. L. Juliano, Biological approaches to the controlled delivery of drugs: a critical review, Pharmacol. Rev. 36 (4) (1984) 277–336.

[162] S. M. Moghimi, S. S. Davis, Innovations in avoiding particle clearance from blood by Kupffer cells: cause for reflection, Crit Rev Ther Drug Carrier Syst 11 (1) (1994) 31–59.

[163] J. Rejman, V. Oberle, I. S. Zuhorn, D. Hoekstra, Size-dependent internalization of particles via the pathways of clathrin- and caveolae-mediated endocytosis, Biochem. J. 377 (Pt 1) (2004) 159–169. doi:10.1042/BJ20031253.

[164] J.-M. Oh, S.-J. Choi, G.-E. Lee, J.-E. Kim, J.-H. Choy, Inorganic metal hydroxide nanoparticles for targeted cellular uptake through clathrin-mediated endocytosis, Chem Asian J 4 (1) (2009) 67–73. doi:10.1002/asia.200800290.

[165] G. Sharma, D. T. Valenta, Y. Altman, S. Harvey, H. Xie, S. Mitragotri, J. W. Smith, Polymer particle shape independently influences binding and internalization by macrophages, J Control Release 147 (3) (2010) 408–412. doi:10.1016/j.jconrel.2010.07.116.

[166] J. A. Champion, A. Walker, S. Mitragotri, Role of particle size in phagocytosis of polymeric microspheres, Pharm. Res. 25 (8) (2008) 1815–1821. doi:10.1007/s11095-008-9562-y.

[167] C. D. Walkey, W. C. W. Chan, Understanding and controlling the interaction of nanomaterials with proteins in a physiological environment, Chem Soc Rev 41 (7) (2012) 2780–2799. doi:10.1039/c1cs15233e.

[168] C. He, Y. Hu, L. Yin, C. Tang, C. Yin, Effects of particle size and surface charge on cellular uptake and biodistribution of polymeric nanoparticles, Biomaterials 31 (13) (2010) 3657–3666. doi:10.1016/j.biomaterials.2010.01.065.

[169] K. A. Beningo, Y.-l. Wang, Fc-receptor-mediated phagocytosis is regulated by mechanical properties of the target, J. Cell. Sci. 115 (Pt 4) (2002) 849–856.

[170] A. C. Anselmo, M. Zhang, S. Kumar, D. R. Vogus, S. Menegatti, M. E. Helgeson, S. Mitragotri, Elasticity of nanoparticles influences their blood circulation, phagocytosis, endocytosis, and targeting, ACS Nano 9 (3) (2015) 3169–3177. doi:10.1021/acsnano.5b00147.

[171] N. Feliu, D. Docter, M. Heine, P. d. Pino, S. Ashraf, J. Kolosnjaj-Tabi, P. Macchiarini, P. Nielsen, D. Alloyeau, F. Gazeau, R. H. Stauber, W. J. Parak, In vivo degeneration and the fate of inorganic nanoparticles, Chemical Society Reviews 45 (9) (2016) 2440–2457. doi:10.1039/C5CS00699F.
URL https://pubs.rsc.org/en/content/articlelanding/2016/cs/c5cs00699f

[172] J. Sanz, Z. A. Fayad, Imaging of atherosclerotic cardiovascular disease, Nature 451 (7181) (2008) 953–957. doi:10.1038/nature06803.

[173] W. Insull, The pathology of atherosclerosis: plaque development and plaque responses to medical treatment, Am. J. Med. 122 (1 Suppl) (2009) S3–S14. doi:10.1016/j.amjmed.2008.10.013.

[174] F. D. Kolodgie, A. P. Burke, A. Farb, H. K. Gold, J. Yuan, J. Narula, A. V. Finn, R. Virmani, The thin-cap fibroatheroma: a type of vulnerable plaque: the major precursor lesion to acute coronary syndromes, Curr. Opin. Cardiol. 16 (5) (2001) 285–292.

[175] Your Heart Is at Risk - Sterling Care - In-Home Care Westchester NY - In-Home Health Care CT.
URL https://www.sterlingcare.com/resources/resources/diseases-and-conditions-library/view/your-heart-is-at-risk/

[176] B. D. MacNeill, H. C. Lowe, M. Takano, V. Fuster, I.-K. Jang, Intravascular modalities for detection of vulnerable plaque: current status, Arterioscler. Thromb. Vasc. Biol. 23 (8) (2003) 1333–1342. doi:10.1161/01.ATV.0000080948.08888.BF.

[177] H. Sakuma, Magnetic resonance imaging for ischemic heart disease, J Magn Reson Imaging 26 (1) (2007) 3–13. doi:10.1002/jmri.20976.

[178] T. Saam, T. S. Hatsukami, N. Takaya, B. Chu, H. Underhill, W. S. Kerwin, J. Cai, M. S. Ferguson, C. Yuan, The vulnerable, or high-risk, atherosclerotic plaque: noninvasive MR imaging for characterization and assessment, Radiology 244 (1) (2007) 64–77. doi:10.1148/radiol.2441051769.

[179] K. C. Briley-Saebo, W. J. M. Mulder, V. Mani, F. Hyafil, V. Amirbekian, J. G. S. Aguinaldo, E. A. Fisher, Z. A. Fayad, Magnetic resonance imaging of vulnerable atherosclerotic plaques: current imaging strategies and molecular imaging probes, J Magn Reson Imaging 26 (3) (2007) 460–479. doi:10.1002/jmri.20989.

[180] F. Hyafil, J.-C. Cornily, J. E. Feig, R. Gordon, E. Vucic, V. Amirbekian, E. A. Fisher, V. Fuster, L. J. Feldman, Z. A. Fayad, Noninvasive detection of macrophages using a nanoparticulate contrast agent for computed tomography, Nat. Med. 13 (5) (2007) 636–641. doi:10.1038/nm1571.

[181] D. P. Cormode, E. Roessl, A. Thran, T. Skajaa, R. E. Gordon, J.-P. Schlomka, V. Fuster, E. A. Fisher, W. J. M. Mulder, R. Proksa, Z. A. Fayad, Atherosclerotic Plaque Composition: Analysis with Multicolor CT and Targeted Gold Nanoparticles1, Radiology 256 (3) (2010) 774–782. doi:10.1148/radiol.10092473.

[182] M. Nahrendorf, F. A. Jaffer, K. A. Kelly, D. E. Sosnovik, E. Aikawa, P. Libby, R. Weissleder, Noninvasive vascular cell adhesion molecule-1 imaging identifies inflammatory activation of cells in atherosclerosis, Circulation 114 (14) (2006) 1504–1511. doi:10.1161/CIRCULATIONAHA.106.646380.

[183] F. S. Villanueva, E. Lu, S. Bowry, S. Kilic, E. Tom, J. Wang, J. Gretton, J. J. Pacella, W. R. Wagner, Myocardial Ischemic Memory Imaging With Molecular Echocardiography, Circulation 115 (3) (2007) 345–352. doi:10.1161/CIRCULATIONAHA.106.633917.
URL https://www.ncbi.nlm.nih.gov/pmc/articles/PMC4142344/

[184] A. Protti, B. Lavin, X. Dong, S. Lorrio, S. Robinson, D. Onthank, A. M. Shah, R. M. Botnar, Assessment of Myocardial Remodeling Using an Elastin/Tropoelastin Specific Agent with High Field Magnetic Resonance Imaging (MRI), J Am Heart Assoc 4 (8). doi:10.1161/JAHA.115.001851.

[185] Phinikaridou Alkystis, Lacerda Sara, Lavin Begoña, Andia Marcelo E., Smith Alberto, Saha Prakash, Botnar René M., Tropoelastin, Circulation: Cardiovascular Imaging 11 (8) (2018) e007303. doi:10.1161/CIRCIMAGING.117.007303.
URL https://www.ahajournals.org/doi/10.1161/CIRCIMAGING.117.007303

[186] D. P. Cormode, T. Skajaa, Z. A. Fayad, W. J. M. Mulder, Nanotechnology in medical imaging: probe design and applications, Arterioscler Thromb Vasc Biol 29 (7) (2009) 992–1000. doi:10.1161/ATVBAHA.108.165506.
URL https://www.ncbi.nlm.nih.gov/pmc/articles/PMC2844987/

[187] M. W. Ahmad, W. Xu, S. J. Kim, J. S. Baeck, Y. Chang, J. E. Bae, K. S. Chae, J. A. Park, T. J. Kim, G. H. Lee, Potential dual imaging nanoparticle: Gd2o3 nanoparticle, Scientific Reports 5 (2015) 8549. doi:10.1038/srep08549.
URL https://www.nature.com/articles/srep08549

[188] D. Pan, C. O. Schirra, A. Senpan, A. H. Schmieder, A. J. Stacy, E. Roessl, A. Thran, S. A. Wickline, R. Proska, G. M. Lanza, An early investigation of ytterbium nanocolloids for selective and quantitative "multicolor" spectral CT imaging, ACS Nano 6 (4) (2012) 3364–3370. doi:10.1021/nn300392x.

[189] Y. Liu, K. Ai, J. Liu, Q. Yuan, Y. He, L. Lu, A high-performance ytterbium-based nanoparticulate contrast agent for in vivo X-ray computed tomography imaging, Angew. Chem. Int. Ed. Engl. 51 (6) (2012) 1437–1442. doi:10.1002/anie.201106686.

[190] Y. Liu, J. Liu, K. Ai, Q. Yuan, L. Lu, Recent advances in ytterbium-based contrast agents for in vivo X-ray computed tomography imaging: promises and prospects, Contrast Media Mol Imaging 9 (1) (2014) 26–36. doi:10.1002/cmmi.1537.

[191] O. Rabin, J. M. Perez, J. Grimm, G. Wojtkiewicz, R. Weissleder, An X-ray computed tomography imaging agent based on long-circulating bismuth sulphide nanoparticles, Nature Materials 5 (2) (2006) 118–122. doi:10.1038/nmat1571.

[192] J. M. Kinsella, R. E. Jimenez, P. P. Karmali, A. M. Rush, V. R. Kotamraju, N. C. Gianneschi, E. Ruoslahti, D. Stupack, M. J. Sailor, X-ray computed tomography imaging of breast cancer by using targeted peptide-labeled bismuth sulfide nanoparticles, Angew. Chem. Int. Ed. Engl. 50 (51) (2011) 12308–12311. doi:10.1002/anie.201104507.

[193] H. Aviv, S. Bartling, I. Grinberg, S. Margel, Synthesis and characterization of Bi2o3/HSA core-shell nanoparticles for X-ray imaging applications, Journal of Biomedical Materials Research Part B: Applied Biomaterials 101B (1) (2013) 131–138. doi:10.1002/jbm.b.32826.
URL https://onlinelibrary.wiley.com/doi/abs/10.1002/jbm.b.32826

[194] A. Jakhmola, N. Anton, H. Anton, N. Messaddeq, F. Hallouard, A. Klymchenko, Y. Mely, T. F. Vandamme, Poly-caprolactone tungsten oxide nanoparticles as a contrast agent for X-ray computed tomography, Biomaterials 35 (9) (2014) 2981–2986. doi:10.1016/j.biomaterials.2013.12.032.

[195] J. Liu, J. Han, Z. Kang, R. Golamaully, N. Xu, H. Li, X. Han, In vivo near-infrared photothermal therapy and computed tomography imaging of cancer cells using novel tungsten-based theranostic probe, Nanoscale 6 (11) (2014) 5770–5776. doi:10.1039/c3nr06292a.

[196] K. Dong, Z. Liu, J. Liu, S. Huang, Z. Li, Q. Yuan, J. Ren, X. Qu, Biocompatible and high-performance amino acids-capped MnWO4 nanocasting as a novel non-lanthanide contrast agent for X-ray computed tomography and T(1)-weighted magnetic resonance imaging, Nanoscale 6 (4) (2014) 2211–2217. doi:10.1039/c3nr05455a.

[197] J. F. Hainfeld, D. N. Slatkin, T. M. Focella, H. M. Smilowitz, Gold nanoparticles: a new X-ray contrast agent, Br J Radiol 79 (939) (2006) 248–253. doi:10.1259/bjr/13169882.

[198] D. A. Giljohann, D. S. Seferos, W. L. Daniel, M. D. Massich, P. C. Patel, C. A. Mirkin, Gold nanoparticles for biology and medicine, Angew. Chem. Int. Ed. Engl. 49 (19) (2010) 3280–3294. doi:10.1002/anie.200904359.

[199] D. Stojanov, A. Aracki-Trenkic, D. Benedeto-Stojanov, Gadolinium deposition within the dentate nucleus and globus pallidus after repeated administrations of gadolinium-based contrast agents-current status, Neuroradiology 58 (5) (2016) 433–441. doi:10.1007/s00234-016-1658-1.

[200] E. Y. Zhuravleva, New materials for medicine, M. G. Zuev and L. P. Larionov, Eds., Yekaterinburg: Ural. Otd., Ross. Akad. Nauk, 2006, Inorg Mater 43 (9) (2007) 1034–1034. doi:10.1134/S0020168507090221.
URL https://doi.org/10.1134/S0020168507090221

[201] P. J. Bonitatibus, A. S. Torres, G. D. Goddard, P. F. FitzGerald, A. M. Kulkarni, Synthesis, characterization, and computed tomography imaging of a tantalum oxide nanoparticle imaging agent, Chem. Commun. (Camb.) 46 (47) (2010) 8956–8958. doi:10.1039/c0cc03302b.

[202] P. J. Bonitatibus, A. S. Torres, B. Kandapallil, B. D. Lee, G. D. Goddard, R. E. Colborn, M. E. Marino, Preclinical Assessment of a Zwitterionic Tantalum Oxide Nanoparticle X-ray Contrast Agent, ACS Nano 6 (8) (2012) 6650–6658. doi:10.1021/nn300928g.
URL https://doi.org/10.1021/nn300928g

[203] M. H. Oh, N. Lee, H. Kim, S. P. Park, Y. Piao, J. Lee, S. W. Jun, W. K. Moon, S. H. Choi, T. Hyeon, Large-scale synthesis of bioinert tantalum oxide nanoparticles for X-ray computed tomography imaging and bimodal image-guided sentinel lymph node mapping, J. Am. Chem. Soc. 133 (14) (2011) 5508–5515. doi:10.1021/ja200120k.

[204] C.-L. Chang, H. S. Fogler, Controlled Formation of Silica Particles from Tetraethyl Orthosilicate in Nonionic Water-in-Oil Microemulsions, Langmuir 13 (13) (1997) 3295–3307. doi:10.1021/la961062z.
URL https://doi.org/10.1021/la961062z

[205] n. Arriagada, n. Osseo-Asare, Synthesis of Nanosize Silica in a Nonionic Water-in-Oil Microemulsion: Effects of the Water/Surfactant Molar Ratio and Ammonia Concentration, J Colloid Interface Sci 211 (2) (1999) 210–220. doi:10.1006/jcis.1998.5985.

[206] U. Schubert, Chemistry and Fundamentals of the Sol–Gel Process, in: The Sol-Gel Handbook, John Wiley & Sons, Ltd, 2015, pp. 1–28. doi:10.1002/9783527670819.ch01.
URL https://onlinelibrary.wiley.com/doi/abs/10.1002/9783527670819.ch01

[207] M. D. Butts, R. E. Colborn, P. J. B. JR, A. M. Kulkarni, B. A. Hay, A. S. Torres, B. C. Bales, M. E. Marino, Nanoparticle contrast agents for diagnostic imaging (Nov. 2013).
URL https://patents.google.com/patent/US8574549B2/en

[208] W. St\"{o}ber, A. Fink, E. Bohn, Controlled growth of monodisperse silica spheres in the micron size range, Journal of Colloid and Interface Science 26 (1) (1968) 62–69. doi:10.1016/0021-9797(68)90272-5.
URL http://www.sciencedirect.com/science/article/pii/0021979768902725

[209] B. Baruwati, R. S. Varma, Synthesis of Monodispersed Tantalum(V) oxide Nanospheres by an Ethylene Glycol Mediated Route, Crystal Growth & Design 10 (8) (2010) 3424–3428. doi:10.1021/cg100123q.
URL https://doi.org/10.1021/cg100123q

[210] J. A. D. Feijter, J. Benjamins, F. A. Veer, Ellipsometry as a tool to study the adsorption behavior of synthetic and biopolymers at the air–water interface, Biopolymers 17 (7) (1978) 1759–1772. doi:10.1002/bip.1978.360170711.
URL https://onlinelibrary.wiley.com/doi/abs/10.1002/bip.1978.360170711